

https://dspace.org/

Property correlations in materials for energy applications utilising advanced X-ray and photophysical techniques

Shnier, Adam

2024
https://hdl.handle.net/10539/37515

Downloaded from a DSpace repository. https://dspace.org/



Property correlations in materials for energy applications utilising advanced X-ray and photophysical techniques

by

Adam Shnier

(608825)

Thesis

Submitted in fulfilment of the requirements for the degree

Doctor of Philosophy

in

Chemistry

in the Faculty of Science, University of the Witwatersrand, Johannesburg, South Africa

Supervisor: Prof. David Billing

Co-supervisors: Prof. Daniel Wamwangi, Prof. Caren Billing

June 2023

DECLARATION

I declare that this thesis is my own, unaided work. It is being submitted for the Degree of Doctor of Philosophy at the University of the Witwatersrand, Johannesburg. It has not been submitted before for any degree or examination at any other University.

_____

(Signature of candidate)

____**12**__day of ___**June**___**2023**____at____**Johannesburg**

Abstract

Hybrid-perovskites are an emerging material class, with optoelectronic properties highly suited for photovoltaics (PV), light emitting diode, and phosphor applications. Among PVs they have seen a meteoric rise in photon conversion efficiency (PCE) over the last decade, exceeding that of thin-film and multi-crystallite Si PV. Despite the rapid evolution of PCE within these materials, environmental and thermal stability remain the major impediment for their commercial viability. The use of A site cation substitution is an approach to enhance performance and stability in the versatile family of hybrid perovskites.

In this thesis, the effect of A site cation substitution on the phase transitions and stability is explored, for both cations which appropriate for the $APbX_3$ structure, and a larger organo-ammonium cation (A′) associated with the formation of lower dimensionality hybrid perovskite derivative structures. Both approaches are reported in literature to provide exceptional stability and PV PCE improvements.

The hybrid perovskite $(FAPbI3)_{0.85}(MAPbBr3)_{0.15}$ was characterised using *in-situ* variable-temperature X-ray diffraction (VT-XRD) data. Sequential Rietveld refinements were employed to explore phase stability, and structural characteristics of this data (FA = formamidinium, MA = methylammonium). A more gradual $\alpha \rightarrow \beta$ phase transition is identified, compared to the single cation systems in literature. The effect of Caesium (Cs) substitution on $(FAPbI3)_{0.85}(MAPbBr3)_{0.15}$ has been characterised across a series of VT-XRD measurements through parametric Rietveld refinement. The introduction of Cs is correlated to divergence between the observed onset temperatures for the cubic to tetragonal and $a^0a^0a^0$ to $a^0a^0c^+$ (Glazer notation) transitions in the systems, which occur for the α/β phase transition.

Beyond the performance improvements, the inclusion of larger A′ cations, have been associated with structural defect passivation, and electronic property tuning due to quantum confinement effects in perovskite derived structures. Hybrid perovskite based systems containing the A′ cation, propylammonium are studied to gain insights on phase stability and phase formation, and optical properties in these systems. The phase composition, structural

properties, and optical properties of $(PABr)_{2x}(MABr)_{1-x}PbBr_2$, $0 \leq x \leq 1$ and $PABr/MAPbBr_3$ systems were studied using *ex-situ* XRD, optical absorbance spectroscopy. and photoluminescence measurements (PA = propylammonium). These systems were fabricated by spin coating, with the former from a single well mixed precursor solution and latter a 2-stage process, where PABr was added in various concentrations to a fully formed $MAPbBr_3$ film. Mixed phase compositions were formed of $(PA)_2MA_{n-1}PbBr_{3n+1}$ 2-dimensional (2D) and quasi-2D hybrid-perovskite derivative phases, where n determines the layer thickness and $n = \infty$ is a $MAPbBr_3$ phase. The difference in the kinetic and thermodynamic aspects of film formation in these systems was leveraged to propose a set of controlling factors responsible for the phase formation behaviour of the varied formation conditions.

Structure and outputs of the thesis

This thesis is divided into 3 parts:

1. Part I Chapter 1-3: Theory
2. Part II Chapter 4-5: Investigative methods
3. Part III Chapter 6-9: Investigation
4. Part III Chapter 10: General conclusions

Research outputs comprises of *primary* and *secondary* publications, as well as oral and poster presentations in local and international conferences.

The primary publications are a direct part of this thesis including, two published manuscripts. The secondary publications are related to the development of X-ray diffraction (XRD) related knowledge and techniques towards this thesis.

Primary publications:

1. Greenland, C., **Shnier, A.**, Rajendran, S.K., Smith, J.A., Game, O.S., Wamwangi, D., Turnbull, G.A., Samuel, I.D., Billing, D.G. and Lidzey, D.G., **(2020)**. Correlating phase behavior with photophysical properties in mixed-cation mixed-halide perovskite thin-films. *Advanced Energy Materials*, 10(4), p.1901350.

    - Greenland, C.: Sample fabrication, optical measurements and analysis, final editing and manuscript submission .
    - Shnier, A.: Model development and analysis of the variable temperature X-ray diffraction data-set. Draft and editing of the associated sections in the manuscript.

2. **Shnier, A.**, Otieno, F., Billing, C., Wamwangi, D. and Billing, D.G., **(2023)**. Robust Arduino controlled spin coater using a novel and simple gravity chuck design *HardwareX*, 14, p.e00422.

    - Shnier, A.: Conducted the research, prototyping, testing, and wrote the manuscript.
    - Otieno, F.: Contributed atomic force microscopy data and the associated

samples.

- Billing, C.: Supervised the research and reviewed the manuscript.
- Wamwangi, D.: Supervised the research and reviewed the manuscript.
- Billing, D.G.: Supervised the research and reviewed the manuscript

Secondary publications:

In the following publications I , A. Shnier was responsible for the range of XRD measurements and related analysis contained, including grazing-incidence XRD for 5. The manuscript draft and final editing of these papers were carried out by the first authors of the respective publications.

1. Masenya, M., Halindintwali, S., Madhuku, M., Mtshali, C., Cummings, F., **Shnier, A.**, Billing, D. and Wamwangi, D., **(2022)**. The effects of the thickness of the sandwiched layer and of the annealing time on induced nanostructures during solid state dewetting of a metal-semiconductor-substrate triple layer structure. *Surfaces and Interfaces*, 29, p.101783.

2. Mwendwa, G., Wamwangi, D., Mathe, B., Erasmus, R., Billing, D., **Shnier, A.** and Madhuku, M., **(2021)**. Elastic and magnetic properties of Tb-MnO based thin-films. *Journal of Magnetism and Magnetic Materials*, 537, p.168199.

3. Gatsi, N.C., **Shnier, A.**, Mujaji, M. and Wamwangi, D., **(2021)**. Indirect and direct excitation of Nd^{3+} ions in as-deposited and annealed Nd^{3+}-doped ZnO films. *Journal of Luminescence*, 237, p.118198.

4. Kirui, J.K., Olaleru, S.A., Jhamba, L., Wamwangi, D., Roro, K., **Shnier, A.**, Erasmus, R. and Mwakikunga, B., **(2021)**. Elucidating the Trajectory of the Charge Transfer Mechanism and Recombination Process of Hybrid Perovskite Solar Cells. *Materials*, 14(11), p.2698.

5. Falch, A., **Shnier, A.**, Wamwangi, D., Billing, D., Kriek, R.J. and Geldenhuys, Z., **(2019)**. The Effect of Sputtered $Pt_{40}Pd_{57}Al_3$ Thin Film Thickness on SO_2 (aq) Electro-Oxidation. *Electrocatalysis*, 10, pp.399-405.

6. Fortuin, A.C., Jackson, C., Carleschi, E., Doyle, B.P., **Shnier, A.**, Kriek, R.J., Ray, S.C., Billing, D.G., Wamwangi, D., Scherer, G.G. and Levecque, P.B., **(2018)**. Towards practical applications of EQCN experiments to study

Pt anchor sites on carbon surfaces. *Electrocatalysis*, 9, pp.271-278.

Conferences: Oral

1. **Shnier, A. (2021)** "A brief overview: considerations and effects in X-ray diffraction" *Eastern Africa Microscopy 2020 Workshop* (Virtual presentation)

2. **Shnier, A. (2020)** "A very brief overview: considerations and effects in X-ray diffraction" *Eastern Africa Microscopy 2020 Workshop* (Virtual presentation)

3. **Shnier, A.**, Greenland, C., Smith, J.A. Wamwangi, D., Lidzey D. and Billing, D.G., **(2019)** "The effect of Cs content in the structural and photophysical properties in mixed cation hybrid-perovskites." (oral presentation) at *SA-ESRF Light Source Conference* in Johannesburg, RSA 11-13 Nov 2019.

4. **Shnier, A.**, Billing, C., Wamwangi, D. and Billing, D.G., **(2017)** "Impedance of Methylammonium Lead Iodide and Band Gap Tuning 2-Bromoethylammonium Lead Halide" at the *Materials and Energy Research Group Workshop*, at Societa Dante Alighieri, Johannesburg, RSA

Conferences: Poster

1. **Shnier, A.**, Greenland, C., Smith, J.A. Wamwangi, D., Lidzey D. and Billing, D.G., **(2023)** "Cs in mixed cation hybrid-perovskites, the use of parameter trends in parametric Rietveld refinements for low signal-to-noise data." at *the Southern Africa Powder Diffraction Conference* at Midgard Country Estate, Namibia 16-21 Apr 2023

2. **Shnier, A.**, Billing, C., Wamwangi, D. and Billing, D.G., **(2019)** "Emerging Thin Film Energy Materials Focusing on Hybrid-Perovskite and Kesterite Materials" for *The Annual CoE-SM/AMSEN Student Presentation Workshop*, South Africa 21 May 2019

3. **Shnier, A.**, Greenland, C., Smith, J.A. Wamwangi, D., Lidzey D. and Billing, D.G., **(2019)** "The effect of Cs content in the structural and photophysical properties in mixed cation hybrid-perovskites." at *SA-ESRF Light*

Source Conference in Johannesburg, RSA 11-13 Nov 2019. (poster)

4. **Shnier, A.**, Billing, C., Wamwangi, D. and Billing, D.G., **(2018)** "Emerging Thin Film Energy Materials Focusing on Hybrid-Perovskite and Kesterite Materials" at *The 16th European Powder Diffraction Conference*, in Edinburgh, UK.

5. **Shnier, A.**, Billing, C., Wamwangi, D. and Billing, D.G., **(2017)** "Structure-property correlation of thin-films for energy applications" at the *South African Institute of Physics Conference* in Stellenbosch, RSA.

Prototypes

1. Spin coater Version 1 (2018), [Shnier, 2019]

2. Spin coater Version 2 (2019), Chapter 5

3. Spin coater Version 3 (2021), Chapter 5

4. UV-ozone substrate cleaner (2019)
   - Shnier, A.: Design and initial prototype
   - Ozone Purification Technology, South Africa: Final product assembly

Acknowledgements

I would like to thank my supervisors, Prof. Daniel Wamwangi, Prof. Caren Billing, Prof. Dave Billing for their guidance and support.

I would also like to thank Prof. Rudolph Erasmus, Prof. Manuel Fernandez for their guidance, insights, and access to equipment. Additionally, Sikhumbuzo Masina, Dr. Joel Smith, Dr. Francis Otieno, Gerry Germishuizen, Sandile Kumalo, Dr. Jacques Gerber, Dr. Deran Reddy, Dr. Kevin Stone, Dr. Claire Greenland, and Gugulethu Nkala for their insights, and in the case of Joel and Skhu, enthusiasm and insights.

The financial assistance of the National Research Foundation (NRF), University of the Witwatersrand - Material and Energy Research Group (MERG), DSI-NRF Centre of Excellence in Strong Materials (CoE-SM) and UKRI GCRF-START towards this research is hereby acknowledged. The use of resources and equipment of the University of the Witwatersrand is hereby acknowledged.

Lastly, I would like to show appreciation for the support of my family, friends, and colleagues.

Contents

Front matter **II**

Abstract III

Structure and outputs of the thesis V

Acknowledgements IX

List of figures XIX

List of tables XXVIII

Abbreviations and definitions XXX

I Theory **1**

1 Getting to know hybrid-perovskites **2**

1.1 What are hybrid-perovskites? 3

1.2 Structure and potential of hybrid-perovskites 5

1.2.1 Basic perovskite structure 5

1.2.2 Layered hybrid-perovskites derivative structures 6

1.2.3 Shockley-Queisser limits 9

1.2.4 Goldschmidt tolerance and octahedral factors 11

1.3 Importance of compositional tuning in hybrid perovskites . . . 12

1.4 Applications of layered hybrid-perovskite derivatives and related organic cations. 14

1.5 Structure transitions in perovskites 15

1.5.1 Glazer notation 15

1.5.2 Temperature induced phase changes 16

1.5.3 Phase stability at operational temperatures 20

2 Electronic properties and defects **21**
2.1 Performance metrics of photovoltaics 22
2.2 Band structure, defects, and related processes 24
2.2.1 Electronic band structure of hybrid-perovskites 24
2.2.2 Band-gap in low dimensional hybrid-perovskites derivatives. 27
2.2.3 Polarons 30
2.3 Defects 32
2.3.1 Point defects 33
2.3.2 Grain boundaries, interfaces, and surfaces 34
2.3.3 Defect and ion mobility, and current-voltage curve hysteresis 37
2.3.4 Surface and grain boundary passivation 38
2.4 Optical transitions: Luminescence and absorption 40
2.4.1 Optical absorption 41
2.4.2 Photoluminescence 43

3 Rietveld refinement and TOPAS-Academic **44**
3.1 Sample effects in diffraction patterns 46
3.1.1 Sample related peak broadening: Crystallite size and micro-strain 46
3.1.2 Crystallite size broadening 47
3.1.3 Micro-strain broadening 48
3.1.4 Determination of crystallite size and micro-strain . . . 48
3.2 Effects of sample preparation, packing and mounting 50
3.2.1 Intensity errors: Crystallite size 50
3.2.2 Preferred orientation 51
3.2.3 Sample alignment effects 53
3.3 Peak shape and profile 55
3.3.1 Standard reference materials 56
3.3.2 Analytical peak profiles 57
3.3.3 Fundamental parameter peak profiles 58

3.4 Agreement factors . . . 59
3.5 Limitations of powder X-ray diffraction . . . 61
3.5.1 Light atoms in a heavier matrix . . . 61
3.5.2 Resolving atom identity . . . 62
3.5.3 Real Structure? . . . 63
3.6 Diffraction pattern fingerprinting . . . 65
3.6.1 Assignment considerations . . . 65
3.7 Indexing . . . 67
3.8 Whole powder pattern decomposition . . . 68
3.8.1 Individual peak fitting . . . 68
3.8.2 Pawley and Le Bail refinements . . . 69
3.9 Structure based (Rietveld) refinement . . . 70
3.9.1 Atomic position refinement . . . 70
3.9.2 Atomic displacement parameter . . . 71
3.10 Sequential and parametric refinement . . . 72
3.10.1 Sequential refinement . . . 73
3.10.2 Parametric refinement . . . 74

II Investigative methods 76

4 Investigative methods 77
4.1 Overview . . . 79
4.2 List of chemicals and materials . . . 79
4.3 Organo-amine salt synthesis . . . 79
4.4 Thin film fabrication . . . 81
4.4.1 Substrate cleaning . . . 81
4.4.2 Substrate etching . . . 81
4.4.3 Precursor solution for spin coating . . . 82
4.4.4 Precursor solutions and dilutions for spin coating $(A'X)_{2x}$ $(AX)_{1-x}PbX_2$ systems . . . 82
4.4.5 Spin coating . . . 83

4.4.6 Sample annealing 84
4.5 Powder samples from thin-films 85
4.6 Optical spectroscopy 87
4.6.1 Optical absorption 87
4.6.2 Photoluminescence measurements 88
4.6.3 Stokes shift 89
4.7 X-ray diffraction: sample mounting and measurement 89
4.7.1 Sample preparation and instrument effects of packed capillary XRD samples 90
4.7.2 X-ray diffraction measurements of thin-films 90
4.8 Instrument profiles for XRD data modelling 91
4.8.1 Capillary samples on a Bruker D8 Advance (CuKα) . . 92
4.8.2 Flat plate sample on a Bruker D2 Phaser (CoKα) . . . 93
4.9 Structure modelling of X-ray diffraction data 94
4.9.1 X-ray diffraction refinement method 94
4.9.2 Modelling an organic cation in a 3D framework 95
4.9.3 Two and four octahedra unit cells 96
4.9.4 Modelling of layered 2D perovskite thin-films 99

5 Robust Arduino controlled spin coater using a novel and simple gravity chuck design 100

III Investigation 122

6 Modelling of $(FAPbI_3)_{0.85}(MAPbBr_3)_{0.15}$ thin-film *in-situ* diffraction data 123
6.1 Overview 125
6.2 Data collection methodology 126
6.3 Data visualisation and individual peak fitting 127
6.3.1 Method 127
6.4 Literature structure refinements 132
6.4.1 Methodology 132

6.4.2 Results and discussion . . . 133
6.5 Investigative Le Bail refinements . . . 136
6.5.1 Methodology . . . 136
6.5.2 Results and discussion . . . 137
6.6 Structure modelling . . . 142
6.6.1 Methodology . . . 142
6.6.2 Results and discussion . . . 144
6.7 Sequential refinements . . . 150
6.7.1 Methodology . . . 150
6.7.2 Discussion . . . 152
6.7.3 Conclusion . . . 163
6.7.4 Future work . . . 163

7 Correlating phase behavior with photophysical properties in mixed-cation mixed-halide perovskite thin-films 166

8 Parametric Rietveld refinement for structural analysis of triple cation hybrid-perovskites 169

8.1 Introduction . . . 171
8.2 Powder X-ray diffraction measurements . . . 172
8.3 Visual and Pawley refinement based comparisons . . . 172
8.4 Parametric refinements . . . 175
8.4.1 Reference refinements of VT-XRD data . . . 176
8.4.2 Parametric refinement of VT-XRD data . . . 177
8.5 Discussion . . . 181
8.6 Conclusion . . . 185

9 Phase composition and photophysical properties of the mixed PA/MA-based lead bromide perovskites systems 188

9.1 Introduction . . . 190
9.2 Structure determination and modelling: $(PABr)_{2x}(MABr)_{1-x}PbBr_2$ . . . 191
9.3 Compositional study of the $(PABr)_{2x}(MABr)_{1-x}PbBr_2$ system . . . 196

9.3.1 XRD: Observations and trends . . . 199
9.3.2 XRD: Data quality, comparing data-sets . . . 201
9.3.3 Photophysical properties . . . 205
9.4 2-Step: PABr on $MAPbBr_3$ . . . 212
9.4.1 Phases as a function of dosage . . . 213
9.4.2 Annealing of 0.1 and 0.2 M films . . . 214
9.4.3 $(\mathbf{PABr})_{\mathbf{2x}}(\mathbf{MABr})_{\mathbf{1-x}}\mathbf{PbBr_2}$, $x = 0.8$ sample ageing . 215
9.5 Discussion . . . 217
9.5.1 Conclusion and future work . . . 221

10 General conclusions **223**

Bibliography **229**

Appendices **257**

A Appendix for Chapter 5 **258**

B Appendix for Section 6.4 and 6.5 **277**
B.1 Additional literature structure refinements on $(FAPbI_3)_{0.85}(MAPbBr_3)_{0.15}$ . . . 277
B.2 Le Bail fits on $(FAPbI_3)_{0.85}(MAPbBr_3)_{0.15}$ for pattern indexing 282

C FAMA sequential refinement sets **283**
C.1 Diffraction patterns list for Chapter 6 . . . 285
C.2 Raw data visualisation . . . 286
C.3 Rigid body models . . . 287
C.3.1 Rigid body model for Pb-X octahedra . . . 287
C.3.2 Rigid body model for FA . . . 288
C.4 Structure model refinements on representative diffraction patterns . . . 288
C.5 Least-square Rietveld refinement based sets . . . 292
C.5.1 Set 1: $a = b$ . . . 292
C.5.2 Set 2: lattice parameters from projections . . . 293
C.5.3 Set 3: distorted octahedra . . . 294

C.5.4 Set 4: a!=b . . . 294
C.5.5 Set 5: a=b, Pb-Oh offset . . . 294
C.5.6 Set 6:: a!=b, Pb-Oh offset . . . 295
C.5.7 Set 7:: a=b, Pb-Oh offset . . . 295
C.5.8 Set 8: repetition of Set 1 . . . 296
C.5.9 Set 8b: repetition of Set 1, rotation limits adjusted . . 296
C.6 Monte-Carlo assisted least-square Rietveld refinement based sets . . . 299
C.6.1 Set 9: Based on Set 3, Distorted Oh . . . 299
C.6.2 Set 10: a=b, Pb-Oh offset . . . 300
C.6.3 Set 11 and 12: a=b, Pb-Oh offset, fixed Pb-X bond length . . . 302
C.6.4 Set 13: a,b,c fixed, Pb-Oh offset, fixed Pb-X bond length 302
C.6.5 Set 14, 14b and 15b: a,b,c fixed, Pb-Oh offset . . . 303
C.6.6 Set 15: a,b,c fixed, Pb-Oh offset . . . 304
C.6.7 Set 16: a,b,c fixed, Pb-Oh offset . . . 305
C.6.8 Set 17: a,b,c fixed, Pb-Oh offset, halide in $P4$ symmetry 305
C.6.9 Set 18: a=b, Pb-Oh offset, halide in $P4$ symmetry . . . 306
C.6.10 Set 19: a=b, Pb-Oh offset, halide in $P4$ symmetry . . . 306
C.6.11 Set 20: a=b, Pb-Oh offset, halide in $P4$ symmetry . . . 307
C.6.12 Set 21: a,b,c fixed, Pb-Oh offset, halide in $P4$ symmetry 310
C.6.13 Set 22: a,b,c fixed, Pb-Oh offset and halide in $P4$ symmetry . . . 310
C.6.14 Set 23: a=b, Pb-Oh offset and halide in $P4$ symmetry 312
C.6.15 Set 26: a=b, Pb-Oh offset and halide in $P4$ symmetry 315
C.6.16 Additional literature data . . . 316
C.6.17 Selected correlation tables . . . 317

D CsFAMA parametric refinement sets 319
D.1 Visual data comparison . . . 319
D.2 Parametric refinement sets . . . 320

E Mixed PA/MA based lead bromide perovskites systems 323

E.1 Optical data for Chapter 9 . . . 325
E.1.1 Photoluminescence measurements of: $(PABr)_{2x}(MABr)_{1-x}PbBr_2$ . . . 325
E.2 Optical data reprocessed from literature for Chapter 9 . . . 327
E.3 Additional XRD reference patterns and structures for Chapter 9 . . . 328
E.3.1 List of structure database searches for organo-lead halides 328
E.3.2 Single-crystal structure of HOEABr . . . 329
E.3.3 TOPAS rigid body for PA_2PbBr_4 model in Chapter 9 . 332
E.3.4 PA_2PbBr_4 structure file determined in Chapter 9 . . . 333
E.3.5 Additional reference pattern comparisons . . . 334
E.3.6 Additional structures model visualisation . . . 335
E.4 Additional optical data and diffraction patterns for Chapter 9 . . . 336
E.4.1 Additional diffraction patterns of PABr on $MAPbBr_3$. 336
E.4.2 Ageing data on $(PABr)_{2x}(MABr)_{1-x}PbBr_2$ . . . 338
E.5 The identification of a problematic diffraction pattern $x = 0.95$ of $(PABr)_{2x}(MABr)_{1-x}PbBr_2$ 9-step dataset. . . . 341
E.6 Reproducibility of $(PA)_2PbBr_4$ thin-films and the effect of short-term sample ageing . . . 344
E.7 Structure parameters of layered lead bromide perovskites . . . 345

F Python code **346**
F.1 Sequential refinement process . . . 346
F.2 Parametric refinement input generation . . . 347
F.2.1 Input file template . . . 348
F.2.2 Python script . . . 351
F.3 Modelling a photoluminescence peak with pseudo-Voigt and split pseudo-Voigt models . . . 353
F.3.1 Setting up equations for pseudo-Voigt and split pseudo Voigt models . . . 353
F.3.2 Modelling of split pseudo-Voigt peaks . . . 354

F.3.3 Modelling of multiple pseudo-Voigt peaks 356

List of Figures

1.1 The perovskite structure in (a) polyhedra and (b) ball and stick representations. The structure has an ABX_3 composition ratio represented as follows, A: green, B: grey, X: purple. . . . 6

1.2 Ruddlesden-Popper layered perovskite structures in the form $(A')_2(A)_{1-n}M_nX_{3n+1}$, for $n \in 1, 2, 3$, COD 2102938, 4003234, 4003235. 7

1.3 Layered perovskite structure with $n = 1$ (a) $(A')_2(A)_{1-n}M_nX_{3n+1}$ Ruddlesden-Popper phase, Section 9.2 (b) $(A')(A)_{1-n}M_nX_{3n+1}$ Dion-Jacobson phase with (0,0.5) effective layer offset, COD 7207478. In these figures (dark grey octahedra) are $PbBr_6^{4-}$ and (light blue spheres) are nitrogen atoms. 8

1.4 Shockley-Queisser (SQ) limits in % PCE for a single junction photovoltaic cell as a function of band-gap and band-gaps values of Pb-based hybrid-perovskite materials with the legend ordered by band-gap value. **SQ limits** at 25 ° C under AM 1.5G Spectral Irradiance (ASTM G173-03): [Rühle, 2016], **Band-gap values:** [Ma et al., 2017, Mannino et al., 2020, Tao et al., 2017, Jesper Jacobsson et al., 2016, Guillemoles et al., 2019]. 10

1.5 Hybrid perovskite structure with and without symmetric Glazer rotation about the c-axis ($a^0b^0c^+$). (a) $Pm\bar{3}m$ and (b) $P4/mbm$ phases at ambient and sub-ambient temperatures respectively. Created in Vesta using structures from Chapter 6. 16

2.1 (a) Current-density vs. voltage characteristics and (b) power-density vs. voltage characteristic, of a hybrid-perovskite photovoltaic. These illustrate V_{OC}, I_{SC}, P_{max} and the effect of scanning direction form a hysteresis. * This device was fabricated with the architecture FTO/ZnO/SnO_2/$Cs_{0.05}((FAPbI_3)_{0.83}(MAPbBr_3)_{0.17})_{0.95}$/Spiro-OMeTAD/Au during a lab visit to the *University of Sheffield, UK*. The related data-set is not explored in this dissertation. 22

3.1 Angular dependence of simulated crystallite size and strain broadening. 49

3.2 Standard error vs number of crystallites 51

3.3 Diffraction patterns collected on hybrid-perovskites thin-films showing (a) complete Debye-Scherrer diffraction rings and (b) segments, where the partial diffraction rings are due to preferred orientation in the sample. ** Synchrotron GIWAXS data collected at i07, Diamond Light Source, Didcot, UK. ** (a) superimposes a 2D pattern and its inverse to display a 180° arc of the diffraction ring in comparison to (b) which corresponds directly to the detector size.* 52

3.4 Height Error vs diffraction angle for a Bragg-Brentano diffraction geometry for selected displacement values. R = 70 mm, corresponding to a Bruker D2 Phaser desktop diffractometer. 54

4.1 Various stages of organo-amine salt synthesis, (a) Vacuum-assisted rotary evaporation of H_2O, (b) Organo-amine salt prior to washing (c) after diethyl-ether wash and (d) single-crystal XRD derived structure motif of HOEABr. 80

4.2 Sample annealing box designed and produced during this dissertation. (a) closed lid, (b) open lid containing four 12.5 x 12.5 mm photovoltaic samples. 85

4.3 Comparison of XRD patterns between (top) thin-film and (bottom) thin-film derived powder samples. Measurement times are presented and (00l) peaks identified with a turquoise vertical line. 86

4.4 A two octahedra unit cell of a Pb-X framework and a representative atom in place of the organic cation (a) with, and (b) without octahedral rotation about the c-axis (Glazer notation: $a^0a^0c^+$). Octahedra are represented in black with X atoms at their corners. Isolated atoms between the octahedra correspond to representative atoms for the A site organic cation. 97
4.5 A four octahedra unit cell of a Pb-X framework and a rigid body model organic cation. 98

6.1 PXRD measurements of $(FAPbI_3)_{0.85}(MAPbBr_3)_{0.15}$ on cooling. Heating data is presented in App. Figure C.1. (a) Diffraction patterns at 315, 150 and 80 K, *'s and x's mark additional peaks observed in the regions represented by the 150 and 80 K patterns respectively. (b) Diffraction intensity changes on cooling from 315 to 80 K. 128
6.2 $(FAPbI_3)_{0.85}(MAPbBr_3)_{0.15}$ on cooling, parameters from individual PVII peak fits, using peak indexing of a $Pm\bar{3}m$ perovskite across the temperature range for convenience. Dotted lines are included as a visual guide. 129
6.3 Structure fit, 1-315K $Pm\bar{3}m$-$(FAPbI_3)_{0.85}(MAPbBr_3)_{0.15}$ (α-phase) This explains the observed peaks completely with minor intensity mismatch. A FP instrument profile is used for this pattern. 134
6.4 Investigative structure fits on the pattern 14-150K. 135
6.5 Pattern fingerprinting comparison, 22-150K is overlaid with the peak positions and intensities of $P4/mbm$ $FAPbI_3$ (β phase) with a halide occupancy of $I_{0.85}Br_{0.15}$ modelled [Weber et al., 2018]. 136
6.6 Refinements using Le Bail structure agnostic fits on Data set 2018-09 137
6.7 Le Bail refinement on 22-150K data, Tetragonal, $P4/mbm$ $a = b$ =8.821/c =6.199, R_{Bragg} = 0.421. The intensities are well explained. (Data set 2018-10) 138
6.8 Lattice parameters from Le Bail fits using a $P4/mbm$ space group. (Data set 2018-10) 139

6.9 Le Bail refinements using a cubic $Pm\bar{3}m$ phase with a tetragonal $P4/mbm$ phase for comparison. A grey dashed vertical line is used to mark 260 K. (a) Unit cell parameter where $P4/mbm$ (average) is defined by $\frac{\frac{a}{\sqrt{2}}+\frac{b}{\sqrt{2}}+c}{3}$, (b) R_{wp} agreement factor (Data set 2018-10). 139

6.10 Set C (Cs0-setC): Rietveld refinements using a $P4$ space group to impart it's symmetry to the Pb-X octahedra. The vertical lines correspond to an amorphous contribution modelled in the refinements. 145

6.11 Set A (Cs0-setA): Rietveld refinements using a structure model with 4 octahedra with free rotation and lattice parameters determined by projections of Pb−X bonds. The vertical lines correspond to an amorphous contribution modelled in the refinements. 146

6.12 Set D (Cs0-setD): Rietveld refinements using a structure model with 2 octahedra with free rotation and lattice parameters constraints a=b, c is free. The vertical lines correspond to an amorphous contribution modelled in the refinements. 147

6.13 R_{wp} of Monte-Carlo assisted sequential refinements. The horizontal lines represent the boundaries of the 4 quartiles of R_{wp} values. The median value is represented by a red horizontal line. Open circles represent outliers. 153

6.14 Reproducibility of bi-directional sequential refinements in comparison to a Monte-Carlo assisted variation. 154

6.15 A comparison of lattice parameters between the Le Bail $P4/mbm$ refinements and Sets 19, 20 and 23. "$P4/mbm$ ave" refers to an average from the tetragonal unit cell parameters to reach a pseudocubic lattice parameter value. 155

6.16 A comparison of parameters in Sets 19, 20 and 23. 156

6.17 Pb-X bond lengths in Set 10 where a rigid body model is used and Set 23 using a $P4$ based symmetry constraint. 159

6.18 (left) Set 12: Effective octahedral rotation about the c-axis. This was evaluated by taking the absolute value of the difference in rotation about the c-axis of the 2 Oh in the unit cell. (right) average rotation about a and b axes. 160

6.19 Set 19, Position data of the halides between Pb atoms along the c-direction (labelled I3 and I6 in refinements) (left) Average magnitude of displacement in the c-direction between I3 and I6. (middle) rotation about the c-axis. This was evaluated by taking the absolute value of the difference in rotation about the c-axis of the 2 Oh in the unit cell. (right) average rotation about a and b axes. 161

8.1 (top) Cs0 data set, blue 1-315K, green 28-90K (bottom) Cs10 data set, blue&red 1-310K, green&red 25-90K. 173

8.2 Modelled peak intensity across 2θ of diffraction patterns at 310 K, ascribed to the perovskite α phase, presented using logarithmic intensity scale. 174

8.3 Modelled peak intensity comparison between room temperature and 90 K patterns in (a) Cs0, and (b) Cs10 data-sets, across 2θ (Cu Kα). 175

8.4 Cs5 diffraction patterns for refinement Set7, for 90 and 310 K. (red) modelled, (green) raw data, (grey) residual. 176

8.5 An overlay of *reference* (Set7) and *parametrised* (Set22) refinements for each sample set. (left) Pb-X-Pb bond angle showing octahedral tilt about the c-axis. (right) Lattice parameter ratio $\frac{a}{c\sqrt{2}}$, ($a = b$). (green lines) parametrised values, (green $\bullet$) freely refined values, (Brown X) freely refined values. 178

8.6 Cs10 diffraction patterns. Positions where perovskite β phase peaks would be expected are marked with a "$*$". 180

8.7 Overlayed c-axis length, axis ratio, and Pb-X bond length for Cs0, Cs5, Cs8 and Cs10 refinement sets (a-c) *reference* refinements.(d-f) *parametrised* refinements. 180

8.8 Tetragonal unit cell parameters of parametric refinement sets (a) a-axis, (b) c-axis. 184

9.1 Structure modelling of a Pb-Br framework of the layered $n = 1$ phase against the $(PA)_2PbBr_4$ XRD pattern (CoKα) 191

9.2 Structure modelling of a Pb-Br framework of the layered $n = 2$ and $n = 2$ phases against the $(PABr)_{2x}(MABr)_{1-x}PbBr_2$, $x = 0.8$ XRD pattern (CoKα), $n = 1$ model revision 8. 192

9.3 $(PABr)_{2x}(MABr)_{1-x}PbBr_2$, (13-step X-ray diffraction data-set) this data set was collected to 80° 2θ and plotted to 60° 2θ. 196
9.4 Refinements showing the faint $n = 1$ phase present at $x \leq 0.5$ in the $(PABr)_{2x}(MABr)_{1-x}PbBr_2$ (13-step X-ray diffraction dataset) 196
9.5 Selected individual refinements of $(PABr)_{2x}(MABr)_{1-x}PbBr_2$ (9-step X-ray diffraction dataset) 197
9.6 Diffraction derived unit cell parameters, normalised peak intensities, and crystallite size of $(PABr)_{2x}(MABr)_{1-x}PbBr_2$, both 9 and 13 step data-sets. 198
9.7 Optical data of the $(PABr)_{2x}(MABr)_{1-x}PbBr_2$ system. (a) Absorbance, (b) Normalised photoluminescence, and (c) absorbance with a y-scale chosen to highlight weaker features in (a). (13-step data-set) 202
9.8 Photoluminescence measurements of $(PABr)_{2x}(MABr)_{1-x}PbBr_2$, (blue) raw data, (orange) fitted function, (green) residual. Fits for the full data-set are provided in App. Figure E.1.1. (13-step data-set) 203
9.9 Photophysical data for the $(PABr)_{2x}(MABr)_{1-x}PbBr_2$ system. (a) Tauc derived band-gap values, open circle refer to faint features (b) photoluminescence (PL) peak maxima. (c) Tauc and PL optical bandgap for the 3D phase, (d) PL peak width, (e) PL peak asymmetry using a width ratio with an offset such that a positive value related to a greater width on the higher energy side. (13-step data-set) 204
9.10 Photoluminescence band-gap values plotted against the most probable layering number n for $PA_2MA_{n-1}PbBr_{3n+1}$ structures 207
9.11 Diffraction data of a $MAPbBr_3$ thin-film (a) as-deposited, and with post-annealing dynamic spin coating of 60 μl of (b) 0.1, (c) 0.2, (e) 0.6 M of PABr in isopropanol at 4000 rpm. (d) 40 μl, 0.6 M. . . . 212

9.12 Diffraction derived unit cell, micro-strain and crystallite size parameters of PABr/$MAPbBr_3$ as a function of annealing time at 90 °C. (a) $n = 1$ and $n = 3$ lattice parameters, (b) "perov" phase lattice parameters, (c) crystallite size and micro-strain for the $n = 3$ phase. 214

9.13 Ageing of $(PABr)_{2x}(MABr)_{1-x}PbBr_2$, $x = 0.8$ over 15 days. (a,b) diffraction derived lattice parameters, (b) modelled micro-strain and crystallite size, (d) Tauc band gap values. 216

B.1 Investigative structure fits on 1-315K. These use fundamental parameter peak profile described in Section 4.8.1. 280

B.2 Investigative structure fits on 22-150K. These use fundamental parameter peak profile described in Section 4.8.1. 281

C.1 PXRD measurements of $(FAPbI_3)_{0.85}(MAPbBr_3)_{0.15}$ showing the log() of diffraction intensity as a function of temperature. Measurements were taken on cooling followed by heating ordered in the figures chronologically from the top down. 286

C.2 Set C (Cs0-setC): Rietveld refinements using a $P4$ space group to impart it's symmetry to the Pb-X octahedra. 289

C.3 Set A (Cs0-setA): Rietveld refinements using a structure model with 4 octahedra with free rotation and lattice parameters determined by projections of Pb-X bonds. 290

C.4 Set D (Cs0-setD): Rietveld refinements using a structure model with 2 octahedra with free rotation and lattice parameters constraints $a = b$, c is free. 291

C.5 Set 1 292

C.6 Set 1 in $(FAPbI_3)_{0.85}(MAPbBr_3)_{0.15}$ analysis 298

C.7 Set 8 in $(FAPbI_3)_{0.85}(MAPbBr_3)_{0.15}$ analysis 298

C.8 Set 8b in $(FAPbI_3)_{0.85}(MAPbBr_3)_{0.15}$ analysis 298

C.9 Set 9: (left) Effective octahedral rotation about the c-axis. This was evaluated by taking the absolute value of the difference in rotation about the c-axis of the 2 Oh in the unit cell. (right) noisy rotation about the a and b axes 300

C.10 Set 10 in $(FAPbI_3)_{0.85}(MAPbBr_3)_{0.15}$ analysis 301

C.11 Set 14: (left) Effective octahedral rotation about the c-axis. This was evaluated by taking the absolute value of the difference in rotation about the c-axis of the 2 Oh in the unit cell. (right) noisy rotation about the a and b axes 304
C.12 Set 19 in $(FAPbI_3)_{0.85}(MAPbBr_3)_{0.15}$ analysis 308
C.13 Set 20 in $(FAPbI_3)_{0.85}(MAPbBr_3)_{0.15}$ analysis 309
C.14 Set 22 in $(FAPbI_3)_{0.85}(MAPbBr_3)_{0.15}$ analysis 311
C.15 Set 23 in $(FAPbI_3)_{0.85}(MAPbBr_3)_{0.15}$ analysis 313
C.16 Set 23: Thermal expansion in $(FAPbI_3)_{0.85}(MAPbBr_3)_{0.15}$ . . 314
C.17 Set 23 correlation tables for 315 and 80 K 317
C.18 Set 10 correlation tables for 315, 90 and 80 K 318

D.1 A visual comparison of Cs10 1-310K, 25-90K and 51-310K . . 320
D.2 Modelled intensities for the α phase of Cs0 and Cs0 compositions using refinements that only differ by the representative atoms' electron density.(blue) Cs0, (red) Cs10, (green) residue between Cs0 and Cs10. 320
D.3 Fit quality comparison between the (a) Cs0_21_2 and Cs0_23 refinement sets 321
D.4 Lattice parameters (left) a, (middle) b, and (right) lattice parameter ratio for (a) Cs0, (b) Cs5, (c) Cs8, and (d) Cs10 refinement sets on cooling and heating. Lattice parameters are presented in Å. 322

E.1 Photo-luminescence measurements of $(PABr)_{2x}(MABr)_{1-x}PbBr_2$ modelled using split pseudo-Voigt functions for single peak patterns and multiple symmetric pseudo-Voigt functions for the deconvolution of multi-peak patterns. A combination of *least-square* and *Nelder* regression methods were utilised in the fitting. 326
E.2 (a) Tauc plot modified from [Ma et al., 2022] with new intercepts drawn as solid lines using Inkscape, (b) Band-gaps extracted from Tauc intercepts. 327
E.3 Single-crystal XRD derived structure of HOEABr (a) motif, (b) packed unit cell, (c) hydrogen bond. (blue) nitrogen, (red) oxygen, (white) hydrogen. 329

E.4 Literature structure of $(HOEA)_2PbBr_4$, COD 4312212 with selected hydrogen bonds shown by purple lines. 331
E.5 X-ray diffraction pattern refinement of an $MAPbI_3$ sample prepared from thin-film samples. 334
E.6 XRD structure model of a Pb-Br framework of the layered $n = 2$ phase after reduction to an equivalent model in a $Cmce$ space group using ISOCIF [Stokes et al., 2017]. 335
E.7 PABr on $MAPbBr_3$ 336
E.8 PABr on $MAPbBr_3$ 337
E.9 Diffraction derived micro-strain and crystallite size parameters of PABr on $MAPbBr_3$ samples. (a,b) "w strain" are parameter values with micro-strain and the adjacent traces without micro-strain modelled in the refinement, (c,d) crystallite size and micro-strain refined parameters with each figure referring to a set with identical refinement considerations, (e) $MAPbBr_3$ lattice parameter for PABr coating of different molar concentrations using a volume (X μl) of 0.X M solution. 338
E.10 Ageing of $(PABr)_{2x}(MABr)_{1-x}PbBr_2$, optical absorption data over 14 days. 339
E.11 Ageing of $(PABr)_{2x}(MABr)_{1-x}PbBr_2$, $x = 0.8$, X-ray diffraction patterns over 14 days. 340
E.12 Interplanar spacing of the "perov 5.8 A" phase of $(PABr)_{2x}(MABr)_{1-x}PbBr_2$, $x = 0.8$, aged over 15 days. As a "perov 5.8 A" rather then a "perov 5.9 A" phase, this is considered a quasi-2D phase with a large n value as discussed in Section 9.3.1. 340
E.13 $(PABr)_{2x}(MABr)_{1-x}PbBr_2$, (9-step data-set, including $x = 0.95$) this data set was collected to 80° 2θ and plotted to 60° 2θ.341
E.14 Diffraction derived unit cell parameters and normalised peak intensities of $(PABr)_{2x}(MABr)_{1-x}PbBr_2$, both 9 and 13 step data-sets. 342
E.15 PA_2PbBr_4 thin-films prior to ageing. 344
E.16 PA_2PbBr_4 thin-films measured after 1, 3 and 15 days. 344
E.17 PABr salts, where older salt has a pink tint. (white) fresh, (pink) aged in a desiccator. 344

List of Tables

1.1 Space group and Glazer notation for hybrid-perovskite materials. 18
1.2 Select non-perovskite phases in a ABX_3 stoichiometry. 18
1.3 Phase transitions between α, β, γ, and δ perovskite derived phases. 19

3.1 Number of diffracting crystallites in 20 mm^3 for a specific instrument configuration is presented in [Smith, 2001] 51

4.1 Dilution scheme for $(A'X)_{2x}(AX)_{1-x}PbX_2$ systems. 83

6.1 Literature structures of similar systems 132
6.2 Le Bail refinements on $(FAPbI_3)_{0.85}(MAPbBr_3)_{0.15}$ (Data set 2018-09) 138
6.3 Summary of fit parameters 148
6.4 A summary of conditions used across refinement sets 9 to 26. 152

8.1 XRD derived significant points for the Cs based data-sets . . 181

9.1 Photoluminescence and Tauc derived bandgaps with literature comparisons for $PA_2MA_{n-1}PbBr_{3n+1}$ structures 206
9.2 Photoluminescence and Tauc derived bandgaps with calculated Stokes shift for the $MAPbBr_3$ based phase 209

C.1 Literature structures of similar systems 285
C.2 Dataset 201810 of in-situ XRD diffraction patterns. 285
C.3 Expanded summary of fit parameters 288
C.4 Set 23: Volume thermal expansion coefficients (α_V) 312

C.5 Table of selected lead halide bond lengths 316
C.6 Literature volume thermal expansion coefficients (α_V) for contrast against Table C.4 316

E.1 Tauc plot band-gap values for a $(PA)_2(MA)_{1-n}Pb_nBr_{3+n}$ system derived from Figure E.2a using Inkscape and plotted with assignments in Figure E.2b. 327
E.2 Sample displacement correction parameters for 9- and 13-step $(PABr)_{2x}(MABr)_{1-x}PbBr_2$ data-sets in millimetres. 341
E.3 Structural parameters of $(A')_2A_{n-1}Pb_nBr_{3n+1}$ and $APbBr_3$ perovskites. 345

Abbreviations and Definitions

List of abbreviations

- 2D: 2-dimensional
- 3D: 3-dimensional
- A: A small organic cation such as methylammonium, formamidinium, or an inorganic cation such as Cs.
- A′: An organic cation larger than formamidinium such as propylammonium, butylammonium, or 2-phenylethylammonium.
- AbsMax: The excitonic peak observed at the absorption maximum.
- App.: appendix
- COD: Crystallography Open Database, [hyperlink]
- csize: a Rietveld refinement parameter used in this work to refer to crystallite size.
- DFT: Density functional theory
- DMF: dimethyl formamide
- DMSO: dimethyl sulfoxide
- EXAFS: Extended X-ray absorption fine structure
- GI-XRD: grazing incidence X-ray diffraction
- ICSD: Inorganic Crystal Structure Database, [hyperlink]
- ITO: indium-tin oxide
- FTO: fluorine doped tin oxide
- LED: light emitting diode
- MA: methylammonium
- FA: formamidinium
- PA: propylammonium
- PL: photoluminescence
- PhEA: 2-phenylethylammonium
- PSD: position sensitive detector, a class of 1-dimensional detectors used in X-ray diffractometers.
- PV: photovoltaic
- PXRD: powder X-ray diffraction
- TOPAS: Brukers' software primarily intended for diffraction pattern modelling.
- VT-XRD: variable temperature X-ray diffraction
- WH: Williamson-Hall method for crystallite size and strain determina-

tion.
- WPPD: whole powder pattern decomposition
- X: a halide such as bromide or iodide.
- XANES: X-ray absorption near edge structure
- XRD: X-ray diffraction

Definitions

- 3D data-set/ 3-dimensional data-set: When used in the context of diffraction in this thesis, such a data set refers to 2θ and intensity as a function of a 3rd external variable, such as time, temperature, or composition.
- data poor: Where a model or function contains more variables than there are observables in a data-set.
- dynamic spin-coating: Spin-coating where a solution is applied while the spin coater is at speed.
- exciton: A bound electron and hole pair.
- fixed: In this document usage frequently refers to refinable parameters used for data modelling which are held at a constant value when *fixed*.
- global parameters: Parameters which are accessible throughout a program.
- point defect: A localised defect such as a vacancy, interstitial or anti-site substitution.
- site occupancy factor: Probability or fraction describing the degree to which a unit cell site is occupied by a given atom.
- tick: in plots or graphs ticks are short lines on an axis marking divisions across the axis. In a diffraction pattern similar ticks can be used inside the plot area to elude to the position of diffraction peaks. Multiple sets of ticks, differentiated by colour and vertical offset can be used in the presence of multiple phases to relate diffraction peaks their respective phases.

Part I

Theory

Chapter 1

Getting to know hybrid-perovskites

Contents

1.1 What are hybrid-perovskites? **3**

1.2 Structure and potential of hybrid-perovskites **5**

1.2.1 Basic perovskite structure 5

1.2.2 Layered hybrid-perovskites derivative structures . 6

1.2.3 Shockley-Queisser limits 9

1.2.4 Goldschmidt tolerance and octahedral factors . . 11

1.3 Importance of compositional tuning in hybrid perovskites **12**

1.4 Applications of layered hybrid-perovskite derivatives and related organic cations. **14**

1.5 Structure transitions in perovskites **15**

1.5.1 Glazer notation 15

1.5.2 Temperature induced phase changes 16

1.5.3 Phase stability at operational temperatures . . . 20

1.1 What are hybrid-perovskites?

Hybrid-perovskites (also called hybrid organic-inorganic perovskites) are a group of materials composed of an organic cation (A) which is typically an amine or imine, a metal such as Pb, Sn or a combination (M), and one or more halides (X). This takes the form AMX_3 composing of a 3-dimensional (3D) framework of M−X octahedra, Section 1.2.1. This can be extended to hybrid perovskite derivatives, such as the layered Ruddlesden-Popper phase, in which the connectivity is reduced by the introduction of a larger organo-amine cation (A′) separating the structure into layers of a controllable thickness, Section 1.2.2.

These materials exhibit exceptional optoelectronic properties, and have gathered wide interest as an *emerging* PV technology. This interest has extended beyond academic circles and has propelled the rapid development of hybrid-perovskite materials, primarily for photovoltaic applications [CNN, 2020, Nasdaq, 2015, NREL, 2023]. This is evident in their application in photovoltaics (PV) for which hybrid perovskites have seen rapid *research cell* efficiency gains from 14.1 % in 2013 to outperforming multi-crystalline and thin-film silicon PV in 2016 and closing in on single crystal silicon (26.1 % PCE) having reached 25.7 % PCE in 2023 [NREL, 2023] [1].

Hybrid perovskites have a direct band-gap and related high absorption coefficient, which allows for far less material use in device fabrication when compared to the indirect bandgap of silicon PV, discussed in Section 2.2. In addition all the layers required for hybrid-perovskite solar cells can be produced at low temperatures below 150 °C using potentially low cost solution processing techniques such as inkjet printing [Miyasaka, 2018]. As an example, the electron transport layer can be based on metal oxides including TiO_2 or SnO_2, and can be prepared as nanoparticle suspensions which can easily be deposited at low temperatures. The hole transport layer can be formed of materials such as NiO_x, or conductive organic polymers including PEDOT or Spiro-OMeTAD [Miyasaka, 2018]. This is compared to Si PV where an Si ingot is prepared at temperatures as high as 1900 °C which is almost paradoxical to their environmentally friendly image [Smets et al., 2015]. This impacts the *energy payback time* for Si PV, which further depends on device

[1] PCE: Photon conversion efficiency, this is defined in Section 2.1.

efficiency and utilisation, with an estimated ∼1.5 - 4.4 years, compared to a few months for hybrid perovskites [Schileo and Grancini, 2021, Yue et al., 2014].

The application of hybrid-perovskites is highly tunable and compositionally dependent exhibiting band gap values from the near infra-red (NIR) for $FAPbI_3$ across the visible spectrum reaching into the violet for $MAPbCl_3$ and low dimensional derivatives such as $(PhEA)_2PbBr_4$, Section 2.2.2 [Tao et al., 2017, Smith et al., 2014]. The effect of composition is discussed further in Section 1.3 with the utility of low dimensional structures in Section 1.4. This tunability, in combination with the materials' high photoluminescence quantum yields, open their application to low cost, high efficiency phosphors and light emitting diodes [Blancon et al., 2018, Congreve et al., 2017].

Additionally, hybrid perovskites can be designed in terms of shape, colour, and transparency, which has allowed their use as a multi-purpose, aesthetic and functional material in architectural design as demonstrated in windows of the SwissTech Convention Center at Ecole polytechnique fédérale de Lausanne. [Miyasaka, 2018, Romande Energie and Mediacom, 2013, Batmunkh et al., 2020]

Current challenges to the commercialisation of hybrid perovskites include environmental stability, thermal stability, and the toxicity of lead (Pb). The small organo-ammonium cations in hybrid perovskites are hydrophilic, in part due to their polarity, and can volatilise with the halide which is accelerated at elevated temperatures [Boyd et al., 2018]. Stability is strongly dependent on device composition and structure as discussed in Sections 1.3 and 1.2.4. Decomposition pathways related to defects and ion mobility can be mitigated through optimising material morphology and defect passivation, while encapsulation and surface coating are used to protect hybrid-perovskites from environmental factors [Boyd et al., 2018, Corsini and Griffini, 2020]. In regards to Pb toxicity, the partial substitution of Sn has been the most promising Pb reduction strategy. Sn, while also toxic, is less environmentally harmful per unit of weight. The lower PCEs currently achieved by $A(Pb, Sn)X_3$ devices offsets the benefit by requiring a larger quantity for the same power output, while $ASnX_3$ devices are not cur-

rently efficient enough to be considered a practical alternative [2] [Schileo and Grancini, 2021]. Pb is exceptionally toxic and efforts are required to minimise its environmental impact wherever possible. The potential benefits of the technology must be considered with the risks, which can and need to be mitigated though careful design, encapsulation and recycling [Chen et al., 2023, Schileo and Grancini, 2021].

We have established some of the attractive properties of hybrid-perovskites providing a degree of insight into their potential. While much progress has been made in their development, we are presented with device stability and lead toxicity as challenges to large scale commercialisation.

This work seeks to further knowledge in the field relating to: **(1)** Compositional tuning of the 3D hybrid perovskite and related temperature dependent phase transition in Chapters 6, 7, and 8, and **(2)** The phase formation and optical characteristics in hybrid-perovskite systems of a mixed dimensionality composition in Chapter 9

1.2 Structure and potential of hybrid-perovskites

1.2.1 Basic perovskite structure

The perovskite structure is composed of 3 atomic sites in an ABX_3 stoichiometry and at its simplest, a $Pm\bar{3}m$ space group. The structure is commonly portrayed either with the B site atoms at origin forming a primitive cubic sub-structure or alternatively with the X site at origin forming a face-centred cubic sub-structure. These two components are offset from each other by half a unit cell along an axis [3]. This forms a network of corner sharing octahedra. Figure 1.1 shows a perovskite structure with the B site at origin, this B-X framework leaves a cavity for the A site at (0.5,0.5,0.5). Lower sym-

[2] Scheleo and Grancini have assessed the potential impact of Pb in PV eluding to the massive 80 000 metric tons of Pb released into the atmosphere by the coal industry and natural Pb soil concentrations per kg multiples larger than the quantity of Pb in a 1 m^2 panel. [Schileo and Grancini, 2021]

[3] In this description an offset in any of the 3 axis is equivalent.

metry structures occur with octahedral tilt as a primary distortion from the symmetry of the $Pm\bar{3}m$ space group, this is further explored in Section 1.5.1.

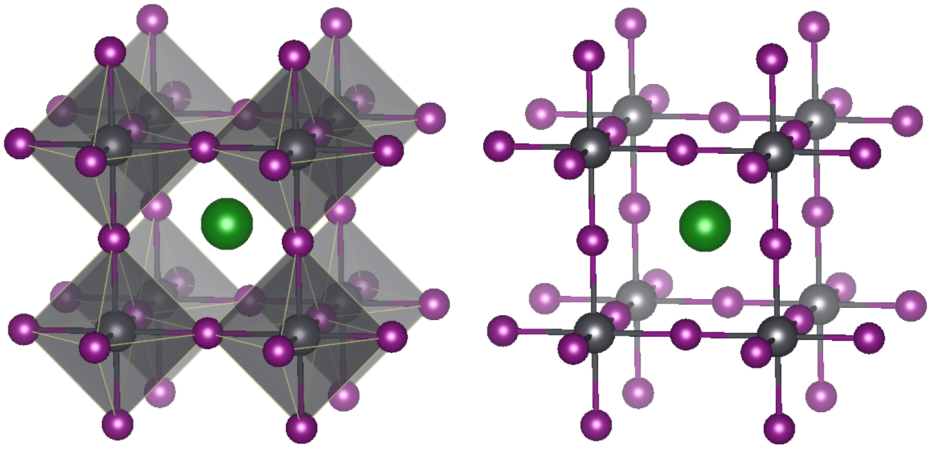

(a) (b)

Figure 1.1: The perovskite structure in (a) polyhedra and (b) ball and stick representations. The structure has an ABX_3 composition ratio represented as follows, A: green, B: grey, X: purple.

In hybrid-perovskites, the A site is an organic cation such as methylammonuim (MA), formamidinium (FA), the B site is a metal such as Pb or Sn, and the X site is a halide such as Br, Cl or I; the effects of such substitutions is discussed in Section 1.3 [4].

1.2.2 Layered hybrid-perovskites derivative structures

The 3D perovskite structure of corner sharing octahedra includes an A site occupied by an organic cation. Organic cations (A′) exceeding a size suitable for a stable 3D structure can lead to 2D perovskite derivatives such as the

[4]While the organics cation can be partially substituted with spherical inorganic cations including Cs^+ or Rb^+, the presence of a non-spherical organic cation is a defining feature across hybrid-perovskites. Entirely inorganic materials such as $CsPbI_3$ which can form perovskites are not hybrid-perovskites. [Chen et al., 2021]

Ruddlesden-Popper and Dion-Jacobson layered phases [5] [6]. These deviate from a true perovskite structure by separating one or more layers of corner sharing octahedra with organic cation layers reducing the dimensionality of the structure.

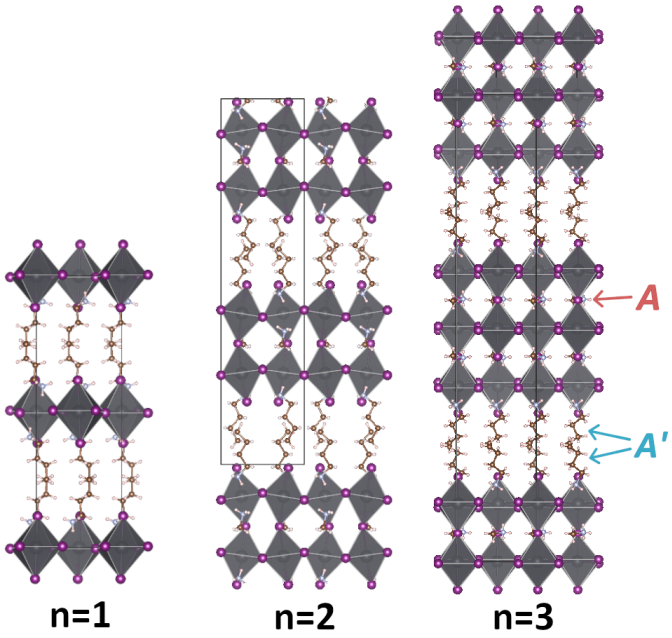

Figure 1.2: Ruddlesden-Popper layered perovskite structures in the form $(A')_2(A)_{1-n}M_nX_{3n+1}$, for $n \in 1, 2, 3$, COD 2102938, 4003234, 4003235.

Layered structures of the form $(A')_2(A)_{1-n}M_nX_{3n+1}$ consist of sets of n octahedra layers separated organic bilayer spacers, where A is the inter-octahedral cation, A′ is the organic cation separating layers of octahedra, M is a metal, X is a halide and n is the number of octahedra layers between organic layers in the layered perovskites, Figure 1.2. The A′ cations form hydrogen bonds with the halides of the metal halide framework forming an organic bilayer with cations hydrogen bonded to opposite sides of the bilayer, bound through van der Waals forces. When there is a relative in-plane offset of the octahedra layer sets by half a unit-cell in both axes of the plane (0.5,

[5]The Goldschmidt tolerance and octahedral factors to estimate the stability of a 3D perovskite based on the size of its constituents, as discussed in Section 1.2.4.

[6]The "2D" phases here are not true 2D structures as they have thickness, the "2D" terminology is used for consistency with literature.

0.5) this constitutes a Ruddlesden-Popper phase [Tremblay et al., 2019, Fu et al., 2021] [7].

Layered structures of the form $(A')(A)_{1-n}M_nX_{3n+1}$ bifunctional spacer cations (A') where opposite ends of the space form hydrogen bonds with the halides of the metal-halide framework on either end of the organic layer. When the in-plane offset between sets of n octahedra is (0,0) or (0.5,0) this constitutes a Dion-Jacobson phase [Tremblay et al., 2019, Fu et al., 2021]. Examples of $(A')_2(A)_{1-n}M_nX_{3n+1}$ and $(A')(A)_{1-n}M_nX_{3n+1}$ layered structures are presented in Figure 1.3.

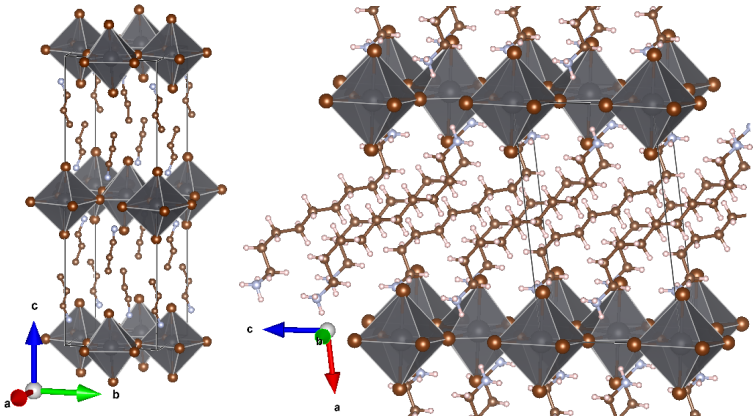

(a) (b)

Figure 1.3: Layered perovskite structure with $n = 1$ (a) $(A')_2(A)_{1-n}M_nX_{3n+1}$ Ruddlesden-Popper phase, Section 9.2 (b) $(A')(A)_{1-n}M_nX_{3n+1}$ Dion-Jacobson phase with (0,0.5) effective layer offset, COD 7207478. In these figures (dark grey octahedra) are $PbBr_6^{4-}$ and (light blue spheres) are nitrogen atoms.

[7] In the literature, $(A')_2(A)_{1-n}M_nX_{3n+1}$ structures tend to either have 2 sets of "*n*octahedra + organic*" layer pairs or a single set. Where two sets are used to describe the unit cell, the second set of octahedra tends to have a half unit cell in-plane displacement described by the symmetry operators of the unit cell. In cells with a single "*n*octahedra + organic*" set, an offset between layers is implemented using non-orthogonal unit cell axes in monoclinic or trigonal unit cells. This was observed for the structures considered in Table E.3. In most instances, n unique octahedra are used in literature as a sufficient basis for the structures.

1.2.3 Shockley-Queisser limits

Single junction devices

The theoretical efficiency limit of single junction photovoltaic (PV) devices can be estimated, as pioneered by Shockley and Queisser, based on the solar spectrum which can be estimated using a black-body radiation model, and the unavoidable energy losses and limitations of a single junction absorber. These include photons of energy lower than the band gap which cannot be absorbed, thermalisation losses from photons with energy higher than the band gap, and radiative recombination which are fundamentally unavoidable [8] [Rühle, 2016, Queisser, 2009, Shockley and Queisser, 1961].

The effect of band-gap on the Shockley-Queisser limit for a single junction PV and it's relation to hybrid-perovskites is illustrated in Figure 1.4. We see a Shockley-Queisser limit for a single junction cell approaching 33 % PCE. The bandgap of $MAPbI_3$ is 1.55 eV, slightly higher than the band-gap required for the peak theoretical efficiency [Futscher and Ehrler, 2016]. $FAPbI_3$ has a lower band gap of 1.47 eV. Compositional tuning of these perovskites is suitable for engineering structures with an intermediate band-gap, as considered further in Section 1.3 [Zhenyi et al., 2020].

Tandem solar cells

The concept of tandem solar cells involves forming a multi-junction cell with a layer stack incorporating two absorber materials with different band gaps for an extended photoabsorption window. This can be in the form of electrically isolated, or connected cells which are optically coupled to absorb different parts of the solar spectrum. The larger band gap material will be on top as photons smaller than the band gap will pass through to the second junction. This reduces losses from thermalisation of high energy photons, allowing improved PCEs. Tandem cell provide higher possible PCEs with a SQ based limit of 45.1 % for a tandem cell of Si and a second absorber with a bandgap

[8] Little attention was initially given to this work with 8 citations in the first five years, since then the Shockley-Queisser limit became renowned in the field.

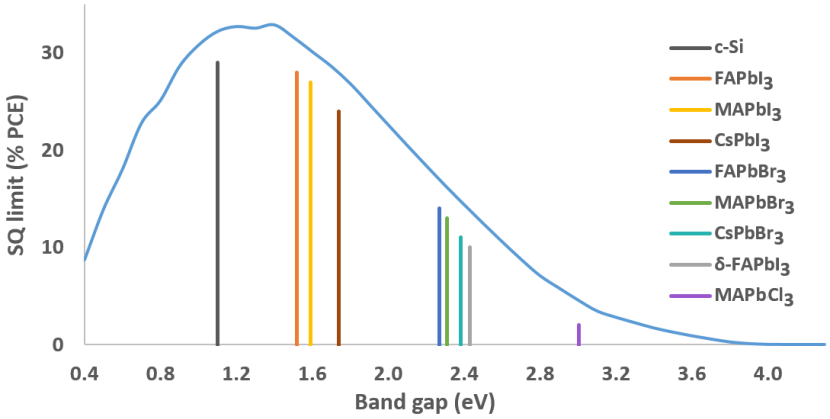

Figure 1.4: Shockley-Queisser (SQ) limits in % PCE for a single junction photovoltaic cell as a function of band-gap and band-gaps values of Pb-based hybrid-perovskite materials with the legend ordered by band-gap value.

SQ limits at 25 ° C under AM 1.5G Spectral Irradiance (ASTM G173-03): [Rühle, 2016],

Band-gap values: [Ma et al., 2017, Mannino et al., 2020, Tao et al., 2017, Jesper Jacobsson et al., 2016, Guillemoles et al., 2019].

of 1.73 eV in a series configuration. Futscher *et al.* investigated various configurations with *series* being the simplest and having the narrowest range near the maximum efficiency while a 4-terminal design provided a very wide range of bandgaps that have a limit exceeding 44 % PCE with a maximum limit calculated to 45.3 % [Futscher and Ehrler, 2016, Pazos-Outon et al., 2017]. The band-gaps afforded through compositional tuning and reducing dimensionality of the hybrid perovskites allows controlled energy tuning for use in multi-junction PV [Eperon et al., 2016, Stoumpos et al., 2017]. Hybrid-perovskite/Si tandem cells fabricated at *Helmholtz-Zentrum Berlin* (2022) have achieved efficiencies of 32.5 % [NREL, 2023].

Further gains in PCE have been achieved by increasing the number of junctions (multi-junction devices) with the theoretical limits reaching 65.4 % (1 sun, AM1.5) [9] [Marti and Araújo, 1996]. A prime example of this is a 6-junction cell reaching 39.2 % produced at NREL [Geisz et al., 2020]. This device is an engineering feat consisting of 140 layers [10].

[9]The use of a concentrator to provide greater illumination results of a theoretical efficiency of 85 % for a multi-junction cell (AM1.5).

[10]Geisz *et al.* achieved a PCE of 47.1 % using a 6-junction cell under concentrated illumination

1.2.4 Goldschmidt tolerance and octahedral factors

The relative size of various components of the perovskite affects how well each atom or molecule fits into a given structural position. The Goldschmidt tolerance factor provides a measure of how close the relative atom sizes are to a geometrically ideal value. This is quantified by the geometric equation of the Goldschmidt tolerance factor as given in Equation 1.1. Therein, r refers to atomic radius and the subscripts A, M and X refer to the respective sites in the AMX_3 perovskite as described in 1.2.1 [Gebhardt and Rappe, 2019]. The tolerance factor is very useful in that it contributes to understanding the stability of mixed composition perovskites. A tolerance factor (t) of 1 represents the ideal set of radii for a perovskite and deviations from this can result in structural distortion. Stable halide perovskite structures are expected to form for t values in the range 0.71 to 1.05. Lower tolerance factors are related to greater structural distortion with an effectively linear trend between octahedral tilt and cation size [11] [Filip et al., 2014, Gebhardt and Rappe, 2019, Li et al., 2016, Zhu et al., 2018]. In structures where the bonding connectivity remains unchanged these distortions can largely be described by Glazer notation, Section 1.5.1 [Glazer, 1972, Gebhardt and Rappe, 2019].

$$t = \frac{r_{\mathrm{A}} + r_{\mathrm{X}}}{\sqrt{2}(r_{\mathrm{M}} + r_{\mathrm{X}})} \tag{1.1}$$

The further the ratio is from the ideal, the more probable a non-perovskite structure will offer greater stability, which may result in a change in structural connectivity. The perovskite phase is composed of corner sharing $BX_6{}^{4-}$ octahedra with the A^+ cation filling the voids created by this structure. Low values of t may result in the more favourable formation of point or edge sharing tetragonal or orthorhombic structure, while high values can make a face sharing hexagonal phase more favourable [12].

[11] Filip *et al.* plots bond angle against steric size in Figure 3a of [Filip et al., 2014]

[12] Organic cations too large (A′) for the 3D framework cause the formation of a structure with reduced dimensionality such as the hexagonal 2H ABX_3 or layered $(A')_2MX_4$ structures as described in Section 1.2.2 [García-Fernández et al., 2019].

Another useful measure is the octahedral factor which is the ratio between the size of metal (Pb or Sn) cation and the halide $\mu = r_M/r_X$. A small μ would suggest that there is insufficient space around the metal cation for the formation of the 6 M-X bonds of the octahedra to be favourable. A lower limit of $\mu = 0.442$ is suggested in the work of Li *et al.*, with a few exceptions [Li et al., 2016].

In the case of hybrid perovskites, the non-spherical molecular nature of organic cations adds complexity to the determination of the ionic radius [13] Similarly bonds between atoms can affect their electron density distribution, changing the effective ionic radii. For MA the ionic radius is estimated to be a value between 2.03 and 2.38 Å depending on the theoretical or semi-empirical approach used [Gebhardt and Rappe, 2019]. This provides a wide range of uncertainty. The tolerance factor is further limited by its inability to take account of bond energies in the structure. These are some of the factors contributing to the presence of outliers from the favourable ranges of t and μ presented in literature. Such halide perovskite outliers include $TlMnI_3$ with $t = 0.910, \mu = 0.377$ and $CsBeF_3$ with $t = 1.107, \mu = 0.541$ [Li et al., 2008, Chen et al., 2015b]. While the tolerance factor has been instrumental in the engineering of mixed composition hybrid perovskites, it does not exclude the possibility of outliers in the observed trend. [Chen et al., 2015b, Li et al., 2008, Gebhardt and Rappe, 2019]

1.3 Importance of compositional tuning in hybrid perovskites

The electronic properties of hybrid-perovskites is highly tunable and compositionally dependent. The $APbI_3$ perovskites have band-gap values in the range ∼1.4 - 1.7 eV (NIR to red) [14] with the lower end of this range most suitable for single junction PV as illustrated by the Shockley-Queisser limits

[13] An empirical correction factor to the cation radii been introduced in literature as a "globularity factor", which considers the ratio of surface area of a cation to the surface area of a sphere of equal volume as an expression of anisotropy [Gholipour et al., 2017].

[14] NIR: near infra-red

in Section 1.2.3 [Tao et al., 2017]. $APbBr_3$ devices have a larger band-gap closer to 2.3 eV (green) which is better suited as a layer in tandem PV where the bandgap can be further increased into the violet using Cl or reducing the dimensionality of the structure, Section 2.2.2 [Mannino et al., 2020]. Intermediate band-gaps between these structures are accessible using mixed compositions and intermediate dimensionalities. This adds to the hybrid-perovskites versatility in PV and luminescent applications.

The structure is further tunable through its A site cation which has a substantial, yet smaller and less direct effect on band-gap, and A is essential for the stability of the structure as formalised by the Goldschmidt tolerance factor, Section 1.2.4.

Considering $MAPbI_3$ as the *base* structure with a Goldschmidt tolerance factor (t) of 0.964 [Gholipour et al., 2017]. The substitution of the larger FA cation or smaller Br halide into the A and X sites respectively increase t and has been reported to stabilise the structure, and improve stability to moisture. Similarly the introduction of Cs, MA and Rb into $FAPbI_3$ reduces the tolerance factor, improved thermodynamic stability, improves the long term stability, and reduces moisture sensitivity [Boyd et al., 2018, Chen et al., 2021].

Compositional tuning in hybrid-perovskites has been instrumental in the optimisation of single junction PV cells, and tandem or multi-junction devices. It has played a strong role in the pursuit of high performing hybrid perovskite devices with greater stability. It has been invaluable in the engineering of a wide range of properties including optoelectronic properties (i.e. band-gap), stability, defect properties, morphology, etc. [Miyasaka, 2018, Jung and Park, 2015, Grätzel, 2017]. Most of the highest performing single junction hybrid perovskite PVs make use of mixed compositions. Many of these make use of a selection from $(Cs, FA, MA)Pb(I, Br, Cl)_3$ with FA and I forming the majority of the composition (commonly > 70 %) for the cation and anion respectively with device lifetimes reaching many hundreds of hours [15] [Koo et al., 2020, Liu et al., 2020, Jeong et al., 2020, Cho et al., 2018, Zheng et al., 2017].

[15] These lifetime includes devices under illumination, high humidity, and/or elevated temperatures.

The composition can further be tuned with organo-amine cations larger than what is suitable for the perovskite structure. These are known to be capable of passivating surface and grain boundary defects, improving PCE in PVs, and can form derivative structures with tunable optoelectronic properties, as discussed in Section 1.4.

1.4 Applications of layered hybrid-perovskite derivatives and related organic cations.

The inclusion of larger organic cations (A′) into and on hybrid-perovskite based structures have been targeted for photovoltaic, light emitting diode, and phosphor applications. [Dohner et al., 2014, Wang et al., 2017b] These A′ molecules have been used in the literature as an additive, a component in the hybrid-perovskite precursor solution, an additional layer in optoelectronic devices, or a coating in the case of nanoparticle phosphors.

As major components in a structure, A′ molecules have been used in the formation of 2D or quasi-2D layered hybrid perovskites [16] such as the Ruddlesden-Popper and Dion-Jacobson phases described in Section 1.2.2 These structures act as self-organised quantum wells in which there is reduced band dispersion compared to the 3D perovskite structure, increasing the band-gap. The width of the well can be readily tuned as a multiple of the size of the constituent PbX_6^{4-} with large layers forming quasi-2D structures allowing a wide range of band-energies to be formed between that of the 2D and 3D band-gap. The dimensionality and band dispersion can be further reduced, increasing the band-gap, with the example of the 1 dimensional 2H hexagonal polytype. The electronic structure and band-gap of hybrid-perovskite and related derivatives is discussed further in Section 2.2.

The inclusion of A′ can improve stability by passivating defects at surfaces and grain boundaries, which greatly improves device performance for both photovoltaic and luminescent applications [Wu et al., 2022]. The passivation grain boundary defects further acts to reduce ion migration and prevent

[16] These are technically perovskite derived structures rather than perovskites.

irreversible film degradation from the loss of MA^+ and I^- ions. [17] [Chen et al., 2020, Kang and Park, 2019, Xia et al., 2023]. These larger organics are hydrophobic, protecting the moisture sensitive hybrid-perovskite bulk from H_2O dependent degradation pathways [Grancini and Nazeeruddin, 2019, Zheng et al., 2017, Xia et al., 2023]. The low dimensionality structures have gained attention for use as low cost, high performance optoelectronic semiconductors. [Blancon et al., 2018, Congreve et al., 2017]. The 2D and quasi-2D structures formed with the inclusion of A′ cations, present a larger band-gap which can be optimised for tandem or multi-junction photovoltaics, light emitting diodes, or phosphors [Congreve et al., 2017, Stoumpos et al., 2017]. The effect of A′ molecules in hybrid-perovskite and for the formation of derivative structures were shown to be a practical means of engineering the properties, and improving the performance of optoelectronic device.

1.5 Structure transitions in perovskites

1.5.1 Glazer notation

The perovskite structure can be described as a network of corner sharing octahedra, and Glazer notation is a formalisation describing tilts in such a system. It makes use of 3 letters, where the 3 positions they fill refer to the a, b and c axes in order. Where a letter is used for more than one position, it refers to the tilt angle being the same magnitude for both axes. A distinction between symmetric, asymmetric, or no rotation is made by use of a superscript "+", "−" or "0" above each letter. Symmetric rotation refers to when successive layers of octahedra in the axis direction rotate in the same magnitude and direction. In the asymmetric case the rotation direction alternates for successive layers [Glazer, 1972, Howard and Stokes, 1998, Howard and Stokes, 2002, Stokes et al., 2002].

When a perovskite is undistorted without tilt, it can be described by the notation $a^0a^0a^0$ which corresponds to a $Pm\bar{3}m$ space group (SG). This describes the α phase of hybrid-perovskites, Figure 1.5. Symmetric or asymmetric rotation about the c-axis can be described by $a^0a^0c^+$ (SG: $P4/mbm$)

[17] Surface passivation further addressed in Section 2.3.4.

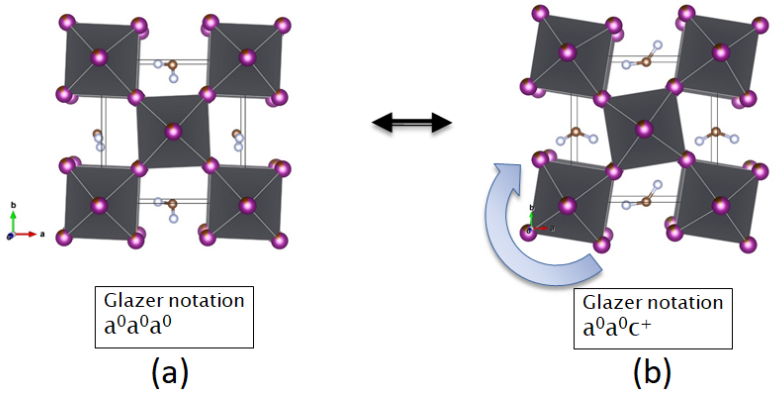

Figure 1.5: Hybrid perovskite structure with and without symmetric Glazer rotation about the c-axis ($a^0b^0c^+$). (a) $Pm\bar{3}m$ and (b) $P4/mbm$ phases at ambient and sub-ambient temperatures respectively. Created in Vesta using structures from Chapter 6.

and $a^0a^0c^-$ (SG: $I4/mcm$) respectively. These correspond to the β phase of $FAPbI_3$ and $MAPbI_3$ respectively. At lower temperatures, perovskites show lower symmetry structures and this is reflected in the octahedral tilts between the α, β, and γ phases of the perovskite structures presented in Table 1.1.

Glazer notation is useful in describing and understanding perovskite structures in terms of octahedral tilts, it does not consider bond length and bond angle distortions within the octahedra eluding to its limitations [Howard and Stokes, 1998, Fabini et al., 2017]. The notation has been extended to account for displacement of the metal cation using an additional subscript as put forward in the work of Stokes *et al.* 2002 [Stokes et al., 2002].

1.5.2 Temperature induced phase changes

The hybrid-perovskite structure consists of a framework of corner sharing octahedra with organic cations occupying the space between these octahedra. The phase changes in hybrid-perovskites occur alongside tilting of these metal halide octahedra, and the evolution of constraints on rotation of the organic cation [Binek et al., 2015, Fabini et al., 2017, Glazer, 1972, Yin et al., 2015].

Hybrid-perovskites contain non-spherical organic cations which are unable to perfectly fit the A lattice site between the octahedra. This is expressed in the organic cations rotational freedom across the various perovskite phases and corresponding temperature ranges. In the high temperature α phase of $MAPbI_3$ and $FAPbI_3$, the thermal energy available is sufficient to readily overcome the hydrogen and electrostatic bonding which MA^+ and FA^+ can participate in allowing it to rotate relatively freely. With the example of $MAPbI_3$, the cations of the α phase are disordered, slightly favouring orientations along the unit cell axes [Fabini et al., 2017, Weller et al., 2015b]. The octahedra $Pb - I - Pb$ bonds are effectively at 180° in line with a $a^0a^0a^0$ Glazer notation and $Pm\bar{3}m$ for this phase. [18] The relationship between octahedra tilts and space-groups are expressed in Howard and Stokes 2002 publication [Howard and Stokes, 2002].

In the β phase, the organic cations' degree of freedom is reduced with the framework of $PbX_6{}^{4-}$ octahedra rotated about the c-axis, breaking the $Pm\bar{3}m$ symmetry, and resulting in an anisotropic site for the cation. In the case of $MAPbI_3$, this is described by the Glazer notation $a^0b^0c^-$ for the framework and the associated $I4/mcm$ space group, Table 1.1. The cation is restricted to a more limited set of rotations such as those described by Fabini *et al.* for FA^+ [19]. The extent of the limitation increases with decreasing temperature. In the example of $MAPbI_3$, this rotation changes the shape of the cavity in which the organic cation is disordered, favouring orientations of the organics' C-N bond parallel or anti-parallel to the a or b axes. This is accompanied by a displacement of the organic cation from its "ideal" position with the NH_3 group closer to the I atoms forming hydrogen bonds and some distortion of the octahedra [Weller et al., 2015b, Fabini et al., 2017].

The low temperature orthorhombic γ phase forms with additional breaking of symmetry through octahedral tilts and structural distortions, Table 1.1. The unit cell of the resulting structure can be subsequently described in a $Pna2_1$ or $Pnma$ space group. At the cryogenic temperatures employed to form the $MAPbI_3$ γ phase, MA^+ is confined by the hydrogen bonding be-

[18] In [Weller et al., 2015b] the position of the heavy atoms were refined from X-ray diffraction data while neutron diffraction was required to refine the position of the organic cations.

[19] Fabini *et al.* calculated the energy of the rotation paths for FA^+ in α, β, and γ perovskite phases [Fabini et al., 2017].

Table 1.1: Space group and Glazer notation for hybrid-perovskite materials.

Composition	γ	β	α	Reference
$MAPbI_3$	$Pnma$	$I4/mcm$	$Pm\bar{3}m$	[Weller et al., 2015b]
	$(a^+b^-b^-)$	$(a^0a^0c^-)$	$(a^0a^0a^0)$	
$FAPbI_3$	$P4/mbm$	$P4/mbm$	$Pm\bar{3}m$	[Fabini et al., 2017]
	(disordered tilts)	$(a^0a^0c^+)$	$(a^0a^0a^0)$	
$CsPbI_3$	$Pnma$ (62)		$Pm\bar{3}m$	[Trots and Myagkota, 2008]
	$(a^+b^-b^-)$		$(a^0a^0a^0)$	
	$Pbnm$ (62)	$P4/mbm$	$Pm\bar{3}m$	[Näsström et al., 2020]
	$(a^+b^-b^-)$	$a^0a^0c^+$	$(a^0a^0a^0)$	[Howard and Stokes, 2002]

Table 1.2: Select non-perovskite phases in a ABX_3 stoichiometry.

Composition	Space group	Temperature (K)	Reference
$FAPbI_3$	$P6_3/mmc$	220	[Chen et al., 2016]
$FAPbI_3$	$P6_3/m$	15	[Chen et al., 2016]

tween its $-NH_3$ group and the halide. The shape of MA^+ with the NH_3 group on the end of its long axis is a better fit for its site between the tilted octahedra at low temperature, and forms stronger hydrogen bond with the halide, allowing a less "frustrated freezing" compared to FA^+. The $FAPbI_3$ γ phase has been modelled as various structures in literature including $P4/mbm$, a $P4bm$ supercell, and in the work of Weber *et al.*, a disordered phase. With FA^+, the NH^+ group is at the centre of the long axis, this contributes to frustrated freezing and greater disorder of the octahedra tilts in the γ phase as described by Fabini *et al.*. This is more consistent with a structure assignment of a supercell or disordered phase[Binek et al., 2015, Boinapally, 2015, Chen et al., 2021, Fabini et al., 2017, Weller et al., 2015b, Weber et al., 2018].

This can be extended to similar hybrid-perovskite systems, which will vary in the relative stability between these perovskite phases and additional derivative non-perovskite phases, such as the hexagonal δ phase of $FAPbI_3$ and orthorhombic δ phase of $CsPbI_3$. This is reflected in the transition temperatures and non-perovskite phases as presented in Tables 1.3 and 1.2 respectively.

The stability of phases, and the temperature where phase transitions occur in a perovskite or hybrid-perovskite system, is influenced by chemical

Table 1.3: Phase transitions between α, β, γ, and δ perovskite derived phases.

Composition	$\beta \rightarrow \gamma$ (K)	$\alpha \rightarrow \beta$ (K)	$\gamma \rightarrow \alpha$	Reference
$MAPbI_3$	165	327		[Weller et al., 2015b]
$MAPb(Br_{0.1}I_{0.9})_3$	∼152	∼330		[Lehmann et al., 2019]
$MAPb(Br_{0.2}I_{0.8})_3$	∼125	∼300		[Lehmann et al., 2019]
$FAPbI_3$	140	275		[Fabini et al., 2017]
$FAPbI_3$	140	285		[Fabini et al., 2016]
$FAPbI_3$	130.2 - 141.2	280		[Kawachi et al., 2019]
$FAPbI_3$			438	[Li et al., 2016]
$FAPbI_3$		∼282		[Weber et al., 2016]
$(Cs_{0.1}FA_{0.9}PbI_3$	149	300		[Kawachi et al., 2019]
$(Cs_{0.15}FA_{0.85})PbI_3$			398	[Li et al., 2016]
$(Cs_{0.3}FA_{0.7})PbI_3$			373	[Li et al., 2016]
$(FA_{0.9}MA_{0.1})PbI_3$		283		[Weber et al., 2016]
$(FA_{0.2}MA_{0.8})PbI_3$		257		[Weber et al., 2016]
$CsPbI_3$	457	506	556	[Näsström et al., 2020]
$CsPbI_3$			563 - 602	[Trots and Myagkota, 2008]
$CsPb(Br_{0.11}I_{0.89})_3$	399	473	526	[Näsström et al., 2020]
$CsPb(Br_{0.23}I_{0.77})_3$	370	439	499	[Näsström et al., 2020]

composition and chemical environment, among other considerations, Table 1.3. Compositional factors include dopants, component substitution, and component ratios, while chemical environment factors include atmosphere and precursor solvents [Chen et al., 2021]. This dependence is observed in literature, where substitutional dopants affect phase transition temperatures, and in the work of Ramirez *et al.* where additives including H_2O and DMSO can effect the $\beta \rightarrow \alpha$ phase transition by 10's of °C (K). A sample's purity and crystal quality may additionally impact phase transitions, as shown by Kawachi *et al.* where the temperature induced phase change of a $FAPbI_3$ single crystal was affected purification through recrystallisation [20] [Kawachi et al., 2019, Li et al., 2016, Ramirez et al., 2018].

[20]The difference between peak shapes in heat capacity vs temperature measurements between a crude and recrystallised hybrid-perovskite sample is available in the supplementary Figure S4 of [Kawachi et al., 2019]

1.5.3 Phase stability at operational temperatures

In practical operation of a photovoltaic device, temperatures can exceed 330 K (57 °C). This is near the $\alpha \leftrightarrow \beta$ transition temperature of $MAPbX_3$ at 327 K [21], repeated structural and lattice parameter changes are unfavourable for long lasting devices, and promote device degradation, additionally this may lead to the delamination of layers in a device [Binek et al., 2015, Dhouib and Filali, 1990, Weller et al., 2015b]. The use of alternative or mixed compositions can lower this transition temperature such as $FAPbI_3$, with an $\alpha \leftrightarrow \beta$ transition temperature closer to 280 K (7 °C) [Kawachi et al., 2019], Table 1.3.

The $FAPbI_3$ α phase ($Pm\bar{3}m$) is metastable at room temperature, and gradually converts into the non-perovskite hexagonal δ phase. The δ phase has a larger band-gap of 2.43 eV compared to the α phase near 1.43 eV reducing the portion of the solar spectrum it can effectively absorb [Ma et al., 2017]. This translates into Shockley-Queisser limits of 32.5 and 13.8 % PCE for α and δ phases respectively, making the δ phase unsuitable for producing a performant single junction photovoltaic device [Rühle, 2016]. The temperature below which the α phase is metastable varies in literature, reported as 60 °C by Weber *et al.* and 120 °C by Fu *et al.* [Fu et al., 2017, Weber et al., 2018].

In $FAPbI_3$ the substitution of the smaller MA^+ cation into the A site, has been used to stabilise the cubic or tetragonal perovskite phase [Binek et al., 2015, Weber et al., 2016]. In $FA_xMA_{1-x}PbI_3$, with $x \geq 0.2$ cubic phases are reported, while phases where $0 \leq x \leq 0.1$ a tetragonal phase is expected. [Weber et al., 2016] The phase stability of hybrid-perovskites is strongly dependent in composition. This allows the tuning of phase transition temperatures to values outside expected photovoltaic operating temperatures, improving device stability.

[21] The mounting type of a photovoltaic panel has a large impact on heat dissipation and can make a difference in the 10's of degrees to a panels operating temperature, direct mounted panels should be able to reach temperatures exceeding 333 K (60 °C). [Faiman, 2008] [Skoplaki and Palyvos, 2009]

Chapter 2

Electronic properties and defects

Contents

2.1 Performance metrics of photovoltaics **22**

2.2 Band structure, defects, and related processes **24**

2.2.1 Electronic band structure of hybrid-perovskites . 24

2.2.2 Band-gap in low dimensional hybrid-perovskites derivatives. 27

2.2.3 Polarons 30

2.3 Defects **32**

2.3.1 Point defects 33

2.3.2 Grain boundaries, interfaces, and surfaces 34

2.3.3 Defect and ion mobility, and current-voltage curve hysteresis 37

2.3.4 Surface and grain boundary passivation 38

2.4 Optical transitions: Luminescence and absorption . . . **40**

2.4.1 Optical absorption 41

2.4.2 Photoluminescence 43

2.1 Performance metrics of photovoltaics

The performance of photovoltaics (PV) is characterised by a number of metrics which depend on every component of a PV device, including the electronic and optical properties of the absorber material. The most ubiquitous metric being the photon conversion efficiency (PCE), which is a figure of merit used across journal publications and textbooks to news articles [1] [Smets et al., 2015, Yoshikawa et al., 2017]. PCE represents overall device efficiency as the ratio of maximum power density, to incident power density, under illumination of 1 sun at 1.5 air-mass (AM) [2], Equation 2.1.

$$\mathrm{PCE}(\%) = \frac{P_{\max}}{P_{\mathrm{in}}} \tag{2.1}$$

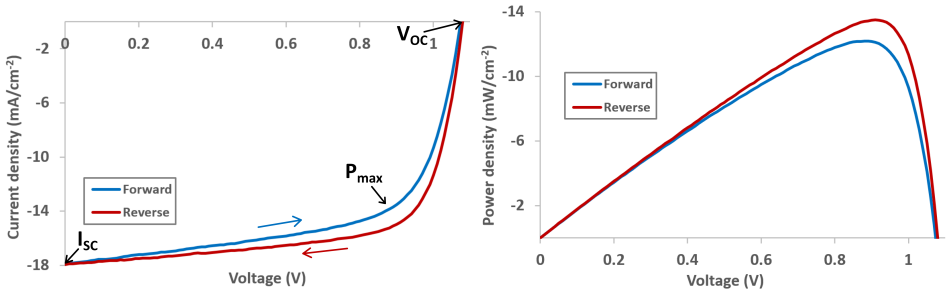

(a) (b)

Figure 2.1: (a) Current-density vs. voltage characteristics and (b) power-density vs. voltage characteristic, of a hybrid-perovskite photovoltaic. These illustrate V_{OC}, I_{SC}, $P_{\max}$ and the effect of scanning direction form a hysteresis.

∗ This device was fabricated with the architecture FTO/ZnO/SnO_2/-$Cs_{0.05}((FAPbI_3)_{0.83}(MAPbBr_3)_{0.17})_{0.95}$/Spiro-OMeTAD/Au during a lab visit to the *University of Sheffield, UK*. The related data-set is not explored in this dissertation.

PCE is a concise and limited representation of the overall cell optimisation, which depends on the current-density/voltage (J-V) characteristics

[1] PCE is at times designated as η in the literature.

[2] AM: This is an *air mass* consideration for atmospheric absorption.

of photovoltaics, Figure 2.1. Open circuit voltage V_{OC}, is the voltage of a cell when no current is extracted due to open-circuit or infinite resistance conditions. V_{OC} will be smaller than the band-gap energy (E_g) due to factors including thermal losses, band mismatch across layers, the quality of the interfaces between layers, resistive losses, etc. [Miyasaka, 2018]. The short-circuit current-density J_{SC}, occurs when the cell is under short-circuit conditions (0 V), where charge carrier transport between the top and bottom electrodes in not impeded by an external load. J_{SC} measures the maximum number of photo-generated charge carriers extracted to an external circuit per unit of area, which is dependent on photon absorption which controls the exciton generation rate, and recombination processes during charge extraction. Naturally a charge carrier extracted at 0 V is not useful for power generation, nor the potential at the V_{OC} where no charge carriers are extracted. The maximum power density which can be extracted P_{max}, occurs at a voltage V_{mpp}, between 0 V and V_{OC} producing a current between 0 mA/cm^2 and J_{SC}. The *fill factor* (FF) is then related to P_{max} by Equation 2.2, which indicates how effectively power can be extracted for a given V_{OC} and J_{SC}.

$$FF = \frac{P_{\mathrm{max}}}{V_{\mathrm{OC}} J_{\mathrm{SC}}} \tag{2.2}$$

In an ideal photovoltaic, P_{max} depends on the effective series and shunt resistances of the cell. These can be estimated from the gradients of the J-V measurement at V_{OC} and I_{SC} points respectively, where the resistance is related to the gradient by $\sim 1/R$, where R is the resistance. Even for a solar cell following ideal diode behaviour, the FF will always be below 1, with some of the highest performing Si based PV achieving 0.83 ± 0.01 [Yoshikawa et al., 2017, Smets et al., 2015]. The FF has a strong dependence on charge carrier recombination and is sensitive to the location and efficiency of recombination channels in a device [Sherkar et al., 2017]. These parameters are discussed further in [Smets et al., 2015] [3], where the ideal thermal dependence of these parameters is presented alongside equivalent circuits which provide a useful framework to understanding the effect of some efficiency losses on the current-voltage characteristics of a solar cell.

In the case of hybrid perovskite PV these metrics are often accompanied by a hysteresis, which is dependent on the scanning rate, scanning direction,

[3] Chapter 9 of [Smets et al., 2015]

amongst other parameters. This is evident between the forward and reverse scanning direction for the hybrid-perovskite PV in Figure 2.1a. Both capacitive effects, and ion migration resulting in the accumulation of charge at interfaces has been attributed to these effects, with origins intrinsically linked to defect properties [Chen et al., 2015a, Kang and Park, 2019]. The hysteresis is exacerbated by a faster scanning rate which can lead to under or overestimated device performance. Good practice for the determination of performance metrics in hybrid-perovskite using J-V measurements, include a slow scan rate which provides values closer that of a steady state measurement and steady-state measurements for the max power point, V_{OC} and I_{SC} [Christians et al., 2015]. The hysteresis is further discussed alongside ion mobility in Section 2.3.3.

2.2 Band structure, defects, and related processes

2.2.1 Electronic band structure of hybrid-perovskites

Lead halide perovskites and layered derivatives present a band structure formed from X p, Pb 6s, and Pb 6p orbitals, where $X \in \{Cl, Br, I\}$ as described in [Green et al., 2015, Hong et al., 1992, Miyasaka, 2018]. For Cl, Br and I based perovskites these are the 3p, 4p, and 5p orbitals respectively. States related to the organic cation do not occur near the band edge or band gap. The role of the organic cation is therefore indirect with the potential to affect Pb-X-Pb bond angles, Pb-X bond lengths, and structure stability [Filip et al., 2014, Green et al., 2015]. The valence and conduction bands are both formed through anti-bonding orbitals compared to other ionic semiconductors, where the valence band is typically formed by bonding orbitals [4] [Miyasaka, 2018, Xie et al., 2020]. The band structure of hybrid-perovskites forms a direct band gap which allows efficient absorption of photons with a high absorption co-efficient of the order of 10^5 cm^{-1} for photons in the

[4] This is well illustrated in Figure 7 of [Umebayashi et al., 2003]

visible and near infra-red (NIR) regions [5] [Green et al., 2014]. This is in contrast to the indirect band gap of Si photovoltaics where the photon absorption requires a momentum transfer to an excited electron provided through electron-phonon coupling [Noffsinger et al., 2012]. This greatly reduces the probability of absorption resulting in an absorption coefficient of 7 x10^3 cm^{-1} [6] [Green, 2008]. With a high absorption co-efficient the optimal thickness for perovskite PV is approximately 0.3 - 0.4 μm, while high efficiency Si PV is orders of magnitude thicker at around 150 μm [Yoshikawa et al., 2017, Batmunkh et al., 2020].

Defects in semiconductors can introduce localised states at different regions in the band-gap. They can be inconsequential when they form exponential decaying states within the vicinity of the band edges, or lead to defects within the band-gap, that affect not only the optical excitation or absorption losses, but also the electronic states due to trapping of the charge carriers. In this respect, therefore a semiconductor can have a suite of defect levels which can be classified either as shallow or deep levels each with a different binding energy, Shallow traps occur within a few multiples of k_BT [7] [De Boer et al., 2004]. Shallow trap states within k_BT of the band edges allow charge carriers to pass through these states without becoming trapped, due to the available ambient kinetic energy. Deep trap states occur at levels much larger than k_BT from the band edges [Park et al., 2018].

Structural defects occurring in many semiconductor materials (Si, CdTe, Kesterites, etc.) can result in deep trap states, which may provide undesired recombination pathways, that reduce the PV performance by changing their optoelectronic properties [Kuciauskas et al., 2021, Park et al., 2018]. Shallow defects are more favourable in hybrid-perovskites, which contributes to their unusually high defect tolerance. This stems from the defects with low formation energies primarily resulting in defect levels near the band-edges, with higher formation energies for deep trap states, discussed in Section 2.3.1. For the shallow defects which form, it has been modelled in literature that levels within k_BT (thermal energy) of the band edge may extend carrier lifetimes though multiple trapping and hopping processes where the carriers rapidly

[5] The absorption coefficient is largest for the visible region decreasing slightly below 10^5 in the NIR region.

[6] 7 x10^3 cm^{-1} across the range 400 - 1100 nm at 300 K.

[7] k_B, Boltzmann's constant, T temperature.

pass in and out of the trapped states as is the case at ambient temperatures [8] [deQuilettes et al., 2019, Miyasaka, 2018].

Apart from shallow and deep trap states, a band tail or trailing edge introduces a continuum of additional states trailing past the band edge into the band gap. These differ from shallow traps with present discrete energy levels separated from the nearest band edge. These can result from structural disorder, and have been attributed to polaron related effects in literature [deQuilettes et al., 2019].

Band structure and defect related properties

This defect tolerance contributes to the long diffusion lengths around 1 μm in polycrystalline thin-films and over 100 μm in single crystals [Miyasaka, 2018]. The photogenerated excitons [9] in $MAPbI_3$ and $FAPbI_3$ have binding energies of 11 $\pm$ 3 meV (140 to 200 K), while the bromine equivalents have binding energies of 23 $\pm$ 7 meV [10]. The exciton binding energy for the iodide variants are well below the thermal energy available at room temperature. This allows the photo-generated exciton to readily dissociate into free charge carriers [Galkowski et al., 2016].

The long charge carrier lifetimes in hybrid-perovskites have been attributed to a number of factors namely: low exciton binding energy that allows easy separation of charge carriers, coulombic screening of charge carriers due to the high ion density, defect tolerance through the formation of shallow defects in the band-gap, and the formation of large polarons (Section 2.2.3) [Miyasaka, 2018, deQuilettes et al., 2019, Franchini et al., 2021].

The charge carrier lifetimes are further extended due to *photon recycling*. *Photon recycling* occurs when a portion of photons generated through radiative recombination are reabsorbed reducing the apparent rate of radiative recombination. This effect is observed in materials with high absorption co-

[8] This effect is an illustration of charge carrier interactions with shallow trap states. The reported extent of this effect varies in literature.

[9] Exciton: A bound electron and hole pair.

[10] Binding energies ($\pm$20 % error): $FAPbBr_3$ 24 meV at 160-170 K, $FAPbBr_3$ 22 meV at 4 K, $MAPbBr_3$ 25 meV at 4 K

efficients such as GaAs and hybrid-perovskite absorber materials. *Photon recycling* can be described as the dampening of the radiative recombination rate (k_2^{int}) by an escape probability, P_{esc} resulting in a reduced effective recombination, $k_2^{\text{ext}} = P_{\text{esc}} k_2^{\text{int}}$; $0 < P_{\text{esc}} < 1$. In a thin-film, P_{esc} is strongly dependent on film thickness and the refractive index of the surrounding layers , to the extent that this can increase carrier lifetimes by as much as an order of magnitude [deQuilettes et al., 2019, Crothers et al., 2017]. This further contributes towards the long carrier lifetimes (100's of nanoseconds) in these materials [deQuilettes et al., 2019]. *Photon recycling* has been shown to be highly efficient in the work of Motti *et al.* for systems containing a combination of conventional 3D hybrid-perovskites and quasi-2D structures, these will be discussed in detail in the following section [Motti et al., 2019].

2.2.2 Band-gap in low dimensional hybrid-perovskites derivatives.

Low dimensional hybrid perovskite derivatives include 2-dimensional (2D) and quasi-2D [11] layered hybrid perovskites. The layering in these structures is based on sets of alternating planes of n corner sharing octahedra, separated by layers of organic cations as described in Section 1.2.2. Stepped derivatives of the $n = 2$ structure have been explored by Hoffman *et al.*, where the $n = 2$ sheets are broken into ribbons with a cross-section of $2 \times m$ octahedra, $m \in \mathbb{N}, m \geq 2$ [Hoffman et al., 2019]. Additional low dimensional structures include the hexagonal polytype of the ABX_3 composition, such as the 2H polytype, which consists of chains of face sharing octahedra.

In layered perovskites, the reduced dimensionality and band dispersion lowers the valence band maximum and raises the conduction band minimum resulting in a wider band-gap. [Grancini and Nazeeruddin, 2019, Stoumpos et al., 2016] This provides a tunability range for $A'A_{n-1}Pb_nI_{3n+1}$ in the range of 1.6 to 2.4 eV (red to green) and 2.3 to 3.2 eV (green to violet) for $A'A_{n-1}Pb_nBr_{3n+1}$ where the band-gap decreases with n [Smith et al., 2014, Smith et al., 2017]. A similar trend is present in hexagonal polytypes where the largest band-gap is observed for the $APbBr_3$ 2H polytype of 3.6 ± 0.1 eV [García-Fernández et al., 2019]. The other experimentally observed

[11] Quasi-2D hybrid perovskites have higher values of n increasing their dimensionality.

and theoretically calculated polytypes present mixed octahedra connectivity between the 2H polytype and 3D structure. The band-gap of these polytypes fall between the 2H and 3D structures with the band-gap decreasing with greater number of corner sharing octahedra and the distribution of these bonding motifs [García-Fernández et al., 2019, Marchenko et al., 2022].

Effects of quantum confinement

The variants for a given layered $A'A_{n-1}Pb_nX_{3n+1}$ structure offer a variety of application-related optimisation, dependent on the thickness of the layer stack n. These alternating sets of sheets containing corner sharing octahedra and organic cation spacer layers forms natural "multiple quantum wells" where octahedra form the potential *wells* and the organic layers compose the *barriers*. The extent of quantum confinement in these layered structures is used to control the size of the band-gap, where dimensional reduction results in an increased band-gap. The electronic confinement effect, reduced dielectric screening and increased Coulombic screening contributes to an increased exciton binding energy. The change in dielectric screening originates from modulation of the dielectric constant within the material between inorganic octahedra and organic spacer layers. The charge screening is due to the alternating layers of anionic octahedra layers and cationic organic layers. [Stoumpos et al., 2016]. This can be extended to hexagonal polytypes of $APbX_3$, where the 1-dimensional chains of the 2H polytype results in an band-gaps larger than those of the layered structures. In this context the 4H, 6H, and 8H structures contain an intermediate degrees of inter-octahedral connectivity between the 3D and 2H polytypes leading to the modulation of intermediate band-gaps [Marchenko et al., 2022].

The layered perovskite derivatives have high exciton binding energy and larger band-gaps for $n = 1$ structure. This energy decreases with n reaching the band-gap of the 3D perovskite at infinite number of layers ($n = \infty$). For organo-lead-iodide structures binding energies of a few hundred meV are reported, with lower values such as 125 meV for $(PhEA)_2(MA)_{1-x}PbI_{3n+1}$, with $n = 5$ [12] [Blancon et al., 2018]. In the context of photovoltaics, this

[12] Binding energies, $(HexA)_2PbI_4$ of 435 meV, where HexA is hexylammonium [Blancon et al., 2018] . $(PhEA)_2PbI_4$ of 200 meV [Grancini and Nazeeruddin, 2019] .

will result in significant drops in open-circuit voltage (V_{OC}) [Grancini and Nazeeruddin, 2019]. In combination with the narrow optical absorption range of low n structures, this results in limited photovoltaic performance [Grancini and Nazeeruddin, 2019]. In contrast to this, the higher exciton binding energy supports a high room temperature photoluminescence yield, which is essential for applications associated with luminescence efficiency, such as in phosphors and LEDs [Smith et al., 2017, Grancini and Nazeeruddin, 2019, Yang et al., 2018b].

With a larger layer stack thickness such as $n \geq 3$, the dielectric contrast and dimensional restriction on charge carriers is diminished resulting in smaller band-gaps and lower exciton binding energies, closer to that of the 3D hybrid perovskites. This is accompanied by a wider range of light absorption in the visible-NIR region [Grancini and Nazeeruddin, 2019, Stoumpos et al., 2016]. These effects enhance the suitability of these materials for applications in multi-junction photovoltaics in combination with smaller band gap materials such as the 3D hybrid perovskites [13].

We have discussed the dependency of band-gap and exciton energy on n. Where an application requires isolated targeting of these properties, the band-gap can be tuned through halide substitution adding the versatility of this class of materials [Smith et al., 2019].

Effects of octahedral tilts and Pb-X-Pb bond angle

The octahedra in 3D perovskites form an interconnected network, where tilts are constrained by the interconnectivity of the Pb−X octahedral framework. This is evident in Glazer notation where tilts are specified about cardinal axes, with each tilt described as either symmetric or asymmetric referring to the relation between successive layers [14] [Howard and Stokes, 1998]. In $n = 1$ layered structures, layers of octahedra are supported by the organic cations forming a barrier layer. This difference has been leveraged in literature to tune the $n = 1$ structure, relating a greater deviation of the Pb-X-Pb bond angle to larger band gaps and larger exciton binding energies in A'_2PbX_4

[13] The efficiency limits of single junction and tandem photovoltaic cells are discussed in Section 1.2.3.

[14] Glazer notation is described in Section 1.5.1

materials, X $\in \{\mathrm{Cl}, \mathrm{Br}, \mathrm{I}\}$ [Cortecchia et al., 2017, Du et al., 2017, Grancini and Nazeeruddin, 2019, Smith et al., 2017]. The effect on band-gap similarly observed in 3D perovskites. With the participation of p orbitals in forming the valence and conduction bands, increasing octahedral tilt reduces orbital overlap and band dispersion, consequently increasing the band-gap and exciton binding energy [15] [Amat et al., 2014, Filip et al., 2014, Smith et al., 2017].

In addition to affecting band-gap width, octahedral tilts can be utilised for the formation of trap-states in the band-gap of layered perovskites. In the work of Smith *et al.*, the average *Pb-Br-Pb* bond angles were related to band-gap width in $n = 1$ perovskites [Smith et al., 2017]. Only the out-of-plane component of this angle was associated with the formation of deep trap-states from which a distinct exciton recombination pathway could be observed. These defects formed the basis for broadband optical emissions from self-trapped excitons (STEs), showing potential for applications as phosphors [Dohner et al., 2014, Smith et al., 2017]. This can be differentiated from defect induced broadband emission observed in layered perovskites by the position of the emission band. When defect-induced, the emission band occurs directly below the band-edge exciton emission, while STE based emission occur from states deeper in the band-gap resulting in a lower energy emission closer to the NIR region [16] [Paritmongkol et al., 2020].

2.2.3 Polarons

Conventional polarons occur with the interaction between a charge carrier (electron or hole) and optical phonons [Byrnes, 2008]. These result in lattice distortions dependent on effects of charge carrier on the charge distribution in its surroundings. This can include the reorientation of molecules containing a dipole, displacement of cations and displacement of anions. [deQuilettes et al., 2019] The charge carrier and its affected or distorted surrounding compose the polaron. Polarons are divided by their spacial localization into

[15] This is well expressed in Figures 2 and S2e of Filip *et al.* There is a second order effect from bond length on band-gap [Filip et al., 2014]

[16] Broadband emission is not expected to result from mixed phase ($n = 1$, $n = 2$, ...) systems due to charge transfer between the phases [Motti et al., 2019].

small and large polarons. Small polarons occur over a single, or a few bond lengths and have a radius smaller than the unit cell. Large polarons feature a radius larger than the unit cell. [Byrnes, 2008].

Hybrid-perovskites can support either small or large polarons. [17] Small polarons have typical mobilities $\ll$1 cm^2/(Vs), and are suggested to have a detrimental effect on charge extraction in the context of hybrid-perovskite PV. They have also been associated with supporting photodegradation and material degradation [Franchini et al., 2021]. Large polarons have typical mobilities $\gg$1 cm^2/(Vs), long carrier lifetimes and long diffusion lengths. Conversely, charged large polarons are predicted to experience short range repulsive effects, protecting against recombination [Franchini et al., 2021, deQuilettes et al., 2019].

The degree to which either small or larger polarons are favoured is compositionally dependent. Composition is interlinked with polaron stability and structural distortion as demonstrated in theoretical study by Mahata *et al.* [Mahata et al., 2019]. Small polarons in hybrid-perovskites result from coupling between excess charges, as well as the orientation of an organic cations' dipole and associated structural distortion. Large polarons result from coupling between charges and a longitudinal optical phonon in the inorganic framework. The resulting deformation modes are independent of the A site cation. The extent of the structural distortion, and small polaron stability is dependent on the A site cation and halide selection. The inorganic Cs^+ results in less distortion in the Pb-X framework compared to dipole containing cations, such as MA^+ or FA^+. Regarding the halide, Br results in more lattice distortion in a polaron compared to I, due to its larger electronegativity which increases Pb$-$X bond polarity. Similarly, considering Sn as an alternative to Pb the metals have a strong effect on polaron stability showing a non-monotonic trend [Mahata et al., 2019, Shin et al., 2021].

The structural distortions resulting from polarons can be observed by structure sensitive tools, such as X-ray and neutron scattering techniques. In a scattering pattern, individual polarons may result in diffuse scattering in the tails of Bragg reflections while correlated polarons may result in well-resolved peaks [Nelson et al., 2001, Franchini et al., 2021]. An overview of

[17] Apart from conventional polarons, evidence of ferrroelectric large polarons in $MAPbI_3$ has been presented in [Miyata and Zhu, 2018]

complementary techniques characterising phonons can be found in [Franchini et al., 2021]. [18] [19]

2.3 Defects

The performance and properties of semiconductor materials are intimately coupled with defects. Conventional semiconductors, such as silicon, are highly sensitive to impurities and crystalline quality, demanding single crystal ingots as a basis of most technological applications. These are then doped to include precise defect concentrations for control of charge carrier types and concentrations. There have been great strides in point defect management and surface passivation [20] for the development and stability of polycrystalline silicon photovoltaics [Park et al., 2018].

Contrasting conventional semiconductors, hybrid-perovskites have an exceptional defect tolerance. This is expressed through well performing optoelectronic devices including photovoltaics, in spite of relatively high defect concentrations, as is explored in this section. This allows for the fabrication of high performing devices through the use of defect prone, low temperature, solution based methods. In hybrid-perovskites, bulk defects are reported to have a negligible impact on performance, while surface, interface and grain boundary defects have established adverse effects on device performance and stability [Xia et al., 2023]. These defects are discussed in Sections 2.3.1 and 2.3.2 with mitigation approaches for the latter discussed in Section 2.2

[18] Depending on the material, for reliable analysis of diffuse scattering a sufficient signal to noise ratio is required, with a well collected background, as is carried out for synchrotron based total scattering measurements.

[19] A general introduction to polarons is provided in [Byrnes, 2008] with more in-depth discussions in [Franchini et al., 2021] which includes a section on hybrid perovskites, and a hybrid-perovskite specific review is available in [deQuilettes et al., 2019].

[20] such as the termination dangling bond with H.

2.3.1 Point defects

Point defects form throughout the material in the bulk, grain boundaries, surfaces, and interfaces. The point defects present in hybrid perovskites can be organised into, vacancies, interstitials, and anti-site defects. The properties of these defects in hybrid-perovskites has been studied in literature through electro-chemical measurement, optical measurements, and *ab-inito* modelling based approaches such as density functional theory (DFT). As with most modelling based approaches, these are very sensitive to the specification of the model and its characteristics or constraints. In addition the hybrid-perovskite range in chemical composition and stoichiometry which has a marked effect on DFT modelled, defect formation energies. This is exemplified by the difference in defect formation energies for MA-poor and MA-rich in the work of [Buin et al., 2014] [21]. As a result, the literature on defects and their formation energies, while valuable and informative, can be inconsistent, and at times contradictory [Lei et al., 2021, Ball and Petrozza, 2016, Buin et al., 2014, Game et al., 2017]. Similar occurrences are evident in experimental works where the density and nature of defect related trap states differ between studies. In part, this originates from the sensitivity of the properties of a hybrid-perovskite film to the synthesis conditions, films quality and composition [deQuilettes et al., 2019].

The common thread in such studies is that the point defects with low formation energies in hybrid perovskites are typically shallow trap states, while defects resulting in deep trap states are energetically unfavourable with higher formation energies. This is exemplified with dominant vacancies predicted for lead iodide hybrid perovskites not forming sub-bandgap energy levels. This is in stark contrast to other semiconductor photovoltaics including Si, Kesterites, and CdTe, where mitigating deep-trap states have required careful attention [Ball and Petrozza, 2016, Buin et al., 2014, Lei et al., 2021, Park et al., 2018, Zhenyi et al., 2020]. Site vacancies of MA, Pb and I are predicted as the most common defects in lead iodide hybrid perovskites [Park et al., 2018].

[21] A number of DFT modelling formalisations are briefly discussed in [Yin et al., 2015].

2.3.2 Grain boundaries, interfaces, and surfaces

The 2-dimensional defects formed at the edges of crystal domains are critical to hybrid perovskite performance and stability. These include grain boundaries, interfaces and surfaces. [Hui et al., 2021, Kang and Park, 2019, Sherkar et al., 2017, Zheng et al., 2017]

Grain boundaries form where adjacent crystallites with different orientations converge. The orientational differences between grains result in various structural defects. This includes point defects such as dislocations, stacking faults, dangling bonds, interstitial atoms and vacancies, alongside deviations in bond lengths and angles [Sherkar et al., 2017, Hui et al., 2021]. Interfaces occur between contacting dissimilar materials or layers. Surfaces and interfaces are expected to contain higher concentrations of point defects, dangling bonds, and varying co-ordination of atoms compared to the bulk. These are often subject to chemical impurities from adjacent layers or contamination by other means, which may form exotic defect states which are not inherent to the bulk material [Ming et al., 2018]. There is a lower energy barrier to structural distortion at surfaces and interfaces allowing larger atoms to occupy sites which may be prohibitively small in the bulk material [Hui et al., 2021]. There is often a crystal structure size and orientation mismatch at an interface resulting in strain and disrupting the translational symmetry of the unit cell. This is accompanied by defect formation. The contact or proximity of two electronically dissimilar materials at the interface may lead to the formation of exotic defect states in the band structure, these states may be localized or pinned at the symmetry points or Dirac points and can possess some topological characteristics.

The mechanistic details regarding the role of grain boundaries on the performance of hybrid perovskite devices, and their stability, remains a continuing subject of active debate [Hui et al., 2021, Sherkar et al., 2017]. They are known to affect the mechanisms of electrical transport and defect mobility within the lattice or grain boundary. The defects variation in materials has been shown in literature as dependent on the fabrication and post-processing methods, which determine the nature and control of the defect densities within the material. [Sherkar et al., 2017]. This is exemplified by Barboni and De Seuza, who reconciles multiple sets of experimental hybrid-perovskite ionic conductivity data, showing the variation defect mediated conductivity

to be a function of defect density and temperature [Barboni and De Souza, 2018]. While the finer stoichiometry in the hybrid-perovskite, and mobile species in adjacent layers (when applicable) impact the formation energies of the possible defect species [Yin et al., 2014]. Some works have used density of states and first-principle calculations to suggest that deep defect states are not expected in grain boundaries and only shallow defect states are expected to form [Hui et al., 2021]. Contrasting works suggest the structural differences at grain boundaries, interfaces and surfaces can result in deep trap states through lowering their formation energies [22] [Lei et al., 2021, Taufique et al., 2018, Zheng et al., 2017, Zhenyi et al., 2020].

Aside from the open question of deep trap states, various beneficial and detrimental properties have been attributed to hybrid perovskite grain boundaries in literature including, improved or reduced conductivity [23], electron-phonon coupling and potential space charged regions subject to the charge of the majority of defect trap states. [Hui et al., 2021]

According to a number of studies, grain boundaries in ionic hybrid perovskites are expected to contain charged iodide vacancies ($V_{\mathrm{I}}^{\bullet}$ [24]) with shallow defect states in the bandgap [25] [Sherkar et al., 2017, Walsh et al., 2015, Barboni and De Souza, 2018, Lei et al., 2021]. On photo-excitation, these states largely saturate with electrons. This can result in a neutral grain boundary, in contrast to the positive charge prior to saturation. The trapping of electrons in the grain boundaries can bias the perovskite to a weakly p-type character (*hole*-rich) subject to compositional effects and defect density [Sherkar et al., 2017]

The density of charged trap states, such as at grain boundaries can affect charge carrier mobility and lifetime due to coulombic and/or many body interactions. In the case of trap states which are charged when empty, once occupied by charge carriers these defects become neutral. Charge trap states associated with anion or cation vacancies can upon occupation by electrons

[22] Once such example is the formation of I_{Pb} has a formation energy calculated at 0.03 eV [Taufique et al., 2018] on a crystal surface under I-rich conditions

[23] The conductivity can be affected in either direction depending on composition [Hui et al., 2021].

[24] Kröger-Vink defect notation

[25] These $V_{\mathrm{I}}^{\bullet}$ defects are reported to have the potential of facilitating Pb dimer formation which result in deep trap states [Lei et al., 2021, Wang et al., 2020].

or holes lead to charge neutrality. This effect has been reported by Sherkar *et al.* in which it was mediated by photo-illumination or soaking, and served to diminish space charge effects [26] [Sherkar et al., 2017].

The effect of grain boundaries on charge carriers is dependent on film quality. For high quality films with "fused" grain boundaries and relatively low trap state densities, the effect on charge transport, recombination, and PV device performance is expected to be tangible yet minimal regardless of whether occupied trap states present a charge. This tolerance is in part due to the long carrier lifetimes [Sherkar et al., 2017]. Conversely, for lower quality films of non-compact morphologies with "open" grain boundaries, and higher defect densities, the effect is more detrimental. The greater density trapped states plays a larger role in non-radiative recombination reducing the maximum current that can be extracted from the active layer [Sherkar et al., 2017].

In a conventional hybrid-perovskite photovoltaic cell, the dominant channel for trap-assisted recombination is at interfaces, and to a lesser degree, at grain boundaries. The recombination is typically far weaker in the material bulk corresponding to the data modelling by Sherkar *et al.* [Sherkar et al., 2017, Hui et al., 2021].

Hybrid perovskites grain boundaries remain an active area of investigation, they can contribute to recombination or be effectively benign. Defects at both grain boundaries and surfaces have higher chemical activity and diffusivity than found in the bulk. These are vulnerable to attack by water and oxygen as part of a decomposition pathway, with the interactions with water being more rapid in grain boundaries. This is sensitive to the nature of the defects present. The reduction of defect density and formation of single crystals has been used to exemplify this in the work of Wang *et al.* [Hui et al., 2021, Wang et al., 2017a, Zheng et al., 2017].

Trap-assisted recombination, defect properties and defect concentrations in the bulk, at grain boundaries and at surfaces can be minimised through

[26] For a device produced by [Sherkar et al., 2017] (PCE 20 %), trap based recombination was dominant below 0.1 suns, while bimolecular recombination was dominant from 0.2 suns. This implies the trap states (including in bulk, at grain boundaries and at interfaces) for the specific fabricated cell become fully occupied at relatively low irradiation as bimolecular recombination becomes dominant.

compositional and morphology control including grain boundary orientation which can be optimised for charge transport. The effect of composition on grain boundary defect formation is more significant for non-compact morphologies where higher defect densities are present [Xi et al., 2019]. Interface quality can be optimised and defects through similar morphology and compositional control. With this high performance PV devices are readily achievable through easily scalable technologies, specifically defect prone solution processing exhibiting the advantages of the defect tolerance inherent to hybrid perovskites. As a currently active field there is continuous improvement in the understanding and management of defect related efficiency losses. With the interface as the dominant channel or trap mediated recombination, over the last few years a great deal of interest has turned to the use of passivation layers on hybrid-perovskite films and their effects on defect passivation. [Bisquert, 2017, Miyasaka, 2018]

2.3.3 Defect and ion mobility, and current-voltage curve hysteresis

Ion mobility has been related to both device degradation and performance losses in hybrid perovskites [Barboni and De Souza, 2018]. While still debated in the literature, in terms of ion mobility of hybrid-perovskite defect species much of the attention has drawn a spotlight on MA vacancies, halide vacancies and halide interstitials [Ball and Petrozza, 2016, Barboni and De Souza, 2018, Hui et al., 2021]. The work of Game *et al.* critically evaluated the mobility of MA and I vacancies ($V_{\mathrm{I}}^{\bullet}$, V'_{MA}) showing a smaller barrier to transport for $V_{\mathrm{I}}^{\bullet}$ compared to V'_{MA} with activation energies of 0.1 and 0.41 eV respectively [Game et al., 2017]. Similar findings have been reported in Sherkar *et al.* comparing complexes of I against ionic MA, Pb, etc. [Sherkar et al., 2017]. Barboni and De Souza have since used a combination of experimental and modelling approaches to support $V_{\mathrm{I}}^{\bullet}$ as the most mobile ionic species in $MAPbI_3$ [Barboni and De Souza, 2018].

Ion migration is expected to be concentrated near grain boundaries and surfaces, due to the reduced coordination of atom. The defect density is much higher at grain boundaries with much lower ion migration activation

energies [27], in part due to their relatively more open structure compared to the bulk material [Hui et al., 2021].

There is a direct correlation between density of trap states, density of mobile ionic defects, and hysteresis in the current-voltage (J-V) measurement of hybrid-perovskites [Sherkar et al., 2017]. The most probable mechanisms for the J-V hysteresis discussed in literature involve capacitive current from ion migration and charge accumulation, and defect mediated recombination [28][Kang and Park, 2019].

Various passivation layers and additives have been effective in mitigating hysteresis as reported in literature. These approaches have been implemented in literature for the passivation of bulk, grain boundary and/or surface defects. They have further been used for selective contact engineering optimising charge extraction at interfaces. Surface and grain boundary passivation as a means of mitigating these effects is discussed in Section 2.3.4 [Kang and Park, 2019, Singh and Parashar, 2020].

2.3.4 Surface and grain boundary passivation

The 2-dimensional defects discussed in Section 2.3.2 can act as non-radiative recombination centres, eroding performance of a semiconductor in optoelectronic applications including photovoltaics and light emitting diodes. They are a primary contributing factor to the hysteresis observed in current-voltage characteristics and related performance degradation [Kang and Park, 2019, Singh and Parashar, 2020]. Additionally, grain boundary defects can facilitate moisture induced degradation pathways [Hui et al., 2021, Wang et al., 2017a].

Surface passivation is considered one of the most practical means of mitigating surface defects. Various approaches have been explored in the liter-

[27]Hui *et al.* reports the activation energy at grain boundaries as "roughly half" that of the bulk [Hui et al., 2021].

[28]Ferroelectricity has been considered as a possible mechanism of the J-V hysteresis in literature. This has been subject to conflicting reports in contrast to the more established alternatives. [Kang and Park, 2019]

ature. These include the use of non-amine Lewis acids and bases [29] , low-dimensional perovskites, organo-amines, inorganic molecules, and polymers [Xia et al., 2023].

A Lewis base and Lewis acid which act as an electron pair donor or acceptor respectively, are able to form coordinate-bonds with the defects which falls into the complementary category. Lewis acids are able to passivate Pb_I anti-site defects and under-coordinated halide ions. Lewis bases can passivate under-coordinated Pb^{2+} cations [Zheng et al., 2017]. Organo-amines readily form Lewis acids as organo-ammonium cations, these are best treated separately due to their potential role in the substituting into the perovskite structure or in the case of larger molecules, forming low-dimensional hybrid perovskite derived structures. The organo-amine passivation layers are of greatest interest in relation to Chapter 9, where mixed composition systems of layered 2D hybrid-perovskite derivatives and 3D hybrid-perovskites are investigated.

The organo-amines used in low-dimensional perovskites are hydrophobic allowing them to be used as a barrier layer improving stability against moisture [Zheng et al., 2017, Xia et al., 2023]. As Lewis acids they are able to passivate negatively charged defects and act as a barrier to ion migration which has been shown to reduce the hysteresis in their current-voltage characteristics (photocurrent hysteresis) [Kang and Park, 2019, Xia et al., 2023]. The use of organo-ammonium halide salts has been suggested to have the additional advantage of filling halide vacancies [Jiang et al., 2019]. The effect of defect passivation on recombination is evident in the work of Luo *et al.* where passivated hybrid-perovskite nano-crystals had photo-luminescent quantum yields of 2.84 % compared to the control of 0.17 % [Luo et al., 2018]. Similar observations are prevalent for photovoltaic devices with *fill factor* increases from 65 to 79 % (PCE 13.6 to 18.0 %) and from 83.0 to 83.9 % (PCE 22.4 to 24.6) [Wu et al., 2022]. As discussed in Section 2.2.2, the band-gap of such passivation layers can be tuned to optimise a device's energy level structure and reduce band mismatch between the absorber and charge transport layers. Large V_{OC} improvements of 100 mV have been observed for guanidinium bro-

[29]Notable mentions include the Lewis base caffeine which has proven effective in improving photovoltaic performance and stability. The publication does not comment on caffeine's effect towards researcher performance [Wang et al., 2019].

mide [30] [Luo et al., 2018, Xia et al., 2023]. These effects cumulatively improve the device performance as evident through improved performance characteristics (I_{SC}, V_{OC}, FF, PCE values [31] [32]) and device lifetimes [Xia et al., 2023]. This is exemplified the $BA_2PbI_4/(FAPbI_3)_{0.95}(MAPbBr_3)_{0.05}$ device [33] where the 2D BA_2PbI_4 layer grown on top of the 3D perovskite layer producing a photovoltaic with an impressive certified PCE of 24.35 % which remained stable for more than 1000 hours under damp heat [34] testing and separately full-sun illumination [Jang et al., 2021].

2.4 Optical transitions: Luminescence and absorption

Hybrid-perovskites have a composition dependent band-gap extending from ∼1.5 eV to energies across the visible region of the solar spectrum, as discussed in detail in sections 1.2.3 and 2.2. Its tunability allow for versatile applications including as a single or multi-junction photovoltaic device, as a phosphor or a light emitting diode [Smith et al., 2017, Yang et al., 2018b]. The band-gap can be further tuned to higher energies by reducing dimensionality of the structure, such as in the case of layered hybrid perovskites, with which the photophysical properties can be tuned with strong effects on both band-gap and exciton binding energies, Section 2.2.2. The band-gap and other optical properties of materials can be probed using techniques such as absorption spectroscopy, photoluminescence and electroluminescence as practiced in literature [Green et al., 2015, Hong et al., 1992, Ishihara, 1994, Makuła et al., 2018].

[30] Luo *et al.* used guanidinium bromide for defect passivation on $(FA_{0.95}PbI_{2.95})_{0.85}(MAPbBr_3)_{0.15}$ resulting in 100 mV V_{OC} 2.1 % PCE improvements [Luo et al., 2018].

[31] These performance metrics are in introduced in Section 2.1.

[32] Xia *et al.* tabulates [Xia et al., 2023] photovoltaic performance metrics for many device passivation approaches reported in literature.

[33] BA: butylammonium, the structure of 2D perovskite derivatives is discussed in Section 1.2.2.

[34] Damp heat testing by Jang *et al.* was performed at: 85 °C and 85 % relative humidity.

The absorption of a photon suitable for an electron transition from the valence to conduction band is highly dependent on the band structure and population distribution in the electronic states of varying momenta. For a transition to occur, the photon energy and momenta must correspond to an energy difference between an occupied and available state. The probability of such a transition is dependent on the wave function overlap between these states, as dictated by the Frank-Condon principle and distribution of electrons across these states which follows a Fermi Dirac distribution. As a consequence, these inter-band transitions are unlikely to result in a transition directly to the lowest conduction band energy level. The conduction band relaxation pathways include thermalisation between neighbouring states within the same band, and recombination during an inter-band transition. Of these two process, thermalisation is far more rapid in comparison to interband transitions. The absorption can be probed using optical absorption spectroscopy and radiative recombination by photoluminescence measurements.

2.4.1 Optical absorption

The absorption onset or edge in a semiconductor is closely related to the features in the band-gap. The Tauc formalism has been used to probe the characteristics of the absorption edge and subsequently determine the band-gap energy, with the consideration that the onset value can be modified by effects such as the exciton binding energy inherent to hybrid perovskites. The exciton binding energies in 3D hybrid-perovskites is ∼25 meV while this can extend from ∼100 to a few hundred meV for 2D layered hybrid-perovskites with intermediate values for quasi-2D structures [Blancon et al., 2018, Galkowski et al., 2016, Grancini and Nazeeruddin, 2019]. [35]

The Tauc method assumes the energy-dependant absorption coefficient follows Equation 2.3, where E_{Tauc} is the Tauc band-gap, α is the absorption coefficient, h is Plank's constant, ν is wavenumber, and B is a constant. γ is dependent on the nature of the electronic transition, for direct transitions $\gamma = 1/2$ which is applicable to hybrid perovskites and 2 for indirect transition such as in silicon semiconductors [Park et al., 2018, Stoumpos et al., 2016, Makuła

[35] Where only reflectance data is available, an absorption spectrum can be generated using the Kubelka-Munk function. [Makuła et al., 2018]

et al., 2018]. In the presence of excitonic effects the $E_{\text{Tauc}} = E_g - E_x$, where E_g is the optical band-gap and E_x is the exciton binding energy [Green et al., 2015].

$$(\alpha \cdot h\nu)^{1/\gamma} = B(h\nu - E_{\text{Tauc}}) \tag{2.3}$$

The E_{Tauc} is determined from the plot of $(\alpha \cdot h\nu)^{1/\gamma}$ against $h\nu$ and extrapolating the absorption feature to intercept the baseline. In the case of a single absorption event in sample where scattering does not effect the transmitted intensity this will occur at the x-intercept. According to the Beer-Lambert law an absorbance spectrum can be represented as a linear combination of its constituents. In absorbance spectra where contributions can be clearly attributed and unambiguously modelled, the individual contributions can be isolated and treated separately using the Tauc method. This approach can offer limited suitability for overlapping contributions in materials such as hybrid-perovskites where the optical properties are sensitive to compositional changes and preparation conditions [Steirer et al., 2016, Stoumpos et al., 2016]. Additionally hybrid-perovskites absorbance characteristics show some variability in literature in the region above the absorption edge [Green et al., 2015].

An empirical approach based on the $(\alpha \cdot h\nu)^{1/\gamma}$ vs $h\nu$ plot has been examined for the use in systems with multiple contributions by Makuła *et al.* [36]. They identify the consideration of a baseline signal as necessary for a reasonable estimate of band-gap values. This method allows partial, although incomplete consideration of the convolution of absorption features [Makuła et al., 2018]. This is exemplified in SI Section E.2, where a Tauc plot from literature was reprocessed resulting in Tauc band-gap values in closer agreement to the authors photoluminescence data as shown in Table 9.1 [Ma et al., 2022].

[36]The application of this approach is exemplified in Figure 2f of [Xiao et al., 2016].

2.4.2 Photoluminescence

Photoluminescence (PL) measurements provide a means to probe the electronic transitions and optical band-gap of materials with a sufficient photoluminescence quantum yield. The measurement provides the signature of the dominant radiative recombination pathways in a material. In hybrid-perovskites, free exciton recombination is a dominant relaxation pathway which can be directly observed in PL measurements [37]. The peak maxima of this process is used to determine the optical band-gap [Green et al., 2015]. This has similarly been shown for electroluminescence in 2-phenylethylammonum lead iodide layered perovskite single crystals [Hong et al., 1992]. The PL signals can be well modelled using the pseudo-Voigt peak shape explained in Section 3.3 and implemented in Python using the *Lmfit*, *scipy.optimise* packages as discussed in Section 4.6.2.

[37] Other recombination pathways have been shown for select hybrid perovskites, specifically recombination of self trapped excitons resulting in broad spectrum white light emissions in the work of [Smith et al., 2017].

Chapter 3

Rietveld refinement and TOPAS-Academic

Contents

3.1 Sample effects in diffraction patterns **46**

3.1.1 Sample related peak broadening: Crystallite size and micro-strain 46

3.1.2 Crystallite size broadening 47

3.1.3 Micro-strain broadening 48

3.1.4 Determination of crystallite size and micro-strain 48

3.2 Effects of sample preparation, packing and mounting . **50**

3.2.1 Intensity errors: Crystallite size 50

3.2.2 Preferred orientation 51

3.2.3 Sample alignment effects 53

3.3 Peak shape and profile **55**

3.3.1 Standard reference materials 56

3.3.2 Analytical peak profiles 57

3.3.3 Fundamental parameter peak profiles 58

3.4 Agreement factors **59**

3.5 Limitations of powder X-ray diffraction **61**

3.5.1 Light atoms in a heavier matrix 61
3.5.2 Resolving atom identity 62
3.5.3 Real Structure? 63
3.6 Diffraction pattern fingerprinting **65**
3.6.1 Assignment considerations 65
3.7 Indexing **67**
3.8 Whole powder pattern decomposition **68**
3.8.1 Individual peak fitting 68
3.8.2 Pawley and Le Bail refinements 69
3.9 Structure based (Rietveld) refinement **70**
3.9.1 Atomic position refinement 70
3.9.2 Atomic displacement parameter 71
3.10 Sequential and parametric refinement **72**
3.10.1 Sequential refinement 73
3.10.2 Parametric refinement 74

3.1 Sample effects in diffraction patterns

3.1.1 Sample related peak broadening:

Crystallite size and micro-strain

The width of the diffracted peaks are subject to a number of sample dependent factors. These include crystallite size (and shape), micro-strain (includes point defects), compositional fluctuations, line defects (such as dislocations), and planar defects (such as stacking faults and twinning). A more extensive list is present by [Scardi, 2008]. Below we discuss crystallite size and micro-strain broadening as these are prevalent effects observable in diffraction patterns [Scardi, 2008].

Broadening can be described using a full-width at half-maximum (FWHM) or integral breadth (IB) approach. FWHM quite simply measure distance between points on the left, and right slope of a peak, at half of the maximum intensity. IB provides a slightly more robust measure defined as $\beta_{IB} = \frac{\text{peak area}}{\text{peak maximum}}$ [Scardi, 2008]. FWHM can provide an empirical estimate of crystallite size, while IB provides a mathematically direct relation [1] [Young, 1993, Leoni, 2019]. For both FWHM and IB approaches, the estimated crystallite size is subject to uncertainties around the contributions of other broadening effects, and the assumption in calculating crystallite size which includes crystallite shape and size distribution. This emphasises the need for careful reporting on the meaning of values derived through this method. Other broadening effects can largely be accounted for using calibrated instrument profiles [2] and isolating size from micro-strain effects as will be discussed with the Williamson-Hall method [3].

The shape of the peaks in the diffraction pattern is dependent on both instrument and sample contributions. We discuss how the instrument contributions are considered in Section 3.3.

[1] Chapter 8 of [Young, 1993]

[2] Instrument profiles for TOPAS-Academic are provided in Section 4.8.

[3] Peak broadening contribution can be summed as follows, Gaussian: $\beta^2 = \beta_1^2 + \beta_2^2 + ...$ Lorentzian: $\beta = \beta_1 + \beta_2 + ...$ For functions which combine these as components, the contributions can be de-convoluted and these equations can be applied [Delhez et al., 1982].

3.1.2 Crystallite size broadening

The crystallite size (D) can be related to an integral breadth contribution (β) by Equation 3.1 where K_β is the Scherrer constant, s is reciprocal space and $1/\beta(s)$ is the volume weighted average size. This relation shows the direct basis of this broadening effect [Young, 1993, Scardi, 2008]. It is typically more convenient to express β as a function of 2θ shown in Equation 3.2. The value of K_β depends on the shape of the crystallite and the specific hkl of the reflection. For spherical particles with a cubic unit cell a K_β of 0.89 is used in calculating β_{IB} [Speakman, 2014]. Scherrer constants are discussed in detail by [Langford and Wilson, 1978].

The crystallite sizes applicable for detection by XRD on conventional lab based equipment have a lower bound of $\approx$ 2 nm, below which the coherent scattering length becomes insufficient for diffraction. The upper bound varies depending on an instruments resolution and is tentatively given as $\approx$ 200 nm in [Scardi, 2008] which can be extended to a few microns with high resolution measurement such as those available at a synchrotron [Scardi, 2008].

$$\beta(s) = \frac{K_\beta}{D} \tag{3.1}$$

$$\beta(2\theta) = \frac{\lambda K_\beta}{D \cos\theta} \tag{3.2}$$

Methods for the determination of crystallite size include the use of XRD data and complimentary techniques such as electron microscopy and dynamic light scattering (DLS) to provide crystallite size or particle size. Diffraction and DLS data provide an average value or distribution over a volume of μL to mL. XRD and DLS collect data from relatively large sample sizes allowing for small statistical errors σ. The particle or crystallite size for a sample evaluated using electron microscopy techniques is typically subject to large uncertainties due to a relatively low number of observed particles or crystallites [4]. The discernibility of crystallite within particles or grains depends on the resolution of an electron microscope. Particles contain one or multiple crystallites, as such particle size can be considered a upper bound for the estimate of crystallite size.

[4] In addition shape information may be limited to a 2-dimensional representation which has the potential to bias results in the case of a preferred sample orientation.

3.1.3 Micro-strain broadening

Macro-strain in a lattice is a directional effect which results in a macroscopically homogenous change in d-spacings in one or multiple directions across a sample [Scardi, 2008]. This can be the result of applied tensile or compressive stress or a residual strain from the processing or formation of a material. For strain to persist an energy barrier preventing relaxation of strain in a material is required and this barrier can typically be overcome through thermal annealing. The effect of macro-strain on peak position in 2θ is provided in Equation 3.3.

$$\Delta 2\theta = -2\frac{\Delta d}{d}\tan\theta \tag{3.3}$$

Micro-strain occurs when defects cause local deviations in d-spacing, with the simplest case being an isotropic effect. While macro-strain results in peak shifts, micro-strain will result in peak broadening as per Equation 3.4 [Speakman, 2014, Mittemeijer and Welzel, 2008].

$$\beta(2\theta) = 4\epsilon\tan\theta \tag{3.4}$$

3.1.4 Determination of crystallite size and micro-strain

A first approximation of crystallite size on materials where the size broadening is expected to be dominant can be determined by application of the Scherrer equation. To simply observe trends in a set of samples it may be passable to directly apply the equation; this is typically applied to the strongest peak. The results from such an approach will certainly be inaccurate and subject to a large uncertainty due to alternative causes of broadening, including instrumental and where applicable micro-strain broadening. Such an approach can be improved though the consideration of instrument broadening and multiple peaks [De Keijser et al., 1982, Mittemeijer and Welzel, 2008].

A more robust method involves considering both size and micro-strain broadening in the Williamson-Hall (WH) method. In this the differing dependence on 2θ of these two factors allows the separation of size and strain

components. Equation 3.5 [5] is derived by converting the sum of crystallite size and micro-strain into the form $y = mx + c$. This is the basis of the WH plot where $y = \beta_{total} \cos\theta$, $x = \sin\theta$. This allows the use of a linear regression across data from multiple peaks to determine the gradient and intercept from which strain and crystallite size can be determined respectively.

$$\beta_{\text{total}} \cos\theta = 4\epsilon \sin\theta + \frac{\lambda K_\beta}{D} \tag{3.5}$$

The WH method allows the subtraction of instrumental broadening. This is trivial for Lorentzian or Gaussian function, yet deconvolution is required for profiles such as a Voigt as described in Section 3.3.2 [6]. Many software implementations for whole powder pattern decomposition (WPPD) such as Brukers TOPAS facilitates the incorporation of more complicated instrument profiles without complicating the extraction of sample related information.

WPPD as discussed in Section 3.8 provides a powerful method for peak shape modelling. This can be used to provide peak widths or integral breadths for methods such as the WH or convolutions for crystallite size,

[5]Equation 3.5 is specific to Lorentzian broadening contributions and is derived by multiplying the following of size and micro-stain broadening by $\cos\theta$, $\beta_{mathrmtotal} = \beta_{size} + \beta_{microstrain} = 4\epsilon \tan\theta + \frac{\lambda K_\beta}{D \cos\theta}$.

[6]Lorentzian: $\beta_{\text{total}} = \beta_{\text{observed}} - \beta_{\text{instrument}}$; Gaussian: $\beta^2_{\text{total}} = \beta^2_{\text{observed}} - \beta^2_{\text{instrument}}$;

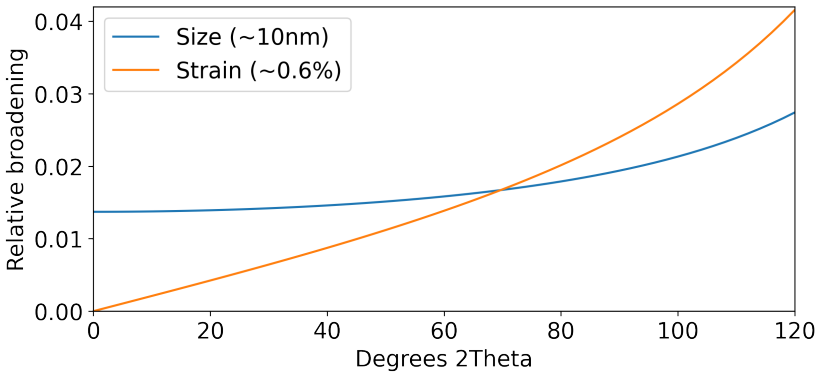

Figure 3.1: Angular dependence of simulated crystallite size and strain broadening.

and strain can be directly used in software based refinements such as in TOPAS [Coelho, 2018].

Like the WH method, WPPD can directly leverage the difference in angular dependence of crystallite size and micro-strain broadening, to separate their contributions to broadening. Additionally it allows the consideration of the relationship between peaks thorough Pawley, Le Bail or structure based refinements. This provides defined relations between peak positions which can improve the refinement stability when working with noisy data [7].

3.2 Effects of sample preparation, packing and mounting

The reliability of data is subject to the quality of instrument and sample alignment and proper sample mounting.

3.2.1 Intensity errors: Crystallite size

The precision and error in the observed intensities of a diffraction pattern depend on the number of diffracting crystallites and the randomness of their orientation. The effect of their orientation is discussed as preferred orientation in Section 3.2.2. The number of diffracting crystallites is related to statistical error by $\sigma = \frac{1}{\sqrt{N_{\text{diff}}}}$ where N_{diff} is the number of diffracting crystallites. From this *standard error* is 2.3σ as presented in Figure 3.2 [Elton and Salt, 1996, Smith, 2001] where a minimum 52 900 diffracting crystallites are required to reach a standard error of 1% [8].

The number of diffracting crystallites can be estimated using: crystallite size, beam footprint, effective penetration depth, and the angular window in which a crystallite will diffract for a specific instrument as discussed in [Smith, 2001]. This is shown in Table 3.1 to illustrate the relation between

[7] This is applied in diffraction pattern refinements of Chapter 9.

[8] The standard error is defined as 2.3σ in [Smith, 2001].

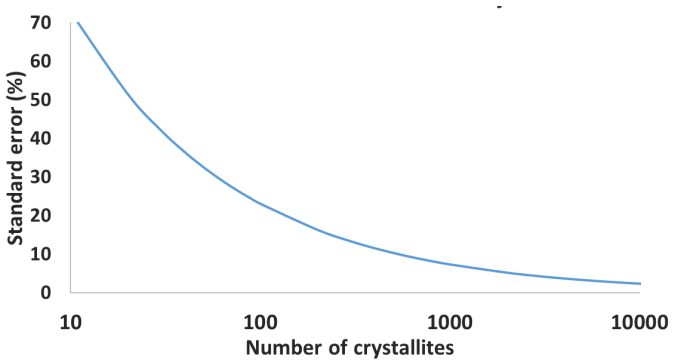

Figure 3.2: Standard error vs number of crystallites

crystallite diameter and *standard error*. These values serve as an estimate and will depend on the specific instrument and the randomness of the crystallite orientations.

The number of crystallites contributing to the collected data can be increased by reducing the crystallite size, sample spinning and/or repacking and remeasuring a powder sample multiple times.

Table 3.1: Number of diffracting crystallites in 20 mm^3 for a specific instrument configuration is presented in [Smith, 2001]

Crystallite diameter	40 μm	10 μm	1 μm
Volume ($\frac{4}{3}\pi r^3$)	3.35 x10^{-5}	5.24 x$10^{-}7$	5.24 x$10^{-}10$
Crystallites per 20 mm^3	5.97 x10^5	3.82 x10^7	3.82 x$10^1$0
Diffracting crystallites	12	760	38 000
Standard error 2.3σ	66.4%	8.3%	1.2%

3.2.2 Preferred orientation

When the crystallites of a sample are highly orientated, we deviate from the ideal of a large number of randomly oriented crystallites. This causes the diffraction pattern to depart from the ideal intensity distribution. This can be seen as a reduction or emphasis in the intensity of specific peaks, or apparent absence of some Bragg reflections, this presents the largest effect when collecting diffraction pattern using point or 1-dimensional detectors,

as are routinely used in lab based instruments, as exemplified in Figure 4.3. Unlike the intensity error in Section 3.2.1, preferred orientation has a non-random nature which can be explained through various mathematical models. These include the March-Dollase and spherical-harmonics approaches [Dollase, 1986, Järvinen, 1993, Pecharsky and Zavalij, 2005].

Preferred orientation is commonly observed in thin-films deposited on various substrates under various conditions. This arises from the packing fraction and the variation in the surface and strain energies of the grains. In *powder* samples, crystallites with a low aspect ratio shape such as needles or platelets tend to align along one or more preferred orientations [Dinnebier et al., 2018].

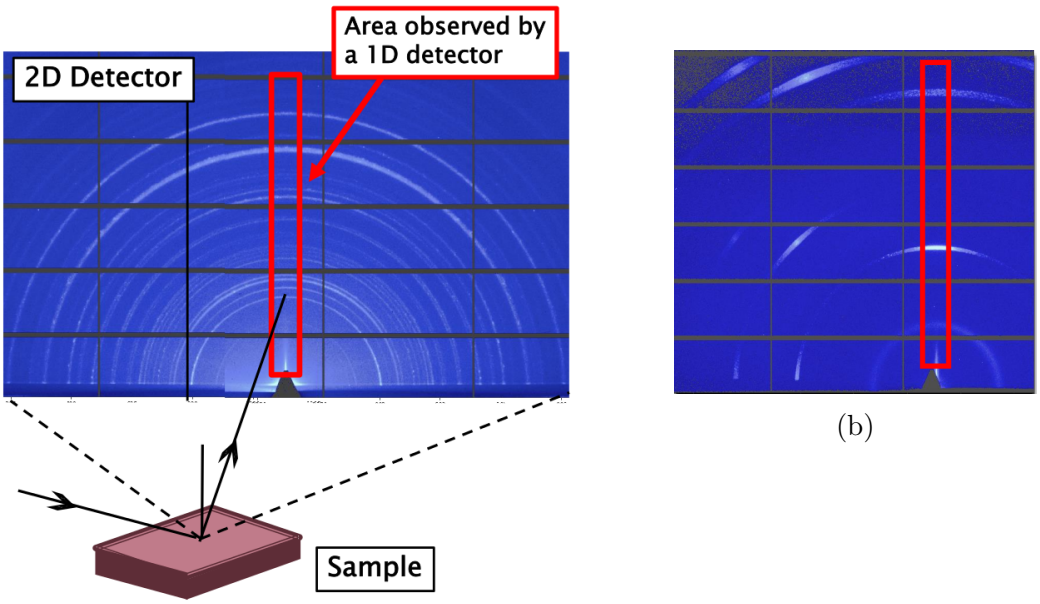

(a) (b)

Figure 3.3: Diffraction patterns collected on hybrid-perovskites thin-films showing (a) complete Debye-Scherrer diffraction rings and (b) segments, where the partial diffraction rings are due to preferred orientation in the sample.

** Synchrotron GIWAXS data collected at i07, Diamond Light Source, Didcot, UK.*

*** (a) superimposes a 2D pattern and its inverse to display a 180° arc of the diffraction ring in comparison to (b) which corresponds directly to the detector size.*

The distribution of sample orientations are reflected in the diffraction pattern. Diffractometers with 2D detectors will show complete Debye-Scherrer diffraction rings for an ideal powder sample, Figure 3.3 a. [9] As the degree of preferred orientation increases the rings become segments occupying a lower fraction of the full ring, Figure 3.3 b. In the case of single crystals well defined spots will be observed. It is the accumulation of these spots from a large number of randomly orientated crystallites which forms the Debye-Scherrer rings.

Lab based diffractometers often incorporate point detectors or PSDs (position sensitive detectors) which are only able to access out-of-plane reflections. In the case of a Bragg Brentano configuration, this is limited to Miller planes with a scattering vector perpendicular to the sample surface. Such instruments can only access a limited segment of reciprocal space and only the portion of the diffraction rings contained within [10]. This could potentially make the analysis of an unknown phase inaccessible, if none of the crystallites meet the diffraction condition for the instrument.

3.2.3 Sample alignment effects

Sample height displacement error

A diffraction pattern as collected, of a well-prepared, well mounted sample is often sufficient for basic pattern analysis such as fingerprinting (Section 3.6). Additional considerations are required when accurate lattice parameters are sought or when optimising a simulated pattern against the diffraction pattern. In a flat-plate Bragg-Brentano geometry a sub-millimetre displacement is expected in the height of a sample deviating from the centre the X-ray source and detector arcs. This causes a shift in the observed peak position.

[9] The pattern in Figure 3.3a does not represent an ideal powder. While the diffraction rings are near complete, they display brighter and dimmer pixels in a seemingly random occurrence. The sample is a thin-film < 1 μm in thickness. The deviation is suggested to be due to an insufficient sample volume as discussed in Section 3.2.1.

[10] Instruments with 2D detectors are able to sample a larger segment of reciprocal space. The accessible range depends on the size of the 2D detector and the available range of motion of the instruments goniometer.

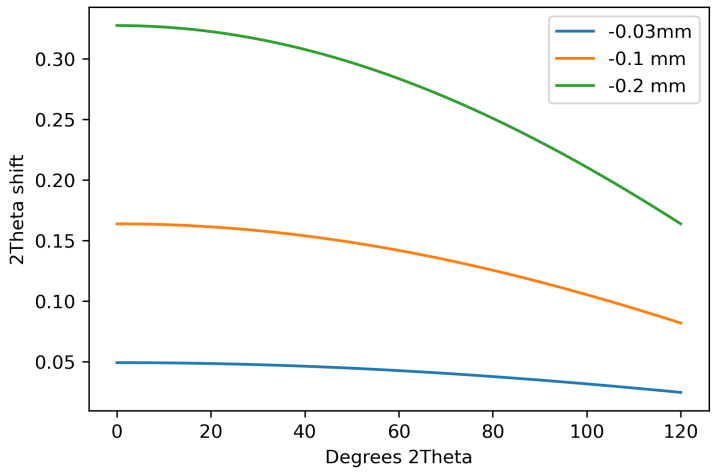

Figure 3.4: Height Error vs diffraction angle for a Bragg-Brentano diffraction geometry for selected displacement values. R = 70 mm, corresponding to a Bruker D2 Phaser desktop diffractometer.

[11] The extent of the shift can be described by the Equations 3.6 and 3.7 for symmetric and asymmetric flat plate measurement conditions respectively. In these equations, s is sample displacement, R is the distance between the sample and detector, and α is the incidence angle for the asymmetric geometry. The extent of the 2θ shift calculated for sample displacements of -0.03, -0.1 and -0.2 mm is illustrated in Figure 3.4.

Bragg-Brentano geometry:

$$\Delta 2\theta = -2s\left(\frac{180^\circ}{\pi}\right)\frac{\cos\theta}{R} \quad \text{[Dinnebier et al., 2018]} \tag{3.6}$$

Asymmetric diffraction/grazing incidence geometry:

$$\Delta 2\theta_\alpha = -2\left(\frac{180^\circ}{\pi}\right)\frac{s}{R\sin(\alpha)}\sin(2\theta) \quad \text{[Masson et al., 1996]} \tag{3.7}$$

[11] Diffractometers capable of attenuated direct beam sample alignment can align a sample far more accurately then diffractometers with a fixed sample holder position.

Capillary sample displacement

When a capillary sample in a Debye-Scherrer geometry is displaced from the centre of a diffractometer's goniometer, there is an associated peak shift. This can be described by Equation 3.8 where, R_{DS} is the detector to sample distance, d_{L} and d_{V} correspond to displacements in the direction of and perpendicular to the incident beam respectively [Dinnebier et al., 2018].

$$\Delta 2\theta = \arcsin\left(\frac{d_{\mathrm{L}}}{R_{\mathrm{DS}}}\sin(2\theta)\right) - \arcsin\left(\frac{d_{\mathrm{V}}}{R_{\mathrm{DS}}}\cos(2\theta)\right) \tag{3.8}$$

The effect of sample absorption will additionally result in sample peak shifts with semi-empirical correction functions dependent on the sample absorption coefficient and capillary diameter presented by Sabine *et al.* 1998 [12] [Sabine et al., 1998]. A more accurate numerical approach has since been developed by A. Coelho and M. Rowles which addresses peak position, intensity, and additionally shape correction, which they validated against a ray tracing simulation as detailed in [Coelho and Rowles, 2017] [13].

3.3 Peak shape and profile

The detail and reliability of information extracted from diffraction data depends on our ability to accurately model the peak shapes or profile. This impacts the determination of peak broadening described in Section 3.1, the atomic position refinement of Section 3.9.1 and many other aspects including thermal displacement and site occupancy.

[12] The peak shape and intensity correction in TOPAS-Academic, which makes use of Sabine's correction can be called by the TOPAS macros *Cylindrical_I_Correction* and *Cylindrical_2Th_Correction*.

[13] The disk "disc convolution" correction by [Coelho and Rowles, 2017] is called by the *capillary_diameter_mm* macro, the usage is described in [Coelho, 2020]

The diffracted peak profile can be well described as a convolution of both sample and instrumental factors. The prominent sample contributions include crystallite size, distortion effects (e.g. defects and compositional fluctuations) and absorption [14]. Sample contributions are independent of the instrument used [15]. This allows the use of standard reference materials (SRMs) with known properties to be used for the determination of an instruments contribution to the overall diffraction pattern [Cline et al., 2012]. The instrument profile can be described using either analytical functions or by a fundamental parameter model. The analytical functions attempt to describe the overall peak shape (or instrument contribution) while the fundamental parameters model is considers the individual effect of specific instrument optics. The application scope of an instrument profile is limited by the choice of SRM and any other uncertainties which may be present.

3.3.1 Standard reference materials

The purpose of a measurement is important in determining a suitable SRM. Different SRMs are best suited for determining different aspects of an instruments characteristics, these include standards for line shape, line position, instrument response, and quantitative analysis [Cline et al., 2012]. One such widely used SRM is NIST's 640 series silicon powder, which (excluding batches prior to 640c) is both a line position and line shape standard for powder diffraction. [Cline et al., 2012, Cline et al., , Black et al., 2020] As a line position standard it is suitable for optimising instrument profiles for accurate determination of lattice parameters. While as a line shape standard it has a crystallite size large enough to result in negligible crystallite size broadening on laboratory X-ray diffractometers [16] [17] [Black et al., 2020]. The SRM is specially annealed by NIST such that no micro-strain broadening is observed

[14] Chapter 5 of [Le Bail et al., 2008, Scardi, 2008]

[15] With the exception of absorption and sample size/footprint effects which can be calculated for specific instruments and configurations. Absorption coefficients are wavelength specific [Cromer and Liberman, 1970].

[16] The particle size of NIST Si 640f is reported in the μm range from laser scattering measurements. When synchrotron data was refined a "volume-weighted mean crystallite size" of 525 nm was determined [Black et al., 2020].

[17] In 2008, Scardi *et al.* estimated $\approx$ 200 nm to be near the limit of the broadening that can be observed on a lab based instrument, presumably with the exception of exotic instrument configurations [Scardi, 2008].

for accurate determination of peak shape [Black et al., 2020]. With these properties considered, silicon SRMs are used in this thesis.

3.3.2 Analytical peak profiles

The instrument function can be defined using analytical functions. These offer a simpler implementation with a quicker set-up compared to a fundamental parameter (FP) approach [18]. Prominent such profiles include Pearson VII, Voigt and pseudo-Voigt functions. These are closely related to, or based on a combination of Gaussian and Lorentzian functions (Equations 3.9 to 3.13, where w = FWHM). To remove the dependence of peak area on w, these functions requires normalisation, as is expressed in Young *et al.*, which is essential for quantitative analysis [Young, 1993].

Equation 3.11 presents the Pearson VII function, which allows the modelled peak shape to vary from a Lorentzian when $m = 1$, to a Gaussian shape as $m \to \infty$. The Voigt function, Equation 3.12 is a convolution of a Lorentzian and Gaussian. The Voigt function is relatively computationally expensive, as such a pseudo-Voigt (pV) function is widely used which serves as an approximation, Equation 3.13. The pV function is a linear combination of Lorentzian and Gaussian scaled by a factor η, with $0 \leq \eta \leq 1$ and usually defined such that $FWHM_{\text{Lorentzian}} = FWHM_{\text{Gaussian}}$ [Barnes et al., 2006, Gupta, 1998, Young, 1993][19].

$$\text{Gaussian (G): } I(2\theta) = I_{\max} e^{-4\ln 2 \frac{(2\theta - 2\theta_0)^2}{w^2}} \tag{3.9}$$

$$\text{Lorentzian (L): } I(2\theta) = I_{\max} \frac{w^2}{w^2 + 4(2\theta - 2\theta_0)^2} \tag{3.10}$$

$$\text{Pearson VII: } I(2\theta) = I_{\max} \frac{w^{2m}}{[w^2 + 4(2^{1/m} - 1)(2\theta - 2\theta_0)^2]^m} \tag{3.11}$$

$$\text{Voigt: } I(2\theta) = (G \circ L)(2\theta) \tag{3.12}$$

$$\text{pseudo-Voigt: } I(2\theta) = I_{\max}(1 - \eta)G(2\theta) + \eta L(2\theta) \tag{3.13}$$

[18] Analytical peak profiles were initially used in Rietveld refinement as they require fewer computational resources compared to a fundamental parameter approach.

[19] Section 7.3 of [Young, 1993]

These function can be split to account for asymmetric peaks by using separate *FWHM* values for the left and right of the peak maximum as presented in the Python code of Appendix F.3. [20] Both the Pearson VII and pseudo-Voigt functions can reasonably describe X-ray diffraction data while Lorentzian and Gaussian functions limited in their ability to provide a good fit of the peak tails. There are some more subtle features where these analytical functions fall short. As an example *tube tails* are not well-described by a split pseudo-Voigt while a FP approach can be effective [Cline et al., 2012, Young, 1993][19].

3.3.3 Fundamental parameter peak profiles

In contrast to analytical functions, a fundamental parameter approach for defining the instrument contribution requires more detailed inspection and characterisation of the instrument [Cheary and Coelho, 1992]. Such is required to define the component dependent convolutions of which the instrument profile is composed. This can be separated into the *source emission profile* and the *geometric instrument profile*. The emission profile can be represented as a series of Lorentzian peaks specific to the X-ray tubes anode material, as characterised in [Hölzer et al., 1997]. Where a monochromator is present, its effect will be considered in the modelled emission profile. The geometric profile is composed of convolutions describing individual effects of components in the instrument's optics [Cline et al., 2012]. These have a variety of forms and angular dependencies resulting in an intricate profile description with a meaningful physical basis. Coupled with the use of an appropriate standard reference material (SRM), a good instrument profile can reduce measurement uncertainty and allowing better access to sample information such as defects and microstructure [Cline et al., 2012, Le Bail et al., 2008] [21].

[20] Equations 3.9 and 3.10 are written such that w is the full-width at half-maximum.
[21] Chapter 6 of [Le Bail et al., 2008].

3.4 Agreement factors

Statistical agreement (R) factors serve as a means to judge the quality of a Rietveld refinement within a reasonable scientific basis. Further, they are a key part of the optimisation process in Rietveld refinement algorithms. The factors discussed here include R_{wp}, R_{exp}, R_{Bragg} and goodness of fit (χ or gof). These are the most relevant R-factors to this dissertation.

R_{wp} utilises a weighted sum of squares across the data set:

$$R_{\text{wp}} = \sqrt{\frac{\sum_{i=1}^{N} W_i (Y_{\text{obs},i} - Y_{\text{calc},i})^2}{\sum_{i=1}^{N} W_i {Y_{\text{obs},i}}^2}} \tag{3.14}$$

Where $Y_{\text{obs},i}$ is the intensity of the collected data, $Y_{\text{calc},i}$ of the simulated/calculated data and W_i is the weighting factor for the ith data point. The default weighting for powder diffraction data in TOPAS is $W_i = \frac{1}{\sigma(Y_{\text{obs},i})^2}$, where σ is the standard uncertainty typically taken as $\sigma = \sqrt{Y_{\text{obs},i}}$, corresponding to Poisson type counting statistics. The inclusion of a weighting factor in R_{wp} solves problems encountered with R_{p}, an unweighed equivalent. R_{p} is prone to overemphasise strong reflections, and doesn't consider experimental uncertainty [Dinnebier et al., 2018].

The R_{wp} value required for a good fit is dependent on the specific instrument, its configuration and the conditions of data collection of a given data set [22]. This makes it more difficult to assess fit quality or compare across datasets without additional information [Toby, 2006].

The lowest achievable R value for a refinement will be limited by the statistical conditions of the specific data set. This is estimated by the expected R-factor (R_{exp}) that is evaluated with the following equation: [Dinnebier et al., 2018, Toby, 2006]

$$R_{\text{exp}} = \sqrt{\frac{N - P}{\sum_{i=1}^{N} W_i {Y_{\text{obs},i}}^2}} \approx \sqrt{\frac{N}{\sum_{i=1}^{N} W_i {Y_{\text{obs},i}}^2}} \tag{3.15}$$

[22] A simple example of this is increasing counting time reduces statistical noise which would reduce R_{wp}.

Here, N is the number of data points and P the number of fit parameters. As the typical case is $N \gg P$ we can neglect P, ignoring the unlikely exception of an overzealous scientist, with an unsuitable sparsely sampled data set. With R_{exp} we can calculate the goodness of fit ($\chi = R_{\text{wp}}/R_{\text{exp}}$) which offers a quality of fit factor that is less dependent on the specific instrument, its configuration and the conditions of data collection of a data set.

χ^2 is the factor typically optimised in Rietveld refinement programs including TOPAS [Coelho, 2018]. χ^2 should ideally be close to 1. if $\chi^2 < 1$ it is possible the standard uncertainties of the data are likely overestimated. A χ^2 of close to 1 does not imply a correct model, there can be many models that will provide an equivalent fit for a given data set. At this point the experimental data is at its limit and cannot differentiate either a more complex nor more correct model. A $\chi^2 \gg 1$ can suggest an incomplete model, incorrect model, an underestimated standard uncertainty or even a structure that can not be well described by conventional models. In cases where R_{exp} is incorrect, a well informed Pawley or Le Bail fit can provide a reasonable measure of the best fit that can be achieved using a related structure model [Toby, 2006].

The last R factor to be discussed here is useful, even if it does not have a statistical basis. R_{Bragg} provides an R value focused on the intensities of reflections for a specific phase compared to a calculated pattern [23]. The equation is given below where k refers to the kth reflection and this is summed across K reflections [Dinnebier et al., 2018, Toby, 2006].

$$R_{\text{Bragg}} = \frac{\sum_{k=1}^{K} |I_{\text{obs},k} - I_{\text{calc},k}|}{\sum_{k=1}^{K} I_{\text{obs},k}} \tag{3.16}$$

R factors provide a useful means of assessing the quality of fit in a refinement which is especially relied upon by refinement algorithms. They serve as a means to compare the effect of changes in finer details within a phase model which may not have a discernible effect by eye [Toby, 2006]. As valuable as R factors can be, a visual comparison between the measured and calculated pattern is indispensable in assessing the quality of a Rietveld refinement. From a visual comparison, an experienced crystallographer can effectively assess the plausibility of model simulated.

[23] R_{Bragg} is calculated separately for each phase present in a refinement.

3.5 Limitations of powder X-ray diffraction

3.5.1 Light atoms in a heavier matrix

The ability of a material to scatter X-rays for diffraction depends on the electron density of the constituent atoms. This is related in the structure factor (F), equation 3.17, in which $\rho(r)$ is electron density, V is the unit cell volume [Von Dreele and Rodriguez-Carvajal, 2008]. The structure factor, F is related to intensity I by $I \propto |F|^2$. Knowing this, heavier atoms will result in more intense scattering contributions, while lighter atoms will produce weaker signals.

$$F(h) = \int_V \rho(r) e^{2\pi i(h \cdot r)} \mathrm{d}r \tag{3.17}$$

When considering light atoms in a matrix of heavier atoms, the small electron density of the lighter atoms can be over-shadowed by that of the heavier atoms in the structure. Inflating this difference, the lighter atoms are expected to have larger thermal motion reducing the intensity of the diffracted signals. [Weller et al., 2015b] This is explored below in the example of MA in a PbI_3 framework.

The contribution of the organic cation to the X-ray diffraction pattern of hybrid perovskites is notably small. Considering the formula $APbX_3$ of hybrid perovskites where A is an organic cation and X is a halide anion; the Pb-X framework in which the organic cation sits will account for most of the e^- density. In the case of $MAPbI_3$ the Pb-I framework accounts for >98% of the diffracted intensity based on Equation 3.17.

The diffracted intensity of the organic cation will be further reduced due to its disorder and freedom of movement at ambient temperatures [Weber et al., 2018, Yang et al., 2018a]. This is evident in equation 3.18 where f_i is the scattering factor for a given atom and $\langle u_i^2 \rangle$ is the mean square of atomic displacement [24] [Von Dreele and Rodriguez-Carvajal, 2008].

[24] Scattering factors are based on the assumption that scattering power is localised at the centre of an atom [Von Dreele and Rodriguez-Carvajal, 2008].

$$F(h) = \sum_{i=1}^{N} f_i(s) e^{2\pi i(h \cdot x_i)} e^{-8\pi^2 s^2 \langle u_i^2 \rangle} \tag{3.18}$$

In-situ lab-based diffraction data collected using conventional sealed tube X-ray sources are usually limited in the time available for each diffraction pattern. In most cases this limits the angular collection range and/or integration time for each diffraction pattern. With these limitations in place, many finer details such as those relevant to the organic are potentially unreliable or inaccessible. The most reliable structural information accessible for a $MAPbI_3$-based data set is expected to be that of the Pb-X framework, while the organic was not expected to have a very significant contribution in the diffraction data. This marginalisation of the organic cation is less significant for larger cations and for structures where the organic component presents a greater fraction of the composition. Approaches to modelling the organic cations are discussed in Section 4.9.2.

3.5.2 Resolving atom identity

For a given structure or unit cell, X-ray diffraction (XRD) is sensitive to the contrast in scattering intensities between the constituent atoms, which depends on their electron scattering cross section. This is a function of the identity of an atom which is not unique to the chemical identity, especially not where charge, thermal displacement, and the potential of atomic site substitution play a role.

In powder XRD (PXRD) it can be it difficult or even untenable to differentiate atoms which are nearly isoelectronic such as carbon (6^{e-}) and nitrogen (7^{e-}) [Weller et al., 2015b]. This is related to the nature of the contrast in scattering intensities, and the information-poor [25] approach inherent to PXRD, where the reciprocal space information represented by a diffraction pattern is compressed into a single dimension.

[25] The number of parameters exceeds the number of observations on which to model them.

3.5.3 Real Structure?

Diffraction patterns provides information on the average structure of a material. This is modelled as the "smallest" repeating unit or **unit cell** which, through translation, can reproduce the material. In such an approach, variations between unit cells are averaged out. In addition, regions without long range order such as surfaces, grain boundaries, and amorphous content can easily be neglected. During a diffraction measurement, other scattering effects may be observed, such as broad humps, which can be related to amorphous content. [26]

The area sampled by a given analysis technique is seldom the entire sample, not every aspect or region of a sample is guaranteed to interact uniformly with a given probe. The smaller the sample volume, the less likely the probed area will be statistically representative of the sample [27]. The sampled volume is related to the probe size and the interactions between the probe and sample. X-ray and neutron techniques provide deep sample penetration resulting from the relatively small scattering cross-sections of X-rays and neutrons in materials. In contrast, electrons have much larger scattering cross sections due to coulombic interactions, making them more surface-sensitive. With the penetration depth of X-rays, the collected information under a standard diffraction experiment is representative of the bulk structure [28][Vonk and Graafsma, 2014]. This is especially the case for diffraction where the surfaces and grain boundaries of a material presenting shorter-ranged structural order do not present a repeating structure necessary for diffraction. [29] Un-

[26]Humps related to amorphous content can be used in quantitative analysis with different amorphous contributions having different positions in the diffraction pattern. Due to the broadness of amorphous signals in a diffraction patterns, if multiple amorphous components are present and close in position the individual contributions may not be able to be resolved.

[27]related to Section 3.2.1

[28]The proportion of signal interaction of the probe with the surface is marginal compared to the large volume of the bulk.

[29]With a combination of high X-ray flux, specialised optics, and specialised detectors, such as can be available at select synchrotron light source facilitates, a scattering volume of 1 μm^3 can be probed with an estimated lower limit of 1000 nm^3 ([Vonk and Graafsma, 2014]). Towards this lower limit the sampled area may deviate from the average bulk structure. Lab-based micro-sources such as Incoatec's $I\mu$ sources can produce beams with dimensions in the 10's of μm's [Graf, 2014]

der certain conditions X-rays can be used to selectively probe a surface, this is used for X-ray reflectometry and grazing-incidence XRD using a shallow incident beam angle of not more than a few degrees to reduce penetration depth of the beam.

Total X-ray scattering analysis by means of a pair-distribution function (PDF) can be used to model the local structure of a material. In some materials, the local structure may correspond to the average structure. The presence of defect, partial occupancies, flexible bonds [30], or other features that have the potential to affect or differentiate the local structure, can cause differentiation between the local structure derived from PDF and average structure from XRD. Both methods provide hints on the *real structure* although even the combination is unable to provide a full picture.

Contrasting large sample volume techniques, high resolution electron microscopy is able to probe surfaces and grain boundaries. Such can provide valuable insights on a material, which are not accessible through diffraction or PDF. However this technique is limited by the sampling size making it time consuming to collect statistically relevant data and impracticable to assess the average structure of a material. The statistics of the data collection can be critical for a robust comparison of similar materials, while a single observation of a feature can be sufficient for proof of concept.

Optical data can be used to infer the electronic structure and bonding within a material. Across diffraction, total scattering, electron microscopy, and optical based techniques, the structural and electronic information determined by any of these techniques can provide valuable insights into the properties and development of materials. The insight from such techniques provide a better picture of the conceptual *real structure*. The *real structure* can be approximated as the total of structural information that can be known of a material including the averaged and dynamic aspects.

[30] Such as octahedral tilts in perovskites, vibrational/rotational modes such as in many organics [Becka and Cruickshank, 1961]

3.6 Diffraction pattern fingerprinting

Fingerprinting of XRD powder patterns is performed by comparing a diffraction pattern against the literature. This can be executed using search/match software by searching for candidates from a structure database [31]. The software makes comparisons using peak positions and relative peak intensities [32]. The lists of candidates can be filtered using chemical composition, environmental conditions such as temperature and pressure alongside many other properties [33].

3.6.1 Assignment considerations

Whether a literature pattern serves as a reasonable assignment can be assessed by considering factors including: additional/absent peaks, peak position, relative peak intensity, and peak profile clustering.

The peak position for a given measurement may deviate from the literature pattern, this can be considered by scaling the size of the unit cell and evaluating the scaling factor. Should there be a substantial difference in the unit cell size, differences in the composition and experimental conditions (such as temperature or pressure) between the experimental and literature data can be assessed to properly scrutinise the differences. Once scaled, the peak positions should coincide, any clear deviations are an indication of an incorrect assignment candidate.

Another key consideration is the relative peak intensities between literature and experimental patterns. The peak intensities hold information on the relative electron densities between atomic sites, and by extension, clues

[31] Examples of search/match software includes Bruker's Eva and Crystal Impact's Match!.

[32] Peak positions measured in 2θ are wavelength specific as per Bragg's law. When comparing diffraction data if the units/X-ray wavelengths are different conversion will be required. This process is partially automated in Diffrac.EVA which may not be representative of other search/match software.

[33] Databases where structures from literature can be found include the Crystallography Open Database, (COD) [Gražulis et al., 2009] and the Inorganic Crystal Structure Database (ICSD) [Hellenbrandt, 2004].

to the elemental composition of a material. Large mismatches in the relative intensity between peaks can be sufficient cause to rule out an assignment candidate. [34] In some samples texturing/preferred orientation affects peak intensities or could even cause the apparent absence of peaks in the experimental data [35]. Small variations are less decisive as they could be due to a variety of causes, such as instrument configuration, incorrect thermal parameters, site occupancies, statistical intensity variations from a small sample sizes or counting statistics, preferred orientation, structure distortion etc..

The absence of peaks or presence of additional peaks in a candidate pattern is indicative of an incorrect assignment candidate. This can be complicated in cases where a strong preferred orientation is present.

For a given structural phase in a diffraction pattern, the peak profile is determined by a combination of sample and instrument contributions, (Section 3.3.3). When a diffraction pattern contains multiple distinct peak profiles, these can be used as a rudimentary means to separate phases in the pattern. This can be subject to ambiguity, as broader peaks observed may originate from overlapping peaks, separate phases, asymmetric broadening factors, etc. [36]. Many of the factors that shape the peak profiles have an angular dependency which may be observed as a gradual shift in the peak profile with 2θ, such as the sample broadening contributions discussed in Section 3.1.1. Some samples experience anisotropic peak broadening effects which is dependent on the Miller indices of a material complicating visual peak grouping and phase separation [37]. The distinct peak profiles can be used as means of grouping contributions in a diffraction pattern. This is invaluable in fingerprinting mixed phase systems, noting a difference in peak

[34] Fingerprinting candidates where the peak positions are a good match with incorrect relative intensities may contain some structure parameters which represent the sample, such as some unit cell parameters and/or the space group.

[35] Preferred orientation is common in solid samples, pressed powders, and thin-films. It is generally expected to have a strong effect for crystallites which form in easily stacked shape such as rods or platelets, discussed in Section 3.2.2.

[36] Asymmetric crystallite shape and micro-strain along specific crystallographic directions can result variations in peak broadening within a phase. One strategy is to consider peak broadening in related reflections for a candidate phase, eg. (100) and (200) would be subject to common sample broadening effects and similarly for (110) and (220).

[37] From limited personal experience, anisotropic effects are not expected unless there is a material property or sample processing likely to induce an anisotropic effect.

profile does not exclude peaks from being related.

Fingerprinting is a useful tool for systems where good assignment candidates are accessible, which is the case for well known structures. It is an ideal approach for initial phase identification or when further structural detail is not required. The considerations outlined above can be more critically assessed within a Rietveld refinement, which provides a more rigorous evaluation of a structure assignment against a given diffraction pattern. Rietveld refinement further provides a means to access finer structural details beyond initial phase assignment. Where a suitable literature structure is not available alternate methods will be needed to gain structural information such as pattern indexing.

3.7 Indexing

Powder pattern indexing tries to establish 3-dimensional structural information including the unit cell dimensions and space group from peak positions and intensities of a 1-dimensional powder pattern. The nature of reconstructing a structure of higher dimensionality than the diffraction data (PXRD) implies this will always be a data-poor process. [38] With good data, indexing can work well and provides one or multiple plausible solutions. With low-quality data, indexing cannot be expected to work at all [Shirley, 1980]. For comparison, indexing of 3-dimensional single crystal data is information rich and can reliably provide a highest symmetry unit cell and space group for reasonable quality samples.

Indexing is considered the first step in *ab initio* structure determination. The lower angle peaks are more important to indexing. There are typically fewer reflections and better peak separation at lower angles. While higher angle peaks are more prone to overlap which may not always be discernable [Bergmann et al., 2004, Altomare et al., 2018]. Ideally, indexing should be

[38] More variables are required for structure determination than there are observables in PXRD data. Features including the peaks and their profiles contribute to the quantity of observed information. The number of data points in the diffraction pattern affects the ability to resolve these observables, once features are well resolved additional data points provide no additional benefit.

performed on a single phase material or in a material where the other phases are known and can be accounted. [39]

Bergmann *et al.* (2004) suggested that the most effective means for successful indexing is the collection of high-quality data, by someone with the experience to obtain it. This includes both accuracy and resolution in 2θ. They found data quality is far more important than the choice of indexing software, and that the use of various software packages increase the likelihood of a good solution. This speaks to the importance of quality data for effective indexing. [Bergmann et al., 2004]

3.8 Whole powder pattern decomposition

The term *whole powder pattern decomposition* (WPPD) is typically used to describe fitting a pattern in absence of a defined structure, which is a subset of WPPD, a broader term that includes typical structure based Rietveld refinement. The use of structure agnostic refinements allows the evaluation of a diffraction pattern with minimal information.

3.8.1 Individual peak fitting

Individually fitted analytical peaks can be used to provide precise peak positions [40]. This can provide peak positions and intensities for powder pattern indexing and it is useful for bare-bones comparisons between diffraction patterns. These fit objects can be used alongside other refinement methods such as to fit peaks of unknown origin [41] or broad amorphous peaks.

[39] Where this is not possible, the chance of solving the structure is often very low, peak profile clustering can be invaluable alongside the well established principle of garbage-in garbage-out. If an algorithm is given an a subset of peaks from multiple phases it can not be expected to provide a sensible result.

[40] Peak profiles are discussed in Section 3.3

[41] Such as impurity related peaks.

3.8.2 Pawley and Le Bail refinements

The use of structure-agnostic refinements allows the evaluation of a diffraction pattern without the use of atomic coordinates. These have been extensively used in this thesis in the form of Pawley and Le Bail fits, which require a set of approximate lattice parameters along with a space group. These fits can then provide refined lattice parameters, peak intensities and agreement factors. Such information is useful as a means to confirm the plausibility of results extracted from pattern indexing, and to support the assignment of space groups to unknown phases. [Le Bail, 2005]

Structure agnostic refinements can be preferred over Rietveld refinements in cases where the structure is unknown or has properties which are not readily described [42]. Pawley and Le Bail refinements are most suitable for structures containing less peak overlap such as smaller, higher symmetry unit cell. In large low symmetry unit cells the presence of overlapping peaks in refinements may introduce ambiguity in the refinements leading to inconsistent results. [Peterson, 2005].

Both methods face the challenge of overlapping reflections. For both it is possible to have results with an unrealistic negative intensity coupled to a compensating positive intensity for overlapping peaks [43]. This is an important issue especially if they are the basis for attempts at structure solution from a powder pattern. Comparisons including a *round-robin* between the Pawley and Le Bail methods as a basis for structure solution from powder patterns have shown that both methods have similar capabilities with neither significantly better than the other. This includes round-robin comparisons. [Le Bail, 2005]

[42] Such properties could include disorder and defects.

[43] With sufficient separation, partially overlapping peaks can be deconvoluted.

3.9 Structure based (Rietveld) refinement

3.9.1 Atomic position refinement

Free atoms

The traditional approach to finding atom coordinates involves first determining the space group and unit cell parameters though indexing (Section 3.7). Atomic coordinates are then refined using fractional coordinates. [David et al., 2006] For each free atom three fractional coordinates may be refined. This is best performed when a reasonable fit is already obtained perhaps with some discrepancies between the calculated and observed data. [Etter et al., 2014]

In this approach the space group is used to populate equivalent sites in the unit cell by symmetry operations. Additionally constraints and boundaries can be applied to refinements of the atomic positions. For atoms in Wyckoff position with the exception of symmetry points, the atom may be refined along planes or lines on which an atoms Wyckoff position is conserved. Additional constrains can be added relating the position of atoms which is the basis for the definition of *rigid-body* and *symmetry mode distortion based refinements*.

Rigid-bodies

Rigid-bodies define connected atoms with constraints of bond length and angle between them. The inclusion of connectivity information into the structural refinement reduces the degrees of freedom and allowing the structure to be easily constrained to physically feasible conditions. This approach is the most advantages for organic components where the connectivity and approximate bond lengths are well known.

Symmetry mode distortion

Symmetry mode distortion includes the description of vibrational and rotational modes in a structure. This can be implemented in TOPAS by defining parameters to augment the coordinates of atoms or rigid-bodies in the unit cell in accordance with specific distortion modes. [44]

Comparisons between this and the other approaches mentioned here in Section 3.9.1 and the refinement types in Section 3.10 have been investigated in the work of Etter *et al.* 2014. In their work they found all of these approaches provided good refinements for their inorganic perovskite based data set in terms of fit quality with the use of symmetry modes proving the most stable refinements. [Etter et al., 2014]

3.9.2 Atomic displacement parameter

Within a material there can be deviations in atomic positions due to static and dynamic displacements from the mean. These can be inherent to a structure, induced by defects [45], or from dynamic thermal motion. The overall effect can be described in an isotropic parameter such as $B = 8\pi^2\langle u_i^2\rangle$, where $\langle u_i^2\rangle$ is the mean square of atomic displacement [46] [Dinnebier et al., 2018, Von Dreele and Rodriguez-Carvajal, 2008]. Following the discussion in Section 3.5.1, this is used in expressing Equation 3.18 as Equation 3.19. This shows an increase in the displacement parameter is accompanied by a decrease in scattered intensity.

$$I \propto |\sum_{i=1}^{N} f_i(s) e^{2\pi i(h\cdot x_i)} e^{-Bs^2}|^2 \tag{3.19}$$

[44] The web based tool ISODISTORT is useful to assist with identifying the distortion symmetry and modes, as well as estimating limits for the distortion and providing a structure with atomic parameters defined in terms of fractional coordinate. [Stokes et al., 2017] [Stokes et al., 2006]

[45] Discussed in Section 2.3.

[46] B is used in TOPAS-Academic.

Similar intensity effects are observed from changes in site occupancy. In structures with partial site occupancies or non-stoichiometric structures, site occupancy and atonic displacement parameters are strongly correlated. As such, only one of these parameters should be refined while the other determined by another means. For single-crystal XRD anisotropic displacement parameters can be refined. This is often beyond the limitations of PXRD data. For strong scatterers in exceptionally high quality powder diffraction data the refinement of anisotropic displacement parameters is possible [Dinnebier et al., 2018].

The ability of B to model a range of effects including atomic displacement, disorder, and unfortunately site occupancy has earned it the title of "*physical trash collector*" [Dinnebier et al., 2018]. The atomic displacement parameter is essential in Rietveld refinement and can provide an indication of disorder in a structure or the direction of displacements in the case of the anisotropic factor. Awareness of its limitations is necessary to avoid over-interpretation.

3.10 Sequential and parametric refinement

Sequential and parametric refinements are capable of efficiently processing large data sets collected as a function of an external variable (3-dimensional data-set) [47] [48]. Such data sets can provide deeper insights of dynamical changes in structural properties of a solid than can be gained from a single diffraction pattern. Additionally these may allow better the separation of dynamic parameters such as thermal parameters from site occupancy in the case of variable temperature diffraction data sets. These data-sets can be very large to the point that individual refinement becomes infeasible [Stinton and Evans, 2007].

Sequential refinement offers a relatively simple software implementation. Should a Rietveld program not offer sequential refinement or the desired control, a scientist can manually (for a small data-set) or through external code perform sequential refinements. Conversely, parametric refinements require a

[47] The external variable is often, but not limited to temperature, time or pressure
[48] Chapters 8, 7, and 8 present temperature dependent 3D data-sets

more computationally involved approach where parameters are refined across the entire 3D data set. Thankfully, the parametric refinement approach is implemented in TOPAS-ACADEMIC which is used in this dissertation [49].

3.10.1 Sequential refinement

Following an initial manual refinement, sequential refinements take advantage of the typical similarity of subsequent scans in a 3-dimensional (3D) data sets. Sequential refinements use the output of the nth scan as the starting parameter for the $(n+1)^{\text{th}}$ refinement [Rowles, 2021]. By having the starting parameters for a refinement closer to the expected refined parameters, the refinement time per scan is reduced and the refinements are less likely to be confined to local minima.

Sequential refinements are well suited to tracking gradual changes in diffraction patterns as a function of some parameter. Some of the advantage of sequential refinements are lost at sudden changes in the data, such as phase changes, where parameters on either side of the transition will be quite different. [Dinnebier et al., 2018] [50]

The effect of a sudden change in subsequent diffraction patterns can be partially mitigated through a bi-directional approach. In a bi-directional approach, sequential refinements are run from both ends of the data-set and a "statistical agreement factor" is used to select the best refinement for each diffraction pattern. Where there is a sudden change in the data between the $(n-1)^{\text{th}}$ and n^{th} data pattern, both $(n-1)$ and $(n+1)$ refinement results are compared as starting parameters for the nth refinement. This is implemented and explored further in Section 6.7.

[49] TOPAS-Academic V6/V7 and GSAS-II are capable of both sequential and parametric refinements [Coelho, 2018, Toby and Von Dreele, 2013].

[50] Discussed in Chapter 12.2 of [Dinnebier et al., 2018]

3.10.2 Parametric refinement

Parametric refinements were introduced by Stinton and Evans in 2007 [Müller et al., 2009, Stinton and Evans, 2007]. These consider the entire 3D data set simultaneously. Their advantage comes from the ability to define *global parameters* for use in individual patterns which can be used directly or as a function defined by physical and/or empirical equations. [51] By acting across the full data set, this can greatly reduce the number of parameters in the refinement, which in turn can stabilise the refinements and their results, as evident in Chapter 8, as well as greatly reduce refinement time [52]. The approach can result in a reduced correlation between parameters in comparison to sequential refinements.

The cases where a parametric approach is most powerful, include where there is significant correlation between refined parameters, where multiple structure models are compared that explain the data equally well, and for the refinement of non-crystallographic parameters such as parameters which relate to trends across the data sets which is not possible in individual data sets. [Dinnebier et al., 2018]

The accuracy of data analysis can benefit from the larger source of information. Parameters such as the zero-point error should be common across a 3D data set, and its accuracy affects that of the lattice parameters. Parametrising the zero-point correction across a 3D data set allows a single common value to be refined, improving both the reliability and providing a common value making comparisons of refined dimensions more stable.

Physically meaningful functions can be used to describe parameters. This can include lattice or thermal parameters to which may follow the form $a(T) = a_0 + \frac{c_1\theta_1}{e^{(\theta_1/T)}-1}$ [Dinnebier et al., 2018]. In data sets tracking chemical reactions or phase transition, rate equations can be used to define scale factors (proportional to quantity of a phase) as demonstrated in [Müller et al., 2009]. Additionally trends in the parameters can be used as a basis for fitting analytical functions such as polynomials across the data set [Stinton

[51] Global in terms of a global variable refers to the variable being accessible throughout a program, here it refers to an equation globally defined across the full data set.

[52] This can be critically important for very large data sets such as those generated by X-ray diffraction tomography.

and Evans, 2007]. Refinement parameters such as fractional coordinates and sample height displacement can be expected to follow polynomial trends. Fractional coordinates and other structural parameters may express discontinuities or for part of the data set be unsuitable for a given function. These can be accommodated by excluding such areas from a parametrised range [Etter et al., 2014].

Parametric refinements allow for the consideration of structurally relevant data obtained from other analysis techniques. Such can be used to constrain parameters to physically meaningful values or limits. These can include phase transition temperatures or lattice expansion relations [53] [Etter et al., 2014, Müller et al., 2009, Stinton and Evans, 2007].

The use of parametrisation can constrain the refinement to within a function or model. If the model is correct this will provide good results, with an incorrect model the results may look good and provide inaccurate information. It is due diligence to perform a set of reference refinements prior to parametrisation.

A reference set can consist of a small number of manually refined patterns or the full set of refinements with only general parametrization such as sample alignment based parameters. A reference set may allows the fitting of data in external programs for the following (1) by fitting functions or models to reference data, appropriate starting values for refinements and parametrisation can be obtained, (2) this provides an opportunity to consider features in the data which may be lost in poor or aggressive parametrisations and (3) to assess the validity of the chosen functions or models. The use of good starting parameters reduces the risk of refining to a local minimum and is better suited to the least-squares optimisation using in Rietveld refinement software such as TOPAS. [Dinnebier et al., 2018]

[53] In Chapter 12 of [Dinnebier et al., 2018], Table 12.1 provides various equations targeted for parametrising Rietveld refinements.

Part II

Investigative methods

Chapter 4

Investigative methods

Contents

4.1 Overview **79**

4.2 List of chemicals and materials **79**

4.3 Organo-amine salt synthesis **79**

4.4 Thin film fabrication **81**

4.4.1 Substrate cleaning 81

4.4.2 Substrate etching 81

4.4.3 Precursor solution for spin coating 82

4.4.4 Precursor solutions and dilutions for spin coating $(A'X)_{2x}(AX)_{1-x}PbX_2$ systems 82

4.4.5 Spin coating 83

4.4.6 Sample annealing 84

4.5 Powder samples from thin-films **85**

4.6 Optical spectroscopy **87**

4.6.1 Optical absorption 87

4.6.2 Photoluminescence measurements 88

4.6.3 Stokes shift 89

4.7 X-ray diffraction: sample mounting and measurement . **89**

4.7.1 Sample preparation and instrument effects of packed capillary XRD samples 90
4.7.2 X-ray diffraction measurements of thin-films . . . 90
4.8 Instrument profiles for XRD data modelling **91**
4.8.1 Capillary samples on a Bruker D8 Advance (CuKα) 92
4.8.2 Flat plate sample on a Bruker D2 Phaser (CoKα) 93
4.9 Structure modelling of X-ray diffraction data **94**
4.9.1 X-ray diffraction refinement method 94
4.9.2 Modelling an organic cation in a 3D framework . 95
4.9.3 Two and four octahedra unit cells 96
4.9.4 Modelling of layered 2D perovskite thin-films . . 99

4.1 Overview

In this chapter a range of methods are covered which are used in the subsequent chapters. Variation and deviations from these methods are expounded in the subsequent chapters. In many cases the comparisons between methods are critical to the interpretation of the chapters results.

4.2 List of chemicals and materials

Starting materials

- Lead(II) bromide 98 %, SAARCHEM UNILAB 390150
- n,n-Dimethylformamide (DMF) 99.5 %, ACE CAS No. 68-12-2
- Dimethyl sulfoxide (DMSO) 99.5 %, Sigma-Aldrich D5879-500ML
- Ethyl acetate, ACE CAS No. 141-78-6
- Diethyl ether, ACE CAS No. 60-29-7

Components for organo-ammonium halide synthesis

- Methylamine (MA) solution, 40 wt % in H_2O, Sigma-Aldrich 426466-1L
- Propylamine (PA) 98 %, Aldrich Cat: 10,981-9
- Ethanolamine (HOEA) 99 %, Sigma-Aldrich 398136-500ML
- Hydrobromic acid 48 wt % in H_2O

4.3 Organo-amine salt synthesis

Organo-ammonium halide salts were prepared from their amines, with the exception of the organo-amines, which started as halide salts. 6-14 ml of the organo-amine was placed in a 100 ml round bottom flask with a magnetic stirrer bar. This was allowed to cool in an ice bath under a fume hood. A volume of 48 wt % hydrobromic acid was measured out in a volume corresponding to 1:1 molar ratio with the organo-amine. The acid was initially added drop-wise to the round bottom flask while stirring, with the addition



(a) (b) (c) (d)

Figure 4.1: Various stages of organo-amine salt synthesis, (a) Vacuum-assisted rotary evaporation of H_2O, (b) Organo-amine salt prior to washing (c) after diethyl-ether wash and (d) single-crystal XRD derived structure motif of HOEABr.

speed increasing as the reaction became less vigorous. The sides of the round bottom flask were washed down with DI H_2O. The solution was left in the ice bath for 2 hours before using a vacuum-assisted rotary evaporator set at $65 - 80$ °C for the evaporation of water present in the solution, Figure 4.1a. The relatively large round bottom flask provides a greater surface area for solvent evaporation.

The precipitate was dried at 90 °C for an hour, presenting an off-white colour, Figure 4.1b. This was then washed three times using a Buchner funnel using 20 ml of diethyl-ether per wash to remove impurities, some observable through their effect on the colour of the powder, Figure 4.1c. The washed powder was dried overnight at 80 °C. These organo-ammonium halides were stored in *poly-top* sample vials in a desiccator and rewashed for experiments when more than two weeks had passed since their preparation.

The synthesis of MABr salts were confirmed through the PXRD structures and the band-gap determined for $MAPbBr_3$ in Chapter 9. The formation of $HO(CH_2)_2NH_2 \cdot HBr$, (HOEABr) was confirmed through the crystallisation of the salt followed by single-crystal XRD and analysis as discussed in SI Section E.3.2.

4.4 Thin film fabrication

Glass substrates with or without a thin conducting oxide coating (TCO) of either ITO or FTO were used. [1] Substrates were cut to size using a table top glass cutter. The samples which were prepared at the University of the Witwatersrand (Wits) primarily used 12.5 x 12.5 mm substrates. This corresponded to the size of the available masks for metallisation of contacts. At the University of Sheffield the spin coater, metallisation mask, and electrochemical characterisation mount accommodated samples 15 x 20 mm. Samples which were prepared at Wits to be scraped off as a powder, were prepared on 25 x 25 mm microscope glass for a larger surface area to achieve a larger sample volume per substrate. The substrates were then marked with sequential names using a tungsten carbide scribe. The text was confined to one edge on the underside of the substrate. For TCO samples this was the same edge that was subsequently etched.

4.4.1 Substrate cleaning

Glass based substrates were rinsed with DI H_2O to remove any loose debris from the cutting and scribing steps. These were then mechanically cleaned with a gloved hand using a soap water solution. Samples were then sonicated in DI H_2O, acetone and isopropanol for 20 minutes in each solvent. The substrates were rinsed with the corresponding solvent prior to each sonication step. Samples were dried with a N_2 stream and sorted for subsequent film deposition.

4.4.2 Substrate etching

For TCO-coated substrates, 3 quarters of the TCO film was covered with acid resistant Kapton (polyimide) tape leaving 1 quarter exposed. To etch the exposed TCO, an aqueous zinc paste (the consistency of toothpaste) was prepared and applied to the exposed section. The substrate was then sub-

[1] ITO: Indium-tin oxide, FTO: Fluorine doped tin oxide

merged in 2 M HCl solution. The substrate was then cleaned with deionized (DI) H_2O and the conductivity of the etched surface was tested and if needed the etching process was repeated until the conductivity of the etched surface was in the MΩ range indicating that the exposed ITO coating was effectively removed.

4.4.3 Precursor solution for spin coating

Organo-amine and lead halide powders of varying mass were weighed into a polytop sample vial using an Ohaus E11140, high precision mass balance, with a ±0.2 mg precision. A magnetic stirrer bar was added followed by the solvents. A 100 - 1000 μL pipette was used for the addition of solvents. The pipette tips were wet with the solvent prior to use. The solvents used for hybrid-perovskite films included a 4:1 DMF:DMSO solution for Chapters 6, 7 and 8, and 7:3 DMF:DMSO solution for Chapter 9. The polytop sample vial containing the precursor solution was sealed with a small strip of Parafilm and stirred using a magnetic stirrer bar for no less than 2 hours at 40 °C prior to spin coating.

4.4.4 Precursor solutions and dilutions for spin coating $(A'X)_{2x}(AX)_{1-x}PbX_2$ systems

Precursors for layered hybrid-perovskites films were produced from two primary solutions of 2 ml each as described in Section 4.4.3. These were (1) a $APbX_3$ solution of 0.6 M AX and 0.6 M PbX_2 and (2) an $(A')_2PbX_4$ solution of 1.2 M A′X and 0.6 M PbX_2 in 7:3 DMF:DMSO. Films following the composition $(A'X)_{2x}(AX)_{1-x}PbX_2$, where A is methylammonium (MA) the inter-octahedral cation, A' is the organic cation separating layers of octahedra, such as propylammonium (PA), and X is the halide, Br. These solutions were then used to produce additional precursor solutions using the dilution scheme in Table 4.1 where $APbX_3$ and $(A')_2PbX_4$ precursor solutions correspond to $x = 0$ and $x = 1$ respectively.

Each solution of composition x in Table 4.1 is composed of additions from two other solutions. As an example, $x = 0.5$ is prepared by mixing 600 μl of the $x = 0$ solution, and 600 μl of the $x = 1$ solution. For the $x = 0.3$ solution, the combination, 200 μl of $x = 0$ and 300 μl of $x = 0.5$ are utilised. This requires that the $x = 0.5$ solution needs to be prepared prior to the $= 0.3$ solution. The initial and final volumes refer the amount of each solution initially prepared and the volume remaining after the full set of dilutions are prepared.

The full set of dilutions produces a 13 sample set, in cases where a 9-step sample set was produced this used the set $x \in \{0, 0.05, 0.1, 0.2, 0.5, 0.8, 0.9, 0.95, 1\}$ [2].

Table 4.1: Dilution scheme for $(A'X)_{2x}(AX)_{1-x}PbX_2$ systems.

x	**0.025**	**0.05**	**0.075**	**0.1**	**0.2**	**0.3**	**0.4**	**0.5**	**0.8**	**0.9**	**0.95**
Solution 1 (x)	0	0	0.05	0	0	0	0.3	0	0.5	0.8	0.9
Volume (μL)	100	200	100	300	300	200	100	600	200	300	200
Solution 2 (x)	0.05	0.1	0.1	0.2	0.5	0.5	0.5	1	1	1	1
Volume (μL)	100	200	100	300	200	300	100	600	300	300	200
Initial vol. (μL)	200	400	200	600	500	500	200	1200	500	600	400
Final vol. (μL)	200	200	200	300	200	400	200	300	200	400	400

4.4.5 Spin coating

The precursor solution was applied to a stationary substrate. The substrates were spun at speed between 2000 and 6000 rpm for a specified time. Hybrid-perovskite films were deposited using a dynamically applied anti-solvent technique. After coating, the samples were annealed in a N_2 atmosphere.

Films produced for Chapters 6, 7, and 8 were spin coated by first applying ramping to 2000 rpm over 10 s before holding for 10 s, before the final stage of 6000 rpm for 20 s. 100 μl of chlorobenzene anti-solvent was applied using a micro-pipette 10 s prior to the end of the spin program. Samples were annealed on a hotplate at 100 °C for 30 min. Both spin coating and annealing was carried out in a single N_2 filled glovebox.

[2]The 9-step sample sets were fabricated chronologically prior to 13-step sample sets.

A subset of films produced for Chapter 9 used a 2-stage spin coating method of 1000 rpm for 5 s, 2000 rpm for 60 s, with a total 5 seconds ramp time. 100 μl of ethylacetate was applied as the anti-solvent. Samples were annealed in an *annealing box* under N_2 flow for 30 minutes in the case of single step deposition, and 20 minutes where a subsequent organic coating was applied as a top layer. Once annealed, samples were stored and transported in an opaque plastic desiccator at standard pressure. The annealing box is described in Section 4.4.6.

Organic coating for $A'/MAPbX_3$ samples

Organic amine salts were used to prepare 0.6 M solutions of organic amine salt solution in isopropanol, or alternate concentrations as specified. The spin coater was set at 4000 rpm for 60 s. Once at speed a micro-pipette was used to deposit 60 μL onto a prepared $MAPbX_3$ perovskite film.

4.4.6 Sample annealing

The majority of researchers working on hybrid-perovskites deposit and anneal their films under an inert atmosphere. In the absence of a glove box, a stainless steel annealing box was designed and produced for the purpose of annealing of hybrid-perovskite films under an inert atmosphere, Figure 4.2. [3] A *room-temperature-vulcanizing* silicon was used to form a seal for the lid of the annealing box. This was allowed to cure before cutting the seal off the lid as visible in Figure 4.2b. The box was subsequently bolted closed (hand tight) when in use as seen in Figure 4.2a. The temperature in the annealing box differed from the set-point value of the KW-4AH hotplate. Temperature measurement for calibration was performed with an open box and a K-type thermocouple after leaving the box closed until the system had equilibrated at the set-point.

[3]This annealing box was produced during this dissertation with the assistance of the Physics Workshop at the University of the Witwatersrand.

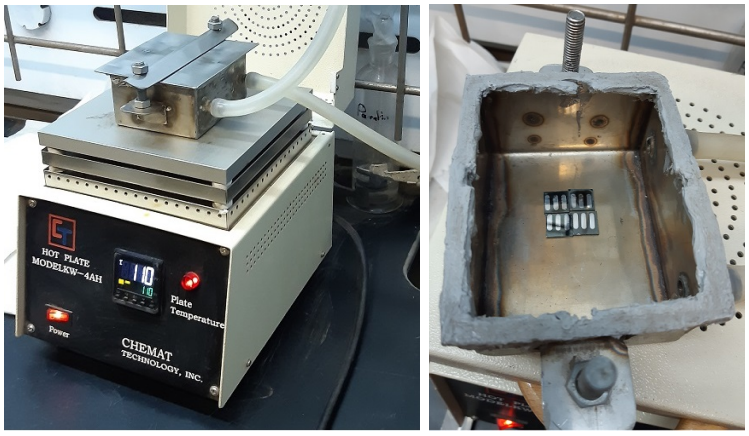

(a) (b)

Figure 4.2: Sample annealing box designed and produced during this dissertation. (a) closed lid, (b) open lid containing four 12.5 x 12.5 mm photovoltaic samples.

Prior to use the chamber was brought to temperature and flushed with N_2 gas for 60 s. Annealing was performed using the annealing box on a Chemat KW-4AH hotplate under a slight positive pressure due to N_2 flow. This provided a low oxygen and low humidity annealing environment.

In the case of multiple samples being produced via spin coating, the annealing box was only loosely sealed during the fabrication. Each sample was added immediately as the spin coating process completed, similarly samples were removed sequentially as each reached their target annealing time. The positive N_2 pressure and continuous flow under these conditions serves to reduce oxygen and humidity exposure during annealing, while some degree of exposure is unavoidable.

4.5 Powder samples from thin-films

In the case of highly textured thin-films or for sample packing in a capillary type diffractometer mount, it was in some cases necessary to process thin-films into powders. This was performed by scraping the thin-film from its

substrate using a razor blade. This powder was then used for either capillary XRD sample holders or placed on a flat plate zero-background holder for measuring diffraction patterns [Rao et al., 1996].

The process of scraping films is expected to reduce the crystallite size by breaking apart the films though mechanical forces to form a powder which reduces grain size and broadens the diffracted peaks. Additionally this process is expected to result in some amorphization of the material. This method is expected to provide crystallites with effectively random orientations. These aspects are evident in the comparison of Figure 4.3 in which the top pattern is a highly orientated film and the bottom prepared as just discussed. Between these measurements, the reduction in crystallite size on processing is clear from the peak broadening, and the effect on preferred orientation is clear from the additional observed peaks and their explanation by the corresponding model in Section 9.1. The potential to amorphize the sample is less clear, although it is noted that the data collection time is 7 times longer for the powder sample which was prepared from multiple thin-film samples and the background appears to increase in the range 5 to 8° 2θ which is consistent with, yet does not confirm, the presence of an amorphous peak below 5° 2θ.

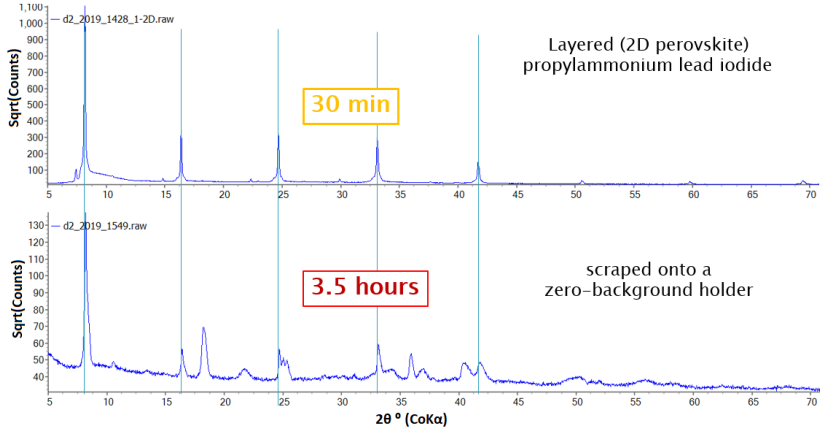

Figure 4.3: Comparison of XRD patterns between (top) thin-film and (bottom) thin-film derived powder samples. Measurement times are presented and (00l) peaks identified with a turquoise vertical line.

4.6 Optical spectroscopy

4.6.1 Optical absorption

Ultraviolet-visible-near IR (UV-Vis-NIR) spectroscopy measurements were made using a Varian Cary 500 UV-Vis-NIR spectro-photometer primarily in the range 300 to 800 nm. In some cases longer wavelengths were used, such as the 300 to 1000 nm range used for the $(PAI)_{2x}(MAI)_{1-x}PbI_2$ where the absorption signal from $MAPbI_3$ occurs near 780 nm. The spectrometer was allowed no less than 1 hour for its emission sources to warm and stabilise prior to data collection. For each session, a baseline spectrum for absorption data was measured using an uncoated glass substrate, of the same type used for the sample preparation. The Cary WinUV software corrects each sample absorption spectrum by using the baseline spectrum at the start of the session. The sample spectrum thus does not have any absorption features specific to the glass substrate. Sample holders with a 5 mm diameter hole through which the measurement was taken were used. Where multiple measurements were taken on a single sample, the sample was repositioned to measure a different area on the sample for each measurement.

Tauc method

The Tauc method and its considerations for hybrid-perovskites is described in Section 2.4.1. Optical absorption data was plotted on the axes $(\alpha \cdot h\nu)^2$ vs $h\nu$ where the exponent 2 assumes a direct band-gap ($\gamma = 1/2$) for Equation 2.3. This was performed using the *matplotlib.pyplot* module in a *Python* with the graphs saved as vector graphics files ".svg").[Van Rossum and Drake, 2009, Hunter, 2007] The tangent and background lines were drawn manually using *Inkscape* [Inkscape Project, 2021]. Co-ordinates of the y-axis plots were used to determine the scale of images. Intercepts on plots were determined using pixel values from the plots. The energy values determined from a Tauc plot are closely related to the optical band-gap yet they may deviate due certain electronic properties including exciton binding energy [Green et al., 2015]. For this reason, we refer to this determined energy values as the Tauc band-gap.

For Tauc plots containing multiple overlapping optical features, there is an inherent error which is partially yet incompletely considered with the inclusion of a baseline as discussed in Section 2.4.1. This is an approximation which becomes increasingly less valid the larger the baseline [Makuła et al., 2018].

4.6.2 Photoluminescence measurements

Photoluminescence (PL) measurements were carried out on a Horiba LabRAM HR spectrometer, with a 150 lines/mm grating, and an excitation in the ultraviolet of 244 nm generated from a frequency doubled Lexel argon ion laser. Multiple PL measurement were taken for each sample. To minimise the risk of beam damage, each measurement was taken from a "fresh" area. The incident beam was focused onto the sample via a 20x ThorLabs UVB microscope objective, and the beam was rastered over an area of 10 um x 10 um using the DuoScan attachment. The power density of the beam at the sample is thus much less, so that very little or no beam damage of the sample is expected during the measurement.

The luminescence data collected on the $(MABr)_{1-x}(PABr)_{2x}PbBr_2$ could be divided into single and multi-peak spectra. For low x and high x, a single peak was observed, dominated by a pristine or modified $MAPbBr_3$ phase or by a pristine or modified PA_2PbBr_4 phase. For $x \in \{0.4, 0.5\}$ the spectra could be clearly decomposed into multiple contributions.

The single peak spectra were modelled using a split pseudo-Voigt peak shape while the multi-peak spectra were modelled using multiple symmetric pseudo-Voigt contributions. The background was included as a single parameter refined baseline [4]. The models were implemented using the *Lmfit Python* module, which extends functionally for the *scipy.optimise* module. [Gommers et al., 2023, Newville et al., 2014, Van Rossum and Drake, 2009] The script written for this purpose required the position limits and initial position to be defined. The optimisation would then cycle through Levenberg-Marquardt least squares and Nelder-Mead based optimisation methods until the R^2 between successive optimisation differed by less than 1×10^{-5}. The

[4] This provides a flat baseline.

fitting models and R^2 calculation are provided in the Appendix Section SI F.3.

4.6.3 Stokes shift

The Stokes shift is usually defined as the energy difference between the optical absorption and emission processes. This definition is used in Chapter 9, and by Kitazawa *et al.* where layered hybrid perovskites are considered [Kitazawa, 1997].

An alternate definition is as the difference between the Tauc band-gap (E_{Tauc}) and optical band-gap [Katan et al., 2019]. The definition of optical band-gap is extracted from various origins for this application such as the PL peak maxima [Greenland et al., 2019, Kitazawa, 1997, Stoumpos et al., 2016].

This is used across many works discussing 3D hybrid-perovskites and in the cited papers is explicitly defined [Green et al., 2015, Greenland et al., 2019]. The optical bandgap can be related to E_{Tauc} by $E_{\text{optical}} - E_x$ where E_x is the exciton binding energy [Green et al., 2015, Katan et al., 2019]. The exciton binding energy is best determined at cryogenic temperatures or using temperature dependent optical measurements [Stoumpos et al., 2016, Ishihara et al., 1989].

4.7 X-ray diffraction: sample mounting and measurement

Hybrid-perovskite thin-films were prepared by spin coating on glass or glass coated with a thin conducting oxide layer as described in Section 4.4. Sample preparation and mounting has a large impact on the resulting X-ray diffraction data. For most, if not all analyses it is necessary to be aware of the sample properties, sample preparation, and the mounting conditions. These can have an impact on factors including peak width, peak position, peak intensity, crystallite size, preferred orientation etc. (Sections 3.1, 3.2).

4.7.1 Sample preparation and instrument effects of packed capillary XRD samples

Following the preparation of thin-film samples, the films were scraped with a razor blade and the resulting powder was loaded into a 0.7 mm borosilicate capillary as discussed in Section 4.5.

Powder diffraction data were obtained on a Bruker D8 Advance powder diffractometer using CuKα radiation and equipped with focusing Göbel mirrors, and a high resolution energy-dispersive Lynxeye XE detector. Data were collected in a Debye-Scherrer geometry with rotating capillary stage. Sample temperature for *in-situ* heating studies was controlled by a co-axial stream of dry nitrogen gas from an Oxford Cryosystems Cryostream 700 Plus.

To account for the instruments contribution to the diffraction pattern, the diffraction pattern of a silicon reference material was measured in a capillary, prior to the measurement of the hybrid-perovskite samples. The refined instrument profile is described in the TOPAS language in Section 4.8.1.

4.7.2 X-ray diffraction measurements of thin-films

For Bragg-Brentano measurements on a Bruker D2 Phaser, 12.5 x 12.5 mm, or 15 x 20 mm samples were mounted in the cavity of a ϕ 40 mm Bruker sample holder. All sample mounting equipment was cleaned with isopropanol. Modelling clay was used to provide height adjustment, and to support the sample in the holder. A pair of 4 mm thick glass pieces were used to press the sample flat, such that it was collinear to the top of the sample holder [5]. This was performed by pressing the glass on 2 opposite edges of the sample to minimise the contact area and the risk of any unintended effects on the sample such as the effects of pressure, abrasion, or contamination. As there is a limit to the precision observable by eye, any deviation in sample height was accounted for during modelling using a refined sample displacement correction factor (discussed in Section 3.2.3).

[5]Sample displacement related peak position shift is covered in Section 3.2.3

For the measurement of a **powder pattern** from a thin-film sample, the samples were scraped from their substrates onto a silicon zero-background holder using a razor blade as discussed in Section 4.5 [6]. Multiple samples on 15x20 mm or 25x25 mm substrates were scraped onto a zero-background holder. The use of multiple equivalent samples was necessary to increased the sample volume for better counting statistics in the measurements.

Samples were then measured on a Bruker D2 phaser with a cobalt source and an Fe filter on the primary beam to attenuate CoKβ emission lines. A fundamental parameter instrument profile was used as described in Section 4.8.2.

4.8 Instrument profiles for XRD data modelling

Instrument profiles were created for the diffractometers used, by measuring a silicon standard reference materials (SRM) which has known properties. For the Bruker D2 Phaser a NIST Si 640 SRM was used [Black et al., 2020]. A Rietveld refinement was carried out for each instrument where the sample properties were *fixed* and a set of physically relevant instrument characteristics were *refined*. These values were then *fixed* for use as a fundamental parameter instrument profile, discussed in Section 3.3.3.

Its important to note that while the starting parameters for the instrument profile were based on physical attributes of the experimental set up, the purpose of this instrument profile is to provide a reasonable description of the instrumental contribution to the diffraction pattern. As such, during the refinement against the SRM, parameters were allowed to refine away from the physically accurate values to provide a better description.

[6] A zero-background holder has a surface made from a single-crystal which is cut at to a specific orientation such that it does not diffract in the measurement range. [Rao et al., 1996]

4.8.1 Capillary samples on a Bruker D8 Advance (CuKα)

The following is an instrument profile created and used for refinements of X-ray diffraction data measured from capillary samples on a Bruker D8 Advance at the University of Sheffield, UK. This diffractometer makes use of a Cu source with a graphite monochromator to exclusively select the CuKα wavelengths as described in Section 4.7.1. A silicon standard was measured at room temperature from 10 to 100 ° 2θ against which the convolution based fundamental parameter instrument profile was refined. This included convolutions specific to capillary type samples and a detailed description of the incident beam profile [7]. The beam profile for CuKα was described using the Lorentzian convolutions identified by Berger and later adjusted by Cheary and Coelho [Cheary and Coelho, 1992, Berger, 1986] [8].

```
lam
ymin_on_ymax  0.0001
    la  0.0159 lo  1.534753 lh  3.6854
    la  0.5691 lo  1.540596 lh  0.437
    la  0.0762 lo  1.541058 lh  0.6
    la  0.2517 lo  1.54441 lh  0.52
    la  0.0871 lo  1.544721 lh  0.62

 '  For a graphite monochromator the LP factor should be set to 26.6 degrees [Dinnebier et al., 2018].
LP_Factor(!th2_monochromator, 0)
Zero_Error(, -0.02645‘_0.00654)
Rp 217.5  // Bruker D8
Rs 217.5
Simple_Axial_Model(, 0.01097‘_805.61880_LIMIT_MIN_0.0001)
  '  The following 2Th and I corrections for cylindrical sample are described by [Sabine et al., 1998].
Cylindrical_2Th_Correction(, 0.19605‘_0.03052)
Cylindrical_I_Correction(@, 2.69002‘_0.16294)
 ' The following correction considers peak shape effects in addition to intensity, making
 ' the previous cylindrical sample corrections redundant [Coelho and Rowles, 2017].
capillary_diameter_mm 0.06042‘_0.00234 max =1.2;
    capillary_u_cm_inv   433.27649‘_131.81041
    capillary_divergent_beam
 '  The following convolutions were added to improve the
 '  instrument profile for use in the CsxFAMA data sets
prm !c1  0.07263‘_0.00060 min 0.00001
prm !c2  0.02378‘_0.00050 min 0.00001
gauss_fwhm = c1 / Cos(Th);
lor_fwhm = c2 / Cos(Th);
```

[7] In the absence of the [Sabine et al., 1998] specific correction used in this instrument profile, the refined values for the [Coelho and Rowles, 2017]-based correction can provide an insight into instrument alignment.

[8] Cheary and Coelho scaled the wavelengths of the Lorentzian convolutions identified by Berger to match a CuKα peak of 1.5405981 Å.

4.8.2 Flat plate sample on a Bruker D2 Phaser (CoKα)

The following is an the instrument profile created and used for refinements of X-ray diffraction data measured on flat plate samples, including thin-films and packed powders on a D2 Phaser at the University of the Witwatersrand, RSA. Parameters preceded by an @ symbol are refined, such as sample absorption. The diffractometer makes use of a Co source with a Fe filter. The use of a Fe filter attenuates the CoKβ peak signal. For high intensity CoKα peaks, the intensity of the corresponding CoKβ is likely to be observed through the Fe filter as additional lower angle peaks in the diffraction pattern.

Both the CoKα and attenuated CoKβ peaks were modelled using the Lorentzian convolutions describing the source radiation identified by Hölzer *et al.* (composed of 7 and 6 Lorentzian peaks respectively) [Hölzer et al., 1997]. The CoKβ peaks uniformly scaled to match the attenuated experimentally observed α/β ratio.

```
LP_Factor( 0)
Rp 70.7
Rs 70.7
lpsd_th2_angular_range_degrees  1.000030518 min =1; max =5.85;
lpsd_equitorial_divergence_degrees  1.224021576 max =1.8;
lpsd_equitorial_sample_length_mm  20 min 3 max 20
lpsd_beam_spill_correct_intensity 1
axial_conv
filament_length  7.320925474 min =0.1; max =12;
sample_length  15
receiving_slit_length  4.594388284 min 3 max 8
secondary_soller_angle  0.0078125 min =0; max =2.5;
axial_n_beta  30
Absorption(@, 19.8121562‘_2.02430036 min 10 max 100)
lam
    ymin_on_ymax  0.0001
     ’CoKa
    la  0.378 lo  1.7889847 lh  0.4633522
    la  0.144 lo  1.7892524 lh  0.6958819
    la  0.127 lo  1.7896946 lh  1.176738
    la  0.088 lo  1.7888515 lh  0.208542
    la  0.197 lo  1.7927905 lh  0.6237179
    la  0.095 lo  1.7930637 lh  0.7190761
    la  0.05 lo  1.7934738 lh  1.1578452
     ’CoKb
    la 0.002240125082  lo 1.6207938  lh  0.6462327
    la 0.00216384066   lo 1.6211689  lh  0.75888
    la 0.001623049949  lo 1.622858   lh  2.0774644
    la 0.003734559008  lo 1.6216651  lh  1.0372054
```

```
la 0.001204623645  lo 1.6236359  lh  2.8895524
la 0.002017396889  lo 1.6198346  lh  0.8020733
```

4.9 Structure modelling of X-ray diffraction data

The structure modelling decisions employed in this work are primarily discussed alongside the results due to their importance in understanding the outcome and its corresponding limitations. Strategies, methods, and models used in the modelling of diffraction data have been discussed in Chapter 3. This section highlights some of the strategies in the context of hybrid-perovskites and related structures along with details regarding the basis of some models used in later chapters.

The use of models describing 3D frameworks as the basis of 3D hybrid perovskites is primary used in Chapters 6, 7, and 8. Discussions around layered structures are pertinent to Chapter 9.

4.9.1 X-ray diffraction refinement method

Diffraction data was refined and modelled using Bruker's TOPAS V6 in launch mode for Chapter 6 and Chapter 7. TOPAS-Academic V7 was used thereafter [Coelho, 2018]. These refinements used the instrument profiles described in Section 4.8 unless otherwise specified.

The background of the diffraction patterns were modelled using a Chebychev polynomial, for the capillary samples of Chapter 6 to 8, this was implemented along with a $1/x$ function for low angle air scattering. Broad features in the patterns which could not be easily fitted using the Chebychev polynomial were fitted with a peak constrained to be broad. In the case of Chapter 6 to 8, the observed feature was consistent with the amorphous glass capillary used for measurements. This was present with varying prominence across the data.

Sequential refinements were controlled using a custom Python script to call TOPAS and, to write the input files. The core functions of the script are provided in Appendix Section F.1.

Parametric refinements were processed in TOPAS-Academic, where a template input file was prepared using a combination of sections and markers as provided in Appendix Section F.2. A Python script was written to process this into a large single input file for a parametric Rietveld refinement.

4.9.2 Modelling an organic cation in a 3D framework

In a 3D hybrid-perovskite, the organic cation's orientation is highly disordered in the α phase and disordered across a handful of favoured orientations in the β phases. It is only expected at cryogenic temperature for the orientation of the organic cation to be effectively frozen. [Weller et al., 2015b] Below methods to approach this are discussed.

Representative atom

It is often the case for hybrid-perovskites that powder X-ray diffraction data is not conducive to determining detail beyond an approximation of the organic cation position (see Section 3.5.1). The most direct method to represent this in a structure is by substituting the molecule with a single atom containing the same number of electrons. To account for the differences in size the thermal parameter for this representative atom is allowed to refine to very large values spreading its electron density [Schueller et al., 2018] [9].

Fixed atomic positions

For known hybrid perovskite structures, a literature reference including the position of the organic cation is often available and can used in as the basis

[9] To consider the dipoles in FA^+ and MA^+ cations, position of a representative can be refined to account for an offset in the average position of the electron density.

of a Rietveld refinement. Where the fit quality is not sufficient the organic cation from the literature structure can serve as a placeholder while the structure of the inorganic framework is refined. The organic cation's atoms and their fractional coordinates can be taken and used directly used, or scaled to maintain the original bond lengths. This approach does not determine information on the organic cation, and as such interpretations should be made with care, detailing the assumptions and implementation.

Rigid body model(s)

A rigid body approach can be used, defining the position of atoms of the organic molecule relative to each other by bond lengths and angles. The position and orientation of the molecule can be refined using relatively few parameters. One such implementation is using a TOPAS rigid body model such as by using the *"z_matrix"* implementation. The starting point for these rigid bodies is ideally a literature structure or structural information which can be implemented as constraints, such as DFT calculations or other measurements that can provide bond length, bond angle, and/or connectivity information.

This can be extended to account for multiple transient orientations as follows. A molecule may have restricted movement in a structure such that it can only occupy one of a small number of orientations in a proposed structure (such can potentially be determined by DFT modelling) [Weller et al., 2015b]. This can be modelled by using multiple equivalent rigid bodies differing by their position and orientation as required. The occupancy factors for these are scaled according to the number of instances. Bond lengths and angles can be implemented as shared parameters. The instances can be further related to each other through equations or be fixed in place.

4.9.3 Two and four octahedra unit cells

Here we describe building a 3D framework using two and four octahedra unit cells based around rigid body modelling of Pb−X octahedra. These are subsequently utilised in Sections 6.6 and 6.7.

Two octahedra unit cell

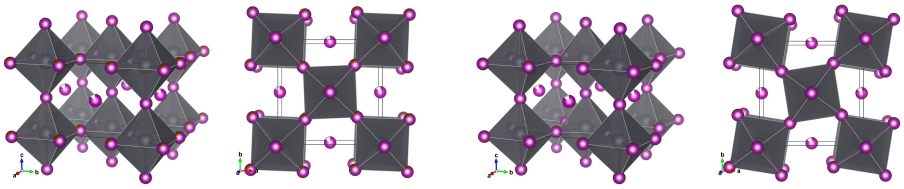

(a) (b)

Figure 4.4: A two octahedra unit cell of a Pb-X framework and a representative atom in place of the organic cation (a) with, and (b) without octahedral rotation about the c-axis (Glazer notation: $a^0a^0c^+$).
Octahedra are represented in black with X atoms at their corners. Isolated atoms between the octahedra correspond to representative atoms for the A site organic cation.

In defining the unit cell, two rigid bodies of 3 Pb-X orthogonal bonds each of a length "r" were described, with the remaining bonds in each octahedra generated by the translational symmetry of the unit cell. An example of TOPAS code for this rigid body as well as the variations are discussed in Appendix C.3. The following is an example of a Pb−X octahedra rigid-body:

```
prm r 3.155 2.9 min 2.9 max 3.5
rigid
    point_for_site Pb1
    point_for_site I1 ux = r;
    point_for_site I2 uy = r;
    point_for_site I3 uz = r;
```

For the modelling of symmetric octahedra, the unit cell parameters were defined in relation to the Pb−X bond lengths through the use of projections. The TOPAS code implementing this is shown below, Oh1, Oh2 and Oh3 are rotation about the a, b and c-axis of the octahedra respectively. This sequence is repeated for Oh4, Oh5 and Oh6 which refer to the second octahedra defined in the unit cell. The octahedral bond lengths perpendicular to the c-axis are defined by "r", while "r1b" is used for bonds along the c-axis. When these are equal the octahedra will be symmetric, although they can be refined independently to accommodate a different length for the c-axis. Limits were used on the rotation with consideration of symmetry to reduce the solution space being searched.

```
a = 2*r*(Cos(Oh2*Pi/180)*Cos(Oh3*Pi/180)+Cos(Oh5*Pi/180)*Cos(Oh6*Pi/180));
b = 2*r*(Cos(Oh1*Pi/180)*Cos(Oh3*Pi/180)+Cos(Oh4*Pi/180)*Cos(Oh6*Pi/180));
c = 2*r1b*(Cos(Oh1*Pi/180)*Cos(Oh2*Pi/180));
```

In cases where projections were not employed to define the unit cell parameters, distortion is introduced into the octahedra by having the unit cell parameters to refine independently. The distortion increases as the unit cell parameter deviates from the values that can be derived from the Pb-X bond length by means of a projection.

Four octahedra unit cell

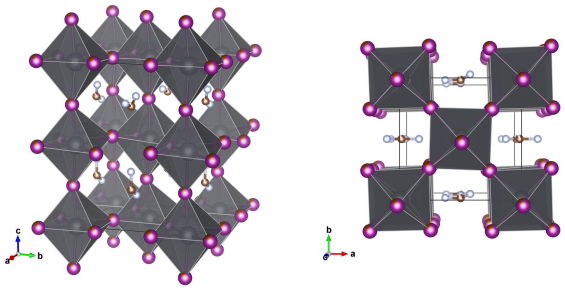

Figure 4.5: A four octahedra unit cell of a Pb-X framework and a rigid body model organic cation.

The two octahedra unit cell can be extended along the *c*-axis to allow both symmetric and asymmetric rotation of the subsequent layers of octahedra. In the two octahedra unit cell, the octahedra can either rotate clockwise or anti-clockwise about the *c*-axis with all subsequent layers in the *c*-direction expressing the same degree and direction of rotation. [10] The use of a larger unit cell consisting of 2 octahedra in the *c*-direction of the unit cell and 4 in total, allows each of the 2 layers to experience different degrees and directions of rotation. This allows the expression of the full set of Glazer notations including $(a^0a^0c^+)$, $(a^0a^0c^-)$ and related tilt systems as introduced in Section 1.5.1.

[10] The unit cell is translated in the *c*-direction to produce subsequent layers.

4.9.4 Modelling of layered 2D perovskite thin-films

Layered 2D perovskites are explored in Chapter 9 where a combination of structure agnostic Pawley refinements, refinement of literature structures using March-Dollase preferred orientation, and structure solution using rigid body models. These approaches have been introduced in Chapter 3 and their application is discussed alongside the related refinements in Section 9.2.

Chapter 5

Robust Arduino controlled spin coater using a novel and simple gravity chuck design

Preface

This chapter contains a manuscript, titled *Robust Arduino controlled spin coater using a novel and simple gravity chuck design* which has been submitted to the *Elsevier* journal *HardwareX*, which describes development and testing of the spin coater used for thin-film fabrication at the *University of the Witwatersrand* (Wits). This served as an essential step for the fabrication, and subsequent study of hybrid-perovskite thin-films, Section 4.4 and Chapter 9. This work included Prof. Caren Billing, Prof. Daniel Wamwangi, and Prof. David Billing as the supervisors of this thesis, and Dr. Francis Otieno of Maseno University, Kenya.

Dr. Otieno contributed the atomic force microscopy (AFM) data and produced the associated samples. Gerry Germishuizen machined the aluminium chuck for the spin coater. All authors contributed to the final editing prior to submission. The balance of work was carried out by the dissertation author, Adam Shnier including the concept, design, fabrication, programming, testing, and X-ray reflectometry measurement and modelling.

The formatted manuscript is included on the following pages. The supplementary information for the manuscript is provided in App. A.

Article title

Robust Arduino controlled spin coater using a novel and simple gravity chuck design

Authors

*Adam Shnier [a,c], Francis Otieno [b,c,d], Caren Billing [a,c], Daniel Wamwangi [b,c], David G. Billing [a,c] **

Affiliations

[a] *School of Chemistry, University of Witwatersrand, Johannesburg 2050, South Africa*

[b] *School of Physics, University of Witwatersrand, Johannesburg 2050, South Africa*

[c] *DSI-NRF Centre of Excellence in Strong Materials (CoE-SM), University of Witwatersrand, Johannesburg 2050, South Africa*

[d] *Department of Physics and Materials science, Maseno University Private Bag Maseno, Kenya*

Corresponding author's email address

Dave.Billing@wits.ac.za

Abstract

Spin coaters offer an invaluable method of thin film fabrication. Various implementations, both proprietary and open-source exist, offering vacuum and gravity samples chucks. These implementations vary in their reliability, ease-of-use, cost, and versatility. Here we present a novel easy-to-use open-source gravity-chuck type spin coater with minimal points of failure at a material cost of around 100 USD (1500 ZAR). The unique chuck design makes use of interchangeable brass plate sample masks, each specific to a sample size, these can be made with basic skills and common hand tools. In comparison, replacement chucks for commercial alternatives can cost as much as the entire spin coater we present. Open-source hardware such as this provides an example for individuals in the field on the design and development of hardware where reliability, cost, and flexibility are most important, as is the case for many institutions in developing countries.

Keywords

Spin coater, Arduino, gravity chuck, thin film, low cost

Specifications table

Hardware name	*Gravity chuck spin coater*
Subject area	• *Engineering and material science* • *Educational tools and open source alternatives to existing infrastructure*
Hardware type	• *Mechanical engineering and materials science*
Closest commercial analog	Ossila Spin Coater [1]
Open source license	Software: MIT Hardware: SHL-2.1
Cost of hardware	$ 80 - $ 120
Source file repository	Mendeley Data, http://doi.org/10.17632/y84tbnfsj4

1. Hardware in context

Spin coating is a widely used process for the deposition of uniform thin films on flat substrates from a precursor solution. The technique is common for fabricating thin films of photovoltaic materials, small organics molecules, polymers, nanoparticles, metal oxides, etc. [2, 3, 4]. A substrate is mounted on the spin coater then a liquid precursor is applied to cover the substrate. The spinning process drains precursor solution from the substrate using centrifugal force, while viscosity and surface tension restrict this process [5]. The film thickness and quality is affected by rotational speed, atmosphere, solvent evaporation, the rheology of the precursor, and surface wetting of the substrate [2, 5].

Commercial spin coaters are most commonly available with either gravity or vacuum chucks to mount the sample. A vacuum chuck exposes a sample to a low vacuum through an opening in the sample chuck. The size and shape of the chuck varies, with the simplest being a small hole in the centre of the chuck. One advantage of vacuum chucks is the ability to accommodate any sample shape and a wide range of sizes, provided the sample's base can make a good seal against the chuck. Vacuum chucks require a vacuum pump and a *rotary union* suitable for high speeds, adding both cost and complexity. Another consideration is that the suction of a vacuum chuck may warp very thin substrates (such as 300 μm Si) [1].

Gravity chucks typically take the form of an inset shape matching a specific sample size. These may require either a different chuck entirely for each sample size, or a compound inset where an inset for a smaller sample is set in an inset for a larger sample. Gravity chucks are mechanically simpler, and are not subject to clogging or failures related to vacuum systems, which are notorious for breaking down or requiring repair. The absence of a vacuum system and rotary union allows for a more cost effective and simpler implementation.

Some more "affordable" vacuum chuck based spin coaters, costing a few thousand dollars (USD) have, at least within our research institution, been unreliable and subject to repeated failure and/or down-time usually related to the vacuum chuck, vacuum system and the path between. This observation is localised and may not be a fair representation of the manufacturers of these devices.

When designing shorter term research projects such as in MSc and undergraduate studies the wait time for new equipment, or for parts to repair existing equipment can elapse a significant fraction of a student's available time. This effect is strongly affected by geo-bureaucratic circumstance. Factors affecting this include, the time required to organise and process funding for equipment, shipping time, customs delays, and costs. Also when working with imported commercial equipment, repair cost and logistics can result in significant down-time while waiting for a technician, shipping the instrument, or arranging finances.

While commercial builds cost a few thousand dollars, with additional sample chucks costing from $90 to a few hundred (examples in SI Section 13), DIY spin coater builds can cost a few hundred dollars or even less making them a far more attractive option when cost, cost of repair and ease of repair are of primary importance.

In this paper, we present a simple, low cost 2-stage spin coater with a novel gravity chuck design. This makes use of a chuck and mask system with the full build planned around repairability, robustness and simplicity. These benefits are in part a result of bypassing the common points of failure in vacuum dependent designs.

2. Hardware description

This spin coater consists of a gravity chuck, motor, power supply, electronics, software, and the enclosure. It is a low cost device with simple circuitry built around an Arduino Nano compatible microcontroller to drive a DC motor, and provide information on a Nokia 5110 display. The novelty of the chuck design lies in the plate like sample holder mask, and the round pins extending from the chuck on which the mask rests as the holding mechanism. In order to accommodate samples of different sizes, only the sample mask needs to be exchanged, in a quick tool free process. Two prototype implementations are presented

in Figure 1.
This hardware can be useful in any facility where thin films are being studied, which includes research in the following fields:

- Thin-films device fabrication, including thin film solar cells.
- The study of optical and optoelectronic properties in thin films.
- Education to show an application of centrifugal force, and the relationship between spin speed and film thickness. This spin coater can be simplified as in hardware Version 1 (hV1) (See reference [6]) for applications such as teaching motor control or optical properties of materials [7].



(a) (b)

Figure 1: The assembled spin coaters, (a) Hardware version 2 (hV2) lined with foil, with an inset showing the pre-run display of the set run parameters, (b) Hardware version 3 (hV3) with the sample mask taped down for transport to Maseno University, Kenya.

2.1 Mechanics and Hardware

Motor
The spin coater is driven by a permanent magnet DC motor which is mounted to the enclosure, with a rubber gasket between as a vibration dampener. In Hardware version 2 (hV2), the motor axle had an M8 thread while hV3 had a 6.35 mm smooth shaft. Some commercial spin coaters have shafts of 3 mm. Under normal operation, it is inconceivable that any issue would arise from this, yet considering the surprising feats students are capable of, the motors were chosen to have thicker shafts which cannot easily be bent. The rotation speed is motor dependent, in the case of hV2 the motor operates comfortably between 600 and 7000 rpm. At lower speeds the force exerted by the motor magnets is significant and when the PWM (pulse-width modulation) duty cycle is below 5 % (PWM 13/255, $\pm$ 500 rpm), the motor magnet and other mechanical resistive forces are very close to or exceed the force generated by the motor coils potentially stalling the motor.
Tachometer
The motor speed was read using an infra-red proximity sensor. In hV2 the underside of the sample chuck was patterned into evenly spaced alternating sections of black 1000 grit sandpaper and bare reflective aluminium, as shown in Figure 2b. The sandpaper provides a very good light absorbing surface, with the roughness diffusing any light that could be reflected by a smooth black surface. This approach required

mounting of the sensor directly under the chuck, as shown in Figure 2a. In hV3 (Figure 2c) this system was replaced by mounting a reflector on the small portion of shaft protruding from the bottom of the motor. This reflector was made from a brass strip bent into a "U" shape. This was painted black with the outer sides covered with a reflective aluminium tape. The infra-red sensor gain/sensitivity needs to be set, such that it is not close to either providing false positive, nor false negative readings. Both implementations make use of a strong reflector/absorber type contrast. This allows strong discrimination between reflective and "dark" conditions. Additionally, the sides of the infra-red receiver on the sensor was covered with black heat shrink (glued in place), to reduce the light received directly from the adjacent transmitter. This allows a higher sensitivity/gain to be set on the sensor, while preventing false positive readings from this effect. Comparing the sensor placement in hV2 and hV3, the sensor in hV2 was in the coating chamber, directly under the sample chuck. This resulted in a more complicated mounting implementation, requiring a protective enclosure. In hV3 the sensor mounting was entirely in the main enclosure. The tachometer assembly is included in SI documents *"Assembly of Spin-Coater hV2.pdf"* and *"Assembly of Spin-Coater hV3.pdf"*.

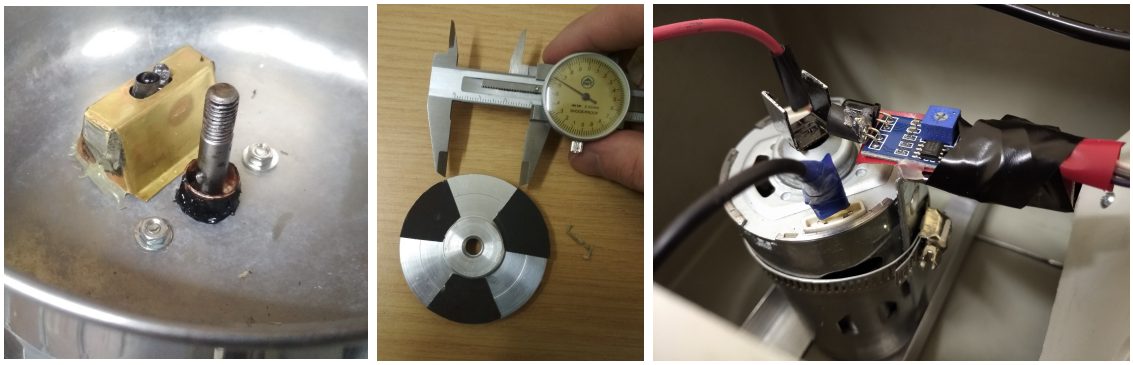

(a) (b) (c)

Figure 2: Tachometer assembly, showing (a) the infra-red proximity sensor for **hV2**, (b) the reflector/absorber pattern on the underside of the chuck in **hV2**, (c) and the reflector/sensor assembly used in **hV3**

Sample chuck and mask

The chuck design (Figure 3) makes use of a flat top with two 3 mm pins positioned 45 mm apart. On these, an easily machined sample mask sits, allowing quick and simple interchange between sample sizes without removing the chuck, and the easy crafting of new masks for different sample sizes. The chuck was machined by a workshop technician from a cylindrical aluminium block with a CNC router to form the top with pins, and a lathe to shape the profile. hV2 makes use of a chuck with a thread tapped in the centre, to fit on a motor with a threaded shaft, while hV3 has a blind hole in the chuck, with 2 grub screws to fix it on a smooth motor shaft. An alternative chuck version for a motor can be made without these machining tools, as described in SI Section 3.1.

The sample mask is a 0.7 mm brass plate that has two 3 mm holes, corresponding to the chuck's 3 mm pins, along with a cut-out in the centre, corresponding to the sample/substrate size used. The sample mask should be thinner than the samples to allow easy drainage of the precursor solution while coating. The 0.7 mm mask was paired with 1.1 mm thick samples, this being the thickness of the microscope slides and ITO coated glass used within our research group. The sample mask is easily exchanged, which is especially valuable in a lab where multiple users work with substrates of different sizes.

The sample chuck and mask system is ideal for substrates slightly thicker than the sample mask. Very thin samples such as a 300 μm silicon wafer risk slipping under the mask. To avoid this, they can be mounted with double sided tape on a glass slide or equivalent for spin coating. As mentioned, vacuum chuck spin coaters risk creating a curvature in ultra thin samples, and this may similarly be remedied

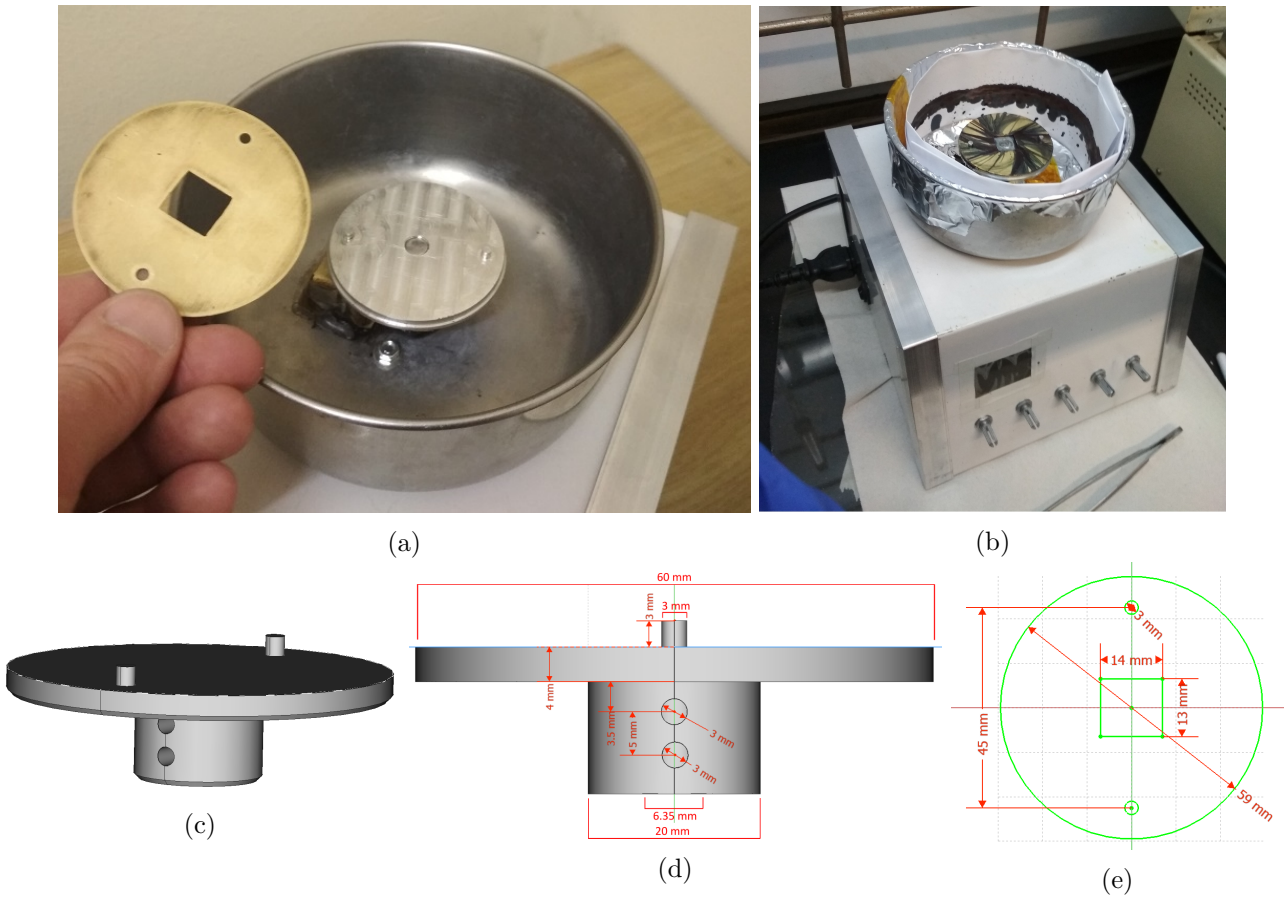

Figure 3: Sample chuck and mask. (a,b) hV2 chuck and sample mask, (c,d) hV3 sample chuck for mounting on the motor shaft using M3 grub screws on the side, with 3 mm pins on top. (e) Sample mask 14x13mm for hand cut "12.5x12.5mm" samples. Design Files are included as "Chuck_smooth-shaft.FCStd" and "Masks.FCStd" drawn in FreeCAD V0.18

by mounting to a glass slide. Another good alternative for very thin samples are inset type chucks [8]. With these thin samples cannot slip between the sample chuck and mask. Inset type sample holders can be made to fit the presented chuck design using holes corresponding pins of the hV2/hV3 chuck for easy mounting. These can be produced by either 3D printing, using a CNC router, or by gluing a sample mask to a backing plate (these have not been produced for this work).

Commercial alternatives using vacuum or gravity chucks typically require the entire chuck to be exchanged to change the sample mount [1, 9, 10, 11]. Mounting systems in open-source designs include the use of double-sided tape, vacuum chucks when using hard drive motors, gravity chucks where adjustment for sample size requires tools and measurement, and chucks using removable screws to secure samples [12, 13, 7, 2, 14]. In comparison, the chuck design presented here provides a simple, rapid, easy, and tool-free method to exchange the sample mounting configuration which takes close to 5 seconds to swap the sample mask.

Commercially, chucks are available at purchase prices ranging from $ 90 to $ 300. In cases where chucks can be 3D printed [8], the associated knowledge and access to a 3D printer with a fine enough print resolution is required. In the design presented, the majority of technical expertise rests in the manufacture of the chuck, while the brass masks which accommodate samples are less sensitive to machining accuracy, and are easily crafted with readily available tools and inexpensive materials, i.e. a drill, saw or tin snips, small metal files and brass sheet. This offers the advantage of lower cost, reliable access without the risk of parts being discontinued, and avoids shipping, logistics and other potential delays in favour of locally

available components. [15, 16]

The need to accommodate a new shape and size of sample can occur long after the spin coater was commissioned. There is no guarantee the same individuals, technical knowledge and resources that were involved when equipment was commissioned will still be accessible. The simplicity and ease of machining a sample mask from brass plate serves as an advantage over other commercial and open source alternatives [15].

All the components are supported by, and housed in the enclosure as shown in Figure 1. It serves to support the motor and protect the electronics in a lab environment, while the stainless steel bowl acts to contain the waste fluid from the spinning process. An enclosure can be bought or built using whatever non-flammable materials are most accessible. In our case, this was offcuts of steel barge flashing (a roofing material). Information regarding the materials for and assembly of the enclosure is provided in the SI documents *"Assembly of Spin-Coater hV2.pdf"* and *"Assembly of Spin-Coater hV3.pdf"*

2.2 Electronics

Inputs

An Arduino Nano compatible microcontroller (Nano) formed the core of the electronics as seen in Figure 4. The Nano functioned to control the DC motor with a pulse-width modulated (PWM) signal through an IRF540 n-channel MOSFET. In hardware version 2 (hV2), 50 kΩ potentiometers (pots) were used to set the spin parameters, with each sending a voltage between 0 and 5 V to the analog pins of the Nano for each parameter. Momentary contact buttons for start and reset functions were included in hV2. The pots used in hV2 provided unstable 10-bit values (0 to 1023). The source of the instability could be related to the 5V 3A USB power supply used for the Nano, which may additionally be affected by the power draw of components directly connected to the Arduino in our build. The instability was managed using a software based approach discussed in the software section.

To simplify the design and side-step the instability of the values read from the pots, hardware version 3 (hV3) replaced the pots and buttons with an incremental type rotary encoder, containing an inbuilt momentary contact button. This functioned using the button to cycle through parameters, while rotation of the encoder adjusted parameter values, as shown in Figure 5. The use of a single rotary encoder replacing the 5 pots and 2 buttons, simplified the enclosure assembly, and provides digital parameter control which bypasses the need to read analogue signals from pots.

Tachometer

The logic level voltages of an Arduino Nano are inherited from its ATMega328 microcontroller. The digital input voltages are > 3.0 V for a digital high and < 1.5 V as a low [17]. An IR-proximity sensor working on 3.3 V was connected to the Nano through a logic level converting NOT gate, with a threshold of 1.7 V and output of 5 V made using a NE555 timer. During testing of hV2, a direct connection between the sensor and Nano did not reliably trigger a digital high input. The *logic level converting NOT gate* was included to address this for the specific IR sensor board used.

Power delivery

The motor was powered by a 24V PSU in hV2, and 12V in hV3. In hV2, power was delivered to the microcontroller by a step-down converter, which delivered 5.2V to the USB port of the Nano; a small voltage drop is expected in the USB cable. In hV3, a L7809 linear regulator reduced the voltage to 9V, which was then fed into the Power in (Vin) pin of the Nano. The Vin pin on the Nano is specified to accept 7-12 V input [18], which is regulated to 5V by a LM1117 regulator. By dropping the voltage to 9 V prior to the Vin pin, the heat which the small onboard regulator will need to dissipate is reduced, $P_{Heat} = (V_{In} - V_{Out}) \cdot I_{Load} + V_{In} I_{Ground}$ [19]. Linear regulators reduce voltage by resistively dissipating energy as heat, while step-down/buck converters use PWM (pulse width modulation) typically followed by low pass filters to provide a reduced DC voltage at a high conversion efficiency.

Testing a 24V PSU with the 9V LM7809 (TO-220 package) for the hV2 configuration resulted in slow heating in a L7809 regulator, leading to thermal overload. While the heat dissipation can be accelerated

with a heatsink, a step-down converter is preferable due to the higher conversion efficiency and reduced heat generation. The lower heat generation is desired as it allows the enclosure to be sealed without a need for vents or a fan. The absence of vents reduces the gradual accumulation of dust. This is of great importance in environments such as fume-hoods, where the strong air flow accelerates dust accumulation. The chemicals a researcher uses can require a spin coater to be used in a fume-hood due to OHS considerations.

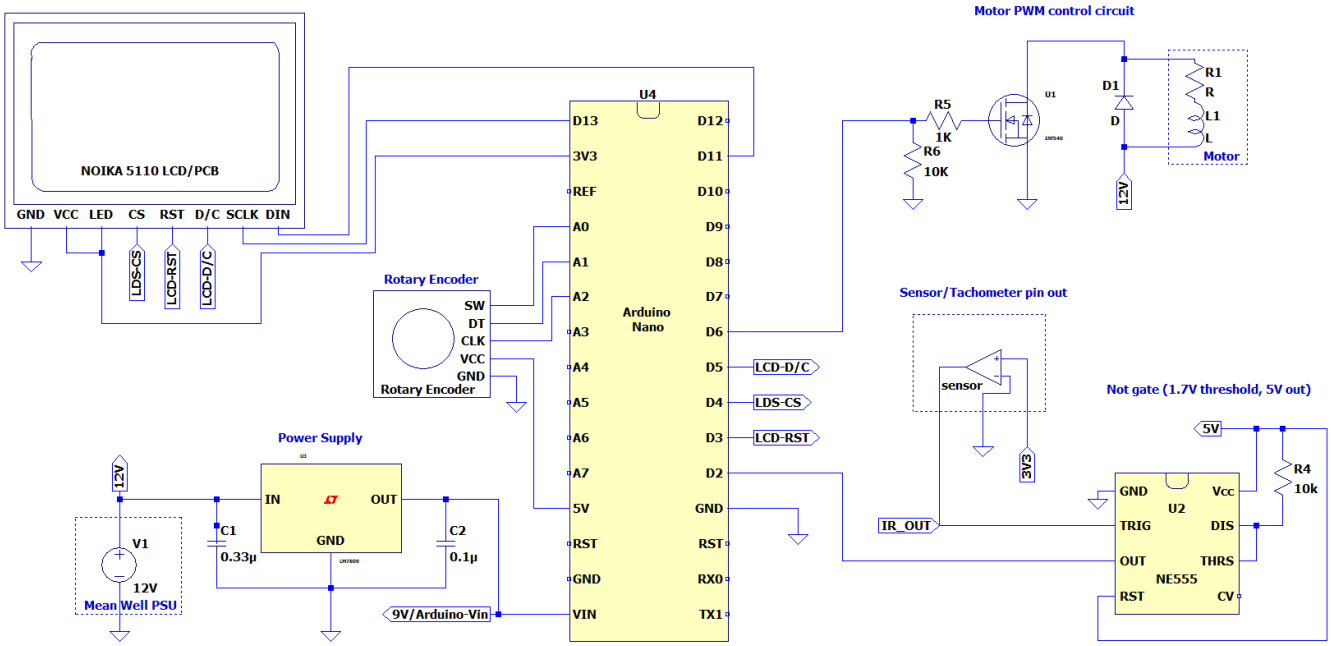

Figure 4: Circuit diagram for hardware version 3

2.3 Software and system

The software is included in SI files *"SpinCoater_v2.3.1(for_hV3).ino"* and *"SpinCoater_v1.4(for_hV2).ino"*. These operate as per the flow diagram in Figure 5 for hV3, and Figure SI-3a for hV2.

Setting parameters

The spin parameters consist of the speed and time for each of the two stages (*speed 1, speed 2, time 1, time 2*), along with the ramp time (*ramp*), which is how long will be allocated in total for ramping up the speed from stationary to the first speed and between the first and second speeds. Parameters are either set using pots in hV2, or an incremental type rotary encoder in hV3. In hV2, 10-bit (0 to 1023) DAC readings are taken from 50 kΩ pots in the range 0 to 5 V. These readings were collected by averaging 5 readings, each 5 milliseconds apart. Parameter values were updated if the new average values differed from the stored values by more than 5 units, equivalent to 24 mV. These values were converted into the spin parameters, of which the parameters with the finest increments are speed. **Speed 1** was defined by *"s1 = byte(float(a[0])*242/1023)+13;"*, where s1 is *speed 1*, and *a[0]* is the averaged value read from the first pot. This converts the 10-bit value averaged from the DAC reading to 8-bit (byte) value with extrema of 13 and 242, defining limits on the minimum and maximum PWM duty cycles chosen for the specific motor. This provided good parameter control, with the caveat that parameter values occasionally shifted by one unit. The parameter values are fixed when a run is started, as such these values should be checked on the display, prior to each operation run.

This minor instability was addressed in hV3 by utilising a rotary encoder in place of relying on DAC read signals from the pots. Each time a parameter is updated on rotation of the rotary encoder in hV3, a

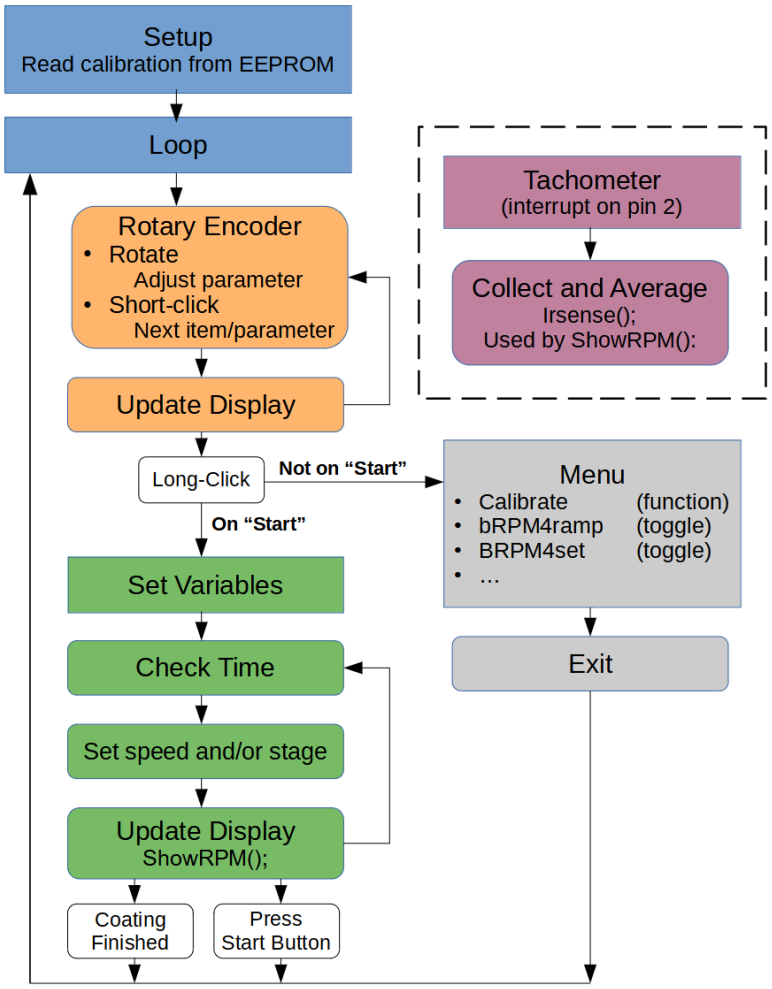

Figure 5: Flow diagram of software version 2.2 operation (used in hV3)

delay of 10 milliseconds is observed to allow for effects such as contact bounce before reading the state of its "SW" and "DT" pins (see Figure 4). This provided a stable, reliable means of adjusting parameters.

Motor control

The motor speed is controlled using a MOSFET driven by a PWM signal. This can be generated by software, switching the signal through loops, or hardware driven, using the Nano's *analogWrite()* command. A software based PWM loop did not provide consistent speed control, which was attributed to the computational processes demanded of the Nano single processing core. The most intensive being the processing and updating of the graphics display, and the hardware interrupt signals from the tachometer, which trigger priority execution of the associated software function. In contrast, consistent operation of a hardware controlled PWM signal was obtained, irrespective of the other demands on the processor. The drawback of the hardware PWM is the fixed PWM frequency and discrete steps in the PWM duty cycle, limiting the accessible speeds to discrete intervals. On a Nano, hardware based PWM is limited to a byte value between 0 and 255, corresponding to a target duty cycle of 0 and 100 % respectively.

Calibration

Prior to the first use, the spin coater should be calibrated (speed in RPM vs duty cycle). Calibration can be accessed though the menu as per Figure 5, which calls a function *void Calibrate()*. Once initiated, the motor speed is measured at values across the *AnalogWrite()* PWM range. The motor is allowed time to get to speed, followed by sampling the tachometer reading and averaging 5 values (hV2), followed by

time idle between each speed. The result for each PWM duty cycle is written to the Nano's EEPROM non-volatile memory.

Bypassing RPM calibration

Operation can rely either entirely on the PWM duty cycle, or on RPM values as determined by the menu parameter *bRPM4ramp*. When *bRPM4ramp* is set to *True*, the speed will ramp linearly with time using the RPM calibration values. When set to *False*, the duty cycle will ramp linearly with time. In hV2, "bRPM4set" toggles whether the speeds are set using RPM or PWM values, while hV3 allows the speed to be set by either at the pre-run display, where parameter are displayed and set.

Tachometer

During operation the tachometer code relies on system interrupts to measure the time between successive transitions of the infra-red sensor's signal from low to high. The motor used in hV2 will not exceed 8000 rpm (7.5 mS per revolution), with 3 interrupts per revolution this leaves 2.5 mS between transitions. The interval between interrupts is stored when successive interrupts occur slower than 2 mS apart. This minimum interval prevents multiple readings for a single transition. When the display refreshes it calls the function *showRPM()*, which averages the last 18 intervals to provide the rotational speed.

Boost function

The DC motors used require more torque to overcome the resistance to rotation when the motor is stationary, compared to when it has some inertia. To allow the motor to run at lower duty cycles, a "boost function" was implemented in hV3. The "boost function" increases the PWM duty cycle for 50 ms to generate additional torque in the motor. The activation criteria for the boost function requires that the tachometer reads 0, and that it is between 50 and 500 ms from the start of the spin program.

Should the tachometer ever fail and be unable to provide the microcontroller with readings, the spin coater can continue to operate provided the boost function is toggled off. This serves to reduce the risk of a user facing unusable equipment while plans are made for hardware inspection and repair.

Modularity

The circuity, motor and tachometer are not specifically paired, allowing easy substitution of these components for repairs and modification. A replacement motor can be easily set-up by running the calibration function accessible in the menu.

There are both DIY and commercial spin coaters available offering more advanced software. Some of these include features such as active speed correction using PID control. Many available spin coaters operate with 2 stages, while some commercial and DIY devices allow for a larger number stages in the coating process. The code written for this project provides 2 stages and an easy-to-use interface.

3. Design files summary

Design filename	File type	Open source license	Location of the file
Shnier2022-SpinCoater-SI.pdf	PDF	SHL-2.1	Available with the article
SpinCoater_parts-list.xlsx	Excel	SHL-2.1	http://doi.org/10.17632/y84tbnfsj4
Chuck_smooth-shaft.FCStd	FreeCAD	SHL-2.1	http://doi.org/10.17632/y84tbnfsj4
Chuck_threaded-shaft.FCStd	FreeCAD	SHL-2.1	http://doi.org/10.17632/y84tbnfsj4
Electronics Spin hV2 20211129.zip	LTSpice	SHL-2.1	http://doi.org/10.17632/y84tbnfsj4
Electronics Spin hV3 20220916.zip	LTSpice	SHL-2.1	http://doi.org/10.17632/y84tbnfsj4
Video of operation (hV2)	Video	MIT	http://doi.org/10.17632/y84tbnfsj4
Assembly of Spin-Coater hV2.pdf	PDF	SHL-2.1	http://doi.org/10.17632/y84tbnfsj4
Assembly of Spin-Coater hV3.pdf	PDF	SHL-2.1	http://doi.org/10.17632/y84tbnfsj4
SpinCoater_v2.3.1(for_hV3).ino	Arduino Sketch	MIT	http://doi.org/10.17632/y84tbnfsj4
SpinCoater_v1.4(for_hV2).ino	Arduino Sketch	MIT	http://doi.org/10.17632/y84tbnfsj4
SpinCoater_not-gate.zip	LTSpice/ various	SHL-2.1	http://doi.org/10.17632/y84tbnfsj4

Design files descriptions

- *Shnier2022-SpinCoater-SI 20220914.pdf* provides additional aspects of and concepts around the spin coater. This includes a list of commercial and DIY or open-source spin coaters.
- *SpinCoater_parts-list.xlsx* is an Excel spreadsheet containing a more detailed list of parts used for spin coaters hV2 and hV3 with the enclosure parts included.
- *Chuck_smooth-shaft.FCStd* and *Chuck_threaded-shaft.FCStd* contain the sample chuck dimensions the 6.35 mm shaft variants of hV3 and the M8 threaded shaft of hV2 respectively. The threads for the shaft is represented with an 8 mm hole in hV2 and the M3 tapped thread for grub screws of hV3 are represented by two 3 mm holes in the CAD drawings.
- *Electronics Spin hV2_20211129.zip* and *Electronics Spin hV3_20210916.zip* are LT spice schematics showing the connectivity of the electronics including the motor, IR sensor, LCD display and rotary encoder.
- *Video of operation (hV2) Shows a typical use case for spin coater hV2.*
- *Assembly of Spin-Coater hV2.pdf* and *Assembly of Spin-Coater hV2.pdf* detail the build processes and techniques for the corresponding spin coaters.
- *SpinCoater_v2.3.1(for_hV3).ino* and *SpinCoater_v1.4(for_hV3).ino* containing the Arduino code designed for the corresponding spin coaters.
- *SpinCoater_not-gate.zip* contains the LTSpice schematic for the NOT gate along with images of the simulations run on the circuit.

4. Bill of materials summary

Designator	Component	Qty	Unit USD	Total USD	Source of materials	Material type
	Common Electronics - Total			$20.79		
COM	Nokia 5110 LCD Module (15M8247)	1	$10.99	$10.99	mantech.co.za	semiconductor
COM	Infrared Obstacle Avoidance Sensor	1	$0.84	$0.84	pishop.co.za	semiconductor
COM	NE555 timer	1	$0.23	$0.23	mantech.co.za	semiconductor
COM	Resistor 10k Ohm	3	$0.04	$0.12	mantech.co.za	other
COM	Resistor 100 Ohm	1	$0.04	$0.04	mantech.co.za	other
COM	Resistor 1k Ohm	1	$0.04	$0.04	mantech.co.za	other
Motor control	MOSFET IRF540	1	$3.00	$3.00	mantech.co.za	semiconductor
Motor control	Rectifier diode DO41 1A 400V	1	$0.01	$0.01	mantech.co.za	semiconductor
COM	PROTOTYPING PCB 2.54 PITCH (14M1306)	1	$1.54	$1.54	mantech.co.za	composite
COM	Female headers (14M6379)	3	$1.02	$3.06	mantech.co.za	composite
COM	JUMPER LEAD PLUG-SOCKET 200mm	1	$1.68	$1.68	mantech.co.za	composite
COM	WIRE SOLID 0.34 1.6MM 250mm (red/black/yellow)	3	$0.14	$0.42	mantech.co.za	composite
COM	Hex Brass M3x10mm Stand off	4	$0.12	$0.47	mantech.co.za	metal
COM	M3 nut	4	$0.02	$0.07	mantech.co.za	metal
	hV2 Specific Electronics - Total			$74.66		
PWR-hV2	Dual USB Output 6-24V To 5.2V 3A Step Down Converter	1	$2.68	$2.68	pishop.co.za	semiconductor /other
PWR-hV2	Mean Well Power supply 24V 100W *1	1	$26.18	$26.18	mantech.co.za	other
hV2	DC motor 24V 6000rpm XD-3420	1	$35.73	$35.73	amazon.com	other
UI-hV2	Buttons (momentary contact) 72M4324/72M2826	2	$1.67	$3.33	mantech.co.za	other
UI-hV2	Potentiometer Linear 17MM 50Kω PCB	6	$1.12	$6.74	mantech.co.za	other
	hV3 Specific Electronics - Total			$54.68		
hV3	Motor JAK Motor 6-18VDC 79W RS-997SH-7013F	1	$16.64	$16.64	mantech.co.za	other
PWR-hV3	Mean Well Power supply 15V 100W *2	1	$33.06	$33.06	mantech.co.za	other
PWR-hV3	REG FIX POS TO220 9V 1A - L7809CV	1	$0.26	$0.26	mantech.co.za	semiconductor
PWR-hV3	Capacitor Ceramic Disc 330nF	1	$0.26	$0.26	mantech.co.za	other
PWR-hV3	Capacitor Ceramic Disc 100nF	1	$0.24	$0.24	mantech.co.za	other
UI-hV3	Rotary Encoder Keyes - KE0053	1	$3.22	$3.22	mantech.co.za	other
-hv3	Brass sheet 0.9mm, 40x10mm	1	<$1	<$1	metalcentre.co.za	metal
	Chuck and Mask - Total			$5.12		
C&M	Aluminium rod, ϕ = 65mm, L = 55mm	0.5	$4.07	$2.04	metalcentre.co.za	metal
C&M	Brass plate 65x65x0.7mm	3	$1.01	$3.03	metalcentre.co.za	metal
C&M-hV3	Grub screw M3	2	$0.03	$0.05	mantech.co.za	metal

* The enclosure components are detailed in the SI document *SpinCoater_parts-list.xlsx*.

∗1 The motor has a rated locked-rotor current of 3.37 A at 24 V (81 W).

∗2 This motor is currently running off a 12V 2A PSU and comfortably reaches 5200 rpm.

COM: Electronic components common to hV2 and hV3.

UI: User interface.

PWR: hV2 and hV3 specific power delivery related components
C&M: Chuck and mask related materials
-hV2 , -hV3 : Components specific to hV2 or hV3, mostly used in combination with other categories

5. Build instructions

The spin coater build consists of an enclosure, motor, and the electronics which include the power supply. Safety should be the first priority when building and operating equipment. A selection of considerations are listed below, with some additional precautions and best practices in the SI Section 10, this is intended as informative and is not comprehensive:

- When working with electricity all connections and wiring should be done while the power is off and the device is disconnected from mains.
- Capacitors, such as those present in power supplies (PSUs) store charge even after the PSU is disconnected from mains power. These can discharge explosively if shorted.
- Soldering involves high heat, care should be take to avoid burns while good ventilation is required for the fumes produced from solder, fluxes, and potentially but hopefully not, your components.
- When working with a motor keep the area clear of anything that could get caught by the motor such as loose clothing, jewellery, or hair.
- The spin coater's chuck and sample mask should not be touched when rotating. At speed the sample mask could potentially mimic a rotary cutting tool.

The components needed for the power supply depend on the chosen motor.

- A 12 V motor should be paired with a 12 V PSU with a sufficient power rating to supply the motor. The voltage of the PSU also affects how power can be supplied for the microcontroller. The microcontroller steps down the input power from the Vin pin using a linear voltage regulator, which dissipates heat proportional to the voltage difference between the input and output voltages. To reduce the heat dissipation on the board itself the 12 V was lowered to 9 V using a LM7809 linear voltage regulator to supply the microcontroller's Vin pin.
- For the 24 V motor and PSU in hV2 there is a much larger voltage difference making a linear voltage regulator less suitable due to heating concerns. For this a buck converter with a 5.2 V USB output was used to power the Nano through its USB port.

The connections for the electronics are as per the circuit diagram in Figure 4. The following considerations were made in assembly:

- Use of female headers on the PCB to allow detachable connections for the *Arduino Nano compatible microcontroller*, *rotary encoder*, *display* and *tachometer sensor*. These connections were made with ribbons of jumper leads.
- For the *power in* and *motor power* connections PCB mounted screw terminals were soldered to the PCB.
- A DIP8 socket was soldered to the PCB to house the NE555 timer chip.
- The remaining connections were soldered in place.
- The use of removable components allows for easier trouble-shooting as components can be disconnected or exchanged for testing.
- The choice of infra-red proximity sensor will affect whether the logic converting circuit is needed for signals to be reliably read by the Nano. For proximity sensors which provide 5V logic signals the *NOT gate* sub-circuit will not be needed. Ideally 3.3V logic signals should work reliably directly connected to the Nano, yet with the sensor tested in our application this was not the case. It is suggested that 3.3V proximity sensors should be tested in a bread board to assess the need for logic level converting circuit, such as the *NOT gate* sub-circuit.

The enclosure can be built in innumerable ways such that the motor is supported, the electronics are

protected, and a chamber is present for collecting the waste liquid thrown off the sample during coating. Enclosure build instructions are available as follows:

- See the SI document, *"Assembly of Spin-Coater hV2.pdf"*
- See the SI document, *"Assembly of Spin-Coater hV3.pdf"*
- Instructions for hV1, which makes use of a simpler design is available at [6]

6. Operation instructions

The spin coater operation consists of loading a sample, setting parameters, and initiating the run. Appropriate safety precautions should be observed when working with spin coaters. A few prominent safety concerns are mentioned here, with the caveat that the list is by no means exhaustive. Precursor solutions used in spin coating are expected to be aerosolised and/or evaporated to some extent. It is necessary to take appropriate precautions such as working in a well ventilated area, in a fume-hood, or in a glovebox as determined by the chemicals in use. The spin coater includes a rotating motor, spinning chuck, and sample, appropriate precautions include not wearing loose clothing, and keeping anything that could potentially get caught by the moving parts clear of the space. Protective eyewear is essential, as the device does not include a cover for the enclosure-bowl. The spin coater chuck and mask should not be touched while in motion. Some additional information on best practices and safety precautions are offered in the SI Sections 10 and 11.

1. Ensure that the inner part of the enclosure-bowl is lined with aluminium foil
2. Make a protective paper ring from strips of A4 paper cut lengthways by joining the paper with folds, masking tape or staples. Place the paper ring inside the enclosure-bowl along the outer edge (see Figure 3b). This collects most of the excess precursor from the spin coating process. This can then be changed after each set of samples to reduce the risk of sample cross-contamination, and prevent gunk build-up in the coater.
3. Ensure the desired sample mask is in place, or change the mask for the substrate being coated.
4. Turn on the spin coater at the power switch.
5. (Calibration, first use) If the spin coater has not been previously calibrated, load a test or old substrate/sample and run the built in calibration program. Calibration is best run with a sample and sample mask in place to provide conditions similar to standard operation.
   Access the menu (described below) and cycle through the options as explained on the screen. Select calibrate and allow the calibration to run. It will cycle through the PWM parameter values up to 255, saving an average RPM for each value as it progresses. (this takes about 2 hours on hV3).
   hV2. To access the menu on hV2, long press the red start button.
   hV3. To access the menu on hV3, long press the rotary encoder with any item other than "Start" selected.
6. Adjust the spin coating parameters as appropriate for the hardware variant:
   hV2. Adjust the 5 pots, each of which correspond to a single parameter. There will be a " > " in front of the parameter while it is being adjusted.
   hV3. Use short presses on the rotary encoder to scroll through parameters, the selected item is indicated with a " > " on the LCD display. Rotate the rotary encoder to adjust the parameters.
7. (Optional) Warm up the motor by running the spin coater for 2 minutes. This affects the motor grease viscosity and coil windings resistance, which can affect motor speed for a specific PWM duty cycle. A comparison of the tachometer reading and spin parameters is valuable to assess whether the motor needs to be warmed up, and as an assessment of the calibration values.
   hV2. Press the red button to start a run.
   hV3. Long press on the rotary encoder with "Start" selected to start a run.
8. Place a substrate in the cut-out of the sample mask.
9. Place precursor solution on the substrate using a dropper or micro-pipette.
10. Start the program as described in Step 7

11. (Optional) To stop the spin coater early press the red button (hV2), rotary encoder (hV3).
12. Remove the coated sample.
13. The spin coater returns to the parameter editing mode after a run and can be started again as done in Step 7, using the red button.
14. Remove and dispose of the contaminated paper ring from Step 2 once finished.
15. Clean and store.

7. Validation and characterization

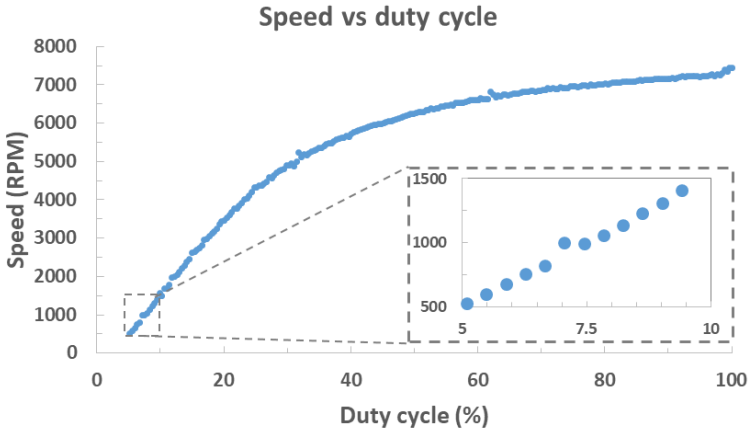

Figure 6: The relationship between motor speed and duty cycle for the 24V DC motor controlled through a n-channel MOSFET with an Arduino Nano equivalent microcontroller as used in hV2.

Direct and indirect indications of spin coater performance were assessed. This includes the stability of the calibration speed vs duty cycle calibration data, the effect of repeated operation, and the analysis of thin films fabricated with hV2 by means of highly sensitive measurements.

The calibration function was run on the spin coater. Once completed, the speed vs. PWM parameter data was read from the spin coater's EEPROM, then converted into speed vs duty cycle for Figure 6. This was fitted with a 6th order polynomial, $R^2 = 0.9997$, Residual std. error = 31.3, Figure SI-14. The magnitude residual std. error is dependent on the choice of motor and power supply stability. At higher speeds the PWM control allows finer increments as the calibration curve's gradient decreases. This is represented by the mean step in the RPM values of 81 below 3000 RPM, and 37 between 4000 and 6000 RPM. This imposes a granular selection of spin speed and informs on the step size limitations of the Nano's hardware based PWM control.

In testing the effect of extended operation of the spin coater, a cycling experiment was conducted. For each cycle, the spin coater was operated at a set duty cycle for 30 s followed by 30 s idle. The spin coater was started on the beginning of each minute over an hour. Multiple readings of the motor speed (> 5) were taken and averaged for each data point during the 30 second active period (Figure 7a). This was carried out with the enclosure fully assembled, as per standard operation.

In a separate instance, K-type thermocouples were placed on the back of the MOSFET used for PWM control, and on the top of the motor housing. The thermocouples were monitored using digital multimeters with a resolution of 1 °C, as shown in Figure 7b. In cases where the multimeter reading was unstable between 2 consecutive integers, the average was taken leading to some values with a half. The cycle number was denoted by n; From time $((n-1) \cdot 60$ s) to $(((n-1) \cdot 60$ s)+30 s) the motor is running, after which the motor is idle until the nth minute. The MOSFET-Hi temperatures were taken at $((n-1) \cdot 60$ s) + 30 s while the MOSFET-low temperatures (Figure SI-15) were taken at the end of the cycle on the minute mark ($n \cdot 60$ s). The motor casing/housing temperature was recorded as the maximum stable value over the 1 minute period of the cycle, Figure 7c.

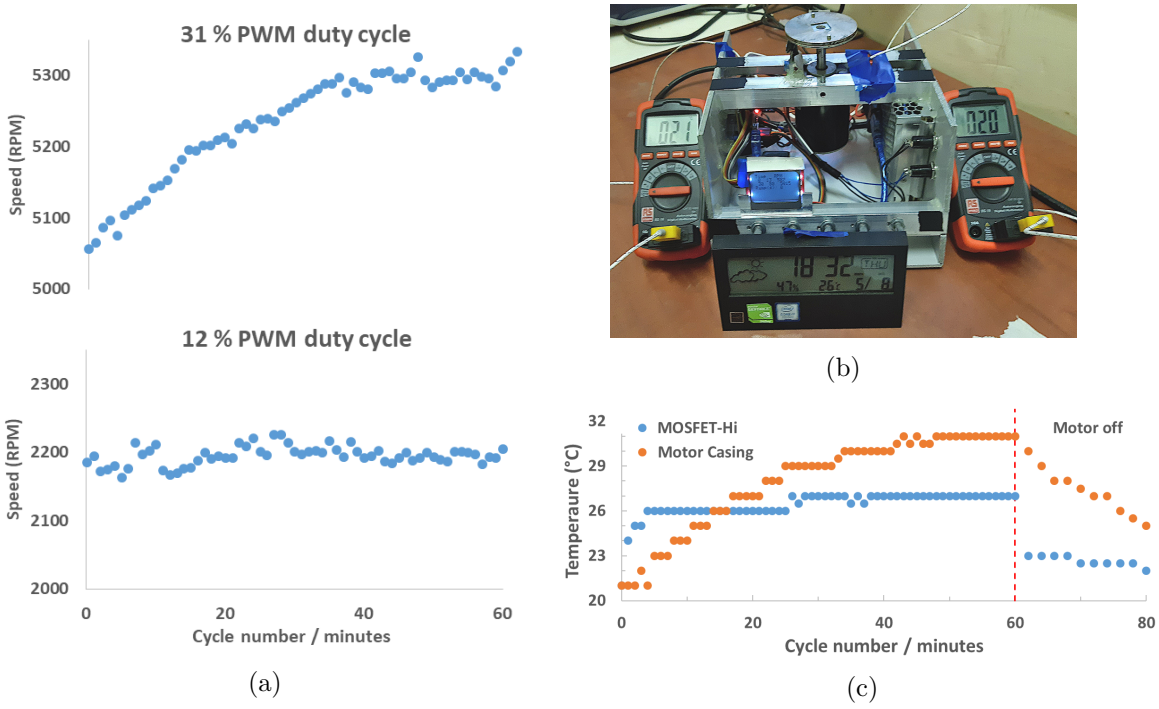

Figure 7: The effect of extended operation observed through cycling of 30 s on, 30 s off for hV2. (a) Motor speed as a function of cycle number with the at PWM duty cycles of 12 and 31 % (nominally 2200 and 5000 rpm respectively). (b) The hV2 spin coater with thermocouples attached for collection of temperature data. (c) Motor housing and MOSFET temperature as a function of cycle number at a 31 % duty cycle.

In Figure 7a, the spin coater (hV2) motor speed remains reasonably steady with cycling at around 2200 rpm while operating at a duty cycle of 12%. When this is increased to a duty cycle of 31%, the motor speed gradually increases from 5050 to 5300 rpm, this constitutes a 5% increase in speed, after an hour of cycling. This was suspected as an effect of heating in either the motor or the MOSFET controlling the motor. The temperatures of both components were tracked using the same 30 s on 30 s off cycling approach (Figure 7c). The MOSFET was quick to stabilise between 26-27 ° C during cycling at a 31% duty cycle, while the temperature of the motor housing rose in a similar trend to the speed in Figure 7a, (see Figure 7c).

To support assignment of motor temperature as the cause of the speed increase, we consider the motors no-load speed n_0 as a suitable indicator for the trend in operational speed. This neglects the effect of the weight of the sample chuck which is minimal. The relation is given in Equation 1 where K_E is the voltage constant of the motors permanent magnets, and α_m is the permanent magnets temperature coefficient [20, 21]. For small changes in $\alpha_m \Delta T$ ($\alpha_m \approx -0.002°C^{-1}$, $< 40°C$, n_0 can be approximated to increase linearly with increasing ΔT.

$$n_0 \propto \frac{V_T}{K_E} \text{ where } K_E = K_E^0[1 + \alpha_m \Delta T] \implies n_0 \propto 1/(1 + \alpha_m \Delta T), \alpha_m < 0 \tag{1}$$

With Equation 1 in consideration, the increase in motor speed was attributed to an increase in motor temperature during cycling at a the higher PWM duty cycle of 31 %. The motor used in hV2 had a sealed housing which does not allow air to pass through for cooling of the motor. It is recommended that either a motor be used that generates less heat or one which has a better heat dissipation. To accommodate this dynamic behaviour in hV2, the PWM duty cycle set point can be monitored and modified in cases

of extended operation to minimise the error in spin speeds. Alternatively a software based correction can be implemented.

7.1 Application example

With the purpose of a spin coater being the fabrication of thin films, such films were fabricated on hV2. These were then assessed using characterisation techniques sensitive to film quality.

Polymer blend thin films were prepared using the hV2 spin coater, followed by surface measurements using atomic force microscopy (AFM). A precursor solution was used containing 20 mg/ml of PBDB-T:PC71BM (1:1 ratio) in chlorobenzene. The solution was stirred overnight at 40 °C. A dropper was used to cover a clean glass substrate with the solution followed by spin coating at between 1000 and 5000 rpm for 60 seconds.

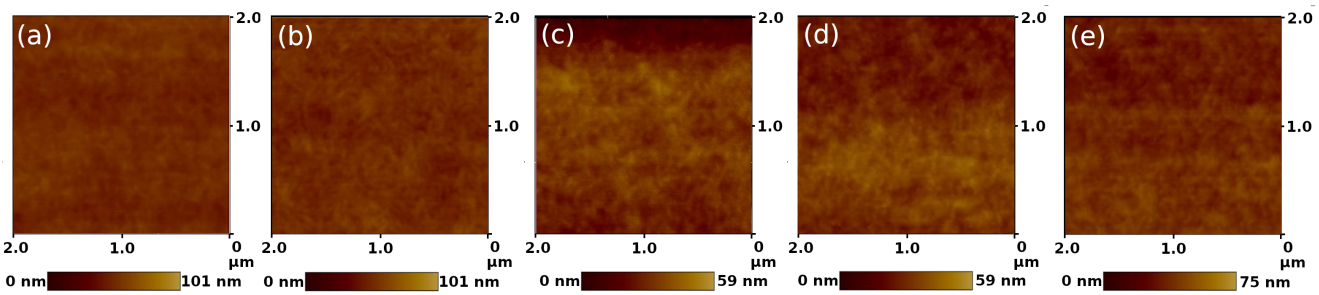

(f)

Speed (rpm)	1000	2000	3000	4000	5000
RMS roughness (nm)	4.200	4.284	6.497	5.846	5.088

Figure 8: Tapping mode AFM of PBDB-T:PC71BM (1:1) thin films, spin coated for 60 s at various speed. (a) 1000 rpm, (b) 2000 rpm, (c) 3000 rpm, (d) 4000 rpm, (e) 5000 rpm (f) Root-mean-square (RMS) roughness for the various spin speeds determined across lengths scales between 2 to 5 μm.

The AFM measurements and roughness of the thin films are presented for various spin speeds in Figure 8. The roughness appeared quite modest and consistent across the measurements. The roughness was lower at 1000 and 2000 rpm, highest at 3000 rpm and decreased thereafter. In a line-trace of the 3000 rpm sample (Figure SI-16) a maximum peak to valley height of 11 nm was observed which is comparable to the 8 nm over a 5 μm length for PCBM in literature [3]. Differences in the viscosity and concentration of the polymer blend solution, and the boiling point of the solvent used will have a strong influence on the film topography and roughness, yet these measured values are sufficient as a positive reflection on the hV2 spin coater.

X-ray reflectometry (XRR) measurements provide an indication of film quality. XRR demands high quality films with a roughness of no more than a few nanometres for the observation of Kiessig fringes. With this in mind PMMA thin films were coated on a glass substrate at 4000 rpm using hV2 with a 0.5 or 1 wt% solution of PMMA (PMMA Sigma-Aldrich 445746). The samples were dried for 20 min at 60 °C then annealed for 60 min at 95 °C in an Ar filled annealing chamber. XRR measurements were then taken on a Bruker D8 Discover with Goebel mirror and 2 bounce Ge (022) monochromator. The data was fitted using LEPTOS (Bruker AXS, V7).

The measurements provided exceptionally good XRR patterns for samples prepared using spin coating, as seen in Figure 9. Due to the low electron density and small volume of the PMMA films its density information was obscured by that of the substrate. The density of the PMMA films was thus fixed to a literature based value of 1.18 g/cm3 [4, 22]. While this assumption reduces the absolute accuracy of the modelled thicknesses, it increases the stability of the determined thicknesses, thus improving the relative accuracy between measurements, which is valuable for the following comparison. The thicknesses for the samples made from the 1 wt% precursor were 27.0 ± 0.3 and 26.2 ± 0.3. For the 0.5 wt% precursor

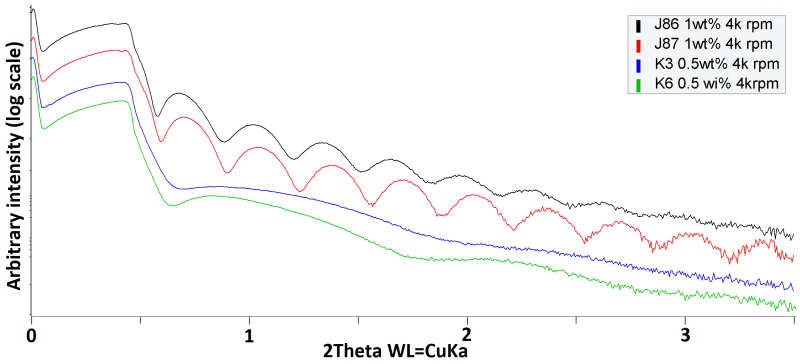

X-Ray Reflectometry fit parameters

Sample	Thickness (nm)	Roughness (nm)
J86	27.0	1.5
J87	26.2	1.0
K3	7.3	1.5
K6	7.9	1.3

Figure 9: X-Ray reflectometry measurements on PMMA spin coated films produced using hV2 and collected on a Bruker D8 Discover.

thickness were modelled to 7.3 ± 0.2 and 7.9 ± 0.2. Comparable values were observed for the resulting films within each precursor weight percent solution, the slight variations observed may have contributions from minor variance in the application of the precursor to the substrate, and the wait time between this application and the start of the spin coating program.

7.2 Capabilities and limitations:

- Quick to change samples and sample masks
- 600 - 7000 rpm
- 2-stage spin program
- Max ϕ 45 mm sample size limited by the distance between pins on the chuck
- Sample masks unsuitable for ultra-thin samples
- In-built speed calibration program
- Absence of a speed correction algorithm
- Intuitive controls and display

7.3 Discussion and future work

The spin coater design presented provides good functionally and ease of use. hV2 as presented has survived use in a multi-user research lab in South Africa since 2019, while hV3 has been in a Kenyan research lab since 2021, without a need for repair or maintenance, exceeding the performance of at least some more costly commercial alternatives. Accommodating additional sample sizes by cutting a new mask from brass sheet is manageable by any individual competent with hand tools. This spin coater is cost effective, and allows the fabrication of high quality thin films. This makes it ideal for research groups where a reliable, repairable product is needed on a minimal budget. The cost and maintenance aspects of open-source hardware can offer utility to low budget institutes and groups where the commercial equivalent may be prohibitively expensive or otherwise inaccessible. Commercial alternatives using motors with less internal resistance provide smoother operation at low speeds compared to the motors used in hV2 and hV3. Since this is entirely dependent on the motor, this can be upgraded in future versions to close this gap.

Many of the design considerations implemented, or features avoided were inspired by the authors experience (direct and indirect) with failure points and repairs of commercial spin coaters and their related vacuum systems. This includes precursor solution clogging vacuum chucks, various problems with vacuum pumps for which vacuum pumps are notorious [1], motor problems, tachometer issues causing glitches in speed regulation, and precession due to a slightly bent motor shaft among other issues.

The motor in hV2 showed gradual heating at higher PWM duty cycles. This is attributed to a closed motor housing design which leads to heat retention. In response to this, hV3 instead uses a motor with an air cooled housing.

Speed correction could be implemented to address the effects of changes in conditions, such as motor temperature on the spin speed, a simple means of speed correction would be to adjust the motor speed towards a target based on the tachometer reading. With the PWM duty cycle set by a byte value, a threshold is required to avoid constantly cycling between two adjacent speeds. The threshold can be defined relative to the step size between consecutive speed calibration values closest to the target speed, this accommodates larger steps at lower speeds and smaller steps at higher speeds consistent with Figure 6. For more advanced speed correction Arduino libraries are available for implementation methods such as PID control [23].

To reduce the size increments of accessible speeds at lower duty cycles, effectively continuous PWM steps can be implemented. This can be achieved by using software controlled PWM. Initial tinkering showed inconsistent speed control when using software based PWM where the same microcontroller was also handling the display and tachometer. This could be easily remedied with a dedicated microcontroller to drive the software based PWM at the expense of additional cost and complexity. The finer speed increments could also benefit any speed correction implementations.

CRediT author statement

***Adam Shnier**: Conceptualization, Methodology, Software, Writing-Original Draft, Investigation. **Francis Otieno**: Investigation. **Daniel Wamwangi**: Supervision, Resources, Writing-Review and Editing. **Caren Billing**: Supervision, Writing-Review and Editing. **David G. Billing**: Supervision, Resources, Writing-Review and Editing.*

Acknowledgements

We would like to thank Gerry Germishuizen who machined the aluminium chuck for the spin coater. Additionally, Lesias Kotane and Nicolette Visser for feedback and discussion.

The financial assistance of the National Research Foundation (NRF), University of the Witwatersrand - Material and Energy Research Group (MERG), DSI-NRF Centre of Excellence in Strong Materials (CoE-SM) and UKRI GCRF-START towards this research is hereby acknowledged. The use of resources and equipment of the University of the Witwatersrand is hereby acknowledged. Francis Otieno would like to highly thank ARUA Centre of Excellence in Materials, Energy and Nanotechnology (CoE-MEN) through the ARUA/Carnegie Early Career Research fellowship for their timely funding.

Opinions expressed and conclusions arrived at are those of the authors and are not necessarily to be attributed to Wits, NRF, MERG DSI-NRF CoE-SM, UKRI GCRF-START, ARUA, nor CECRF.

References

[1] Ossila Limited, Spin coater — low price compact spin coating system, (accessed: 2020-02-04). URL https://www.ossila.com/products/spin-coater?variant=1200242585

[2] R. F. Bianchi, M. Panssiera, J. Lima, L. Yagura, A. Andrade, R. M. Faria, Spin coater based on brushless dc motor of hard disk drivers, Prog. Org. Coat. 57 (1) (2006) 33–36. doi:https://doi.org/10.1016/j.porgcoat.2006.05.004.

[3] Y. Bai, H. Yu, Z. Zhu, K. Jiang, T. Zhang, N. Zhao, S. Yang, H. Yan, High performance inverted structure perovskite solar cells based on a pcbm: polystyrene blend electron transport layer, J. Mater. Chem. A 3 (17) (2015) 9098–9102. doi:https://doi.org/10.1039/C4TA05309E.

[4] A. Van der Lee, L. Hamon, Y. Holl, Y. Grohens, Density profiles in thin pmma supported films investigated by x-ray reflectometry, Langmuir 17 (24) (2001) 7664–7669. doi:https://doi.org/10.1021/la010811w.

[5] L. Scriven, Physics and applications of dip coating and spin coating, MRS Online Proceedings Library 121 (1988). doi:https://doi.org/10.1557/PROC-121-717.

[6] A. Shnier, Spin coater v1 (almost analog), (accessed: 2021-11-23) (2019).
URL https://www.instructables.com/Spin-Coater-V1-almost-Analog/

[7] M. Sadegh-cheri, Design, fabrication, and optical characterization of a low-cost and open-source spin coater, J. Chem. Educ. 96 (6) (2019) 1268–1272. doi:https://doi.org/10.1021/acs.jchemed.9b00013.

[8] Ossila Limited, Spin coater chucks, (accessed: 2021-11-08).
URL https://www.ossila.com/products/spin-coater-chucks

[9] SPI KW-4A, Setcas llc — kw-4a spin coater, (accessed: 2021-11-08).
URL https://www.setcas.online/product-page/kw-4a

[10] SETCAS LLC, Setcas llc — kw-4a spin coater, (accessed: 2021-11-08).
URL https://www.setcas.online/product-page/kw-4a

[11] MTI Corporation, Compact spin coater - vtc-100a, (accessed: 2021-11-08).
URL https://www.mtixtl.com/ProgrammableCompactSpinCoater0-8000rpm4waferMax-VTC-100A.aspx

[12] R. Dabirian, V. H. Guerrero, D. C. L. Matovelle, L. J. Segura, Mechanical and electronic systems of an open source based spin and dip coater, Revista Politécnica 37 (2) (2016) 53–53.

[13] Y. Akyüz, Design and fabrication of a cost-effective spin coater, (accessed: 2021-11-08) (2020).
URL https://github.com/yetkinakyz/SpinCoater

[14] Y. Akyüz, Design and build a spin coater, (accessed: 2021-11-08) (2016).
URL https://benkrasnow.blogspot.com/2016/02/design-and-build-spin-coater.html

[15] J. M. Pearce, Emerging business models for open source hardware, J. Open Hardw. 1 (1) (2017) 2. doi:https://doi.org/10.5334/joh.4.

[16] J. M. Pearce, Quantifying the value of open source hardware development, Modern Economy 6 (2015) 1–11. doi:http://dx.doi.org/10.4236/me.2015.61001.

[17] Arduino, Constants / defining pin levels: High and low, (accessed: 2021-10-04) (2021).
URL https://www.arduino.cc/reference/en/language/variables/constants/constants/

[18] Arduino, Arduino nano specifications, (accessed: 2021-11-15) (2021).
URL http://web.archive.org/web/20211023113957/https://www.arduino.cc/en/pmwiki.php?n=Main%2FArduinoBoardNano

[19] Texas Instruments, Lm1117 800-ma, low-dropout linear regulator, (accessed: 2021-11-30) (2000).
URL https://www.ti.com/lit/ds/symlink/lm1117.pdf

[20] M. Nagrial, J. Rizk, A. Hellany, Design and performance of permanent magnet slotless machines, in: 2008 18th International Conference on Electrical Machines, IEEE, 2008, pp. 1–5. doi:https://doi.org/10.1109/ICELMACH.2008.4799949.

[21] D. Montone, Temperature effects on motor performance, HaydonKerkPittman (2017) 1–10.
URL https://www.haydonkerkpittman.com/-/media/ametekhaydonkerk/downloads/technical-documents/pittman-technical-documents/temperature_effects_on_dc_motor_performance.pdf

[22] CROW, Chemical retrieval on the web — poly(methyl methacrylate), (accessed: 2021-11-03) (2018).
URL https://polymerdatabase.com/polymers/polymethylmethacrylate.html

[23] B. Beauregard, Pid library, (accessed: 2021-11-04) (2021).
URL https://www.arduino.cc/reference/en/libraries/pid/

Part III

Investigation

Chapter 6

Modelling of $(FAPbI_3)_{0.85}(MAPbBr_3)_{0.15}$ thin-film *in-situ* diffraction data

Contents

6.1 Overview **125**

6.2 Data collection methodology **126**

6.3 Data visualisation and individual peak fitting **127**

6.3.1 Method 127

6.4 Literature structure refinements **132**

6.4.1 Methodology 132

6.4.2 Results and discussion 133

6.5 Investigative Le Bail refinements **136**

6.5.1 Methodology 136

6.5.2 Results and discussion 137

6.6 Structure modelling **142**

6.6.1 Methodology 142

6.6.2 Results and discussion 144

6.7 Sequential refinements **150**

6.7.1 Methodology 150

6.7.2 Discussion 152

6.7.3 Conclusion 163

6.7.4 Future work 163

6.1 Overview

The hybrid perovskites $MAPbX_3$ and $FAPbX_3$ both have phase stability challenges as discussed in Section 1.5.3. $MAPbX_3$ is subject to its $\alpha \rightarrow \beta$ phase change near 327 K (54 °C, 1 atm). Temperatures exceeding 330 K (57 °C) are reachable during the standard operation of photovoltaic modules adding to thermal instability. The perovskite phase of $FAPbX_3$ is metastable at room temperature slowly converting to a non-perovskite hexagonal δ phase which is not suitable for photovoltaic applications [Jeon et al., 2015, Fu et al., 2017]. This is evident in Figure 1.4 of Chapter 1 where the Shockley-Queisser efficiency limit is shown as 13.8 % for δ-$FAPbX_3$ compared to >30 % for $MAPbI_3$ and $FAPbX_3$.

The phase stability, environmental stability, and thermally induced transitions of hybrid-perovskites can be optimised through compositional tuning as discussed in Section 1.3 with thermally induced transitions discussed in Section 1.5.2.

The mixed cation hybrid-perovskite $(FAPbI_3)_{0.85}(MAPbBr_3)_{0.15}$ has been identified as a stable mixed cation perovskite at ambient conditions with a reported band-gap of 1.63 eV corresponding to an SQ limit near 30 % PCE [Jesper Jacobsson et al., 2016, Rühle, 2016]. The study undertaken investigates the phase behaviour of the mixed cation and halide perovskite as a function of temperature though modelling X-ray diffraction data. The primary constituent $FAPbI_3$ undergoes phase changes near 285 and 140 K for the $\alpha - \beta$ and $\beta - \gamma$ phase changes respectively [Weber et al., 2018]. A range of 80 to 315 K was investigated, providing a broader temperature range than would be needed to reach the γ phase of the primary constituent $FAPbX_3$ (85 %) for the purpose to better understand the $\alpha \rightarrow \beta$ structural transition for the mixed cation mixed halide $(FAPbI_3)_{0.85}(MAPbBr_3)_{0.15}$ composition.

This chapter discusses in detail the model development applied to X-ray diffraction data resulting in a publication by C. Greenland, A. Shnier *et al.* (2019) [Greenland et al., 2019]. Various refinement strategies have been employed on the data-set in question providing insights into the data characteristics and associated implications. This served as a basis of comparison for various sets of structural refinements.

The degree of freedom of the refinement parameters and structural implications of the models were carefully assessed across the full dataset. These were then chosen to best represent the data. Structure constraints were explored to stabilise the refined parameters. Caution was exercised to avoid considerations and constraints which may over-constrain or threaten the integrity of the refinement models and results. This lead to the methodology and structure model that was used for the publication, where a set of Monte-Carlo assisted refinements has been put forward.

6.2 Data collection methodology

The sample preparation and the refinement of the instrument profile is discussed in Section 4.7.1. For ABX_3 hybrid perovskites, the structure expected to be either in the cubic α phase or a derivative by octahedral rotation of the ${PbX_6}^{4-}$ as described by Glazer *et al.* [Glazer, 1972] and introduced in Section 1.5.1. Considering the absence of a structure prone to preferred orientation, such as a layered or needle like structure, it is less likely to observe preferred orientation in the sample. The sample was removed from its substrate, during which it formed a powder in which the particle orientation is unconstrained by the substrate, and a rotating capillary stage was used for the measurements which allows the sampling of each crystallite in a range of orientations, it follows that preferred orientation would not be expected in the measurements. Measurements started with a cooling sequence from 315 to 80 K followed by a heating sequence returning to 315 K [1]. Samples were allowed 30 minutes to equilibrate at each temperature prior to each diffraction measurement. The scan names are given in the form *Sequence-Temperature* such as 22-150K where this pattern is collected at 150 K, and it is the 22nd diffractogram collected in the data-set. A list of scans is provided in SI Tables C.1 and C.2.

The VT-XRD data set was primarily collected across a range of $5 - 50°$ 2θ. Selected scans at 80, 150, 280, and 315 K were collected over a larger

[1] Some additional measurements were taken on heating up to 350 K these are omitted for (1) to allow the cooling traces such as in Figure 6.2 to have identical aspect ratios which allows for a neater comparison. (2) Significant structural change was not observed in this region.

2θ range of $5 - 80°$ 2θ to provide a larger number of observed peaks. The additional higher angle information is advantageous in the refinement and evaluation of structural models [2].

6.3 Data visualisation and individual peak fitting

Structural reorganisation is routinely accompanied by changes in the X-ray diffraction pattern, in terms of peak position, peak intensity, peak splitting and the appearance of additional peaks. In this section we identify signatures of structural change as a function of temperature for $(FAPbI_3)_{0.85}(MAPbBr_3)_{0.15}$. Figure 6.1 shows an overview though the use of a *colourmap* plot and selected individual plots illustrating the structural evolution of this mixed cation, mixed halide perovskite from 315 to 80 K.

6.3.1 Method

The data was visually inspected to identify characteristics of phase changes, such as the emergence of new peaks, Figure 6.1b.

A selection of peaks were modelled individually using a Pearson VII analytical peak shape with TOPAS V5 across the VT-PXRD data set by means of sequential refinement, Figure 6.2. The formulation of the peak profiles is described and discussed in Section 3.3.2, individual peak fitting in Section 3.8.1, and sequential refinement in Section 3.10.1. This approach served to assess changes in the diffraction pattern with a method unbiased by the constraints of Pawley fits, Le Bail fits, or structural models.

From the refinements, peak width and position parameters, across the temperature range were normalised to allow for comparison between peaks. The normalised peaks position informs on peak shifts and changes in the

[2]The angular collection range could only be extended for a small number of scans due to limitations in available instrument time.

inter-planer spacing within the crystal lattice, while the normalised full width at half maximum (FWHM) informs on peak broadening and potentially peak splitting.

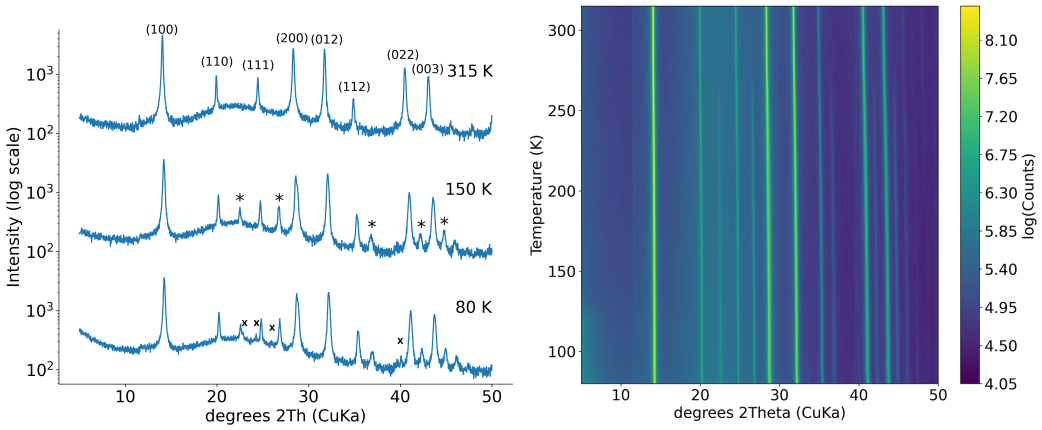

(a) (b)

Figure 6.1: PXRD measurements of $(FAPbI_3)_{0.85}(MAPbBr_3)_{0.15}$ on cooling. Heating data is presented in App. Figure C.1. (a) Diffraction patterns at 315, 150 and 80 K, *'s and x's mark additional peaks observed in the regions represented by the 150 and 80 K patterns respectively. (b) Diffraction intensity changes on cooling from 315 to 80 K.

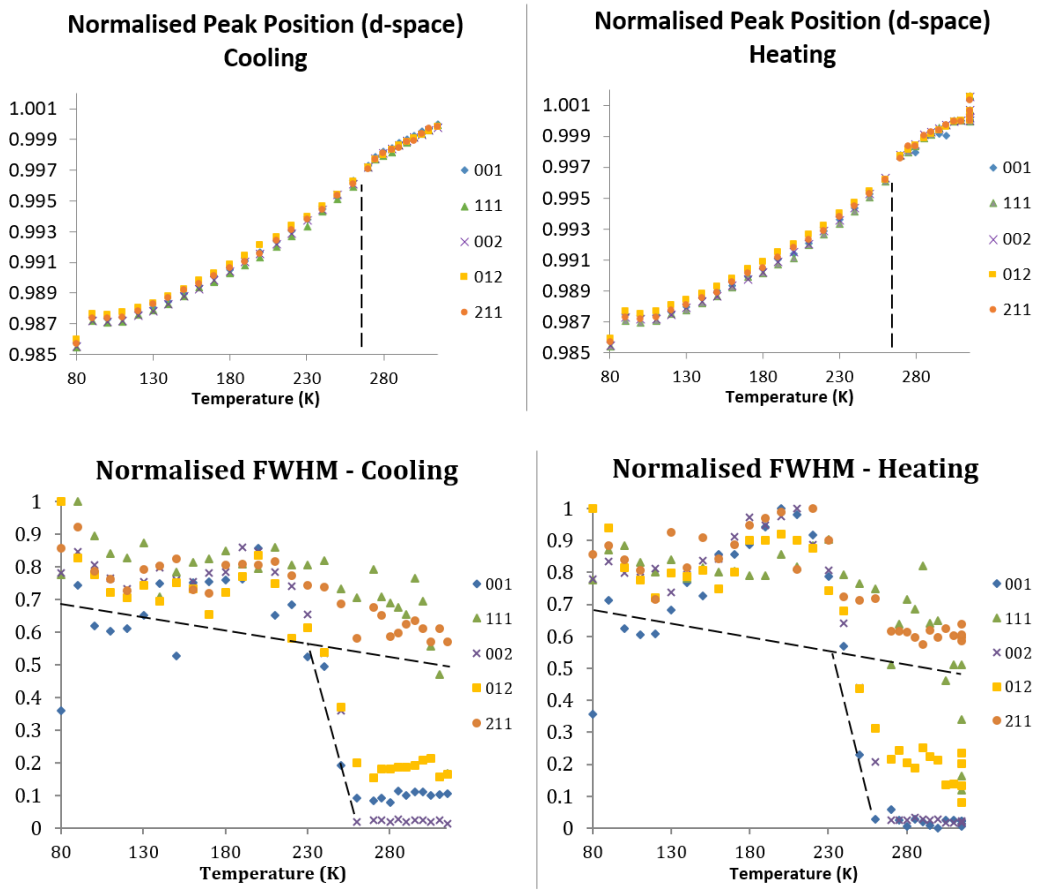

Figure 6.2: $(FAPbI_3)_{0.85}(MAPbBr_3)_{0.15}$ on cooling, parameters from individual PVII peak fits, using peak indexing of a $Pm\bar{3}m$ perovskite across the temperature range for convenience. Dotted lines are included as a visual guide.

Results and Discussion

Peak evolution was observed as a function of temperature, Figures 6.2. Additional peaks were observed on cooling below 260 K, and further additional peaks in the 80 K pattern, as emphasised in Figure 6.1a with *****'s and **x**'s for representative patterns at 315, 150 and 80 K. The diffraction measurements on cooling encompassed all peaks identified across both heating and cooling sections of the VT-XRD measurements. The plot showing intensity changes on heating is available in App. Figure C.1b.

Figure 6.2 shows the trend in the normalised peak positions in d-space, or equivalently the normalised inter-planer spacing as a function of temperature. We see there is a significant decrease in the d-spacing at 80 K. Comparing the 90 - 260 K range with normalised peak positions above 270 K, there is a noticeable change in the gradient.

The evolution of lattice parameters as a function of temperature, and by extension, that of peak position, is expected to follow a similar trend to the simple Einstein-like model, $a(T) = a_0 + \frac{c_1\theta_1}{e^{\theta_1/T}-1}$ [Dinnebier et al., 2018], where a is the lattice parameter, T is temperature and refinable parameters c_1 and θ_1. Deviations from this gradual monotonic function can be considered indications of structural change or rearrangement, as is observed for the change between 80 and 90 K as well as the difference on either side of the 260/270 K step in the normalised peak positions.

A phase change is suspected between 80 and 90 K where there is a sudden jump of 0.17 % [3] in the inter-planar spacing (d-spacing) compared to only 0.016 % between 90 and 100 K [4] as visible in Figures 6.2. This translates to higher angle peaks and smaller unit cell at 80 K. [Cordero et al., 2021]

Between 210 and 270 K, during heating and cooling, the FWHM of many peaks broaden with decreasing temperature. On cooling, the (111) and (211) peaks experience no sudden change in their peak width. On heating, the (111) peak narrows at 315 K and above, similar was not evaluated on cooling as

[3] An average change of 0.17 % was observed from 90 to 80 K on cooling and from 80 to 90 K on heating.

[4] A 0.016 % change in d-spacing was observed from 100 to 90 K on cooling, and 0.017 % on heating from 90 to 100 K.

cooling started from 315 K [5]. Much of the broadening of peaks is attributed crystallographic planes becoming inequivalent as the symmetry of the unit cell changes leading the splitting of peaks such as where 100, 010, and 001 become inequivalent on cooling as would be expected for the $\alpha \rightarrow \beta$, cubic to tetragonal transition. [Weber et al., 2018]

Both the observation of peak evolution in Figure 6.1, and the results of individual peak fitting in Figure 6.2, suggest that the VT-XRD data set can be separated into 3 main divisions, separated by indications of where structural reorganisation is occurring. Each temperature division presented additional peaks on the lower temperature side of the transitions, as marked in Figure 6.1a. The high temperature phase roughly above 260 K followed by a gradual structural reorganisation between about 230 and 260 K, indicated by the gradual peak broadening of the $(00l)$ and (012) peaks in the normalised FWHM plots, Figure 6.2. The 80 K pattern differs from the higher temperature patterns, with a significant change in peak d-spacing, and the observation of additional weak peaks, as evident in Figures 6.2 and 6.1a respectively.

The divisions were assigned as phases by the naming scheme used in literature for similar perovskite systems. These are the α phase at ambient temperature, β phase at sub-ambient temperature, including the gradual transition below $\sim$270 K and a less clear γ phase appearing at 80 K [Cordero et al., 2021]. These assignments are supported by what has been reported for similar systems in literature [Weber et al., 2018, Schueller et al., 2018, Cordero et al., 2021], and this will be reconsidered with the application of structure models in the following sections. This is necessary to verify the validity of these assignments as the structural reorganisations observed are not intrinsically phase changes.

[5] For convenience, in this section the peaks are referred to in terms of the archetypical $Pm\bar{3}m$ perovskite reflections.

6.4 Literature structure refinements

A comparison is made between the collected data and structures of materials with a similar composition. This is carried out through Rietveld refinement, which is subject to the considerations of pattern fingerprinting for qualitative assessment of fit quality as discussed in Section 3.6.1.

6.4.1 Methodology

Candidate structures from the COD and ICSD database were selected and compared to the collected data using a combination pattern fingerprinting and Rietveld refinement [6]. These structures are listed in Table 6.1, while the data collection and labelling scheme is detailed in Section 6.2. Literature reported transition temperatures for hybrid-perovskite materials are provided in Table 1.3 of Chapter 1.

Table 6.1: Literature structures of similar systems

Composition	Phase	Crystal system	Space Group	Database Code
$(FAPbI_3)_{0.85}(MAPbBr_3)_{0.15}$	α	cubic	$Pm\bar{3}m$	COD 4125879
$FAPbI_3$	β	trigonal	$P3m1$	COD 4335631
$FAPbI_3$	β	trigonal	$P\bar{3}$	COD 4335635
$FAPbI_3$	β	tetragonal	$P4/mbm$	ICSD 230492
$MAPbI_3$	β	tetragonal	$I4/mcm$	ICSD 428899
$MAPbI_3$	γ	orthorhombic	$Pnma$	ICSD 428898

Of the data collected, the 315 and 150 K patterns provided good representation of the peaks and features observed above 90K in the VT-XRD data-set. The 80 K pattern possesses additional weak peaks, along with the peaks corresponding to those observed at higher temperatures. As such most Figures in this section are limited to the 315 and 150 K patterns with the full temperature range being examined in subsequent sections.

[6] COD: Crystallography Open Database, ICSD: Inorganic Crystal Structure Database.

Rietveld refinements were performed using a pseudo-Voigt analytical peak shape function in all cases in this section unless otherwise stated [7]. This accounted for the full peak profile allowing for the determination of peak position and relative peak intensities. The refinement of the lattice parameters allows structure models to accommodate variations in unit cell size which is dependent on composition and sample measurement temperature. The halide composition was accounted for using a shared Br/I site, where occupancies were set to 0.15 and 0.85 respectively. Thermal parameters (beq) were refined, representing contributions to disorder and thermal motion, reflecting the electron density distributions of the average structure.

The purpose of these fits were to compare the presence and approximate intensity of peaks between the collected data and simulated patterns. Structure refinements in TOPAS allowed a more reliable comparison than offered by "fingerprinting" the data against literature peak intensity and position values (discussed in Section 3.6.1). The use of an analytical peak profile in contrast to fundamental parameter refinements, allows the refinement of peak shape without the consideration of the specific contributions to peak shape. This is sufficient to evaluate the suitability of a given structure model. The peak profiles as implemented in this section do not consider the instrument profile. This makes them unsuitable for the determination of peak profile dependent parameters such as crystallite size.

6.4.2 Results and discussion

Selected scans from the data-set were compared against the structures in Table 6.1. The phase assignments proposed in Section 6.3 are used for ease of reference in the discussion the different temperature ranges.

The literature $Pm\bar{3}m$ α phase, and the collected data are both of the nominal composition $(FAPbI_3)_{0.85}(MAPbBr_3)_{0.15}$. This cubic structure reasonably describes the reflections of the high temperature phase, Figure 6.3.

[7] Both Pearson VII and pseudo-Voigt functions are suitable for this section, with the caveat that where refined parameters are compared, a common profile should be used across refinements. Additional discussion on peak profiles is provided in Section 3.3.2

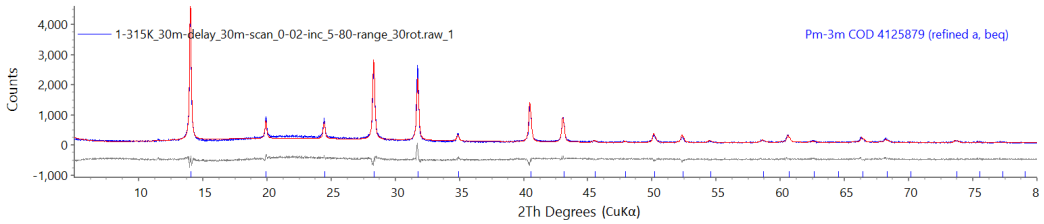

Figure 6.3: Structure fit, 1-315K $Pm\bar{3}m$-$(FAPbI_3)_{0.85}(MAPbBr_3)_{0.15}$ (α-phase) This explains the observed peaks completely with minor intensity mismatch. A FP instrument profile is used for this pattern.

After the $\alpha \rightarrow \beta$ phase transition, the additional peaks of the β phase are accounted for by literature $Pm\bar{3}m$ α structure, Figure 6.4. The additional peaks are considered as the effect of symmetry breaking from the $Pm\bar{3}m$ space group [Glazer, 1972, Weller et al., 2015b, Weber et al., 2018].

Literature structures from Table 6.1, with lower symmetry space groups were assessed to explain the additional peaks in the β phase. $FAPbI_3$ is the closest single cation, single halide composition for the measured sample, making its well studied structures a valuable comparison. The trigonal $P3m1$ $FAPbI_3$ structure is considered in Figure 6.4b, where it provides an unwanted peak near 11.8° 2θ and leaving a series of 3 peaks unindexed peaks in the 22 to 28° 2θ range. The $P3$ $FAPbI_3$ structure is considered in Figure 6.4c, where it accounts for all the peaks in the measured patterns with underestimated peak intensities near 14.2 and 24.7° 2θ. This simulated structure provides additional peaks near 10.0 and 17.4° 2θ making it unsuitable for refinement of the $(FAPbI_3)_{0.85}(MAPbBr_3)_{0.15}$ data. The $P4/mbm$ $FAPbI_3$, β phase was compared against the 150 K data in Figure 6.5. Many of the simulated reflections do not overlap with peaks in the collected data. It is noted that the (001) reflection is near an observed peak at approx. 14° 2θ. In contrast the (110) peak is far from an observed peak, and would require a and b lattice parameters of nearly 8 % larger to meet the (001) peak at the observed peak.

The β phase of MA based hybrid-perovskites have been reported in literature as in the $I4/mcm$ symmetry for both Br and I halide variants. With the Br/I site occupancy ratio of $(FAPbI_3)_{0.85}(MAPbBr_3)_{0.15}$ accounted for, the structure provided a poor match, App. B.1. The literature structures of both β ($I4/mcm$) and γ ($Pmna$) phases of $MAPbI_3$ provides a unsatisfactory

relative peak intensities with additional peaks near 23 and 26° 2θ respectively as discussed in App. B.1 [Weller et al., 2015b, Weber et al., 2018] [8].

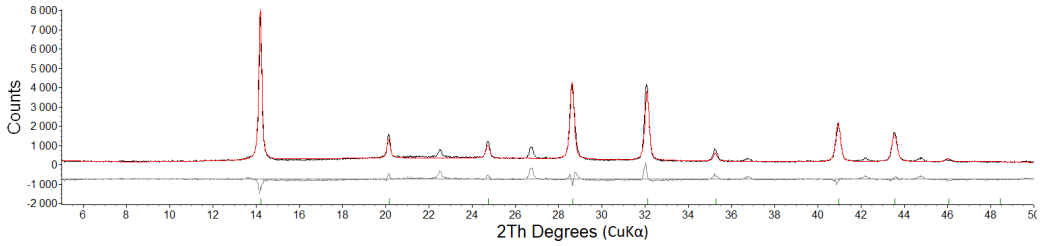

(a) 22-150K, $Pm\bar{3}m$ $(FAPbI_3)_{0.85}(MAPbBr_3)_{0.15}$ (α-phase) This does not explain the full pattern. The intensities are explained reasonably with room for improvement

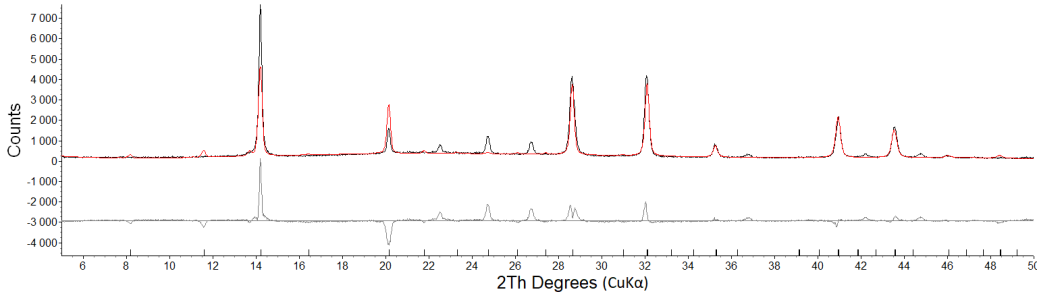

(b) 22-150K, Trigonal, $P3m1$ $FAPbI_3$ (β-phase) This does not explain the full pattern. The intensities are not well explained

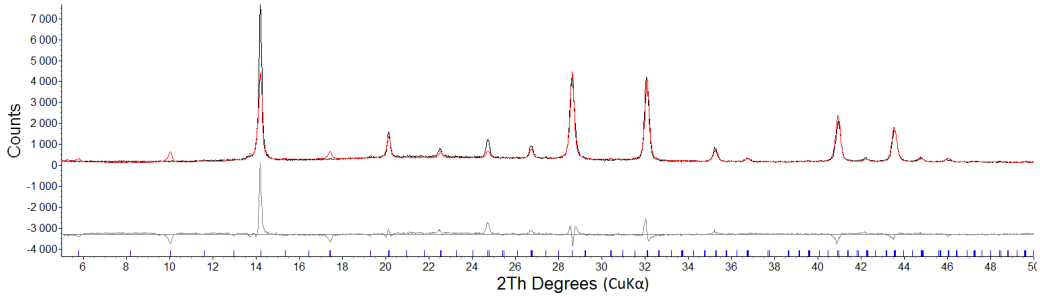

(c) 22-150K, Trigonal, $P3$ $FAPbI_3$ (β-phase) This pattern covers all the present peaks, but also includes peaks not present in the data. The intensities are explained reasonably with room for improvement.

Figure 6.4: Investigative structure fits on the pattern 14-150K.

[8] The β phase of $MAPbBr_3$ also occurs in the $I4/mcm$ space group [Chen et al., 2018].

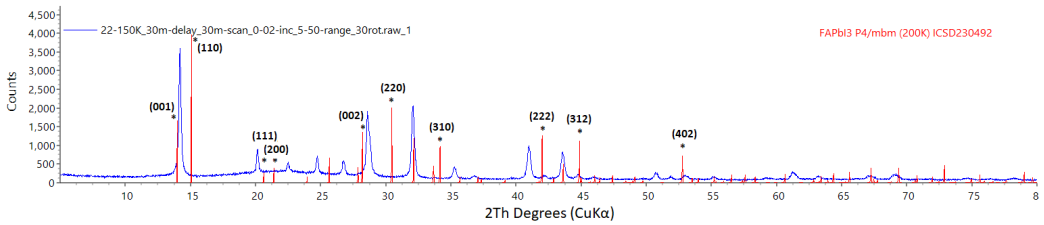

Figure 6.5: Pattern fingerprinting comparison, 22-150K is overlaid with the peak positions and intensities of $P4/mbm$ $FAPbI_3$ (β phase) with a halide occupancy of $I_{0.85}Br_{0.15}$ modelled [Weber et al., 2018].

6.5 Investigative Le Bail refinements

Since the structures tested for the sub-ambient scans did not provide satisfactory fits, pattern indexing and structure agnostic Le Bail refinements were pursued. A collection of space group and lattice parameter sets were generated through indexing, Section 3.7. These were tested against the data using Le Bail fits to provide insights into the most likely structures, space groups and/or structure parameters.

Le Bail refinements are not subject to the constraints on relative peak intensities which are present in structure based refinements. This makes them invaluable for structures which are not accurately known. The Pawley and Le Bail methods are discussed in Section 3.8.2

6.5.1 Methodology

The individual peaks of the patterns collected at 315, 150, and 100 K were fitted with using a *peaks* phase in TOPAS and where the individual peak positions and intensities were refined. These resulting peak positions and intensities were used as an input for diffraction pattern indexing in TOPAS, to generate a list of space-group, lattice parameter combinations. Selected entries were then refined against the data using the Le Bail method, as a means to better evaluate each combinations ability to account for peaks in the measured data. While indexing allows for an offset in peak positions between the simulated and experimental, Le Bail refinements provide a strictly defined

relationship between peak positions of a given simulated phase. If any peak is not well positioned or explained in a Le Bail refinement for a given set of unit cell parameters then either the peak is not part of the phase in question or the candidate combination is incorrect.

6.5.2 Results and discussion

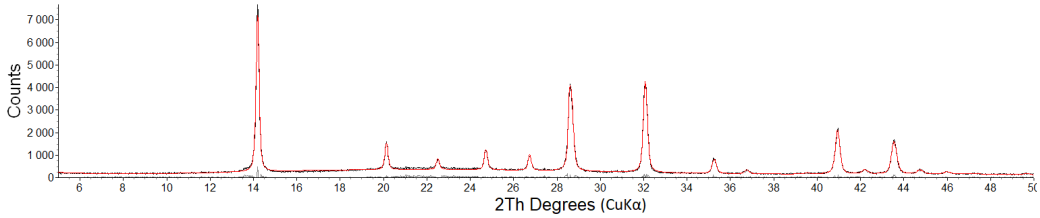

(a) Le Bail refinement on 150 K data, Orthorhombic, $Pba2$ a=8.843/b=8.817/c=6.219, $R_{\text{Bragg}} = 0.231$. The intensities are well explained

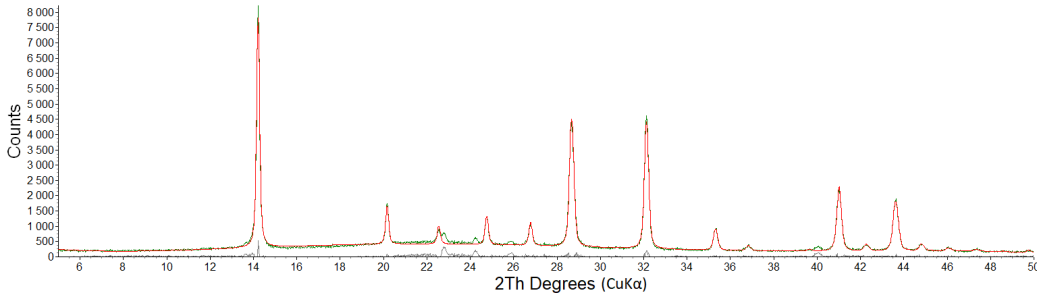

(b) Le Bail refinement on 100 K data, Orthorhombic, $Pba2$ a=8.789/b=8.806/c=6.199, $R_{\text{Bragg}} = 0.267$. The intensities are well explained, 4 weak peaks were not accounted for by the Le Bail fit.

Figure 6.6: Refinements using Le Bail structure agnostic fits on Data set 2018-09

As established in the previous section, $Pm\bar{3}m$ is able to account for the 315 K pattern (α-phase). The lower temperature patterns collected at 150 and 100 K were best described by the $Pba2$ and $P4/mbm$ based phases, Figure 6.6. The results of additional Le Bail refinements provided in Table 6.2.

Table 6.2: Le Bail refinements on $(FAPbI_3)_{0.85}(MAPbBr_3)_{0.15}$ (Data set 2018-09)

Data file	R Bragg	Crystal system	Space group	Lattice parameters a/b/c	Missing peaks/ Extra peaks
1-315K	0.432	Cubic	Pm-3m	6.285/-/-	0/0
1-315K	0.452	Trigonal	P3	8.926/-/10.894	0/0
1-315K	1.262	Trigonal	P3m1	8.881/-/10.951	0/0
1-315K	0.378	Trigonal	R3	8.913/-/10.951	0/0
1-315K	0.537	Orthorhombic	Pba2	6.456/6.177/8.085	4/1
1-315K	0.685	*Tetragonal	Pba2	8.899/8.899/6.290	0/0
1-315K	0.478	Tetragonal	P4cc	4.451/-/12.561	0/0
1-315K	0.717	Cubic	P23	6.488/-/-	0/0
14-150K	0.294	Orthorhombic	Pna21	8.845/8.807/12.438	0/0
14-150K	0.556	Orthorhombic	Pcca	11.754/7.944/12.473	2/3
14-150K	0.231	Orthorhombic	Pba2	8.843/8.817/6.219	0/0
14-150K	0.643	Trigonal	P3	8.816/-/10.774	5/0
14-150K	0.540	Cubic	Pm-3m	6.228/-/-	5/0
14-150K	0.474	Tetragonal	P4cc	4.405/-/12.437	5/0
16-100K	0.313	Tetragonal	P4cc	4.395/-/12.413	9/0
16-100K	0.267	Orthorhombic	Pba2	8.789/8.806/6.199	4/0
16-100K	0.521	Trigonal	P3	8.798/-/10.758	8/0

** Here the orthorhombic phase is representing a tetragonal phase as a = b*

Greyed out rows are considered exceptionally poor fits.

The unit cell parameters from the $Pba2$ and $P4/mbm$ refinements are of suitable size for a hybrid-perovskite unit cell containing 2 octahedra across

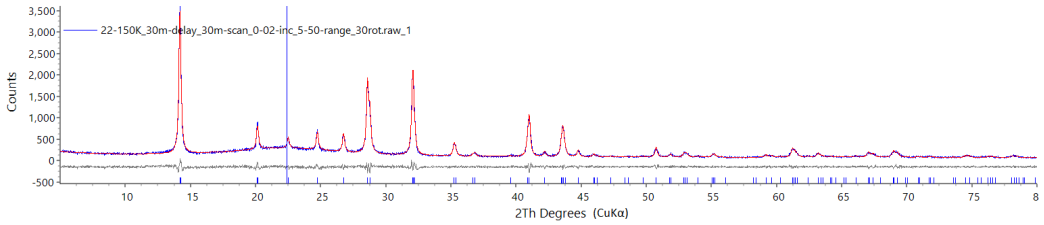

Figure 6.7: Le Bail refinement on 22-150K data, Tetragonal, $P4/mbm$ $a = b$ =8.821/c =6.199, $R_{\text{Bragg}} = 0.421$. The intensities are well explained. (Data set 2018-10)

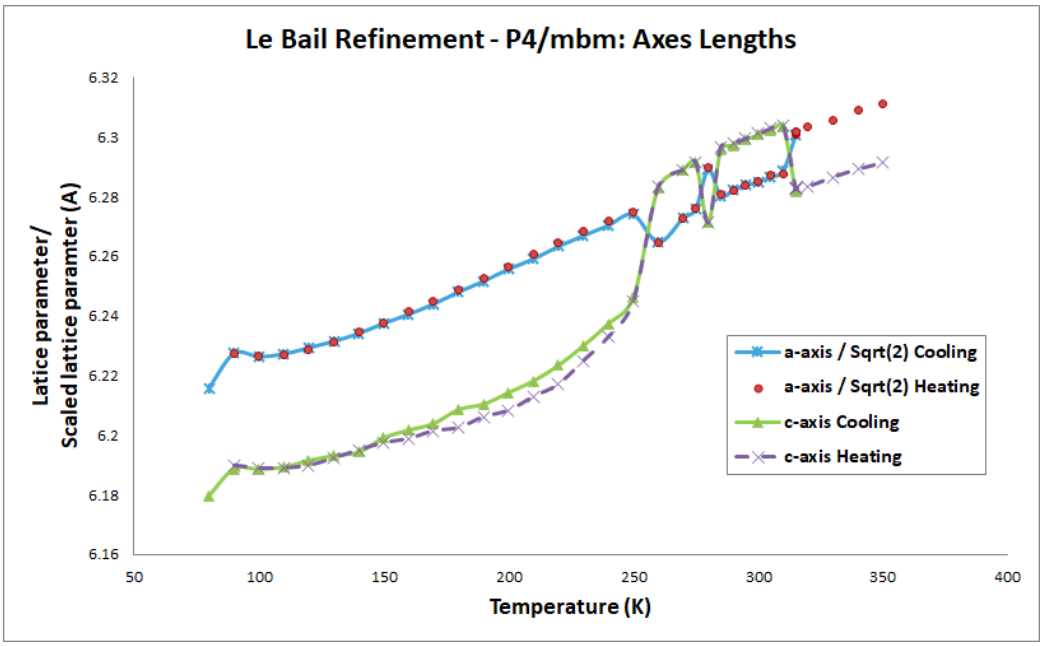

Figure 6.8: Lattice parameters from Le Bail fits using a $P4/mbm$ space group. (Data set 2018-10)

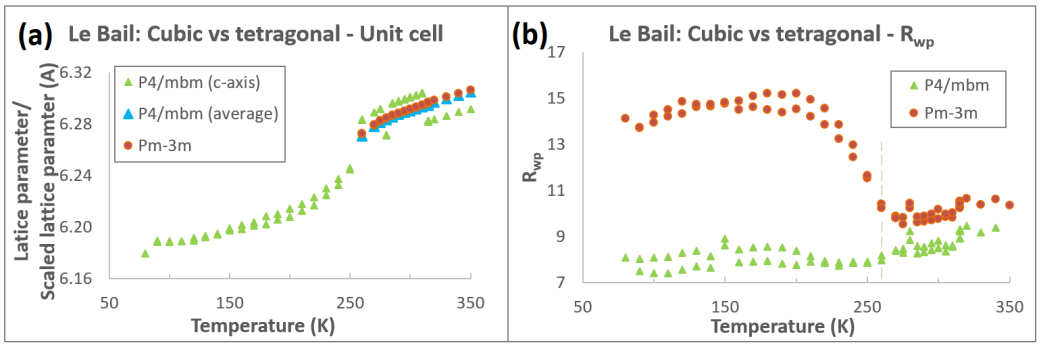

Figure 6.9: Le Bail refinements using a cubic $Pm\bar{3}m$ phase with a tetragonal $P4/mbm$ phase for comparison. A grey dashed vertical line is used to mark 260 K. (a) Unit cell parameter where $P4/mbm$ (average) is defined by $\frac{\frac{a}{\sqrt{2}}+\frac{b}{\sqrt{2}}+c}{3}$, (b) R_{wp} agreement factor (Data set 2018-10).

the [110] direction. $P4/mbm$ is a higher symmetry than $Pba2$, and includes all the symmetry operations of $Pba2$. The use of $P4/mbm$ is a favoured over $Pba2$, since it has a higher symmetry and provides a virtually equivalent fit of the data [9].

The P4/mbm based structure agnostic refinement was applied to the full data set with the resulting lattice parameters plotted in Figure 6.8. Below 260 K the refinements provide a steady trend with a sudden drop for the 80 K scan. For T $\geq$ 260 K $a/\sqrt{2}$ and c are more similar, and are strongly correlated, sharing a common yet inverted pattern across the 2 parameter sets. This is evident in the correlation tables of App. C.17, where a strong inverse correlation is observed between the a and c lattice parameters at 315 K, while minimal correlation is observed at 80 K. This is suggestive of potentially equal lattice parameters, as would be found in a cubic phase. This relationship between the a and c lattice parameters is consistent with the indications of peak splitting on the low temperature side of the $\alpha \rightarrow \beta$ transition observed in Section 6.3, and $Pm\bar{3}m$ structural refinement in Section 6.4, Figure 6.3. The drop in the lattice parameters from 90 to 80 K is similarly observed with the discussion around the normalised peak positions in Figure 6.2.

Le Bail refinements of a cubic $Pm\bar{3}m$ α phase and were performed across the data set, Figure 6.9. Theses were examined and compared to the $P4/mbm$ set alongside the associated pseudocubic averages of the $P4/mbm$ based refinement lattice parameters for T $\geq$ 260 K, pseudocubic average lattice parameters for each $P4/mbm$ refinement were determined as per Equation 6.1, Figure 6.9. [10] At T $\geq$ 260K, the $Pm\bar{3}m$ lattice parameter and the $P4/mbm$ derived pseudocubic values are almost overlapping with the $P4/mbm$ phase.We see these values fall neatly between the data points of the $P4/mbm$ c-axis in Figure 6.9a. For the $Pm\bar{3}m$ cubic phase, the R_{wp} values show the best fits where we expect the α phase, at T $\geq$ 260 K (grey dashed line). From 260 K these R_{wp} values are slightly worse than the tetragonal $P4/mbm$ Le Bail refinements. The difference is significant enough that there is a defi-

[9] Both space groups are mentioned since earlier work was done around the $Pba2$ space group.

[10] Cubic and "pseudo-cubic" lattice parameters are not shown for lower temperatures in Figure 6.9a. This is due to the poor fit quality of the $Pm\bar{3}m$ phase as evident from the high R_{wp} values in Figure 6.9b.

nite benefit to fit quality using a tetragonal unit cell. Figures 6.8 and 6.9 show how the lattice parameter for the cubic phase follows a stable trend through the approx. centre between the a and c lattice parameters of the tetragonal phase. In the absence of suitable constraints capable of mitigating the correlation between the a and c unit cell parameters, the use of a cubic phase offers benefits over the tetragonal for its lattice parameter stability. The tetragonal phase provides a significant improvement in the fit quality (Figure 6.9b) where the α phase is expected.

$$\text{Pseudocubic average unit cell} = \left(\frac{a}{\sqrt{2}} + \frac{b}{\sqrt{2}} + c \right) /3 \tag{6.1}$$

These Le Bail refinements serve as reference for parameters refined in the later section of structure based sequential refinements, Section 6.7. The $Pm\bar{3}m$ Le Bail refinements provide fits that are suitable as a guideline on the expected parameters for T $\geq$ 260 K while the $P4/mbm$ refinements provide suitable reference parameters for T $<$ 260 K. The better fit figure of merit for the tetragonal phase demonstrates the value of a tetragonal model for this data set.

6.6 Structure modelling

In this section, a selection of octahedra-based structures were considered and refined, primarily against the 315 and 80 K diffraction patterns, these show the least and most observed peaks in the material respectively. Refinements against 280 and 150 K diffraction patterns provide minimal additional insight and are thus confined to the Appendix, Section C.4.

6.6.1 Methodology

These structure-based refinements make use of a Fundamental Parameter method described in Section 4.7.1. A split halide site, and appropriate occupancies account for the presence of 85 % I and 15 % Br in the sample. The organic cation was either defined by a rigid body of FA or by a representative atom with a similar electron count to the FA/MA composition as specified in the results. To optimise fit quality, fits were executed in TOPAS using a combination approach of least-square refinement and guided Monte-Carlo randomisation. [Coelho, 2018]

Octahedra based hybrid-perovskite structures with variation on their constraints were designed, refined against the data and compared. The structure tested with the most freedoms (Set A) made use of 4 rigid body octahedra defined in a $P1$ space group, allowing rotations to form any of the perovskite tilt systems identified in literature and discussed in Section 1.5.1 on Glazer notation. [Glazer, 1972].

A more restrictive, smaller unit cell was evaluated which consisted of a 2 octahedra tetragonal unit cell categorised as $a^0b^0c^+$ (Glazer notation) which means symmetric rotation of the octahedra about the c-axis. The octahedra Set C's unit cell were kept symmetric, with elongation allowed along the c-axis, while in Set D, a degree of distortion was permitted. The rigid bodies models for this section, and the projections for unit cell parameters are described in Section 4.9.3 [11].

[11] The sets of this section are presented in a non-alphabetic order due to a preference of the order in which the models were to be explained, rather than any desire to spell out the acronym for computer aided design.

Set C: $P4$ space group

A 2 Oh unit cell was defined to include the 4 fold rotational symmetry of the $P4$ space group. The approximate dimensions used were $a = b \sim 8.9$ Å and $c \sim 6.3$ Å. The organic cation was represented by a single atom with an equivalent electron count to the average of the FA/MA composition in the sample, this was realised by use of site occupancy. The occupancy and thermal parameter for this representative Mn atom were refined. The positioning and refinement of atomic positions was as follows:

- The Pb atom and organic cation positions were fixed at (0, 0, 0) and (0, 0.5, 0.5) respectively.
- Halide atoms (X) on the a-b plane were defined by (x, y, 0). The position for a structure without rotation is (0.25, 0.25, 0). Rotation with the halide equidistant to both Pb atoms is described by (0.25+δ, 0.25-δ, 0). Both x and y were constrained to between the fractional coordinates 0.15 and 0.35. The limits restrict the rotation to within reasonable values [12]. The additional atoms to form the octahedra were generated by the $P4$ symmetry of the unit cell.
- The X atom between Pb atoms along the c-axis was defined by (0, 0, z) where z was refined.

Set A: 4 Octahedra with free rotation; lattice parameters determined by projections of Pb-X bonds.

The use of a 4 octahedra (Oh) unit cell allows for all symmetric and asymmetric rotation of Oh about each of the 3 rotational degrees of freedom. [13]. The unit cell axes were defined by projections of the Pb−X bonds. The organic cation was defined as a rigid body and fixed to the centre between the

[12] In the case where the halide is in the position (0.25,0.25,0) of the $P4$ symmetry unit cell, each of the halides generated by the rotational symmetry will be directly centred between the Pb atoms. If this halide is shifted to a position (0.25+δ,0.25-δ,0), the halide atoms generated by symmetry will shift, rotating the octahedra. If this position deviates an alternative to (x,y,0), there will be alternating expansion and contraction of adjacent octahedra, such a distortion will only occur if favourable in the refinements.

[13] see Section 1.5.1, [Glazer, 1972] and [Howard and Stokes, 1998] for more information of Oh rotation in the perovskite structure type

Pb atoms, its occupancy was refined. This modelling approach is discussed further in Section 4.9.3.

Set D: 2 Octahedra with free rotation; lattice parameters $a = b\ c$ free.

The use of a unit cell composed of 2 $PbX_6{}^{4-}$ octahedra (Oh) centred at (0,0,0) and (0.5,0.5,0) allows for symmetric rotation about the c-axis of Oh ($a^0b^0c^+$), Figure 6.12a and 6.12b. The rigid body model used for Oh in this set is described in the "Methods" Chapter, Section 4.9.3. Unlike in Set A all rotation or tilt is refined about the a and b axes of the octahedra which manifests as distortion of the structure. The organic cation was defined at as a rigid body and constrained to allow rotation and minimal translation within its lattice site. The organic cation's occupancy was refined.

6.6.2 Results and discussion

The investigative Le Bail refinements of Section 6.5 provided insights regarding a probable unit cell size, and symmetry which may be present at the various temperatures across the data set. The unit cell parameters of Set C and Set D were similar to that extracted from the Le Bail refinements, while Set A was appropriately twice the size in the c-direction. Considering the $P4/mbm$ space groups from the Le Bail refinements, with the exception of the organic cation, Set C shares the same symmetry elements. A special case occurs for the halide position of (0.25,0.25,0) where the octahedra framework has the symmetry elements of the $Pm\bar{3}m$ space group. Set A and Set D break symmetry from the constraints of Set C potentially allowing a greater ability to account for the relative peak intensities of the structure.

Visual observation are employed alongside the consideration of the figure of merit, R_{wp} to compare the different structure descriptions used. These focus on the 315 and 80 K patterns, representing the patterns in the data-set with the fewest and the most peaks respectively.

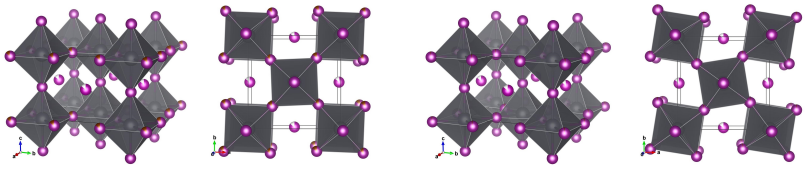

(a) Cs0-setC-315K (b) Cs0-setC-80K

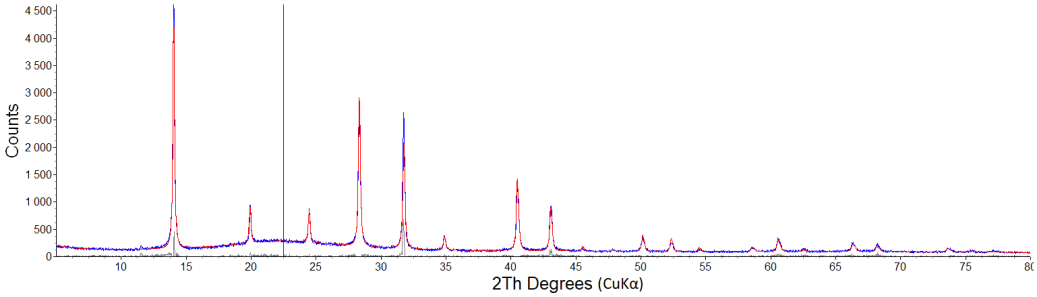

(c) Cs0-setC-315K

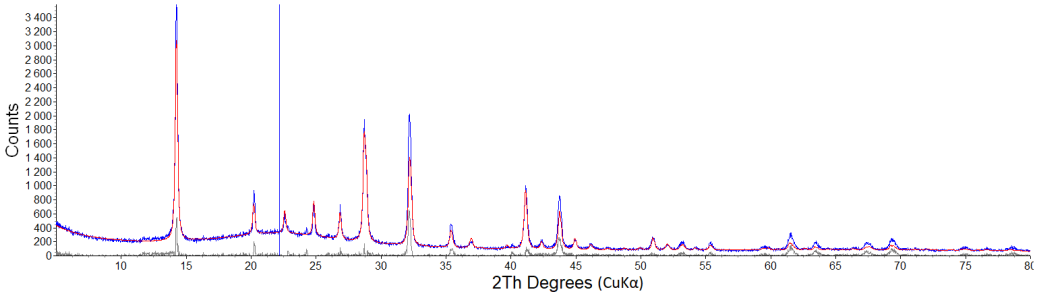

(d) Cs0-setC-80K

Figure 6.10: Set C (Cs0-setC): Rietveld refinements using a $P4$ space group to impart it's symmetry to the Pb-X octahedra. The vertical lines correspond to an amorphous contribution modelled in the refinements.

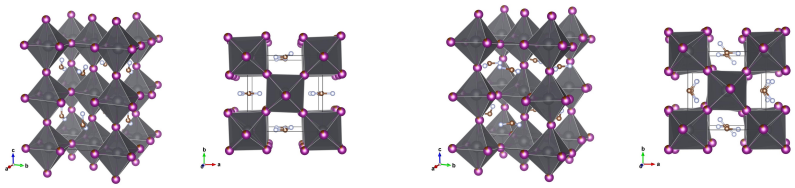

(a) Cs0-setA-315K

(b) Cs0-setA-80K

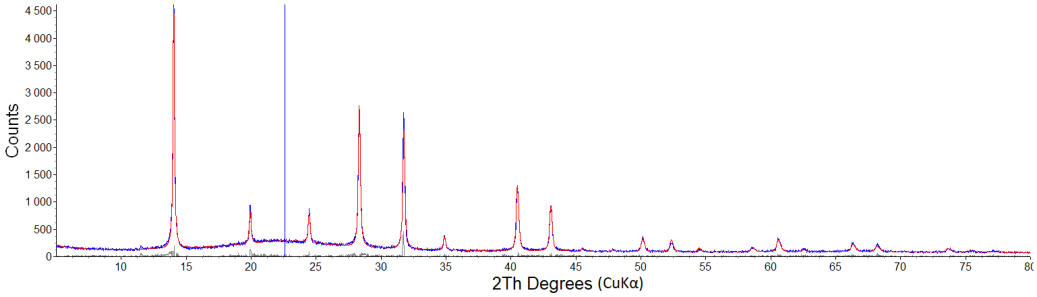

(c) Cs0-setA-315K

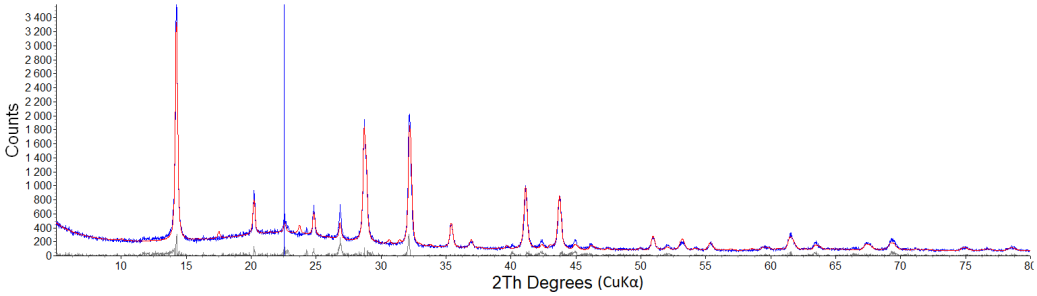

(d) Cs0-setA-80K

Figure 6.11: Set A (Cs0-setA): Rietveld refinements using a structure model with 4 octahedra with free rotation and lattice parameters determined by projections of Pb−X bonds. The vertical lines correspond to an amorphous contribution modelled in the refinements.

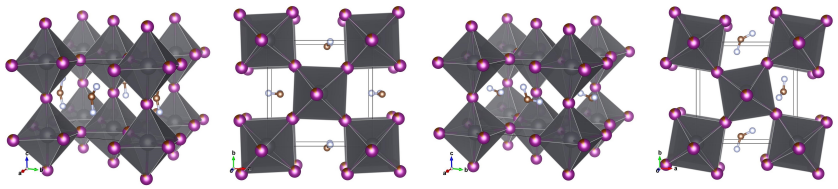

(a) Cs0-setD-315K (b) Cs0-setD-80K

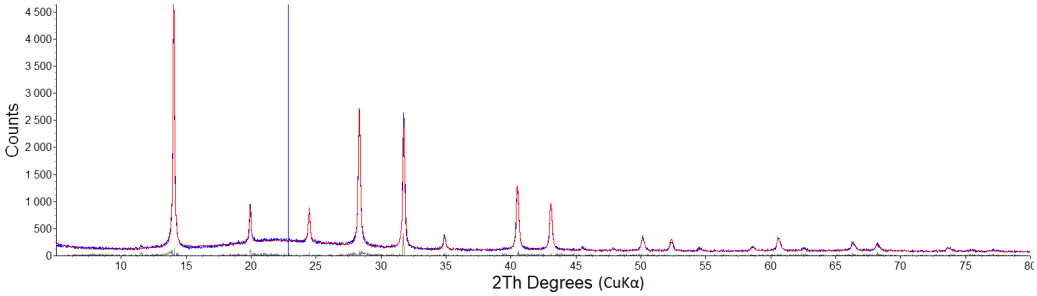

(c) Cs0-setD-315K

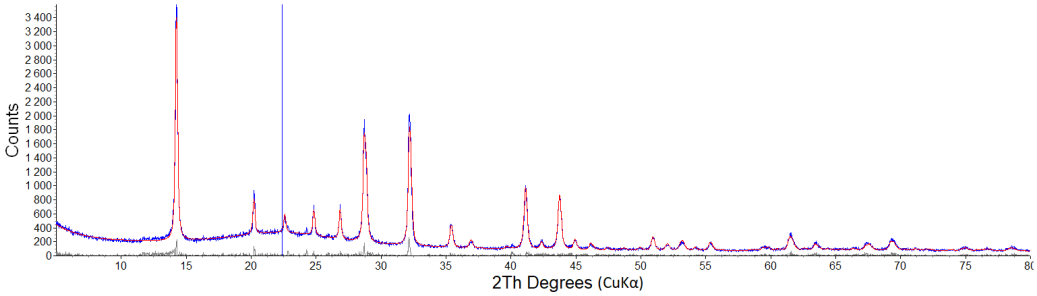

(d) Cs0-setD-80K

Figure 6.12: Set D (Cs0-setD): Rietveld refinements using a structure model with 2 octahedra with free rotation and lattice parameters constraints a=b, c is free. The vertical lines correspond to an amorphous contribution modelled in the refinements.

Table 6.3: Summary of fit parameters

Set	R_{wp}**(80 K)**	R_{wp}**(315 K)**	**Location**	Model basis
Set C	13.01	10.96	Figure 6.10	$P4$ symmetry
Set A	10.90	9.94	Figure 6.11	4 Octahedra
Set D	8.74	10.23	Figure 6.12	2 Octahedra

Note: R_{exp} is 6.87 and 7.33 for 80 and 315 K respectively.

Considering R_{wp} across the sets (Table 6.3, Set D as providing the best fit at 80K with an R_{wp} 20 % lower than the next best fit, Set A. In the case of the 315 K pattern Set A offer a slightly better R_{wp} with Set D having a value 3 % larger. For both patterns Set C offered the highest R_{wp} values.

Between the sets, the most constricted structure was considered in Set C, where Oh were defined using a $P4$ unit cell (Figure 6.10), this allowed a symmetric rotation of the Oh about the c-axis ($a^0b^0c^+$). The absence of freedom for the structure to distort evidently provided a reduced fit quality, seen by insufficient intensity modelled for the peak near 32.4° 2θ (CuKα). This is reflected in with Set C having the highest R_{wp} values of the variation in this section.

Set D, used rigid body model based fits with a 2 octahedra (Oh) unit cell provided reasonable fits at both low and high temperatures (Figure 6.12). Any rotation of the Oh about the a or b-axis translates into distortion of the octahedra in a 2 Oh unit cell. Set A allowed this rotation without causing distortion of the octahedra by using a 4 Oh unit cell which is capable of the full range of the rotations in perovskite structures identified by Glazer [Glazer, 1972]. The 4 Oh rigid body model used in Set A provided a no clear benefit to the 2 Oh model of Set D, and resulted a lower fit quality for the 80 K pattern which is most prominent in the in the 22 to 28° 2θ range, this is reflected in Table 6.3 with a much smaller R_{wp} value for Set D, 80 K, Figure 6.11. This is attributed to the absence of distortion in the octahedra of Set A, and a greater chance of reaching a local minima in Set D considering the higher dimensionality of the solution space of Set A. This suggests a 2 Oh unit cell of Set D is sufficient to describe the structure, leaving a $a^0b^0c^+$ or distorted $a^0b^0c^+$ structures as the most probable.

An undistorted $a^0b^0c^+$ corresponds to a $P4/mbm$ space group [Howard and Stokes, 1998]. Hybrid perovskites within this tilt system include the β phase of $FAPbI_3$ and $CsPbI_3$ as well as the γ phase of $FAPbI_3$ which is closely related to the data set under investigation, $(FAPbI_3)_{0.85}(MAPbBr_3)_{0.15}$. [14].

Structure modelling of individual scans in the this section served to identify flexible structure models, suitable for application across the full temperature range. This includes the $\alpha \rightarrow \beta$ phase transition as the most prominent transition identified in Section 6.3. These refinements provide a starting point for the application of sequential refinements executed in Section 6.7. The models are then further investigated in Section 6.7, where more detailed comparisons and finer tuned considerations have been made, afforded by considering the full data set through the use of sequential refinements.

[14]These literature structures with their space groups and Glazer notation is provided in Table 1.1)

6.7 Sequential refinements

The use of Rietveld refinements across a full dataset can provide far more information compared to the individual refinements. The use of sequential refinement is one such method used to model larger datasets as discussed in Section 3.10.1 with the implementation outlined in Section 4.9.1.

In the current section, each set of sequential refinements uses a single model to describe the full temperature range. Variations on the model were refined against the data and compared. This facilitated evaluating the influence that different parameters have on the refinement and structure fits across the temperature range. Analysis using the full data-set provided a larger information base to draw comparisons from. Additionally, this reduces the impact of statistical noise from the sub optimal counting statistics typical in lab based *in-situ* data collection.

6.7.1 Methodology

Bi-directional refinement approach, Refinement sets 1, 8 and 8b made use of a bi-directional sequential refinement approach. This consisted of two sets of sequential refinements which were performed from opposite ends of the data-set collected in the VT-XRD run [15]. For each pattern, the refinement with a lower R_{Bragg} was selected using logic statements in Microsoft Excel. This serves to reduce directional effects in the data processing, especially the effects of any sudden changes in the data such as around phase transitions. [16] [17]

Set 1 and 8 were run from the same initial input file with slightly different boundary conditions. While in Set 8b, an additional constraint on rotation of octahedra about the c-axis was imposed. One octahedra is limited to clockwise rotation and the second, anti-clockwise. The additional constraint brings the system closer to symmetric $a^0b^0c^+$ rotation.

[15] The dataset consists of patterns collected during heating followed by patterns during cooling as described in Section 6.2.

[16] R_{Bragg} and other statistical agreement factors are discussed in Section 3.4

[17] The bi-direction approach is briefly discussed in Section 3.10.1

Monte-Carlo assisted refinement approach, Refinement sets 9 to 26 make use of a combination approach of least-square refinement with a guided Monte-Carlo randomisation (Monte-Carlo assisted) [18]. This approach was utilised to better allow the refinement to overcome local minima which would otherwise contribute to inaccuracy in the refinements. Such local minima may impede the refinement from effectively tracking changes between sequential diffraction scans. The refinements were first run sequentially using the *randomize_on_errors* function in TOPAS. The resulting TOPAS output files were edited using a Python script to be reprocessed in TOPAS using a least-squares method (without randomisation). This resulted in improved fits as indicated by lower R_{wp} values. Additional details for the individual sets are presented in Appendix C.

Halide rigid body model, Refinement sets 9 to 15 make use of a rigid body model describing the halide positions as introduced in Section 4.9.3. The rigid body model is centred either at a Pb atom or at a place holder atom. Using a place holder allows the refinement of the Pb position independently of the rigid body's centre.

Halide P4 symmetry based model, Refinement Sets 17 to 26 use a $P4$ symmetry based model to define the position of the halide atoms on the ab plane. The symmetry centres are at the centres of the octahedra [19] with the rotation axis in the c-direction. The halides that falls between Pb atoms along the c-direction are refined independently for Sets 17 to 19 while these halide atoms fixed at (0,0,0.5) and (0.5,0.5,0.5), centred between the "ideal" positions for the Pb atoms in Sets 20 to 26.

[18] The Monte-Carlo method randomises based on calculated errors in the refined parameter as designed Alan Coelho in TOPAS [Coelho, 2018]

[19] The octahedra centres are at (0,0,0) and (0.5,0.5,0), this is considered the "ideal" position for the Pb atoms.

Table 6.4: A summary of conditions used across refinement sets 9 to 26.

Property\Set	9	10	11	11f	12	18	19	20	23	26
Lattice parameter										
constraint on a, b	a=b	a=b	a=b	a=b	a=b	free	a=b	a=b	a=b	a=b
c by bond projection	yes									
Pb position refined										
not refined	fixed	fixed	fixed	fixed	fixed					
refined, sites independent						yes	yes	yes		
refined in P4 symmetry									yes	yes
Octahedra(Oh) type										
Rigid body	yes	yes	yes	yes	yes					
P4 symmetry in ab plane						yes	yes	yes	yes	yes
Remaining halide refined*4						yes	yes	no	no	no
Octahedra(Oh) centre refined	yes	yes	yes	yes	yes					
x limits	-0.05/+0.1				±0.05					
y limits	±0.1	Set9	Set9	Set9	±0.02					
z limits	-0.02/+0.05				0					
Independent Pb-X bond lengths	3	1	0	0	0	3	1	1	1	1
Bond length fixed to Set average			Set10	Set10	Set10					
Independent Oh rotation parameters	6	6	6	6	6	1	1	1	1	1
Rotation about a, b	±12°	±12°	±12°	±12°	±12°	0	0	0	0	0
Rotation about c (Oh3)	±12°	-12°	-12°	--17/+3	-12°	*1	*1	*1	*2	*2
Rotation about c (Oh6)	±12°	+12°	+12°	Oh3/+17	+12°	*1	*1	*1	*2	*2
Organic cation										
Rigid body	yes	yes	yes	yes	yes	yes	yes	yes	yes	
Representative atom										yes
Agreement factor										
Rwp mean value	9.27	9.27	9.26	9.36	9.00	8.97	8.99	9.11	9.12	9.40
Rwp standard deviation	0.54	0.49	0.53	0.48	0.66	0.64	0.69	0.66	0.60	0.48

**1: Defined by fractional co-ordinate parameter p1, min -0.05 max 0.15*
**2: Defined by fractional co-ordinate parameter p1, min -0.0001 max 0.15*
**3: Fixed to values from Le Bail fits using a Pba2 space group*
**4: The refined halide is between Pb atoms along the c-axis direction*
Note: Where parameter p1 is used, Oh rotation = f(p1) and bond length = f(p1,a,b,c)

6.7.2 Discussion

Modelling approaches

The bi-directional approach used in Sets 1 and 8 was intended to reduce the impact of sudden changes in the data, which can be poorly tracked by sequential refinements. Comparisons of the *c*-axis lattice parameter between Sets 1 and 8 show significant differences in the hysteresis between the heating

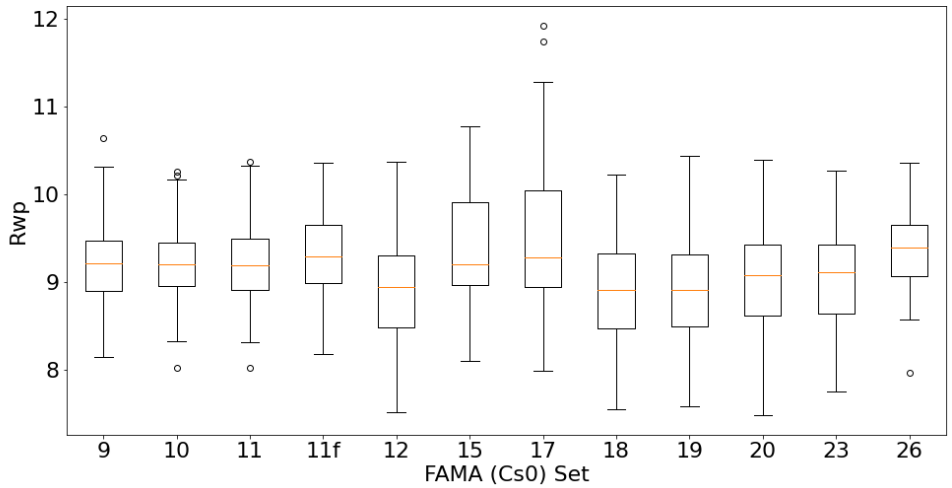

Figure 6.13: R_{wp} of Monte-Carlo assisted sequential refinements. The horizontal lines represent the boundaries of the 4 quartiles of R_{wp} values. The median value is represented by a red horizontal line. Open circles represent outliers.

and cooling traces. (Figure 6.14) [20] Set 1 and 8 were expected to have near identical results with the refinements of Set 8b subject to only a slight difference in the rotational constraints of the octahedra. This show a lack of refinement stability with the bi-directional approach as applied to the current dataset [21].

The effect of using the Monte-Carlo assisted approach produced a greater overlap and similarity between the heating and cooling traces of the c lattice parameter, as seen in Set 23, Figure 6.14d. The comparison between the c lattice parameter for Set 23 and the $P4/mbm$ Le Bail refinement in Figure 6.15 shows that the traces follow a similar trend with a near linear slope at T $\geq$ 260 K and a sudden drop in the lattice parameter between 250 and 260 K. Neither of these sets show the same degree of hysteresis apparent in Set 1 and 8. [22]

[20] Set details are given in Appendix Section C.5.

[21] For additional plots see the Appendix Figures C.6, C.7, C.8 and C.15 for Sets 1, 8, 8b and 23 respectively. Set 8b is similar to Sets 1 and 8 with the exception of slightly more restrictive limits. Set 8b illustrates that the choice of limits and constraints can greatly reduce the hysteresis effect, still this refinement set does not compare well with the Le Bail refinements in Figure 6.14b.

[22] Additional details for the individual sets are presented in Appendix C.

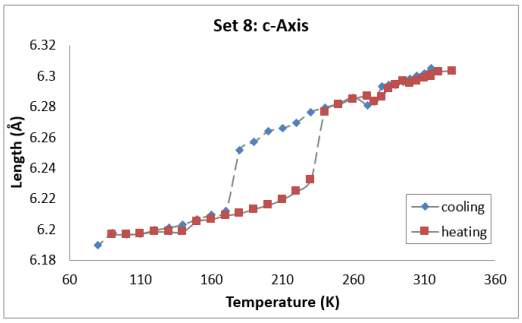

(a) Set 8, rigid-body sequential refinement (repetition of Set 1

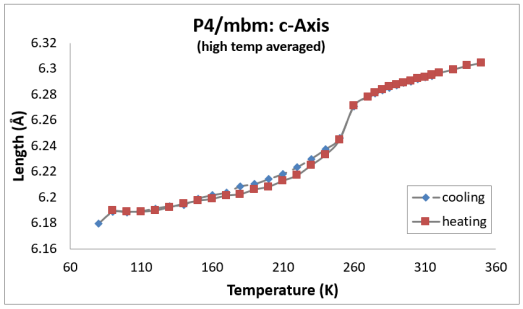

(b) Le Bail P4/mbm, high temp values as per Figure 6.9

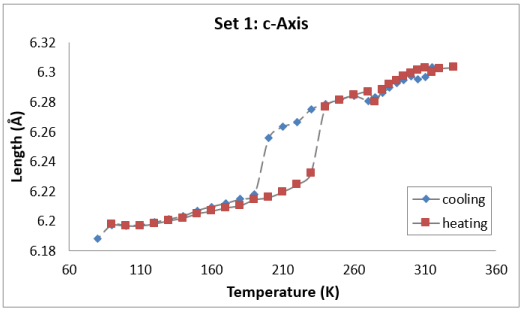

(c) Set 1, simple rigid-body sequential refinement

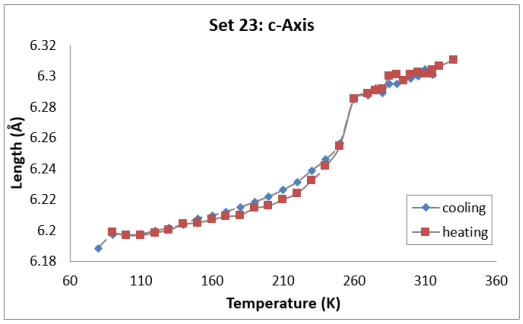

(d) Set 23, Monte-Carlo assisted rigid-body sequential Rietveld refinement

Figure 6.14: Reproducibility of bi-directional sequential refinements in comparison to a Monte-Carlo assisted variation.

The Monte-Carlo assisted approach provided more reproducible refinements compared to the bi-directional refinement approach. The randomisation for the Monte-Carlo resulted in processing time close to 2 hours for the data-set compared to a few minutes required for the bi-directional approach. This is viable for to handle a small number of refinements, such as the single data set focused on in this Chapter for a more scalable refinement method see Section 8 where parametric refinements are discussed.

Lattice parameters

Considering $a \neq b$ in Set 18 compared to Set 19 where $a = b$, with R_{wp} values of 8.97 and 8.99 respectively which is marginal showing not significant benefit gained by allowing the unit cell to assume an orthorhombic shape.

In terms of the $a = b$ lattice parameter, Set 23 shows a reduced a-axis length at T = 260 K, at the $\alpha \rightarrow \beta$ transition. This is consistent with the $P4/mbm$ refinements in Figure 6.15 and observed to a more subtle extent in Set 20 while the same feature is absent from Set 19 (Figure 6.16) [23].

For both the a and c lattice parameters, the trend of Set 23 follows most closely to the Le bail $P4/mbm$ refinement set. The Le Bail refinement values are slightly lower than those of the structure based model. This is likely a consequence of using an analytical function for the $P4/mbm$ refinements while using a refined instrument profile in Sets 19, 20 and 23. The structure-agnostic Le Bail refinements do not possess the same constraints present in structure based refinements, as such the similarity between Set 23 and the $P4/mbm$ Le Bail refinements in indicative of fit quality.

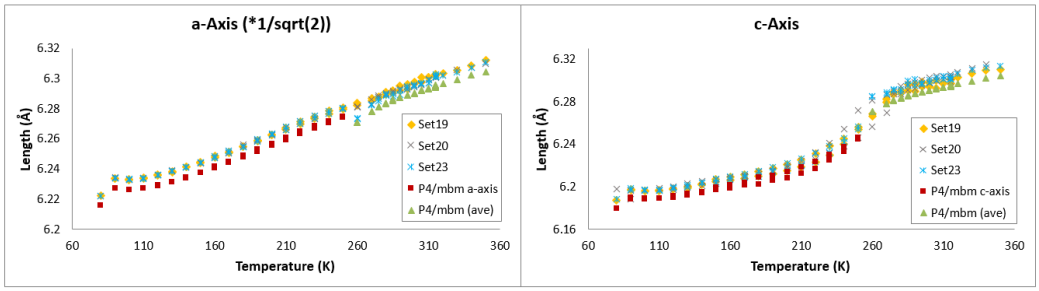

Figure 6.15: A comparison of lattice parameters between the Le Bail $P4/mbm$ refinements and Sets 19, 20 and 23. "$P4/mbm$ ave" refers to an average from the tetragonal unit cell parameters to reach a pseudocubic lattice parameter value.

[23] Figure 6.8 and the related section show and explain the $P4/mbm$ refinements. Figure 6.15 provides an overlay of Sets 19, 20, 23 and the $P4/mbm$ refinements.

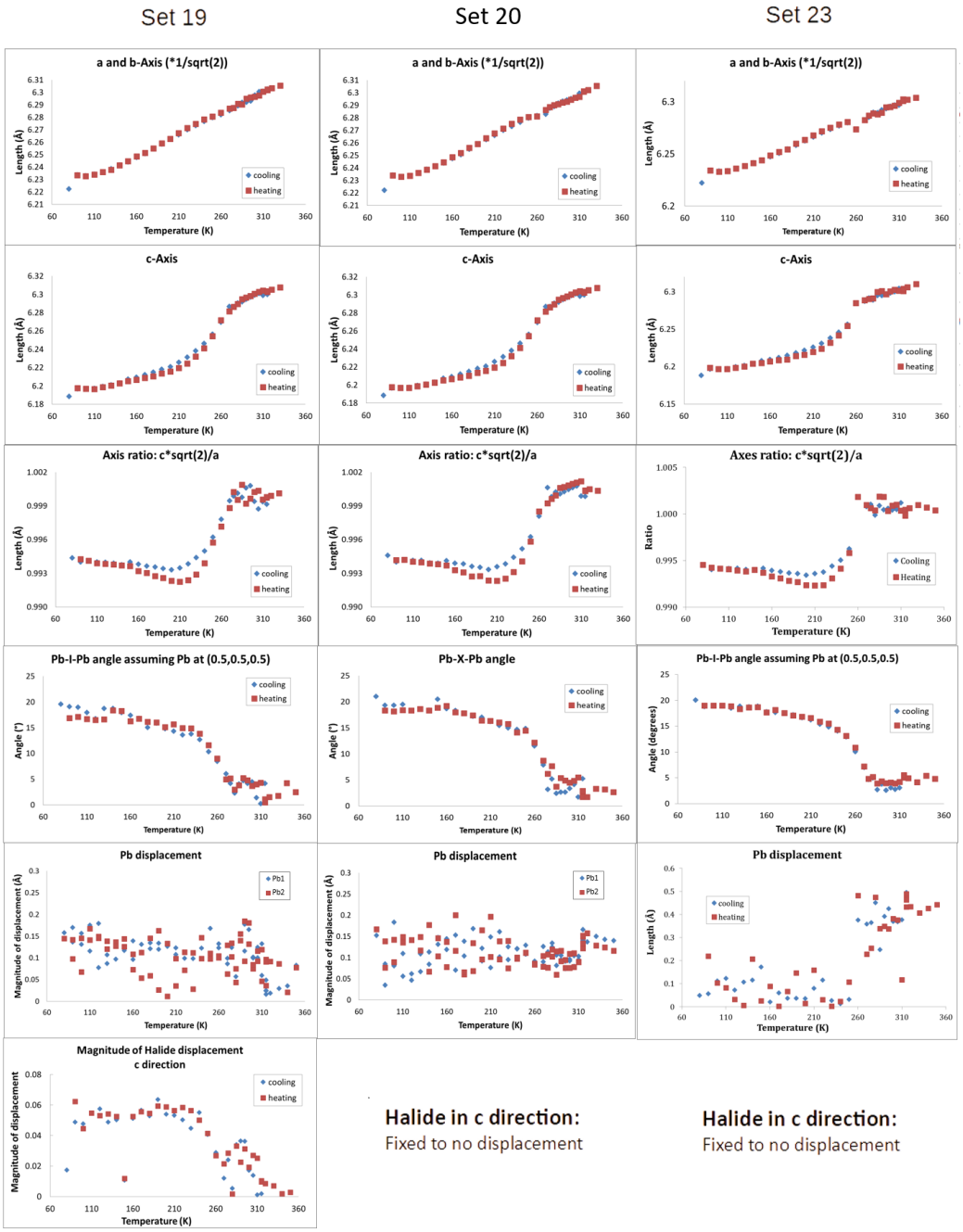

Figure 6.16: A comparison of parameters in Sets 19, 20 and 23.

Pb-X bond length

In the absence of structural change, the true Pb-X bond length in a structure is expected to increase in temperature [24]. The refined Pb-X bond length is inter-dependent on the unit cell size, octahedra rotation, and any distortions of the octahedral shape. The diffraction intensity, from which the refined Pb-X bond length is indirectly extracted, represents an average structure, and in powder diffraction the structure information is condensed into a single dimension. With this in consideration anisotropic vibrations within the structure have the potential to present as an inaccurate reduced bond length as one example of how the real and refined values may differ [Becka and Cruickshank, 1961].

The refined Pb-X bond lengths for Sets 10 and 23 are presented in Figure 6.17. These represent the use of a rigid body model, and $P4$ symmetry respectively for modelling the halide positions. The bond lengths for Set 10 show no clear trend as a function of temperature and vary by as much as $\pm$ 0.4 Å (Figure 6.17). In the absence of structural changes, the bond length is expected to follow a function similar to $r_{bond}(T) = r_0 + \frac{c_1\theta_0}{e^{(\theta_1/T)}-1}$ ([Dinnebier et al., 2018]) with a smaller change over the temperature range by roughly an order of magnitude. Correlation is evident between Pb-X bond length parameter and a series of parameters including Pb-X octahedra tilt and translation parameters as displayed in the correlation tables of App. Figure C.18. With this correlation considered, the refined parameter cannot be taken as an accurate representation of bond length. Subsequent sets attempt to mitigate the effect of an seemingly unstable bond length parameter with two approaches investigated below.

Sets 12 uses a rigid body model with the Pb-X bond length of the rigid bodies fixed to the average bond length determined across Set 10. The model still allows a degree of compensation as the lattice parameters and orientation of the rigid body models are not constrained based on the Pb-X bond length. The reasonable fit quality in terms of R_{wp}, Figure 6.13 indicate that thermally driven Pb-X bond length expansion in the ab plane may be well compensated for by correlated parameters, or possibly overshadowed by other temperature dependent structural changes.

[24] Structural change can be co-incident with changes in bonding angles and orbital overlap impacting bond strength and length, Section 2.2.

Sets 20 and 23 employ a $P4$ symmetry based model (as opposed to a rigid body model) in which the Pb-X bond length was a function of the unit cell parameters and a single position parameter corresponding to the octahedra rotation. This can be calculated by $length = a1\sqrt{(0.25+p1)^2+(0.25-p1)^2}$, where $a1$ is the $a = b$ lattice parameter, and $p1$ describes the change in fractional co-ordinates such that the position of halide I1 is (0.25+$p1$, 0.25-$p1$, 0). This model reduces the number of refined parameters associated with the Pb-X octahedra and its rotation and resulted in a model with far less parameter correlation, Appendix Figure C.17.

The bond length parameter of Set 23, Figure 6.17 falls within the range 3.145 to 3.167 Å. This metric refers to ab plane of the structure and falls within the range Pb-I bond lengths for the equivalent bonds found in literature, including values between 3.13 and 3.20 Å [25]. Lower values for such as 2.98 Å, (*COD 1545319*) have been observed for Pb-Br bonds. With 15 % Br it is reasonable for $(FAPbI_3)_{0.85}(MAPbBr_3)_{0.15}$ to be at the lower end of the Pb-I range. In measurements by Weller *et al.* a bond length change in the ab plane of 0.015 Å was observed from 3.1870 Å at 100 K to 3.1720 at 180 K [Weller et al., 2015b] [26]. This shows a longer bond length for the lower temperature measurement with a comparable to the increase in bond length across the phase transition near 260 K.

The bond length parameter in Set 23 (Figure 6.17) follows a trend of gradually increasing with temperature prior to the $\beta \rightarrow \alpha$ phase change. The bond length parameter shows a slight decrease between 230 and 250 K with a sudden drop between 250 and 260 K before continuing to increase. This is consistent with the gradual structural change between 230 and 260 K identified in previous sections. Considering bond length in Figure 6.17(right) and octahedra rotation represented by the Pb-X-Pb bond angle in Figure 6.16, thermal energy acts to increase the Pb-X bond length with the exception of the range 230 to 260 K. In this range octahedra rotation is dominant during the structural reorganisation concluding with the $\beta \rightarrow \alpha$ between 250 and 260 K. Here we observe shortening of the apparent bond length as the Pb-X-Pb angle increase approaches its minimum.

[25] Bond lengths from selected literature structure files are provided in App. Table C.5.

[26] Structure files ICSD 428899 and ICSD 428898. For these structures the Pb-I bond lengths along the c-axis were 3.1970 and 3.1872 Å for 100 and 180 K respectively

What is observed could be the result of changes in bonding as a result of changes in orbital overlap and/or an effect of how an "average structure" accessible with XRD represents a real material. XRD diffraction patterns contain information on average structure of a material. The average position of any bond rotations will be observed which can result in an atom appearing in the centre of the axis-of-rotation resulting in a shorter apparent bond length. The average structure can alternatively be a simplified approximation of the real structure should there be a number of short range order configurations which the observed structure will represent the average [Becka and Cruickshank, 1961].

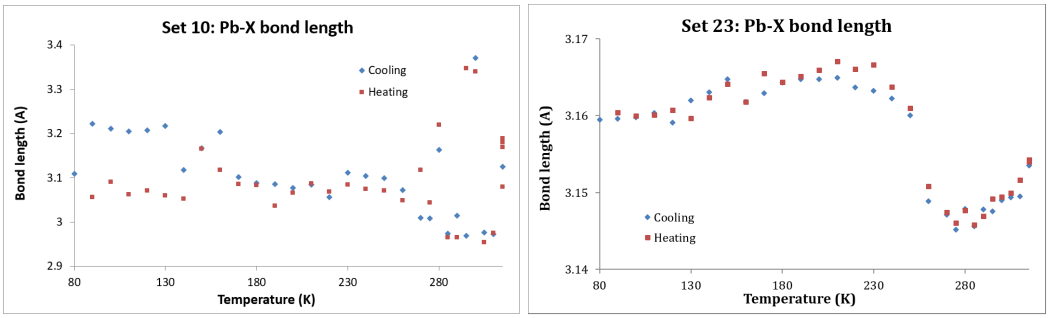

Figure 6.17: Pb-X bond lengths in Set 10 where a rigid body model is used and Set 23 using a $P4$ based symmetry constraint.

Halide position refinement

Across the sets, the halide positions were defined either by a rigid body model or as sites constrained to a $P4$ symmetry. The use of a **rigid body model** facilitated the inclusion of octahedra (Oh) rotation about the a and b axes in addition to the dominant rotation expected about the c-axis. Using a rigid body model, the refined rotation parameters about the a and/or b axis for Set 12 provided an average magnitude of 3.6 ($\sigma = 0.9$) with no clear trend in the parameter as seen in Figure 6.18.

Comparing Sets 12, 19, and 20, where Set 12 makes use of a Rigid body octahedra model. Set 19 defines its halides in the ab plane coplanar with the Pb atom using a $P4$ symmetry, with the position of halide in the c-direction refined, Set 19 is similar to Set 23 with the exception that halides in the c-direction is fixed to the centre between two Pb atoms.

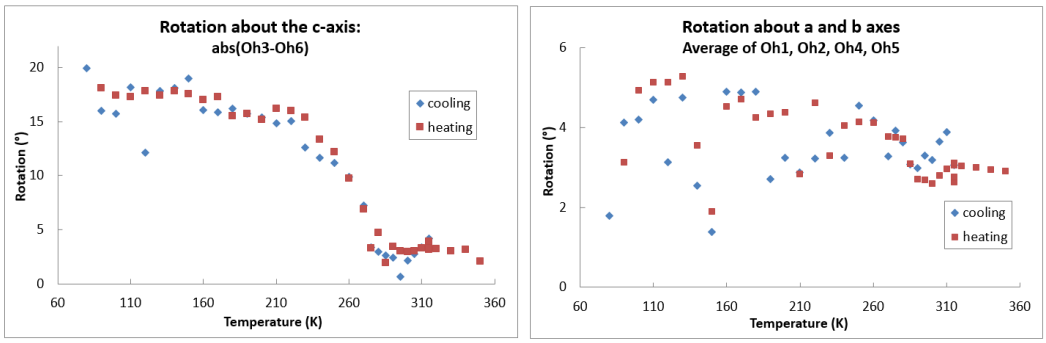

Figure 6.18: (left) Set 12: Effective octahedral rotation about the c-axis. This was evaluated by taking the absolute value of the difference in rotation about the c-axis of the 2 Oh in the unit cell. (right) average rotation about a and b axes.

These sets provide a well defined trend in rotation about the c-axis as seen in Figures 6.18 and 6.16. The trend becomes clearer with less apparent noise and fewer outliers as we increase the set number towards more constrained models. This is in part due to parameter correlation such as the correlation between octahedral rotation parameters and parameters displacing the octahedra centre seen in Appendix Figure C.18. The correlation is greatly reduced in the later more constrained sets with the example of Set23 in App. Figure C.17. Sets 12 and 19 result in near identical R_{wp} values of of 9.00 and 8.99 respectively, while Set 20 has a slightly worse R_{wp} of 9.11. Similar is observed in their R_{wp} box and whisker plots as seen in Figure 6.13. It is suggested that the one refined halide in Set 19 comparable effect in the simulated pattern to rotation of the Oh about the a and b axes, especially since both approaches result in the movement of the halide in question.

In Set 19, the position of the halide present between Pb atoms in the c-direction refined closer to a centred position at high temperatures, compared to low temperatures, Figure 6.19. This coincides with the drop in the c-axis lattice parameter and the $\alpha \rightarrow \beta$ transition, Figure 6.14d. The mean magnitude of displacement in the ab plane was 0.039 Å ($\sigma = 0.011$) showing no clear sign of temperature dependence. The angle between the displacement of halide between the 2 Oh remains low with a mean value of 16.5° ($\sigma = 12.1$), this is similar to how polarisation is expected to appear in a structure. Polarisation if present, would be expected at lower temperatures

while absent at higher temperatures. Since there is no additional information supporting polarisation in [Greenland et al., 2019], this is considered a likely false positive. Set 20 constrains this halide at the expense of a slightly higher R_{wp}. The possibility of polarisation is discussed further under the title "Pb position refinement" below.

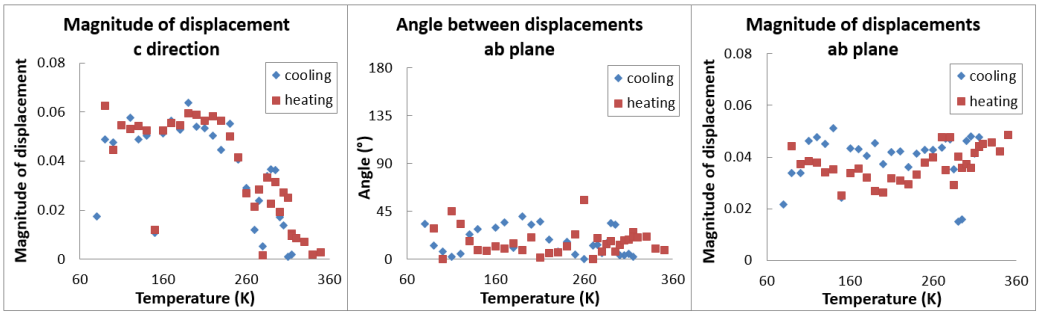

Figure 6.19: Set 19, Position data of the halides between Pb atoms along the c-direction (labelled I3 and I6 in refinements) (left) Average magnitude of displacement in the c-direction between I3 and I6. (middle) rotation about the c-axis. This was evaluated by taking the absolute value of the difference in rotation about the c-axis of the 2 Oh in the unit cell. (right) average rotation about a and b axes.

Pb position refinement

The use of solely refining halide positions, through rigid body Oh or symmetry constraints was insufficient to well describe the data. In Section 6.6 we observed a reduced fit quality where the lattice parameters were defined in relation to bond projections which were refinements using undistorted Oh, and a fixed Pb position. In the previous section on "Halide Position Refinement", distortion is an inherent capability of the structure models discussed, noting that Set 23 was restricted to very limited means of distortion, primarily elongation of the octahedra.

All the Sets included in Table 6.3 make use of either a form of relative displacement between the Pb atoms and halide framework or a spreading of the Pb atoms electron density across nearby sites in a $P4$ symmetry. The variations includes:

1. The centre of the halides octahedra rigid body was refined (2x2 or 2x3 parameters).
2. The centre of the halide octahedra rigid body is fixed and the position of the Pb atoms are refined (2 sets of 2 or 3 parameters each).
3. The Pb atom was allowed to displace in the x and y directions and replicated by a $P4$ symmetry resulting in 4 Pb sites with occupancies of 0.25 to represent uncertainty in the Pb position (2 parameters).

The gains in fit quality from permitting distortion and/or refinement of the Pb atomic position in the structure, lead to the consideration of dipoles in the structure which can be expected at low temperatures in response to the inherent dipole present in MA and FA cations [Lee et al., 2021].

To test whether the collected data contains accessible information on the directionality of Pb displacement, Set 20 which refined the position of its Pb atoms independently was compared to Set 23 which implemented displacement of Pb in the ab plane using four Pb atoms with 0.25 site occupancy in a $P4$ symmetry, this removes the ability of the model to represent a dipole in the structure and since the magnitude of displacement is small this approximates isotropic displacement in the ab plane. (Figure 6.4) Both sets provide similar R_{wp} values of 9.11 and 9.12 respectively. Implying that there were no significant gains in fit quality from allowing the Pb atoms to form dipoles over the $P4$ symmetry based approach making the model of more restrictive Set 23 favoured over Set 20. This informs us that at least on the scale of average structure we are not expecting a dipole.

The consideration of the Pb atom being distributed around a point in $P4$ symmetry can be reframed. We assume the modelled scattering interactions between the adjacent Pb atoms in the model negligible. If we take each of the four Pb atoms as the origin of a distinct unit cell and overlap them. The resulting unit cell presents the effect is the spreading of the halide electron density as observed in literature structures where the electron density of the halides are distributed due to thermal motion in the "soft" Pb-X framework [27] [Kieslich et al., 2018, Weller et al., 2015b].

[27] The effect on the organic cation on the diffraction pattern neglected in this comparison for the reasons discussed in Section 3.5.1.

6.7.3 Conclusion

The structure models evaluated considered the impact of various structural constraints and freedoms progression from initially over parametrised models towards more restrictive models reducing parameter correlation [28]. Care was taken to slowly develop the structure model, with the intent to avoid both inaccuracies and information loss due to the choice of model constraints. This included the progression from a relatively free rigid body model for the octahedra, to halide positions strictly defined by a $P4$ symmetry. The freedoms given to the Pb position were reduced from two Pb atoms with three freedoms each to set of sites in $P4$ symmetry with shared parameter refined defining their x and y coordinates. This indicated that the average structure of $(FAPbI_3)_{0.85}(MAPbBr_3)_{0.15}$ does not show polarisation. An attempt was made to reduce the organic cation to a single representative atom resulting in a substantially reduced fit quality (R_{wp}) as seen in Figure 6.13.

Set 23 was found suitable to stabilise the sequential refinement results with focus on the Pb-X-Pb bond angle, where a cleaner plot of Pb-X-Pb bond angle in the ab plane is observed, Figure 6.16. The R_{wp} indicating quality of fit was slightly higher than for Set 19, which was attributed to the presence of fewer refined parameters. Set 23 does not offer meaningful information on position or orientation of the organic cation. Nor can it differentiate the possibility of a disordered dipole in the structure, from the electron density of the halide position being distributed due to vibrational modes. With awareness of these limitations, Set 23 was sufficient to investigate the phase changes present and the rotation of the octahedra. For this reason it was chosen for use in the research paper [Greenland et al., 2019] resulting from this work.

6.7.4 Future work

Compared to the current structural work, similar experimental and theoretical transitions observed in literature show the changes in symmetry are

[28] A comparison between the parameter correlation can be seen in App. C.6.17 where Set23 expresses far less parameter correlation compared to Set10 as previously discussed in Section 6.7.2.

accompanied by changes in the orientational disorder of the organic cation. For the high temperature α phase, there is sufficient thermal energy such that the organic is in effect completely disordered. The transition to the tetragonal β phase in the literature included a reduced orientational disorder accompanied by the rotation of octahedra. For the $\gamma \rightarrow \beta$ transition literature supports a sharp structural change in the case of $MAPbI_3$ and $FAPbI_3$ where the hydrogen bonds between the organic cation and I are broken with the increase in thermal energy [Cordero et al., 2021, Mattoni et al., 2015, Weller et al., 2015b].

The orientation and motion of the organic cations in single cation systems as a function of temperature has been well studied in literature. [Weller et al., 2015b] [Mattoni et al., 2015] [Cordero et al., 2021] This is less well covered in multi-cation systems such $(FAPbI_3)_{0.85}(MAPbBr_3)_{0.15}$. Considering the sharp transition in single cation systems between the β and γ phases which are a related to the breaking of hydrogen bonds between the organic cation and the framework. We note that data of a higher temperature resolution would be required to establish the sharpness of the transition for $(FAPbI_3)_{0.85}(MAPbBr_3)_{0.15}$ while data with better definition of the weak peaks would be required to extract greater structural detail.

Recent literature has shown the transition rate of similar mixed-cation mixed-halide hybrid-perovskite systems to be dependent on nano-structural heterogeneity, which is determined by synthesis conditions and crystal quality [Barrier et al., 2021, Mundt et al., 2021]. The synthesis and diffraction measurement of a $(FAPbI_3)_{0.85}(MAPbBr_3)_{0.15}$ single crystal, alongside thin-films, may provide insights on how the structural transition behaviour, and inferred nano-scale heterogeneity compares to the $(Cs, FA)Pb(Br, I)_3$ based compositions in the works of Barrier *et al.* 2021 and Mundt *et al.* 2021 [Barrier et al., 2021, Mundt et al., 2021].

The presence of multiple cations and multiple halides would be expected to result in hydrogen bonding with a distribution of bond energies, as such we theorise that the $\gamma \rightarrow \beta$ transition could follow a number of schema such as gradual, stepped, or sharp depending on the pattern in which the hydrogen bonds break and whether the same or a different scheme is followed on the heating and cooling direction of the phase change. A sharp transition may indicate that the a single hydrogen bond dominates the transition which

would have implication in the distribution of the halides and/or the orientation of the organic cations. A more gradual transition may indicate a greater independence across the structure with some extent of localised structural environments. A further question to be asked regarding the effect of entropy gained from a more diverse composition, and whether this has an identifiable effect on the transition temperature between the β and γ phases and on the gradual reorientation of the octahedra after the $\alpha \rightarrow \beta$ transition [Kieslich et al., 2018]. We suggest that understanding of such effects could provide additional insight to the stability gained by double and triple cation systems.

This work can be extended to study the system using variable temperature neutron diffraction coupled with DFT for the comparison of energy differences between similar structural configurations [29]. Neutron diffraction is far more sensitive to hydrogen atoms and provides a far better diffraction contrast between the light elements in the organic cation. For a better signal-to-noise ratio in neutron diffraction, deuterated samples are often required, which affects the strength of hydrogen bonding and in consequence the crystal structure [30] [Whitfield et al., 2016]. Insights from DFT can be used to understand impact of thermal energy on specific structural transitions and orientational freedoms. [Mattoni et al., 2015]

XANES could be used to inform whether the halides atoms are in the same chemical environments or if each halide exists in multiple environments [31] [Henderson et al., 2014]. To further explore the bond length trend with a focus on the $\alpha \rightarrow \beta$ transition, EXAFS and/or X-ray total scattering for a pair-distribution function can be used to determine local bond lengths including Pb-X bonds [32]. EXAFS provides element specific measurements which could be used to compare Br and I halide bond lengths in sample. [Hennig et al., 2001]. Such measurements and analysis could then be contrasted to the average structure modelled using PXRD data.

[29] DFT: Density functional theory.

[30] A temperature dependent, neutron and X-ray diffraction study between protium, deuterium, and partially deuterated hybrid-perovskites materials has been explored in the work of Whitfield *et al.*. They considered the effect on noise in neutron diffraction data, bond-lengths, and phase transition temperatures in detail [Whitfield et al., 2016].

[31] XANES: X-ray absorption near edge structure

[32] EXAFS: Extended X-ray absorption fine structure

Chapter 7

Correlating phase behavior with photophysical properties in mixed-cation mixed-halide perovskite thin-films

Preface

This chapter introduces a published work, which correlates structural and photophysical changes that occur in a $(FAPbI_3)_{0.85}(MAPbBr_3)_{0.15}$ hybrid perovskite material as a function of temperature.

My role in this investigation was centred around the model development and analysis of a variable temperature X-ray diffraction data-set, with efforts to determine as much structural information as could be reasonably attained with the methods, resources, and data quality available. The development of the model used is discussed in Chapter 6.

The results of the work in Chapter 6 were presented in the article "Correlating Phase Behavior with Photophysical Properties in Mixed-Cation Mixed-Halide Perovskite Thin Films", published by C. Greenland, A. Shnier *et al.* (2019) [Greenland et al., 2019].

The abstract and authors list is presented on the following page with the published manuscript available via its DOI at [link], and via *Researchgate.net* at [link].

Correlating Phase Behavior with Photophysical Properties in Mixed-Cation Mixed-Halide Perovskite Thin Films

Claire Greenland[1], Adam Shnier[2], Sai K. Rajendran[3], Joel A. Smith[1], Onkar S. Game[1], Daniel Wamwangi[4], Graham A. Turnbull[3], Ifor D. W. Samuel[3], David G. Billing[2], and David G. Lidzey[1*]

1 Department of Physics and Astronomy, University of Sheffield, Hicks Building, Hounsfield Road, Sheffield S3 7RH, United Kingdom
2 School of Chemistry, University of the Witwatersrand, Johannesburg 2050, South Africa
3 Organic Semiconductor Centre, SUPA, School of Physics and Astronomy, University of St Andrews, North Haugh, St Andrews KY16 9SS, United Kingdom
4 School of Physics, University of the Witwatersrand, Johannesburg 2050, South Africa
∗E-mail: d.g.lidzey@sheffield.ac.uk

Advanced Energy Materials
Volume 10, Issue 4, January 2020
DOI: 10.1002/aenm.201901350

Abstract:

Mixed cation perovskites currently achieve very promising efficiency and operational stability when used as the active semiconductor in thin-film photovoltaic devices. However, an in-depth understanding of the structural and photophysical properties that drive this enhanced performance is still lacking. Here the prototypical mixed-cation mixed-halide perovskite (FAPbI3)0.85(MAPbBr3)0.15 is explored, and temperature-dependent X-ray diffraction measurements that are correlated with steady state and time-resolved photoluminescence data are presented. The measurements indicate that this material adopts a pseudocubic perovskite α phase at room temperature, with a transition to a pseudotetragonal β phase occurring at ≈260 K. It is found that the temperature dependence of the radiative recombination rates correlates with temperature-dependent changes in the structural configuration, and observed phase transitions also mark changes in the gradient of the optical bandgap. The work illustrates that temperature-dependent changes in the perovskite crystal structure alter the charge carrier recombination processes and photoluminescence properties within such hybrid organic-inorganic materials. The findings have significant implications for photovoltaic performance at different operating temperatures, as well as providing new insight on the effect of alloying cations and halides on the phase behavior of hybrid perovskite materials.

Chapter 8

Parametric Rietveld refinement for structural analysis of triple cation hybrid-perovskites

Contents

8.1 Introduction **171**

8.2 Powder X-ray diffraction measurements **172**

8.3 Visual and Pawley refinement based comparisons **172**

8.4 Parametric refinements **175**

8.4.1 Reference refinements of VT-XRD data 176

8.4.2 Parametric refinement of VT-XRD data 177

8.5 Discussion **181**

8.6 Conclusion **185**

8.1 Introduction

The crystal structure of the hybrid-perovskites has been discussed in Section 1.2.1. In Section 1.3 we discussed benefits of compositional turning, including the substitution of Cs into hybrid-perovskite materials as a means of improving device stability and PV performance.

In $FAPbI_3$ hybrid perovskites, thermally activated phase transitions involve a higher temperature cubic or pseudo-cubic α phase, and an ambient or sub-ambient phase transition to a tetragonal β phase. The thermally induced phase transition temperatures of $FAPbI_3$ and related structures have been previously discussed in detail in Section 1.5.2. The phase changes in hybrid-perovskites involve the rotation of these octahedra configurations as prescribed by the Glazer notation in Section 1.5.1. The α to β phase transition of $FAPbI_3$ has been described by the transition from the $a^0a^0a^0$ to $a^0a^0c^+$ tilt system corresponding the $Pm\bar{3}m$ to $P4/mbm$ space groups [Weber et al., 2018]. In the case of the $\beta \rightarrow \gamma$ low temperature phase transition, this leads to a less clearly agreed upon γ phase, with structures proposed amongst tetragonal, orthorhombic and disordered pseudo-cubic crystal systems [Fabini et al., 2017, Weber et al., 2018]. The addition of a percentage of MA and Br has been found to be effective in improving the phase stability against thermal decomposition and the performances of FA based perovskites [Koo et al., 2020, Zheng et al., 2017].

Our recent study on $(FAPbI_3)_{0.85}(MAPbBr_3)_{0.15}$ has explored the thermally activated structural transitions in this class materials. Since the optical properties are sensitive to structure, we have also correlated the corresponding photophysical changes [Chapter 7]. The addition of Cs has shown even more promise, having a strong effect on the morphology, stability, and performance of these photovoltaic materials [Cho et al., 2018, Liu et al., 2020].

In this chapter we explore the effect of substituting Cs into the A site of $(FAPbI_3)_{0.85}(MAPbBr_3)_{0.15}$ on temperature induced structural transitions in the form $Cs_x(FA_{0.85}MA_{0.15})_{1-x}PbBr_{0.45}I_{2.55}$. In a previous work, a distinct phase transition for the pseudo-cubic α to tetragonal β at 260 K, with the onset of octahedral rotation at 275 K was established [Greenland et al., 2019].

8.2 Powder X-ray diffraction measurements

Thin film samples were prepared using the protocol described in Section 4.4. Powder diffraction data were obtained using a Bruker D8 Advance, with a copper source and graphite monochromator, as detailed in Section 4.7.1. The Rietveld refinements used the fundamental parameter approach, with an instrument profile refined against a poly-crystalline silicon reference material as described in Section 4.8.1 [Rietveld, 1969]. The data collection, methodology, and sample naming conventions are described in Section 6.2.

8.3 Visual and Pawley refinement based comparisons

In this section, we identify and relate features of the X-ray diffraction patterns for the collected data, and compare the data quality between sets using visual analysis and peak intensities derived from Pawley refinements.

The collected data on $Cs_x(FA_{0.85}MA_{0.15})_{1-x}PbBr_{0.45}I_{2.55}$ for Cs0 ($x = 0$) as analysed for Chapter 6, provided sufficiently resolved peaks to meaningfully explore phase transitions and a number of structural parameters, as discussed in Chapter 6. When we compare this to the Cs10 ($x = 0.10$) data-set in Figure 8.1, weaker peak intensities are observed. Such an effect on intensity can be considered either an experimental effect, such as smaller sample volume available for diffraction, or a material effect where the addition of Cs is directly or indirectly reduces the diffracted intensity. In addition, peak broadening observed between the 315/310 K and 90 K patterns of Figure 8.1, this is ascribed to peak splitting due to a pseudo-cubic to tetragonal phase transition as explored in Chapter 6, and supported by the low residuals in the tetragonal $P4/mbm$ Pawley refinements of Figure 8.1.

In Figure 8.2, we consider modelled peak intensities of the 310 K patterns, where the α phase is expected across the data-sets, Table 1.5.2. These data-sets were collected using a common data integration times, with samples prepared in 0.7 mm borosilicate capillaries, as explained in Sections 4.5 and 4.7.1. The intensities were modelled using $P4/mbm$ based Pawley re-

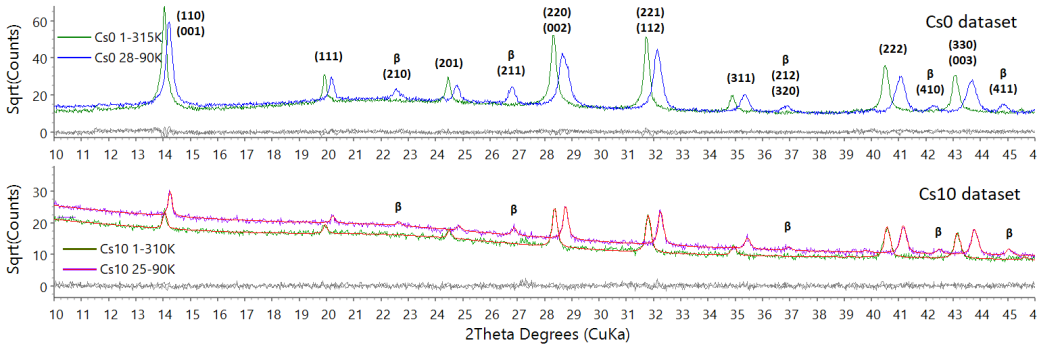

Figure 8.1: (top) Cs0 data set, blue 1-315K, green 28-90K (bottom) Cs10 data set, blue&red 1-310K, green&red 25-90K.

finements [1]. The Cs0 peaks presented the strongest peak intensity, with the weakest observed for Cs10, noting the exception of the 20° 2θ peak, corresponding to the (111) reflection. This is of interest, as this peak is not expected to loose significant intensity with the octahedral rotation across the $\alpha \rightarrow \beta$ phase change [2], as evident in Figure 8.1(top). With the exception of the (111) reflection, the Cs5 and Cs8 peak intensities are stronger than those of Cs10. The intensities for Cs8 are greater than those of Cs5, which indicate the inclusion of Cs does not result in a monotonic trend of intensity loss. All Cs containing data-sets presented lower intensity, and similar intensity values for observed for the Cs5 and Cs10 data-sets. The inclusion of Cs is correlated with the reduction in the diffraction intensity. This observation corroborates a similar effect, albeit smaller, observed for the $Cs_x(MA_{0.17}FA_{0.83})_{(1-x)}Pb(I_{0.83}Br_{0.17})_3$ in the work of Saliba *et al.*, between their sample with and without 10 % of Cs substitution [3] [Saliba et al., 2016]. Changes in electron density at the A site due to inclusion of Cs was considered. This was modelled in App D.1, Figure D.2 and was not significant enough to explain the observed intensity differences. A proposed mechanism is an effect of the altered composition on fabricated samples' morphology, and/or increases disorder in the structure which could act on intensity in a comparable form to that of thermal displacement, Equation 3.18 [Braunger et al., 2018].

[1] For Cs0 the 315 K pattern was refined.
[2] Octahedral rotation is discussed in Chapter 6
[3] SI Figure 2 of [Saliba et al., 2016].

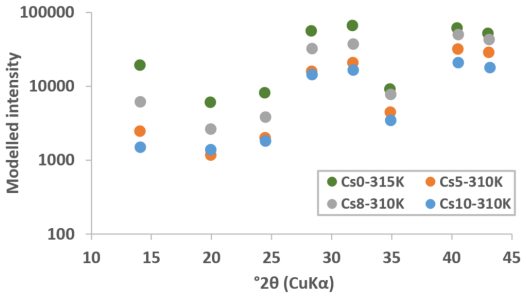

Figure 8.2: Modelled peak intensity across 2θ of diffraction patterns at 310 K, ascribed to the perovskite α phase, presented using logarithmic intensity scale.

To assess if temperature and structural changes are accessible across the Cs based data-sets, the phase with the weakest peak intensities, Cs10 is taken into consideration. A comparison was made between the peak intensity of the room temperature and 90 K patterns using modelled peak intensities from Cs0 as a reference. [4] [5]. This is presented in Figure 8.3, where there is little difference in the relationships across the peak intensities between the Cs0 and Cs10. The peak positions for the lower temperatures of both sets show a shift towards higher angles which is more pronounced at higher angles where greater peak separation is expected [6]. We note a larger intensity difference for the peaks Cs10 peaks at 14° 2θ, with the high temperature phase lower in intensity. The 310 K before and after heating is presented in App. Figure D.1, where the intensity of the (110)/(001) 14° 2θ peak is stronger after temperature cycling to 80 K, while the balance of the pattern is virtually identical in peak shape and intensity, including higher order (220)/(002) and (330)/(003) peaks. This is suggested as due to a degree of disorder on the length scale corresponding to the low angle (larger inter-planar spacing) (110)/(001) peak. In addition for both the Cs0 and Cs10 data-sets we see peaks modelled at 22.6, 26.9, 37.0, 42.5, and 45.0° 2θ corresponding to (210), (211), (212)/(320), (410) and (411) reflections of a the perovskite β phase identified in Chapter 6.

[4]Peak intensities for Figure 8.3 were modelled using $P4/mbm$ based Pawley refinements.

[5]The 90 K pattern was chosen as a reference over the 80 K pattern due to the $\beta \rightarrow \gamma$ transition observed between these temperatures in Chapter 6.

[6]This corresponds to thermal contraction of the unit cell with decreasing temperature.

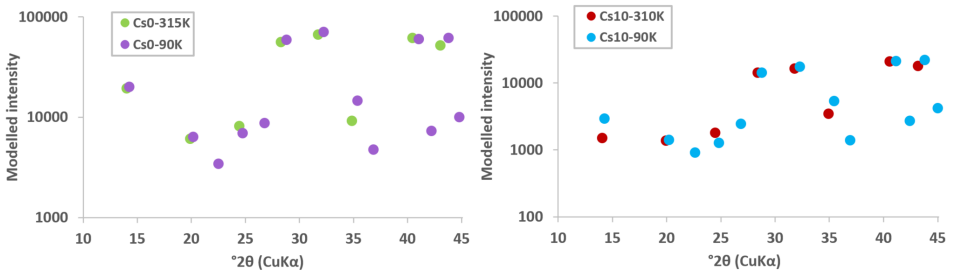

(a) (b)

Figure 8.3: Modelled peak intensity comparison between room temperature and 90 K patterns in (a) Cs0, and (b) Cs10 data-sets, across 2θ (Cu Kα).

The observations of this section establish that in spite of the poor diffraction pattern intensity evident in the weakest data-set Cs10, the peak position informing on the unit cell parameters, relative peak intensity related to octahedral rotation, and the appearance of additional β phase peaks, are accessible in the data. In the following sections, we parametrise refinements of the full data sets to mitigate noise in modelled parameters, which originates from the poor signal-to-noise ratio of the measured data.

8.4 Parametric refinements

The parametric refinement based modelling in this chapter follows the input file preprocessing method, and includes refinement contributions discussed in Section 4.9.1.

The following sections compare two refinement sets per data-set. For Cs5, 8, and 10, these are group (A) Set 7, a minimally parametrised set in which crystallite size broadening was refined as a global parameter across the data-set, and group (B) Set 22, where simple empirical equations are applied based on trends observed in the minimally constrained refinement sets. For Cs0, group (A) sequentially refined data of Chapter 6 is compared to group (B) of the parametrised Set 23. As no Set 7 or 22 exist for the Cs0, when referring to Set 7 or Set 22 across the compositions the Chapter 6 and Set 23 models are used.

Group (A) is considered *reference* refinements, and (B) *parametrised* refinements, while group (A) is technically parametrised, this use is limited to crystallite broadening.

8.4.1 Reference refinements of VT-XRD data

The refinement model of the FAMA based sample (Cs0) is explained in Chapter 6 and 7. A simpler $P4/mbm$ based model, with a fixed Pb atom position within the unit cell, and *representative atom* in place of the organic cation, was suitable for the sets containing Cs, Figure 8.4 [7]. The unit cell was constrained to be tetragonal ($a = b$). Rotation of the octahedra about the c-axis was refined, consistent with the Glazer notation $a^0a^0c^+$.

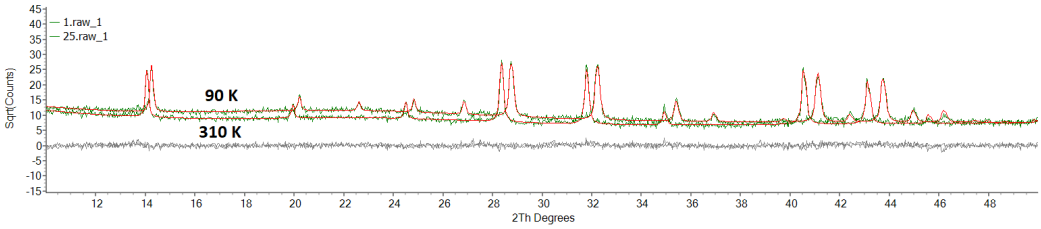

Figure 8.4: Cs5 diffraction patterns for refinement Set7, for 90 and 310 K. (red) modelled, (green) raw data, (grey) residual.

The parameters, shown in Figure 8.7 for Refinement Set 7, show more noise than desirable for the intended analysis, especially for the $a/(c\sqrt{2})$ ratio above ∼260 K and the bond length parameters, with the most erratic values observed for the Cs10 diffraction data. The Cs10 data-set had the lowest diffracted intensity of the sets investigated as shown in Figure 8.1. This could be a result of overall sample volume or crystallinity. The weak reflections are associated with larger uncertainty and reduced stability of refinement parameters. [Stinton and Evans, 2007] To extract more reliable parameters, the use of careful modelling using more advanced analysis techniques was employed, specifically parametric refinements.

[7] Organic cation modelling approached are discussed in Section 4.9.2, including the use of a *representative atom*.

8.4.2 Parametric refinement of VT-XRD data

Refinements of Set 22 are discussed for Cs5, Cs8, and Cs10. For Cs0, Set23 is utilised. The primary difference between Sets 22 and Set 23 rest in the Pb atom. In Set 22, this is a fixed representative atom. For Set 23, this is replaced by 4 coplanar Pb atoms each with 0.25 site occupancy in a $P4$ symmetry about the ideal position, as was introduced and implemented in Chapter 6. The effect on R_{wp} is shown in a between Set 21 and 23 for Cs0 in App. Figure D.3, where there is a significantly worse in fit quality at higher temperatures for Set 21, with R_{wp} values as high as 14.5 far exceeding that of Set 23 and the Cs containing sets.

These refinements included all the features of the above *reference* refinements, with additional parametrisation across each data-set. The additional constraints were applied to within specific temperature ranges. One such range was the region where the high temperature α phase is clearly identified. In this range, the lattice parameter ratio, $(\frac{a}{c\sqrt{2}})$ and octahedra rotation were each defined by single global variable, as a straight line [8]. To further reduce noise, and improve reliability of the refined parameters, Set 22 refined a 4th order polynomial for selected temperature ranges, (Figure 8.5), to describe the parameter associated with $a^0a^0c^+$ octahedra rotation (Pb-X-Pb bond angle) in a region between the $\alpha \rightarrow \beta$ and $\beta \rightarrow \gamma$ transitions. In the case of Set 23 for Cs0, a polynomial constraint was not applied as this parameter, as reasonable parameters were achieved without the additional constraint. These constraints are illustrated, as applied to each data-set in Figure 8.5, where the parametrised values are plotted as solid green lines with free parameters in the same refinement represented as green •'s.

The initial parameters for the polynomial constraints were determined by fitting against locally free parameters, such as in Set 7. To prevent over constraining the data, this region was chosen for each sample composition to exclude sudden shifts in the parameters. The two parametrised regions was decided separately for each composition and were chosen conservatively. This is exemplified in the Pb-X-Pb angle plots for the region ∼250 to ∼280 K, where a number of data points were exempted from the polynomial constraint, in part due to their proximity to the phase transition. This addi-

[8] A tetragonal unit cell is modelled such that $a = b$.

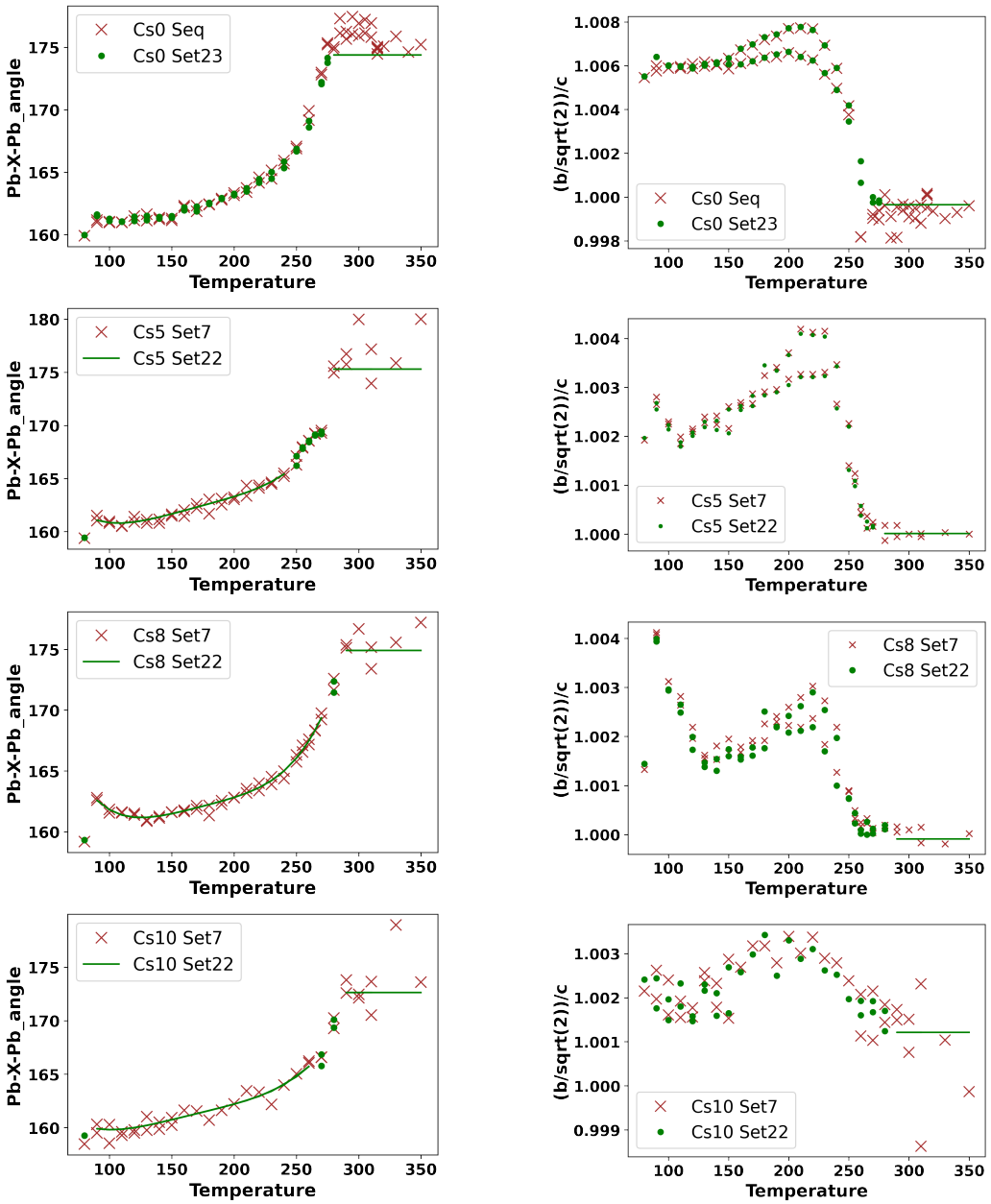

Figure 8.5: An overlay of *reference* (Set7) and *parametrised* (Set22) refinements for each sample set. (left) Pb-X-Pb bond angle showing octahedral tilt about the c-axis. (right) Lattice parameter ratio $\frac{a}{c\sqrt{2}}$, $(a = b)$. (green lines) parametrised values, (green •) freely refined values, (Brown X) freely refined values.

tionally prevents a miss-representation of data points near the transition, where the noise in the refined parameter values could allow some values to be related to either side of the transition.

For the Cs5 and Cs8 sets, the parametrised lines shown in Figure 8.5 is closely aligned with the *reference* refinements. Cs0 provides a close fit for the low temperature region with a greater difference above 275 K. This is attributed to differences between the models, where Cs0 Seq includes a rigid body model organic cation with a refined position while Cs0 Set23 has a fixed position representative atom.

In the case of Cs10, we have identified evidence of octahedral tilt, by means of the (210) and (211) reflections, attributable to a $P4/mbm$ unit cell and $a^0a^0c^+$ tilt system in Section 8.3, the presence of these reflections on become weakly discernable at 260 K with increasing intensity with decreasing temperature [9]. This is presented in Figure 8.6, where the expected positions of the β phase peaks are marked. There is a slight, poorly defined raise in the observed signal of the 7-260K pattern at both marked positions above the background of the higher temperature 1-310K pattern [10]. These signals continue to increase in intensity with decreasing temperature as expected across an $\alpha \rightarrow \beta$ phase transition. The formation of these peaks is related to the $a^0a^0a^0$ to $a^0a^0c^+$ transition, with the refined Pb-X-Pb angle showing this in the set of reference refinements (Set 7), Figure 8.5. A possible trend is evident in the Pb-X-Pb angle from 80 to 290 K. Qualitative analysis on the balance of refined parameters for Cs10 provided no additional insights beyond a general decrease in unit cell size.

With the observations we have discussed, $T \geq 290$ K was a reasonable point to consider as the onset for the formation of the α phase in Cs10, and the corresponding parametrisation was applied as presented in Figure 8.5. Similarly the polynomial parametrisation was applied in the range $90 \leq T \leq 260$ K for Cs10. It is noted that qualitatively, the parametrization can be extended to 280 K, however concerns on the nature of the appropriate constraints demerit the modelling range, noting that the 280 K data point

[9] Peaks at these positions do not occur for a $Pm\bar{3}m$ perovskite phase.

[10] It is noted that the collection of each VT-XRD data-set elapsed slightly over 40 hours. With approx. total of 1 hour per temperature, including ramp and dwell time prior to measurement. As such, longer collection times for these samples proved infeasible.

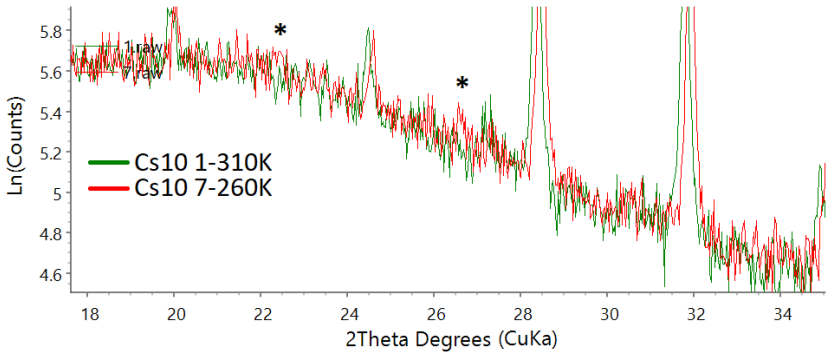

Figure 8.6: Cs10 diffraction patterns. Positions where perovskite β phase peaks would be expected are marked with a "$*$".

is ambiguous in that is could be related to either the linear or polynomial constraints.

The effect of the parametrisation is evident in for the Pb-X-Pb bond angle and lattice parameter ratio in Figure 8.5, where the constraints are applied, and indirectly for the c-axis length and apparent Pb-X bond length in Figure 8.7. Additional plots of the lattice parameters and lattice parameter ratio for the *parametrised* sets is provided in App. Figure D.4.

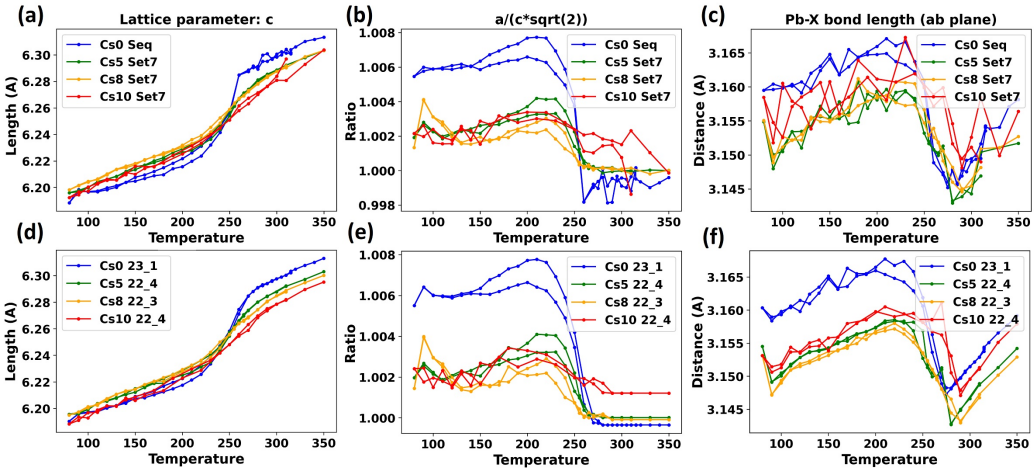

Figure 8.7: Overlayed c-axis length, axis ratio, and Pb-X bond length for Cs0, Cs5, Cs8 and Cs10 refinement sets (a-c) *reference* refinements.(d-f) *parametrised* refinements.

8.5 Discussion

Significant points relating to the $\alpha \rightarrow \beta$ transition are presented in Table 8.1 describing features evident in the data presented in Figures 8.5 and 8.7, with the individual plots for the lattice parameters and axis ratio provided in App. Figure D.4. These include the *bond angle drop off* which is the last temperature at which the bond angle follows the high temperature cubic phase trend, before decreasing for the $\alpha \rightarrow \beta$ phase transition. Similarly the $a/(c\sqrt{2})$ *ratio shift* refers to the last data point where the a and c axis ratio follows the high temperature trend.

The *bond angle drop off* corresponds to the symmetry breaking from a $a^0a^0a^0$ to $a^0a^0c^+$, which is responsible for the formation of β phase peaks [11] [12], while the $a/(c\sqrt{2})$ *ratio shift* is informed by peak broadening associated with a shift from a cubic or pseudo-cubic unit cell to a tetragonal unit cell. The effective bond length is a function of the thermal expansion and octahedral tilt (Pb-X-Pb bond angle). These act to increase and decrease the apparent bond length with temperature respectively, providing minimum where there is a change in the trend of octahedral tilt. This provides an additional means to assess the $a^0a^0a^0$ to $a^0a^0c^+$ symmetry breaking [13].

The refined α phase $a/(c\sqrt{2})$ parameter slightly increased with Cs con-

[11] Glazer notation is discussed in Section 1.5.1.

[12] The modelled bond angle stabilises near, yet does not reach 180°, as such the use of $a^0a^0a^0$ is an approximation.

[13] These tilt systems correspond to the $Pm\bar{3}m$ and $P4/mbm$ space groups, which describe unit cell symmetry [Howard and Stokes, 1998].

Table 8.1: XRD derived significant points for the Cs based data-sets

Set	Bond angle drop off	α phase $a/(c\sqrt{2})$ ratio	$a/(c\sqrt{2})$ ratio shift	Bond length linear start
Cs0 23_2	275	0.9997	270	275
Cs5 22_4	280	1.0000	265	280
Cs8 22_3	290	0.9999	260	290
Cs10 22_4	290	1.0012	∼260-290	290

tent. The Cs5 and Cs8 samples were effectively of the same value with the most significant change for between the Cs8 and Cs10 samples by 0.0013 reaching 1.0012 ± 0.0002 for Cs10 [14]. This is similar to the observations of Weber *et al.*, in which the larger a fraction of MA in $FA_{1-x}MA_x$, ($R_{MA+} < R_{FA+}$), resulted in a larger $a/(c\sqrt{2})$ ratio [15]. Their results have further illustrated that this ratio approximates to 1, 1.0002 and 1.0030 for MA compositions of $x = 0.7$, 0.8 and 0.9 respectively. These effects were evident in peak broadening ascribed to the departure from a cubic symmetry [Weber et al., 2016].

With increasing Cs content, we observe the $a^0a^0a^0$ to $a^0a^0c^+$ transition shifting to higher temperatures [16]. This is the opposite trend in the pseudo-cubic to tetragonal shift. Cs10 is an exception to this for two reasons,

- The refined α phase $a/(c\sqrt{2})$ parameter was 1.0012 ± 0.0002 which is significantly larger than observed for samples with less Cs,
- The transition point was unclear in part due to the raised $a/(c\sqrt{2})$ values.

In the single cation system $FAPbI_3$ of Fabini *et al.*, both the $a^0a^0a^0$ to $a^0a^0c^+$, and pseudo-cubic to tetragonal transitions occurs at a common temperature [Fabini et al., 2016]. These points do not coincide for the Cs0, which has the composition $(FAPbI_3)_{0.85}(MAPbBr_3)_{0.15}$, Table 8.1, and further diverge with the inclusion of Cs on forming a triple cation perovskite in Cs5, with a larger difference in the Cs8 sample.

The heat capacity measurements of Kawachi *et al.*, which show a similar trend to the $a^0a^0a^0$ to $a^0a^0c^+$ transition temperatures on the inclusion of Cs, where a shift from an $\alpha \rightarrow \beta$ transition of 280 K for $FAPbI_3$, to 300 K for $Cs_{0.1}FA_{0.9}PbI_3$ was reported, Table 1.3 [Kawachi et al., 2019]. In the recent work of Barrier et al, phase transition temperatures were similarly reported to increase with Cs content, and decrease with Br content in $Cs_yFA_{1-y}Pb(Br_xI_{1-x})_3$ systems with $0.05 \leq x \leq 0.30; 0.17 \leq y \leq 0.40$. Additionally they showed that the d-spacing of the tetragonal peaks imme-

[14] The TOPAS refined error for Cs10 is considered to be appreciably low for the data-set, and may be an underestimation.

[15] R_{MA+} and R_{FA+} refer to the radii for MA^+ and FA^+ respectively.

[16] The $a^0a^0a^0$ to $a^0a^0c^+$ transition is illustrated in Figure 1.5.

diately after the $a^0a^0a^0$ to $a^0a^0c^+$ transition, were related to a composition with low Br and high Cs content corresponding to a unit cell with a smaller Goldschmidt tolerance factor, which would favour a tetragonal unit cell. The regions with a higher tolerance factor related composition, would transition at lower temperatures broadening the observed structural transition [Barrier et al., 2021]. The presence of structural heterogeneity suggested is as a likely cause of the divergence between the $a^0a^0a^0$ to $a^0a^0c^+$ and $a/(c\sqrt{2})$ transition points.

The high temperature Pb-X-Pb octahedral tilt angles stabilise at values below 180°, with an average of the Cs0, Cs5 and Cs8 values at 175°, this is contrasted to Sun *et al.* with a value of 180° for $FAPbI_3$. [Sun et al., 2017]. An increase of the octahedral tilt of 2° is observed in the α phase region of Figure 8.5 from the Cs0, Cs5, and Cs8 sets which have similar values to the Cs10 data-set. This is consistent with the greater relative (111) peak intensity in the Cs10 310 K pattern, compared to other samples as evident in Figure 8.3, and discussed in Section 8.3. In both this work and that of Weber *et al.*, the addition of the smaller cation reduces the Goldschmidt tolerance factors, which is correlated with an increase in structural disorder, and the introduction of octahedral tilt, and greater stability of a tetragonal perovskite phase [Ahn et al., 2016, Filip et al., 2014, Gebhardt and Rappe, 2019].

In assessing the effect of Cs on the $\alpha \rightarrow \beta$ phase transition, we consider the c-axis of Cs0, Figures 8.8 and App Figure D.4. Two well-defined regions with a shallow gradient are observed on either side of the steeper sloped area, the latter between 220 to 260 K near the centre of the plot is related to the $\alpha \rightarrow \beta$ phase transition occurs. With the inclusion of Cs, the impact of the transition $\alpha \rightarrow \beta$ is weakened, with suppression of the phase change features in the c-axis. We find on the inclusion of Cs the a-axis lattice parameter drops significantly across the temperature range, with a less significant additional drop between ∼150 and 260 K from the Cs5, to Cs8 and Cs10 sets, as shown in Figure 8.8 [17]. This brings the unit cell to be closer to cubic in the β phase range as is seen in the $a/(c\sqrt{2})$ ratio.

The data presents an additional shift beyond the symmetry breaking asso-

[17] A observation in the set of a- and c-axis parameters is observed for $FAPbI_3$ in [Weber et al., 2018].

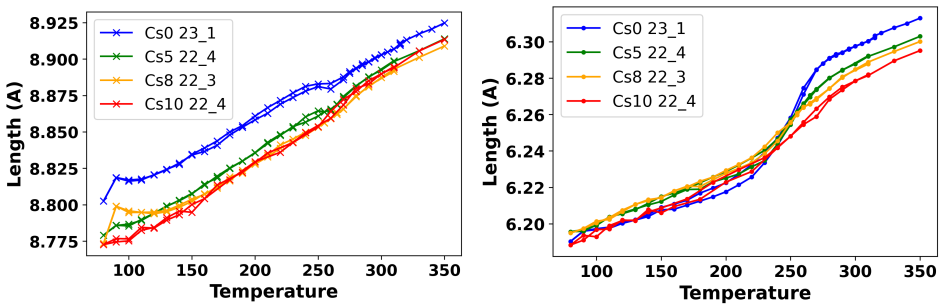

(a) (b)

Figure 8.8: Tetragonal unit cell parameters of parametric refinement sets (a) a-axis, (b) c-axis.

ciated with the $\alpha \rightarrow \beta$ transition between 80 and 90 K. This is accompanied by a levelling off of the a-axis length at the temperatures above this point for Cs0 and Cs8, with an insignificant effect on the trend for Cs5 and Cs8, Figure 8.8. In addition there is a discontinuity in the $a/(c\sqrt{2})$ and octahedral tilt parameters of Figure 8.5. For $a/(c\sqrt{2})$ the discontinuity grows from Cs0 to Cs8. For octahedral tilt, the difference for Cs0 and Cs5 is smaller than that of Cs8. For Cs10 the discontinuity is insignificant both parameters, the octahedral tilt parameter offers stable values, while the noise in the $a/(c\sqrt{2})$ prevents a meaningful comparison. This is attributed to the peak intensities being the more reliable observation in the noisy Cs10 data, compared to the peak shape (broadening), as discussed in Section 8.3. In the case of the apparent bond length, Figure 8.7, the Cs containing sample appears to converge to similar values at 80 K with the Cs5 slightly larger than the Cs8 value, in contrast the significantly larger Cs0 value.

Sudden shifts in lattice parameter at a temperature lower than the $\alpha \rightarrow \beta$ transition is most commonly attributed to a γ phase in hybrid perovskites [Fabini et al., 2016]. In Chapter 7, the presence of weak additional peaks were established below 90 K, which could not be attributed to a the presence of an orthorhombic phase [18]. In the Cs containing sets, the lower peak intensities prevent the identification of such peaks. The lattice parameter shift is compared to the work of Weller *et al.*, where a discontinuity in peak

[18]The $FAPbI_3$ phase has been reported in literature as a tetragonal symmetry [Weber et al., 2018].

positions was observed for the $\beta \rightarrow \gamma$ transition of $MAPbI_3$ at 165 K [Weller et al., 2015b]. In Lehmann *et al.*, the substitution of Br into this composition resulted in a $\beta \rightarrow \gamma$ transition at $\sim$125K for $MAPb(Br_{0.2}I_{0.8})_3$ [Lehmann et al., 2019]. An addition, the literature values for $FAPbI_3$ are lower than $MAPbI_3$ at 132−141 K, Table 1.3 [Kawachi et al., 2019]. It is considered that the inclusion of Br for the present data could suppress the $\beta \rightarrow \gamma$ transition to lower temperatures than observed Lehmann *et al.*'s $MAPb(Br_{0.2}I_{0.8})_3$.

An additional consideration is the glassy freezing of the organic cation which has been reported for $FAPbI_3$ below 100 K by Fabini *et al.* and below 140 by Weber *et al.* with the latter corresponding to the $\beta \rightarrow \gamma$ phase change [19]. [Fabini et al., 2017, Weber et al., 2018]. This is intrinsically linked with phase transitions in the perovskite structure, and may have been responsible for the weak additional peaks at 80 K in the Cs0 data-set [Fabini et al., 2017, Kawamura et al., 2002, Weber et al., 2018].

8.6 Conclusion

We have assessed the effect of Cs addition on structurally related features using the parametrisation of simultaneously refined data-sets. For Cs containing triple cation hybrid-perovskites, which have been shown in literature to suppress the δ phase in $FAPbI_3$ and $(FA, MA)PbI_3$ hybrid-perovskites [Saliba et al., 2016, Syzgantseva et al., 2017] The addition of Cs into mixed and triple cation hybrid-perovskites is well established for improving the PCE and stability to light and moisture PVs. [Kawachi et al., 2019, Saliba et al., 2016] The data quality, imposed refinement constraints have been discussed with the application of parametrisation shown in Figure 8.5, and the resulting effect on unconstrained parameters in Figure 8.7.

This included the *bond angle drop off*, Table 8.1, which corresponds to the onset of the $\alpha \rightarrow \beta$ transition. The increase with Cs was suggested as related to relative stabilisation of the tetragonal phase, in part due a corresponding

[19] Cation orientation in $FAPbI_3$ as a function of temperature in the works of Fabini *et al.* by neutron total scattering at various temperatures and DFT modelling and Weber *et al.* by variable temperature neutron diffraction, DFT modelling, and Ab initio molecular dynamics calculations.

decrease of the tolerance factor by the smaller cation. With this, a divergence between the *bond angle drop off* and the $a/(c\sqrt{2})$ ratio shift was observed to increased with Cs content, corresponding to a delayed response in the diffraction patterns showing tetragonal character on cooling. This is proposed as consistent with the presence of heterogeneous domains in the mixed cation, mixed halide perovskites, as has been reported by Barrier *et al.*, where variation in composition result in domains with varying Goldschmidt tolerance factors and related tetragonal phase stability [Barrier et al., 2021]. In addition the inclusion of Br in the structure has been discussed in association with a $\beta \rightarrow \gamma$ transition, which was suppressed to lower temperatures than what has been observed in similar systems.

Within the Cs0 and Cs5 compositions, a slightly larger $a/(c\sqrt{2})$ ratio is noted around the local maxima near 220 K on heating, compared to the cooling data. It is unclear, if similar observations or trends may be present in Cs8, while the difference between heating and cooling traces is in Cs10 data could not be evaluated with the present data. In future work, temperature cycling from room temperature to a temperature which does not pass the $\beta \rightarrow \gamma$ transition could inform the whether structural changes of the $\beta \rightarrow \gamma$ transition are related to the difference observed in cooling and heating direction for the $a/(c\sqrt{2})$ ratio. The collection of such diffraction data with a well resolved peak shape could inform whether micro-strain is related to the observed difference. In addition, variable temperature neutron diffraction and neutron total scattering can inform on structural effects related to the organic cation.

Attempts have been made to reliably and critically assess the Cs10 dataset, the investigation of this set provided an interesting exercise of working with low intensity data, as exemplified by Figures 8.1, 8.3 and 8.6, and by the discussions featured in Section 8.3. The intensity difference between the Cs5 and Cs10 samples in Figure 8.2 showed indications of greater octahedra tilt in the Cs10 sample which was later reflected in the parametrised refinements of Figure 8.5. The clear trends observed in this data, such as the Pb-X-Pb bond angle are considered reasonable indications of the system, while the values for the $a/(c\sqrt{2})$ ratio are subject to greater scrutiny, especially for their α phase values which deviated further from the idealised value of 1, compared to the Cs0, Cs5, and Cs8 sets.

This work can be extended by the collection of high resolution XRD data using larger sample volume for better intensity to access finer structural details. Heat capacity measurements across a corresponding temperature range would be a valued addition, to assess the energy barriers of the pseudo-cubic to tetragonal and $a^0a^0a^0$ to $a^0a^0c^+$ symmetry breaking events in the Cs containing triple cation hybrid-perovskites.

Chapter 9

Phase composition and photophysical properties of the mixed PA/MA-based lead bromide perovskites systems

Contents

9.1 Introduction **190**

9.2 Structure determination and modelling: $(PABr)_{2x}(MABr)_{1-x}PbBr_2$ **191**

9.3 Compositional study of the $(PABr)_{2x}(MABr)_{1-x}PbBr_2$ system **196**

9.3.1 XRD: Observations and trends 199

9.3.2 XRD: Data quality, comparing data-sets 201

9.3.3 Photophysical properties 205

9.4 2-Step: PABr on $MAPbBr_3$ **212**

9.4.1 Phases as a function of dosage 213

9.4.2 Annealing of 0.1 and 0.2 M films 214

9.4.3 $\mathbf{(PABr)_{2x}(MABr)_{1-x}PbBr_2}$, $x = 0.8$ sample ageing 215

9.5 Discussion **217**

9.5.1 Conclusion and future work 221

9.1 Introduction

In the previous chapters, we have discussed the properties and modelling of 3-dimensional (3D) hybrid-perovskites. In this chapter we explore layered hybrid-perovskites which form 2-dimensional (2D) and quasi-2D systems, and mixed 2D/3D systems. The crystal structure of these materials has been described in Section 1.2, with the applications and performance of these materials discussed in Section 1.4.

The formation of 2D and quasi-2D perovskites takes the form $(A')_2A_{n-1}PbX_{3n+1}$, in which A' is the organo-ammonium cation, forms a barrier layer between PbX_6^{4-} octahedra. These materials have tunable electronic properties that can be optimised for photovoltaic and luminescence properties among other applications, as described in Section 2.2. The A' cations have additionally been used as either an additive or capping layer, for defect passivation and reducing ion mobility in high performance hybrid-perovskite devices such as photovoltaics, as discussed in Section 2.3.4.

In the following sections, starting with Section 9.2 we identify and model structures for $(PA)_2MA_{n-1}PbBr_{3n+1}$ phases [1]. In Section 9.3, we follow the relationship between phase formation and composition in the $(PABr)_{2x}(MABr)_{1-x}PbBr_2$ system, where $x = 0$ and $x = 1$ correspond to 3D and an $n = 1$ layered structures respectively. This is considered using XRD, optical absorption spectroscopy, and photoluminescence (PL) spectra. In Section 9.4 we consider an alternative fabrication process to assess any changes in the formation of phases, where a PABr in isopropanol solution is coated onto an annealed $MAPbBr_3$ film at various solution concentrations. The results are discussed in their respective sections, with additional discussion in Section 9.5 in which broader comparisons are considered.

Thin film samples were prepared by spin coating, as described in Section 4.4. For Section 9.2 powder samples were prepared from thin-films as per Section 4.5. The precursor dilutions for the $(PABr)_{2x}(MABr)_{1-x}PbBr_2$ system are described in Section 4.4.4. The absorption and PL spectra were collected and analysed, as described in Section 4.6. The XRD data was collected on a Bruker D2 Phaser using CoKα radiation, and analysed using the TOPAS-Academic as per Sections 4.7.2 and 4.9.1, using the refined instrument profile in Section 4.8.2.

[1] PA: propylammonium, MA: methylammonium

9.2 Structure determination and modelling: $(PABr)_{2x}(MABr)_{1-x}PbBr_2$

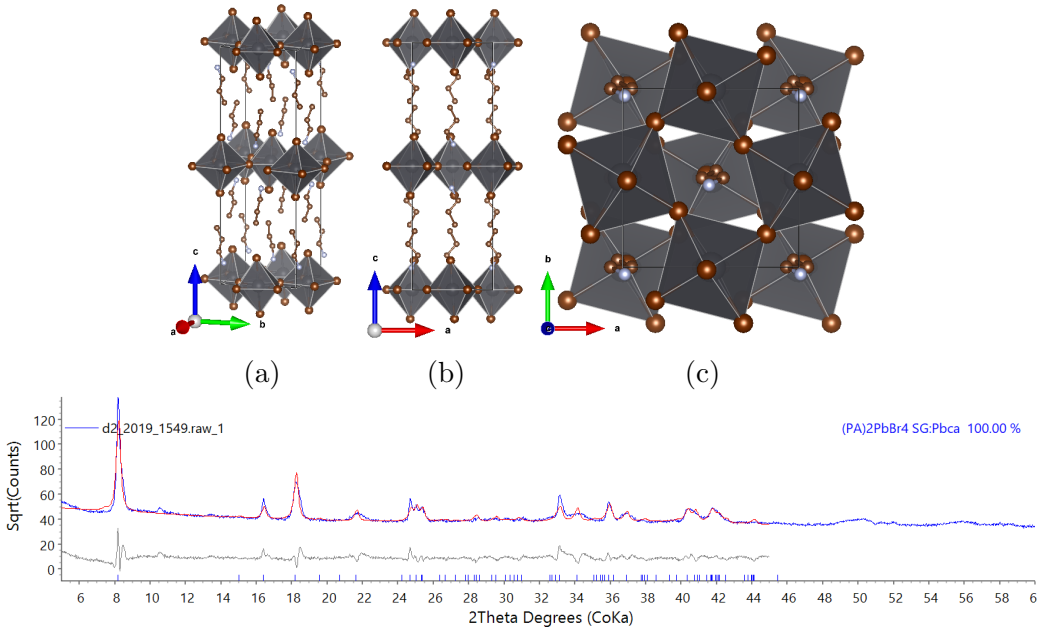

Figure 9.1: Structure modelling of a Pb-Br framework of the layered $n = 1$ phase against the $(PA)_2PbBr_4$ XRD pattern (CoKα)

Layered structure models were developed and refined against thin-film samples of a $(PA)_2PbBr_4$ and $(PABr)_{2x}(MABr)_{1-x}PbBr_2$, $x = 0.8$ compositions, corresponding to an $n = 1$, and a mixed $n = 1$ and $n = 2$ phase composition respectively, Figure 9.1 and 9.2. The structure models are composed of symmetry related rigid-bodies. For the $n = 1$ phase, the rigid body octahedra and a PA^+ organic chain are replicated through the structure by the symmetry of a *Pbca* space group, provided in App. E.3.3. In the $n = 2$ structure model half of the octahedra in the cell are defined, and replicated using a $P11m$ space group across the cell. The a and b unit cell parameters were defined as using projections of Pb−Br bonds of the octahedra while the c-axis was free as the stacking direction of the layers, with constraints such that $a = b$ in the final model. The refinements made use of both least square, and combination Monte-Carlo/least squares optimisation.

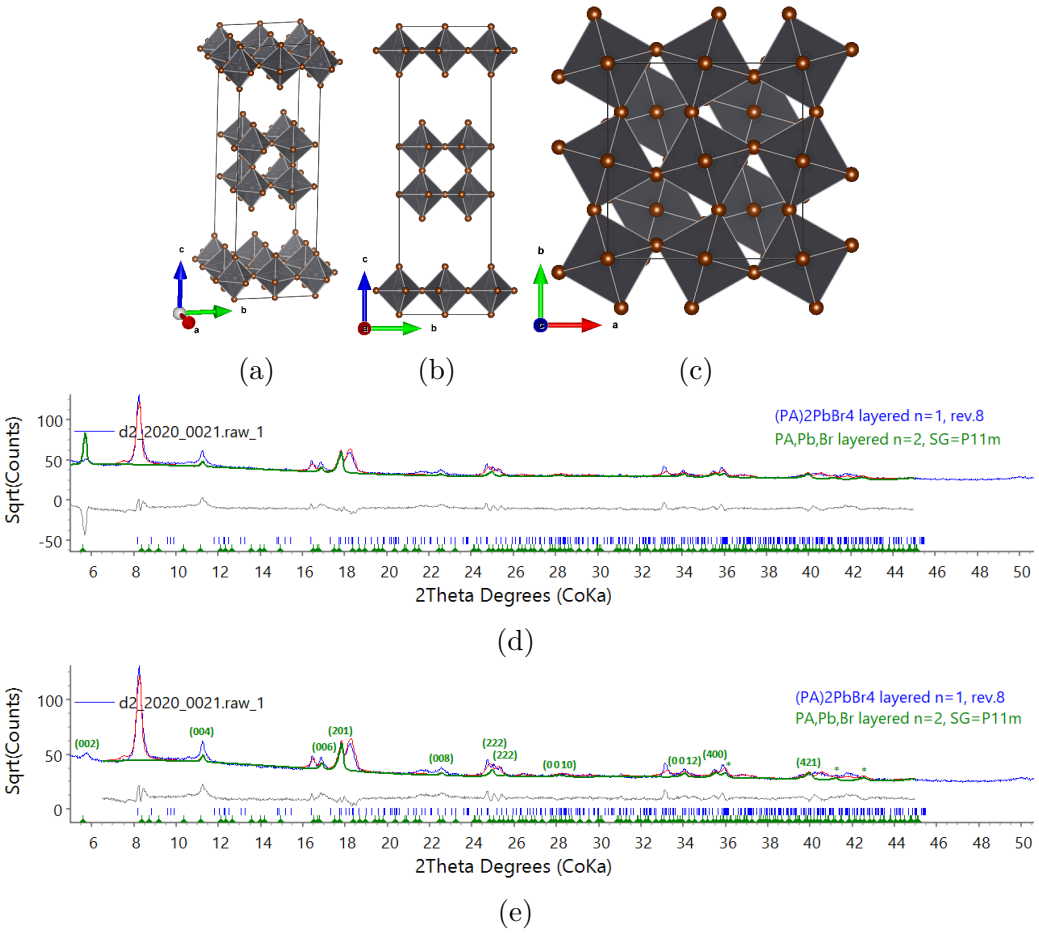

Figure 9.2: Structure modelling of a Pb-Br framework of the layered $n = 2$ and $n = 2$ phases against the $(PABr)_{2x}(MABr)_{1-x}PbBr_2$, $x = 0.8$ XRD pattern (CoKα), $n = 1$ model revision 8.

The $n = 1$ phase model in Figure 9.1d was refined against the $(PA)_2PbBr_4$ sample. The model made use of an orthorhombic unit cell with a *Pbca* space group with unit cell parameters refined to a, b, c of 8.152, 8.255, 25.092 Å [2]. The half cell c-axis parameter is 12.546 Å describing a layer of n octahedra and a single organic barrier layer [3] [4]. The inter octahedral rotation is represented by 14.7° rotation about the c axis and 5.7° about an axis perpendicular to this, this is comparable to the literature $(BABr)_2Pb_4$ structure, COD 1545801 with angles 12.6 and 6.3° respectively [5]. Within the octahedra we refine a Br-Pb-Br angle offset of 5.4° which is similar to the 4.9°, of COD 1545801. The rigid body PA^+ chain was defined using a $(PA)_2PbBr_4$ single crystal diffraction derived structure from literature [6] [Meresse and Daoud, 1989]. Hydrogen atoms were not considered due to their marginal electron density and corresponding marginal impact in the XRD pattern. The position and orientation of the $PABr^+$ cation was refined, while the bond lengths and angles were maintained at the literature values, as detailed in the rigid body model of App. E.3.3. The inclusion of the organic cation improves the refinement although the features for which the cation is responsible are insufficient for confidence in the placement and orientation of the cation, Section 3.5.1. The slight intensity differences between the model and raw data may result from subtle structural differences which may not be accessible by this *Pbca* space group constrained model. This could include relative displacement of the octahedra layers or non-orthogonal unit cell axes. This structure model is sufficient to assign a layered $n = 1$ Ruddlesden-Popper phase to the pattern of the $(PA)_2PbBr_4$ composition.

The sample prepared from a $(PABr)_{2x}(MABr)_{1-x}PbBr_2$, $x = 0.8$ composition, Figure 9.2 provided only a few well defined peaks which did not originate from the $n = 1$ phase. The clearest of these signals being at 5.6, 11.2, 16.8 and 17.8° 2θ. The previously modelled $n = 1$ structure model is evident as the dominant phase in the pattern. This was fitted to the $x = 0.8$ pattern with only lattice parameters, scaling, and crystallite size refined. The

[2] The structure file of the refined $(PA)_2PbBr_4$ phase is provided in App. E.3.4.

[3] A *Pbca* space-group is similarly observed for the $(BA)_2PbBr_4$ structure, COD 1545801.

[4] The half-cell c-axis length is used for Pawley refinements throughout this chapter.

[5] *BA*: butylammonium

[6] No experimental *(XRD or neutron diffraction)* $(PA)_2PbBr_4$ Ruddlesden-Popper structures found in the COD nor ICSD databases at the time of writing, database searches provided in App. E.3.

a and b lattice parameters were scaled by a single variable, while c was refined freely. The $n = 2$ phase was subsequently refined.

The $n = 2$ phase model included peaks at the positions 5.6, 11.2, 16.8 and 17.8° 2θ matching the raw data, and corresponding to the (002), (004), (006), and (201) Miller planes as labelled in Figure 9.2e. Here the (201) peak is exceptionally important, as this is essential for the determination of an $a = b$ lattice parameter [7]. The other non (00L) peaks observed in Figure 9.2e correspond to many of the subtle features in the diffraction pattern adding to the models legitimacy. In contrast to the well placed peak positions, the relative peak intensities are explained well above 12° 2θ with the (002) and (002) peaks at 5.6 and 11.2° 2θ being weaker and stronger than the model respectively, Figures 9.2d and 9.2d.

The $n = 2$ phase model, in Figure 9.1d refined an octahedral rotation about the c axis of 16° which is similar to the 15° observed for the $n = 1$ model. The $n = 2$ model made use of a unit cell with tetragonal restrictions in a *P11m* space group, with unit cell parameters, $a = b$ of 11.755 Å, c of 36.753 Å and β of 90°. For this unit cell the $a/2$ value of 5.863 Å corresponds to a single octahedra unit cell. This is comparable to a cubic $MAPbBr_3$ unit cell parameter of 5.920 Å with the difference attributed to octahedral rotation. Similar values are observed for literature for $n = 1$ and $n = 2$ structures, where this value is reported as low as 5.854 Å for $(BA)_2PbBr_4$ $n = 1$ (COD 1545801), Table E.3. The half-cell c-axis parameter is 18.378 Å which will be compared to Pawley refinements in which c-axis corresponds to a single set of n octahedra and a single organic cation layer in contrast to two of each for many Ruddlesden-Popper cells. This unit cell was reduced using ISOCIF [Stokes et al., 2006, Stokes et al., 2017] for an equivalent unit cell with a *Cmce* space group and the lattice parameters a, b, and c of 36.753, 8.312, and 8.312 Å, App. Figure E.6.

For an $n = 2$ phase, the c-axis parameter should be approximately the sum of the $\frac{(a+b)}{\sqrt{2}}$ and c lattice parameter of the $n = 1$, *P11m* modelled structure, this corresponds to adding space an extra row of $PbBr_6^{4-}$ octahedra along the c-axis for between each set of successive layers. This is calculated

[7] The values for the a and b lattice parameters are expected to be similar vales in this system. For the diffraction pattern in question, there is insufficient information differentiate a from b.

to $\frac{(8.152+8.255)}{\sqrt{2}} + 25.092 = 36.694$ Å which is close to the 36.753 Å of the modelled $n = 2$ phase, such that it is reasonable to expected closely related PA^+ packing between the structures.

The peak positions and c-axis length were in agreement with the expected value calculated from the $n = 1$ phase. This provides a strong indication of an appropriate unit cell size, while the low angle (002) and (004) peak intensity mismatch indicate the presence of some discrepancies between the measured pattern and the longer range inter-planar spacing in the unit cell. This would be consistent with a slight variations in the stacking layer spacing of the $n = 2$ phase leading to intensity loss for the related peaks, especially these low angle peaks which correspond to a longer range order and larger d-spacing. This provides a reasonable case for the assignment of the $n = 2$ phase to the additional peaks observed in the $(PABr)_{2x}(MABr)_{1-x}PbBr_2$, $x = 0.8$.

9.3 Compositional study of the $(PABr)_{2x}(MABr)_{1-x}PbBr_2$ system

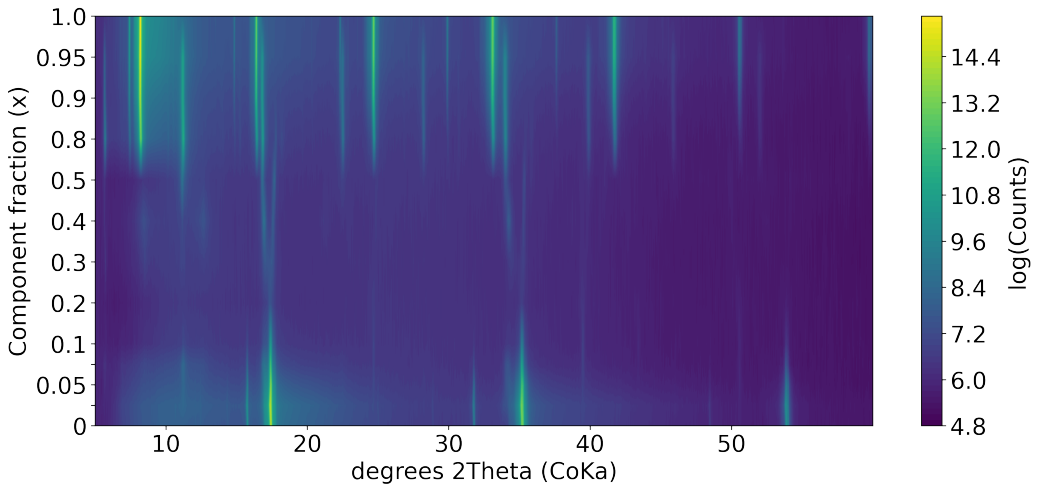

Figure 9.3: $(PABr)_{2x}(MABr)_{1-x}PbBr_2$, (13-step X-ray diffraction data-set) this data set was collected to 80° 2θ and plotted to 60° 2θ.

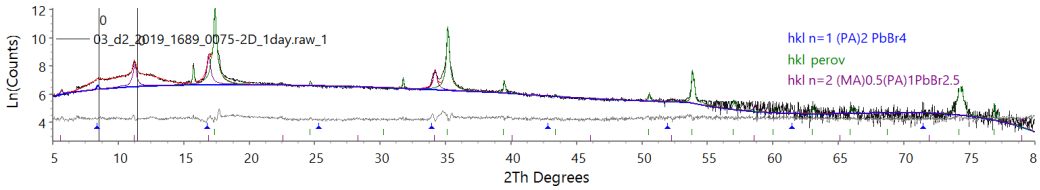

(a) $x = 0.075$, natural logarithm y-axis scale

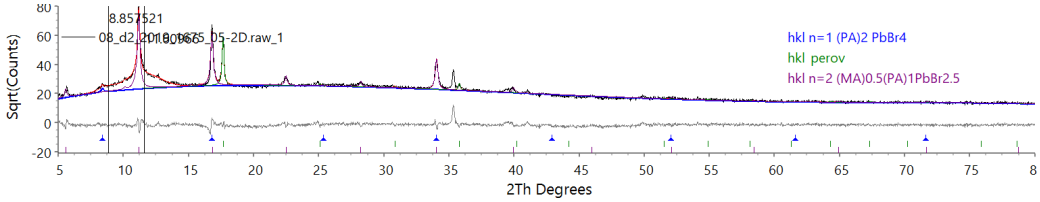

(b) $x = 0.5$

Figure 9.4: Refinements showing the faint $n = 1$ phase present at $x \leq 0.5$ in the $(PABr)_{2x}(MABr)_{1-x}PbBr_2$ (13-step X-ray diffraction dataset)

.

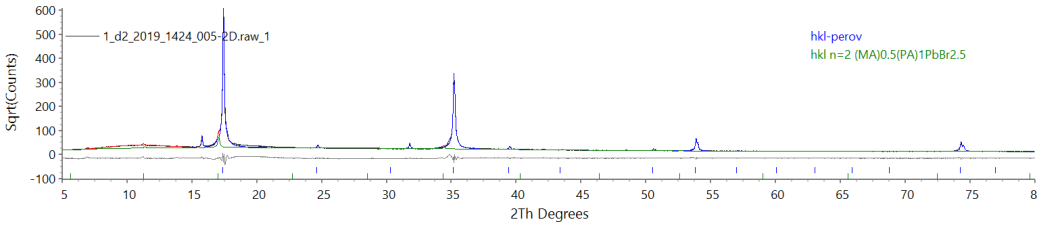

(a) $x = 0.05$

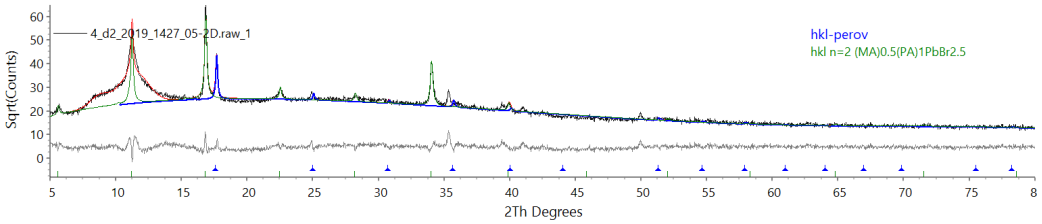

(b) $x = 0.5$

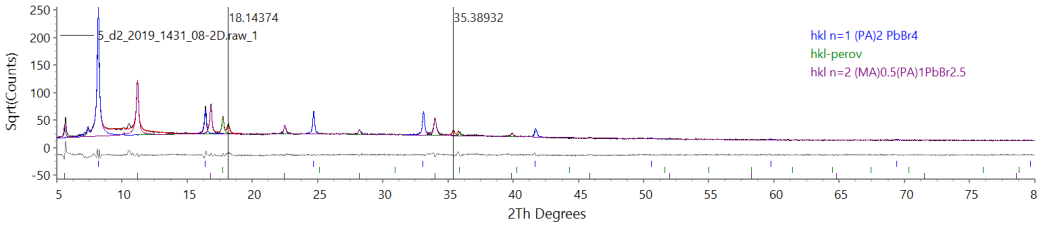

(c) $x = 0.8$

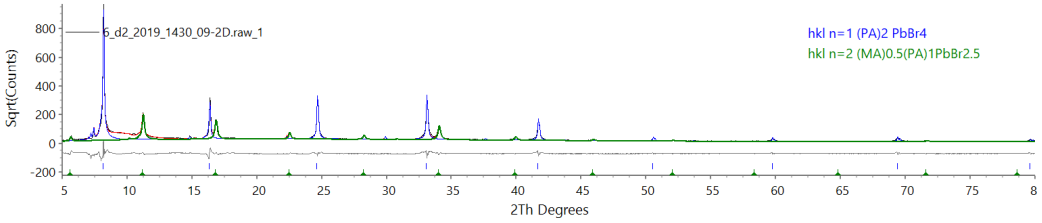

(d) $x = 0.9$

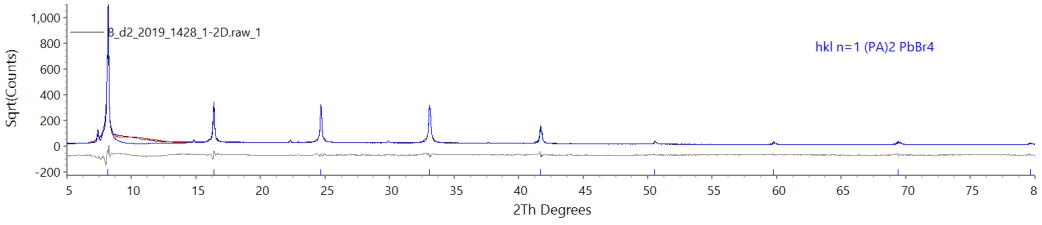

(e) $x = 1.0$

Figure 9.5: Selected individual refinements of $(PABr)_{2x}(MABr)_{1-x}PbBr_2$ (9-step X-ray diffraction dataset)

.

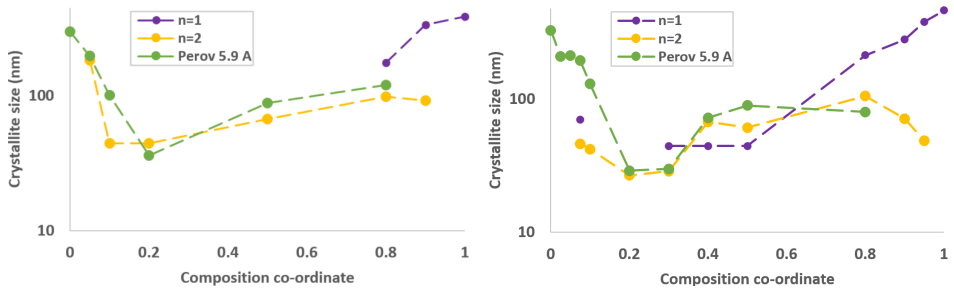

(a) 9-step

(b) 13-step

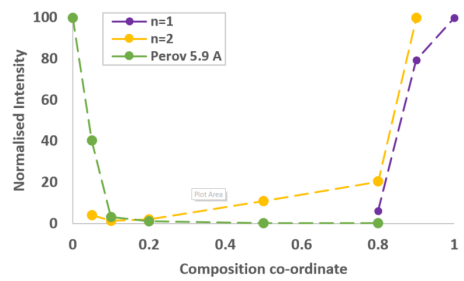

(c) 9-step

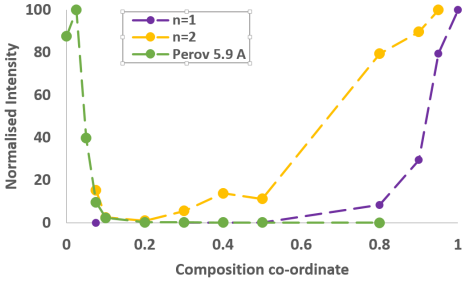

(d) 13-step

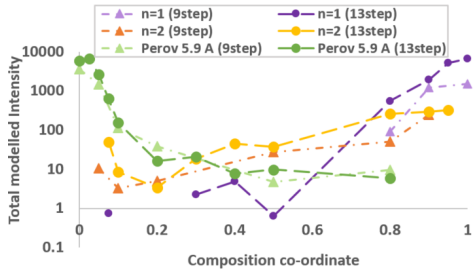

(e)

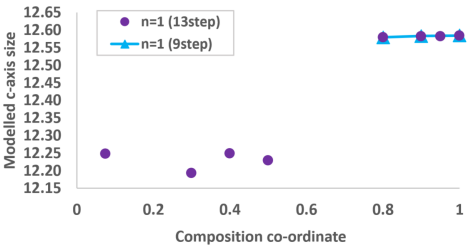

(f)

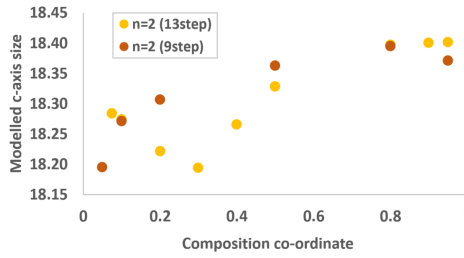

(g)

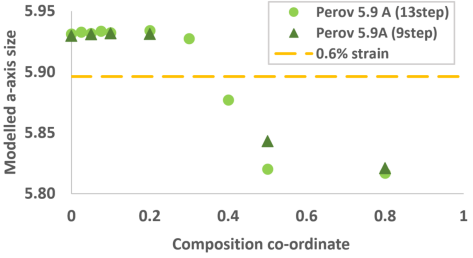

(h)

Figure 9.6: Diffraction derived unit cell parameters, normalised peak intensities, and crystallite size of $(PABr)_{2x}(MABr)_{1-x}PbBr_2$, both 9 and 13 step data-sets.

9.3.1 XRD: Observations and trends

The $(PABr)_{2x}(MABr)_{1-x}PbBr_2$ data consists of two data-sets, a 9-step and a 13-step set. The 13-step data-set offers a finer compositional resolution towards low x compared to the 9-step set. In the low x region, higher n 2D and quasi-2D structures have the highest probability of occurring [Quintero-Bermudez et al., 2018]. The duplication additionally provides means to evaluate consistency on repetition as discussed in Section 9.3.2. The x values for these sets are provided in Section 4.4.4. XRD data was collected using a CoKα source from 5 to 80° 2θ with a 0.026° step size. The 13-step XRD data-set is plotted in Figure 9.3, a selection of modelled patterns are presented in Figure 9.5, and the fit parameters in Figure 9.6 [8].

The presence of phases is the 9- and 13-step XRD data-sets are evident from the normalised refined intensities of Figures 9.6c and 9.6d respectively. On the addition of PA_2PbBr_4 to $MAPbBr_3$ with increasing x, we observe a rapid decline in the "perov 5.9 A" phase with the normalised intensity dropping below 4 % at $x = 0.1$ for both data-sets. For the peaks modelled using this phase, a strong shift in peak position is observed in the range $0.3 \leq x \leq 0.8$. These peak shifts exceed the strain reported by Wang *et al.* of ∼0.6 % from the inclusion of BA^+ into a $FA_{0.83}Cs_{0.17}Pb(I_{0.6}Br_{0.4})_3$ system as plotted in Figure 9.6h [9]. In the work of Wang *et al.* strain was observed to gradually increase with BA concentration, in contrast to the step like trend in Figure 9.6h [Wang et al., 2017b]. In addition, the modelled crystallite size is expected to decrease with a decreasing phase fraction of the "perov 5.9 A" phase. We observe such a trend for $x \leq 0.3$ after which there is an increase in crystallite size with continued decreasing intensity for the associated peaks. These observations suggest the formation of a distinct phase other than $MAPbBr_3$, for $x \geq 0.4$ with quasi-2D phases available as the closest related structure which would be expected in this system. In relation to this, we have established the $n = 1$ and $n = 2$ phases for this system as Ruddlesden-Popper (RP) 2D phases in Section 9.2. RP structures have an offset between successive layers of octahedra, which results in destructive interference, and a subsequent absence of the peak related to the 3D (100) reflection. This is incompatible with the present data where such a peak is observed.

[8] The 9-step XRD data-set is plotted in App. Figure E.13.

[9] This is both a larger A′ cation and larger perovskite unit cell than the PA and $MAPbBr_3$ combination.

It is considered that for structures with a small n, the growth and orientation is controlled by the energy barrier in forming new layers, leading to the formation of new layers on previous layers, anchored to the substrate with wide coverage leading to a preferred horizontal stacking direction. In contrast large n structures growth is controlled by the octahedra which anchor to the substrate with vertical formation of the organic layered [Quintero-Bermudez et al., 2018]. While we observed Ruddlesden-Popper phases for $n = 1$ and $n = 2$, the different formation dynamics expected for quasi-2D structure allow the consideration of an alternate offsets between successive layers of n octahedra, which do not result in an absence of the peak related to the 3D (100) reflection. Such structures may include mono-cation Dion-Jacobson phases in which either no offset is observed, or an in-plane offset which is orthogonal to the scattering vector in the symmetric Bragg-Brentano measurement, thus would not directly affect the measured scattering [Tremblay et al., 2019].

The $n = 2$ phase first appears at $x = 0.05$ and $x = 0.075$ for the 9- and 13-step data-sets, respectively (Figures 9.5a and 9.4a). In Figure 9.3, the strongest peak of $n = 2$ at $11.2°$ 2θ shows a sudden drop in intensity followed by a gradual increase with x until the last data-point before $x = 1$.

The $n = 1$ phase is observed with strong clear peaks for $x \geq 0.8$ in both sets, with a peak at 8.164 ± 0.003 and 8.157 ± 0.001 ° 2θ for the 9 and 13-step data-sets respectively, Figure 9.5c. [10]. For $x \leq 0.5$, only the strongest $(00l)$ peak of the $n = 1$ phase is observed in 13-step data-set, with intensity faintly visible for $x \in \{0.075, 0.5\}$ near $8.374 - 8.380°$ 2θ, Figure 9.4. Stronger peaks were observed for $x \in \{0.3, 0.4\}$ at 8.403 ± 0.003 ° 2θ, with an absence for $x \in \{0.1, 0.2\}$, Figure 9.6e [11]. The $n = 1$ peak for $x = 0.075$ is weak to the point of barely being distinguishable, even with intensity plotted in a *ln()* scale, shown in Figure 9.4a. This makes the absence for $x \in \{0.1, 0.2\}$ explainable by the expected variations resulting from the manually executed sample fabrication process.

[10] Plus-minus ($\pm$) is used to indicate the value range rather than an error for this section.

[11] In the PABr 13-step data-set, weak n=1 peaks had their relative intensities fixed to that of the $x = 1$ refinement

The peak position and corresponding unit cell parameters of the $n = 1$ assigned phase appears as two distinct segments, Figure 9.6f corresponding to the mean unit cell parameters, 12.23 and 12.58 Å for the $x \leq 0.5$ and $x \geq 0.8$ respectively. This presents a large 0.35 Å difference. The difference for the $n = 1$ phase would correspond to a strain of 2.8 % which is exceptionally large for a structure not under mechanical stress. Compositionally and mechanically induced strain no larger than 0.7 % has been reported for hybrid-perovskites literature [Wang et al., 2017b, Zhao et al., 2017]. The stepped nature of the segmentation is not consistent with substitutional effects expected by *Vergards'* law, nor it this an expected behaviour of a strain related process. This alongside the intensity minimum for $n = 1$ at $x = 0.5$ offers a reasonable case for structural or compositional differences of the segments, if not distinct origins.

9.3.2 XRD: Data quality, comparing data-sets

The XRD derived parameters of the 9- and 13-step data-sets were compared as a means to consider and critique the data integrity.

For this the total modelled phase intensities are compared, Figure 9.6e. The layered $n = 1$ and $n = 2$ show lower total intensities for most values of x. In the case of $n = 2$ both the values at $x \leq 0.2$ and $x \geq 0.8$ would better fit the observed trend if shifted towards the centre $x = 0.5$. As these are opposite directions this is inconsistent with a systematic error related to the organic cation concentrations.

The peak intensities of the effectively phase pure $x = 0$ and $x = 1$ refinements were compared. At $x = 0$ a relatively small difference between the 9- and 13-step values was observed, with a much larger distinction for $x = 1$. An example of the variation between these $x = 1$ and an additional $(PA)_2PbBr_4$ sample is provided in App. Figure E.15, where the additional sample presented an intermediate intensity between the patterns. Each of the films were prepared on separate days, under an ambient uncontrolled atmosphere, from PABr salts which varied in the time between when they had been synthesised or washed with diethyl-ether and used for fabrication

[12]. These inter-sample variations presented a larger effect than the variation observed from 15 days of ageing on a $(PA)_2PbBr_4$ film, App. Figure E.16. The total modelled intensity of the "perov 5.9 A" phase in Figure 9.6e, shows separate instances where each data-set presents stronger values. In the case of $x = 0.2$ both the "perov 5.9 A" and $n = 2$ phases are weaker in the 13-step data-set, while for $x = 0.5$ the opposite is true.

Considering the lattice parameters, close agreements between the sets was observed for $n = 1$, $x \geq 0.8$ and the "perov 5.9 A" phase for $x \leq 0.3$. One distinguished difference is the unit cell parameter of the "perov 5.9 A" phase, where there is close positioning of all but the value at $x = 0.5$ where the values differ by 0.02 Å, Figure 9.6h.

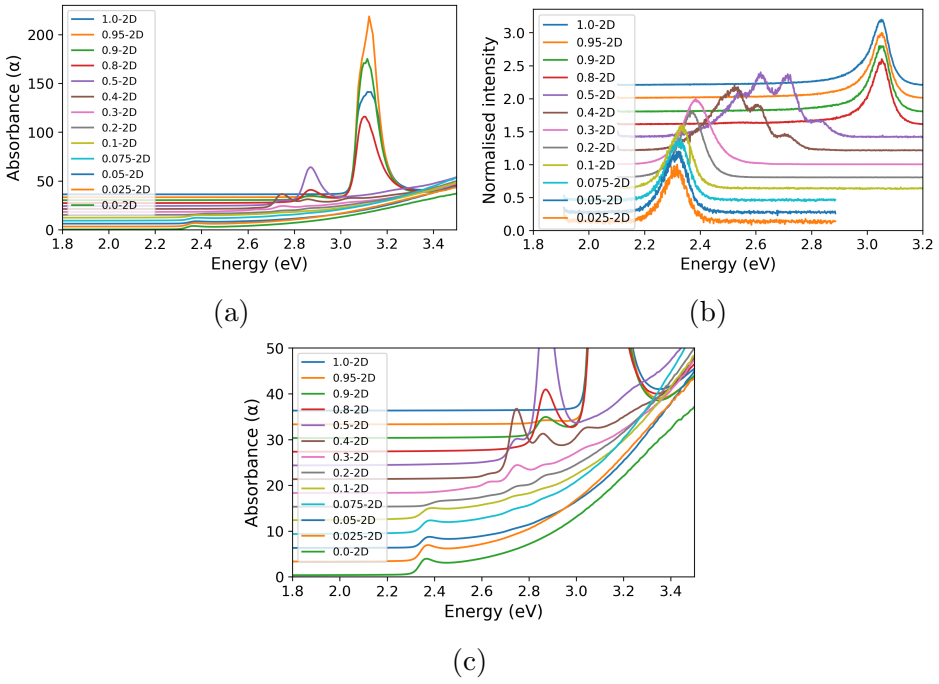

Figure 9.7: Optical data of the $(PABr)_{2x}(MABr)_{1-x}PbBr_2$ system. (a) Absorbance, (b) Normalised photoluminescence, and (c) absorbance with a y-scale chosen to highlight weaker features in (a). (13-step data-set)

[12]The quality and purity of the PABr precursor salt can have a substantial impact on the diffraction pattern intensity of the salt as demonstrated in App. Figure E.17

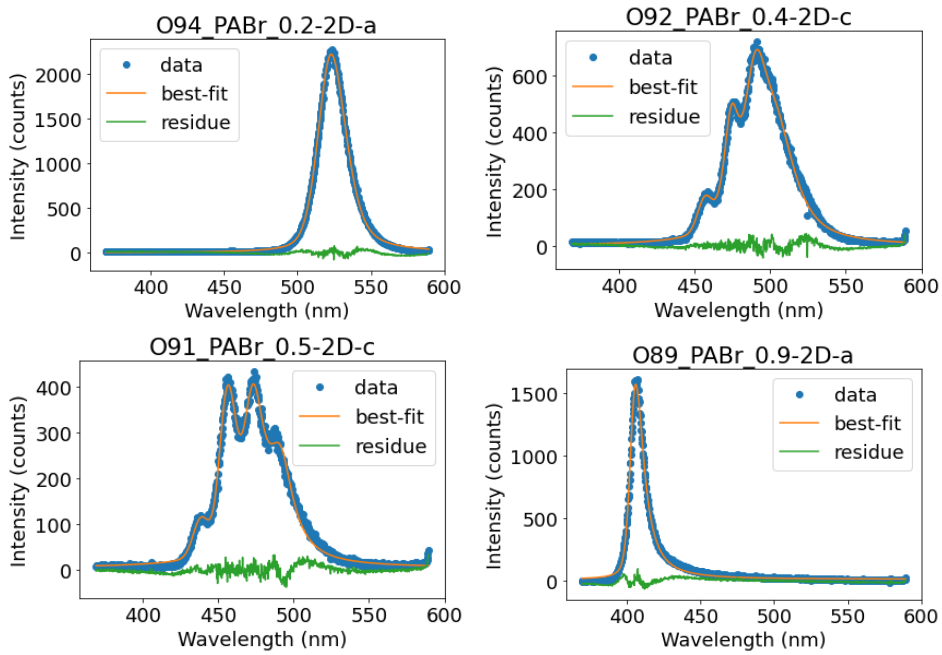

Figure 9.8: Photoluminescence measurements of $(PABr)_{2x}(MABr)_{1-x}PbBr_2$, (blue) raw data, (orange) fitted function, (green) residual. Fits for the full data-set are provided in App. Figure E.1.1. (13-step data-set)

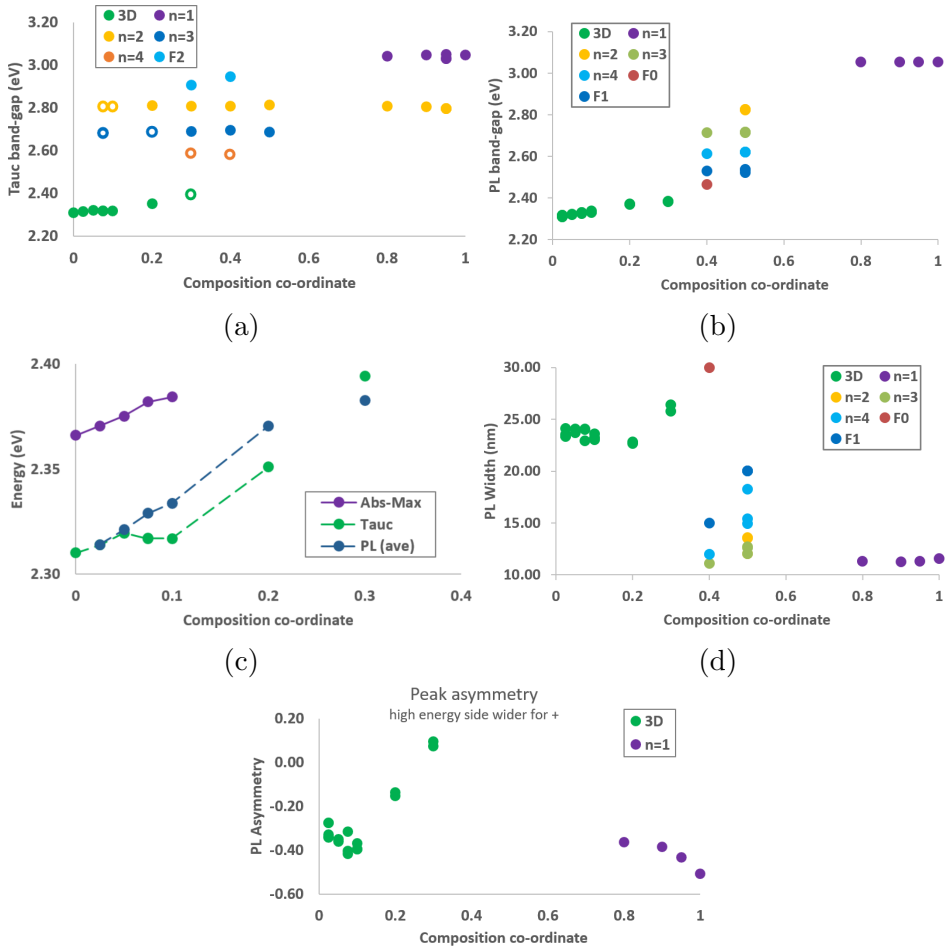

Figure 9.9: Photophysical data for the $(PABr)_{2x}(MABr)_{1-x}PbBr_2$ system. (a) Tauc derived band-gap values, open circle refer to faint features (b) photoluminescence (PL) peak maxima. (c) Tauc and PL optical bandgap for the 3D phase, (d) PL peak width, (e) PL peak asymmetry using a width ratio with an offset such that a positive value related to a greater width on the higher energy side. (13-step data-set)

9.3.3 Photophysical properties

Optical absorbance and photoluminescence (PL) data was collected on the $(PABr)_{2x}(MABr)_{1-x}PbBr_2$ sample-set, Figure 9.7. Absorbance data was analysed using Tauc plots with a direct band-gap consideration. The photoluminescence data was modelled using split pseudo-Voigt functions where a single peak was observed. In the case of multiple overlapping peaks, symmetric pseudo-Voigt peaks were utilised to reduce parameter correlation between peaks. A selection of fits are provided in Figure 9.8. The methodologies are detailed in 4.6 with the considerations discussed in Section 2.4. One consideration worth reiterating is, in the presence of excitonic effects, the Tauc band-gap diverges from the optical bandgap by $E_{\text{Tauc}} = E_{\text{gap}} - E_x$, referring to the Tauc band-gap, optical band-gap, and excitonic binding energy respectively. The resulting Tauc band-gap values and fit parameters from the PL data are presented in Figure 9.9 and Table 9.1.

Phase identification

In Table 9.1, the Tauc band-gaps from *this work* were compared to the values determined in App. E.2 using data from Ma *et al.* [Ma et al., 2022] [13]. The original values from Ma *et al.* deviate significantly from the PL derived values of the same work. A comparison of the reprocessed Tauc values (App. E.2) showed a much closer agreement with a difference in the 10's of meV. A difference between the PL and Tauc derived values is expected due to exciton binding energies inherent in layered perovskites, Section 2.2.2.

For the optical data in Figure 9.9, phases were assigned for the 3D phase, and $(PA)_2MA_{n-1}PbBr_{3n+1}$ $n = 1$ to $n = 4$ phases as indicated in Table 9.1 with a basis as follows. The assigned phases expressed Tauc band-gaps and PL maxima within 10's of meV of the reprocessed Tauc and as reported PL data from Ma *et al.*. The largest difference was observed for the $n = 1$ Tauc band-gaps of 3.041 eV ($\sigma = 0.009$ eV) and 3.00 eV with a difference of 44 meV

[13] App. Section E.2 accounts for the background and multiphase nature of the Ma *et al.* optical data using the approach discussed in Section 2.4.1 based on a 2018 publication by Makiła *et al.* [Makuła et al., 2018].

Table 9.1: Photoluminescence and Tauc derived bandgaps with literature comparisons for $PA_2MA_{n-1}PbBr_{3n+1}$ structures

Reference	**Method**	$n = 1$	$n = 2$	$n = 3$	$n = 4$	**F1**	**F0**	**3D**
Ma *et al.*, 2022	Tauc	3.63	3.02	2.80	2.65			2.30
Appendix E.2	Tauc	3.00	2.81	2.72	2.55			2.33
Ma *et al.*, 2022	PL max	3.05	2.86	2.74	2.62			2.37
This work	Tauc	3.041	2.805	2.687	2.584			2.310
	(σ)	(0.009)	(0.006)	(0.006)	$\pm$0.008			$x = 0$
This work	PL max	3.055	2.824	2.715	2.619	2.531	2.465	2.314
	(σ)	(0.001)	(0.001)	(0.002)	(0.004)	(0.006)	-	$x = 0.025$
This work	AbsMax	3.118	2.869	2.749	2.638			
Stokes shift (meV)		63	44	34	19			57 *2
$E_{\mathrm{PL}} - E_{\mathrm{Tauc}}$ (meV)		13	20	28	34			0 *2

Average values are provided for *this work*, Standards deviations given between bracket, the value with a "$\pm$" symbol represents a range of 2 values, and where an x coordinate is specified a single value is presented.

Stokes shift: $E_{\mathrm{AbsMax}} - E_{\mathrm{PL}}$

AbsMax: The excitonic peak observed at the absorption maximum.

*2: The Stokes shift for the 3D phase refer to the $x = 0.025$ composition coordinate.

[14]. This is contrasted with similar variations between literature PL derived band-gaps for the BA_2PbBr_4, $n = 1$ layered structure of 2.97 and 3.01 eV from Yukta *et al.* and Shen *et al.* respectively [Shen et al., 2020, Yukta et al., 2021]. Such differences are attributed at least in part to the effect of preparation conditions on the electronic structure [Stoumpos et al., 2016]. Across the composition coordinate x in the diffraction and optical data-sets, the presence of Tauc plot features for the $n = 1$ and $n = 2$ phases at 3.055 eV ($\sigma = 0.009$ eV) and 2.805 eV ($\sigma = 0.006$ eV) largely corresponded to the presence of the $n = 1$ and $n = 2$ phases in the diffraction data, Figures 9.6d and 9.9a. One deviation from this is the presence of the $n = 1$ phase in patterns $x \leq 0.5$ in the diffraction data where the observed phase was exceptionally weak. These cases were only observed for the 13-step data-set and not in the 9-step data-set.

The absence of $n = 3$ and $n = 4$ in the diffraction data is suggested due to preferred orientation in the thin-film samples, coupled with the reciprocal

[14]The reprocessed value prior to rounding to significance was used for the difference $(3.041 - 2.997)$.

space accessible by PSD type detector of the diffractometer employed [15] [16]. This would be consistent with literature, where horizontal growth of the layers is reported to dominate in $n = 1$ structures while in $n > 4$ vertical growth is favoured. The intermediate stack thicknesses may have a mixed growth with compositional and kinetic effects such as solvent choice playing a role [Quintero-Bermudez et al., 2018]. Considering the 1-dimensional X-ray detector and symmetric diffraction geometry used for measurements, phases which do not have any crystallites with layers orientated horizontally [17], will not present diffraction peaks corresponding to the layering of the phase.

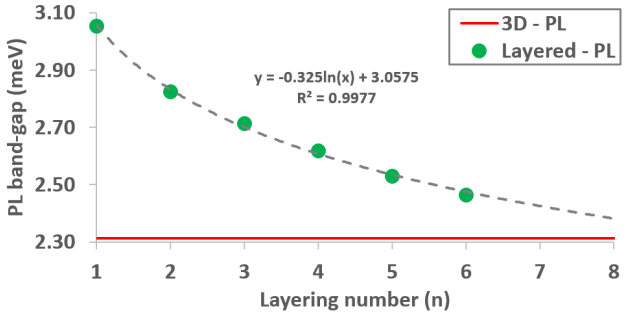

Figure 9.10: Photoluminescence band-gap values plotted against the most probable layering number n for $PA_2MA_{n-1}PbBr_{3n+1}$ structures

The identified phases $n = 1$ to $n = 4$ phases were plotted in Figure 9.10. With increasing n, the band-gap is expected to progressively get closer to the 3D limit as the quantum (and dielectric) confinement effects are reduced. The observed trend was fitted using a logarithmic function as an empirical approximation of this effect. The *F1* and *F0* PL features were tested as $n = 5$ and $n = 6$ providing an R^2 values of 0.9977, and as $n = 6$ and $n = 8$ for an R^2 of 0.9931 with the former presented in Figure 9.10. Structures with a lower n have been theoretically predicted to have a slightly greater thermodynamic stability as shown in the work of Quan *et al.*, this is not sufficient to result in the exclusive formation of a structure, rather a distribution of n is expected, as experimentally observed in literature [Quan et al., 2016, Quintero-Bermudez et al., 2018]. In addition Quintero-Bermudez *et al.*

[15] PSD: position sensitive detector, a class of 1-dimensional detectors used in X-ray diffractometers.

[16] Preferred orientation is discussed in Section 3.2.2.

[17] with their stacking direction perpendicular to the scattering vector

shows how the smaller butylammonium cation (BA^+) favoured lower n structure in comparison to the larger phenylethylammonium cations ($PhEA^+$) inferring mobility as a driving factor. Similar should hold for the PA^+ cation which is slightly smaller than BA^+. An assignment of $n = 5$ and $n = 6$ is reasonable as it exhibits a well fitting trend in optical band-gap alongside the previously identified layered structures, and it follows the sequential trend in n established by the $n \leq 4$ values for this set.

For the consideration of $n \geq 7$, the trend-line of Figure 9.10 was extrapolated to ∼2.425 eV for $n = 7$ which is ∼90 meV greater than the $x = 0.1$ 3D E_{PL} of 3.334 eV, Table 9.2. The PL peak full widths at half maximum are 85 and 100 meV for the $n = 1$ and $MAPbBr_3$ phases respectively, Figure 9.9d. Thus, should a $n \geq 7$ phase occur we would expect PL peak overlap with the 3D phase. We can subtly observe this expected effect in Figure 9.9e, where 3D phase peak for $x = 0.2$ shows asymmetry with the bias towards a higher energy, with a stronger effect observed in $x = 0.3$. The peak width at $x = 0.3$ show broadening in Figure 9.9d, and additionally for the PL feature *F0* at $x = 0.4$, supporting the possibility of a convolution of overlapping peaks. The low energy sides of the PL spectra for $x \in \{0.4, 0.5\}$ of Figure 9.8 show a positive *residual* trace which is an indication of weak unaccounted for intensity potentially corresponding to higher n phases peaks.

There is evidence of higher n phases of $n > 6$, limited information is accessible on these in regards to band-gap, layering thickness (n), and intensity. The feature *F0* has significantly larger broadening than similar PL peaks. This would be most convincingly explained by the convolution of additional weaker peaks of higher n, as such the observed PL intensity is expected to be red-shifted from a pure-phase $n = 6$ value.

Phases observed: absorption vs photoluminescence

Different optoelectronic processes are accessible by using absorbance and PL spectroscopy. This leads to a discrepancy between the observed features between these techniques, as evident from Figures 9.9a and 9.9b corresponding to optical transitions observed in the absorption and photoluminescence spectra respectively.

Table 9.2: Photoluminescence and Tauc derived bandgaps with calculated Stokes shift for the $MAPbBr_3$ based phase

x	**0**	**0.025**	**0.05**	**0.075**	**0.1**	**0.2**	**0.3**
Tauc (eV)	2.310	2.314	2.320	2.317	2.317	2.351	2.394
AbsMax (eV)	2.366	2.371	2.375	2.382	2.384	2.384	*1
PL average (eV)	-	2.314	2.321	2.329	2.334	2.371	2.383
Stokes shift (meV)	-	57	54	52	53	51	
$E_{\mathrm{PL}} - E_{\mathrm{Tauc}}$ (meV)	-	0.0	1.6	12	17	20	

***1:** An absorption maximum could not be clearly identified.

AbsMax: The excitonic peak observed at the absorption maximum.

Stokes shift: $E_{\mathrm{AbsMax}} - E_{\mathrm{PL}}$

In the absorption spectra features *F1* and *F0* could not be clearly identified which is attributed to their weak signal and the overlap with the 3D phase absorption features. In the PL spectra the $n = 1$ peak is exclusively observed for $x \geq 0.8$ and the $n = 2$ is only observed for $x = 0.5$ despite its wide range of presence in the absorption spectra. For $x \leq 0.3$ the 3D phase is the only clear PL peak. We relate this to the phase intensity modelled in the diffraction data, Figure 9.6e. For $x \geq 0.8$ the $n = 1$ phase was most intense dropping to orders of magnitude lower if observed at all for $x < 0.8$. For $x \in \{0.5, 0.4\}$, $n = 2$ is the most intense phase with the 3D phase most intense thereafter.

The layered phases identified in the absorption data for $x \leq 0.3$ were not observed in the PL data where the 3D phase is present. This is suggested to be the result of charge carrier transfer to the 3D phase occurring on a faster timescale than radiative recombination in the layered phases. This allows electrons to transfer to a lower energy level in the conduction band and hole to a higher level in the valence which are both energetically favourable processes [18] [Motti et al., 2019, Zou et al., 2018]. This can be accompanied by *photon recycling* in which the 3D phase, which has a smaller band-gap can absorbs emissions from the layered structures [Motti et al., 2019]. For the absence of the $n = 2$ phase in the PL data of samples where $n = 1$ is dominant, the mechanism is less clear. The stronger exciton binding energy of the $n = 1$ structure may prevent charge transfer to the lower energy conduction band of the $n = 2$ phase. It is evident that the multiphase nature of the system is closely linked to the absence of some phases in the PL data.

[18] Band structure and dispersion effects are discussed in Section 2.2.2.

Optical transitions

The electronic structure of 2D and 3D perovskites can be described using crystal field theory where the band-gap occurs between a Γ_6^+ energy state corresponding to the valence band, and a state derived from a Γ_6^- as the conduction bands [19]. In the case of the 3D structure the Γ_6^- state splits into Γ_4^- and Γ_1^- states with the former being the higher energy state. For the 2D structures the Γ_4^- is further split into the Γ_5^- and Γ_2^- states, from highest to lowest energy these are Γ_5^-, Γ_2^-, Γ_1^-. This is illustrated in the work of Tanaka *et al.* [Tanaka et al., 2003, Tanaka et al., 2005].

The absorption excitation is predicted to be strongest for the transition from ground to Γ_5^- with photoluminescence dominated by the Γ_2^- to ground [20] [21]. This is understood by the very fast $\Gamma_5^- \rightarrow \Gamma_2^-$ relaxation of $\sim$10 ps decreasing the probability of radiative recombination from this energy state, contrasting a Γ_2^- and Γ_1^- of $\sim$10 ns lifetimes [Tanaka et al., 2005, Yamamoto et al., 2012].

The Stokes shift is the difference between the excitation from ground to Γ_5^- and relaxation from Γ_2^- to ground. In Table 9.1 we observed a decreasing Stokes shift from 63 meV for $n = 1$ decreasing to 19 meV for $n = 4$. This is suggested due to reduction in band splitting between the Γ_5^- and Γ_2^- bands with increasing 3D character. This band splitting converges to 0 meV for the 3D phase where the Γ_5^- and Γ_2^- combine into Γ_4^-. While a Stokes shift is routinely reported for the 3D phase, this is often based on an alternate definition such as $E_{AbsMax} - E_{\mathrm{PL}}$, which can be expected to be defined within these manuscripts as discussed in Section 4.6.3.

Composition effects

The use of alkylammonium cations such as butylammonium for surface passivation has been discussed in Section 2.3.4. Following from the identification

[19] The Γ states and band splitting are discussed in detail in Tanaka *et al.* 2003 and 2005 [Tanaka et al., 2003, Tanaka et al., 2005].

[20] Ground is the valence band maximum.

[21] Excitation from the ground state to Γ_1^- is largely dipole forbidden with spin orbit coupling effects due to the heavy atoms partially allowing the transition.

of the $MAPbBr_3$ based phase, for the $(PABr)_{2x}(MABr)_{1-x}PbBr_2$ system, in Section 9.3.1. The effect of PA^+ and the compositional coordinate (x) on the optical properties of the 3D phase is explored using the data presented in Figure 9.9 and Table 9.2.

The Tauc band-gap (E_{Tauc}) for the $MAPbBr_3$ structure is initially 2.310 eV at $x = 0.0$, which gradually increases with x alongside the PL maximum (E_{PL}), Figure 9.9c. E_{PL} continues to increase while E_{Tauc} branches off to a lower energy when an additional phase appears in the system at $x = 0.075$, Figure 9.9a. Similar values for $E_{\text{PL}} - E_{\text{Tauc}}$ of 17 an 20 meV are observed for $x = 0.1$ and $x = 0.2$ respectively, Table 9.2. E_{PL} and excitonic absorption (E_{AbsMax}) energies show a closely related trend with the difference between them showing a marginal decrease with x of 6 meV between $x = 0.025$ and $x = 0.2$.

The initial $E_{\text{PL}} - E_{\text{Tauc}}$ of 0 meV for $x \leq 0.025$ is consistent with the observation for the $(FAPbI_3)_{0.85}(MAPbBr_3)_{0.15}$ 3D phase at ambient temperatures, Chapter 7 [Greenland et al., 2019] [22]. This value subsequently increases with x. The $E_{\text{PL}} - E_{\text{Tauc}}$ difference is related to the formation of sub-conduction band states in the band gap. These can be related to the exciton binding energies as the absorption spectra of the 3D hybrid-perovskites is composed of an overlapping excitonic peak and continuum [Yang et al., 2015].

The observed E_{PL} and E_{Tauc} blueshifts with increasing x is consistent with the observation of Wang *et al.* for the BA^+ cation. This was attributed to a combination of strain relaxation and improved crystallisation, with strain considered further in Sections 9.4 and 9.5 [Wang et al., 2017b]. In addition Wang *et al.* used a mixed halide (Br,I) system and considered inhomogeneous distribution as an alternative mechanism for the blue shift. As this is not applicable to our single halide system, this latter mechanism is unlikely a dominant contribution in their work.

[22] See Section 4.6.3 regarding multiple literature definitions of the *Stokes shift*.

9.4 2-Step: PABr on $MAPbBr_3$

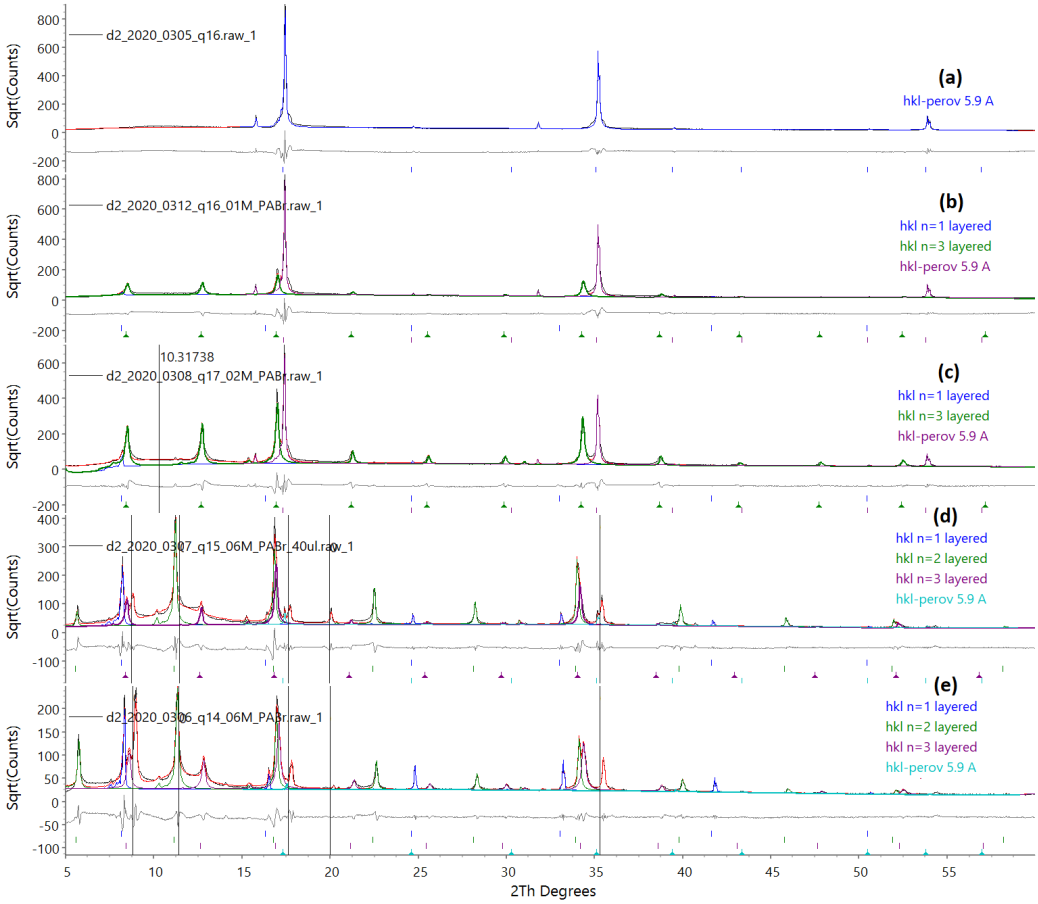

Figure 9.11: Diffraction data of a $MAPbBr_3$ thin-film (a) as-deposited, and with post-annealing dynamic spin coating of 60 μl of (b) 0.1, (c) 0.2, (e) 0.6 M of PABr in isopropanol at 4000 rpm. (d) 40 μl, 0.6 M.

The thin-film samples based on a single precursor solution for each compositional co-ordinate allowed free association of the various precursor components in solution. This supports thermodynamically controlled phase formation. Complimentary to this, a series of thin-film samples were prepared in a two step process, where a $MAPbBr_3$ layer was prepared and annealed. These films were then coated with isopropanol solutions of PABr of varying concentrations by dynamic spin-coating at 4000 rpm as described in Section 4.4. In this case the integration of the larger cation occurs through diffusion at the interface with the $MAPbBr_3$ film, which can be a kinetically controlled processes. The PABr dose dependent phase formation was investigated, using 0.1, 0.2 and 0.6 M PABr solution concentration as means of controlling the dose. The effect of annealing was considered for the 0.1 and 0.2 M films using *ex-situ* X-ray diffraction.

9.4.1 Phases as a function of dosage

The effect of increasing the PABr dosage applied to the surface of the $MAPbBr_3$ film is presented in Figure 9.11. The identity and quality of starting film is confirmed in Figure 9.11(a). This presents narrow peaks and a strong (100) preferred orientation [23]. On exposure to PABr for 0.1 and 0.2 M, we observe an $n = 3$ layered phase with a faint $n = 1$ related shoulder near 8.2 ° 2θ, and a strong "perov" phase. In the 40 and 60 μl 0.6 M samples, $n = 1$ and $n = 2$ phases are observed, where both are more intense than the $n = 3$ phase. These are accompanied by a very weak "perov" phase.

The $n = 3$ phase was most intense at 0.2 M after which the other layered phases dominate. The (001) peak of $n = 1$ appeared as a very weak shoulder near 7° 2θ in the 0.1 M pattern with its intensity increasing up to the 0.6 M patterns. As the PABr loading increases the $MAPbBr_3$ phase intensity decreases. A strong intensity drop is observed from 0.2 (60 μl) to 0.6 M (40 μl), which coincides with the emergence of the $n = 2$ at 0.6 M (40 μl). The $n = 2$ phase is then of lower intensity at 0.6 M (60 μl). This is not dissimilar from the trend from the precursor ratio based set in Figure 9.6e, where there is an intensity drop of 2 orders of magnitude for the $MAPbBr_3$ phase with increasing x prior to the formation of the $n = 2$ phase.

[23] The observed broadening in 9.11(a) is due to the instrument profile, the crystallite size refined to the set parameter limit of 445 nm.

9.4.2 Annealing of 0.1 and 0.2 M films

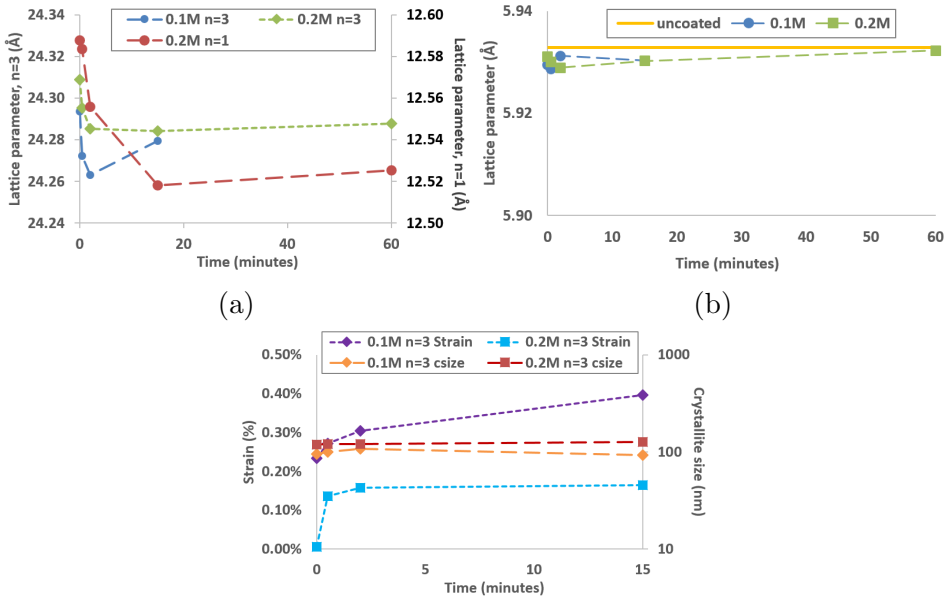

Figure 9.12: Diffraction derived unit cell, micro-strain and crystallite size parameters of PABr/MAPbBr$_3$ as a function of annealing time at 90 °C. (a) $n = 1$ and $n = 3$ lattice parameters, (b) "perov" phase lattice parameters, (c) crystallite size and micro-strain for the $n = 3$ phase.

Annealing of the 0.1 and 0.2 M PABr/MAPbBr$_3$ films showed no notable changes in the intensity of the layered phases. A slight intensity reduction of the 3D "perov" phase was observed on annealing for 0.1 M, and no notable intensity effects for 0.2 M, as shown in App. E.4.1. Macro- and micro- strain effects were observed for the layered phases, with the macro-strain evident from the lattice parameters of Figure 9.12a and the micro-strain in Figure 9.12. No signifiant macro-strain was observed for the "perov" phase, and consideration of micro-strain for the phase was not considered reliable as discussed in App. E.4.1 and App. Figure E.9. In addition, the $n = 1$ phase was of 0.1 and 0.2 M was unsuitable for micro-strain consideration due to its low peak intensity.

The $n = 1$ lattice parameter in the single solution deposition for $x = 1$ was 12.584 Å, is similar to the values, 12.586 Å (0.2 M), 12.587 Å (40 μl, 0.6 M), and 12.584 Å (60 μl, 0.6 M) at 0 min annealing time. Annealing of the 0.2 M sample resulted in a reduction of the $n = 1$ lattice parameter to 12.518 Å after 15 min. This is compressive strain on annealing relative to 0 min value [24]. For the PA_2PbBr_4 powder sample in Figure 9.1, the equivalent c-axis spacing was 12.546 Å which is between values at 0 min and 15 min. A similar relative compressive strain on annealing is seen in the $n = 3$ phase for 0.1 M with an extrema at 2 min, and 0.2 M at 15 min. The macro-strain was accompanied by micro-strain in the $n = 3$ phase, Figure 9.12c. The strongest increase from 0 to 0.5 min for 0.1 and 0.2 M. This was followed by a more gradual increase with annealing thereafter.

We have observed a lattice parameter reduction which can either be interpreted as macro-strain relaxation or the induction of compressive macro-strain for the layered phases on the annealing of the $PABr/MAPbBr_3$ layer stack. This was accompanied by micro-strain for the $n = 3$ phases, while micro-strain could not be calculated for the $n = 1$ phase. The macro- micro-strain relationship may be explained by a strain occurring in localised regions, or a graded strain effect acting on crystallites, broadening the distribution of local lattice parameter values, which increases apparent micro-strain broadening. The origins of the effect are considered at the end of this chapter alongside the ageing of a $(PABr)_{2x}(MABr)_{1-x}PbBr_2$, $x = 0.8$ sample.

9.4.3 $(PABr)_{2x}(MABr)_{1-x}PbBr_2$, $x = 0.8$ sample ageing

For comparison to the evolution of 0.2 M $PABr/MAPbBr_3$ of Section 9.4.2, we consider the ageing data of the multi-phase $(PABr)_{2x}(MABr)_{1-x}PbBr_2$, $x = 0.8$ sample in Figure 9.13. This sample was chosen for its MA^+ content and the joint presence of clear $n = 1$ and $n = 2$ related diffraction peaks, which was unavailable for lower x patterns, Figure 9.5c. This film show no notable change in the modelled crystallite size or micro-strain over the 15 days and the fractional loss of some intensity for the $n = 1$ phase by day 3, App.

[24] As we do not use an idealised strain-sssssssssssssssssssssssfree structure, this can be considered either a relative compressive strain or the relaxation of strain based on the reference point.

Figure E.11. In assessing lattice parameter shifts, the "perov 5.8 A" and $n = 1$ phases have error values of approx. $\pm$ 0.005 and 0.01 Å respectively [25] [26]. The variations of the lattice parameters for these phases are comparable to their modelling errors. The $n = 2$ phase show a slight lattice parameter increase of 0.0124 Å (relative macro-strain of 0.07 %) after 7 days, this is far larger than the modelling error of approx. $\pm$ 0.002 Å. This could be the result of either relaxation of a compressive strain or the introduction of tensile strain with the former being more probable. We explore this alongside other strain effects observed in the chapter in Section 9.5

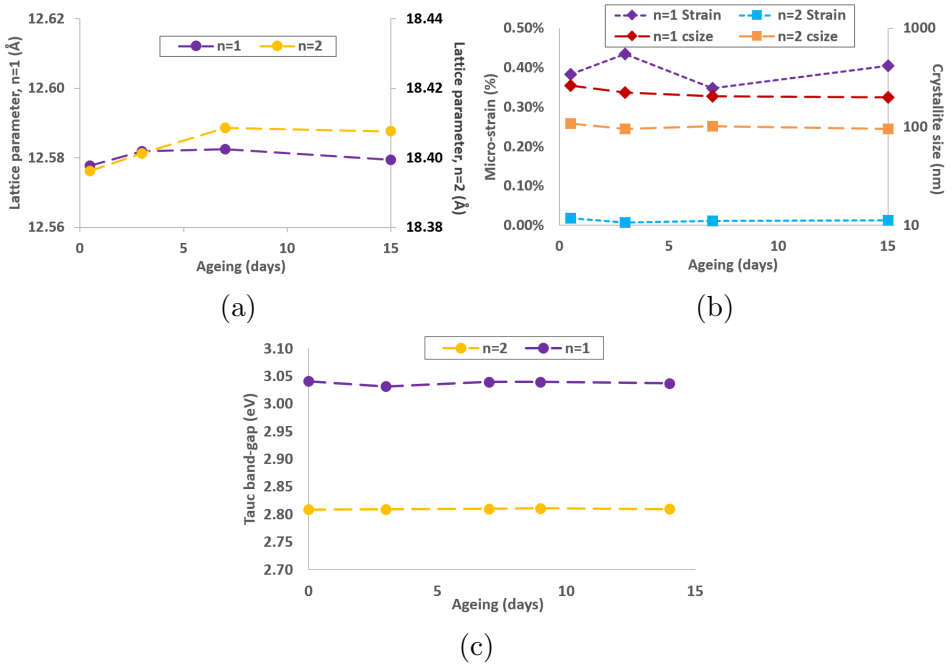

Figure 9.13: Ageing of $(PABr)_{2x}(MABr)_{1-x}PbBr_2$, $x = 0.8$ over 15 days. (a,b) diffraction derived lattice parameters, (b) modelled micro-strain and crystallite size, (d) Tauc band gap values.

[25] The "perov 5.8 A" interplanar spacing values are plotted in App. Figure E.12. This phase has been identified as different to the $MAPbBr_3$ "perov 5.9 A" phase as discussed in Section 9.3.1.

[26] These are TOPAS-Academic outputted error values which account for the modelling-related error.

9.5 Discussion

Phases

Structures of the $PA_2MA_{n-1}PbBr_{3n+1}$, $n = 1$ and $n = 2$ phases were identified and modelled in Section 9.2. The $n = 1$ phase modelling was performed on a phase pure powder sample prepared from thin-films. This structure provided reasonable parameters for the $PbBr_6^{4-}$ octahedral framework, with an estimation of the PA^+ position with the application of rigid body modelling, where the organic cations' bond connectivity extracted from literature [Meresse and Daoud, 1989]. The closest related structure in literature for the Pb−X was identified as the $(BABr)_2PbBr4$ phase in the Crystallography Open Database, COD 1545801 [27]. The refined $(PABr)_2PbBr4$ structure file for this phase is provided in App. E.3.4. The $n = 2$ phase was modelled from weak contributions in a mixed component system of $n = 1$ and $n = 2$ phases. This served as a reasonable assessment of the phases identity while the finer structural details are unreliable for such data.

The phase formation in the $(MABr)_{1-x}(PABr)_{2x}PbBr_2$ has been explored showing $n = 1$, $n = 2$, and 3D $MAPbBr_3$ as the major phases present across the composition range. Additional progressively weaker, and higher n, $PA_2MA_{n-1}PbBr_{3n+1}$ phases were observed in the absorption and photoluminescence data. Optical features up to $n = 4$ were compared between the PL and absorption data, which were consistent with observations in literature, Table 9.1. Beyond these $n = 5$ and $n = 6$ related PL peaks were modelled and assigned. Indications of higher n phases were weakly present, for which the peak position and intensity could not be unambiguously deconvoluted in the spectra. Circumstantial evidence for high n quasi-2D structures was observed in the XRD data-sets through a Pawley phase refinement with (100) and (200) reflections, corresponding to the same crystallographic planes present in the 3D perovskite. In this the inter-planer spacing was smaller than the 3D structure with additional considerations discussed in Section 9.3.1

[27] The relevant database searches and results at the time of execution are provided in App. E.3.

The observation of larger n phases in the optical data, and not in the diffraction data indicates the layer stacking direction is not *normal* to substrate. The layered phases have anisotropic charge transport properties with higher mobilities in-plain with the organic layer acting as a dielectric barrier. This preferred orientation effect is expected to be favourable for photovoltaic and electroluminescence devices. Such preferred orientation is consistent with the work of Quintero-Bermudez *et al.* where layer stacking parallel to the substrate was favoured for low n, and perpendicular stacking for high n quasi-2D structures [Motti et al., 2019, Quintero-Bermudez et al., 2018].

In the PABr/$MAPbBr_3$ data-set, formation of the $n = 3$ phase was prevalent at low dosages, while at higher dosages the lower n phases become more prevalent. The presence of the $n = 3$ phase for all the diffraction patterns of PABr on $MAPbBr_3$ dosages is in strong contrast to the single-step deposition $(MABr)_{1-x}(PABr)_{2x}PbBr_2$ set in Figure 9.3, where an $n = 3$ phase is not observed in the diffraction data and appeared weakly in the optical data, Section 9.3.3.

The annealing of the 0.1 and 0.2 M films in App. E.4.1 does not present a notable effect on phase composition at 90 °C (N_2 atmosphere) over 15 and 60 minutes respectively. A comparable experiment has been reported by Sutanto *et al.* of PhEAI/$MAPbI_3$ and TMAI/$MAPbI_3$ layer stacks, where these systems were measured by GI-XRD with a 2D detector during *in-situ* annealing, where TMAI is 2-thiophenemethylammonium [28]. In Sutanto *et al.*, the initially formed phases in this system favoured $n = 1$ with the reorganisation of the cations on annealing to form higher n phases [Sutanto et al., 2020]. The difference in phase formation is expected as due to a greater mobility of PA^+ compared to larger cations, allowing the formation of higher n phases at ambient temperatures.

For systems formed from a $A'X/APbX_3$ layer stack where A′ is an organic cation suitable for forming a layered perovskite [29], it is proposed that the phase formation is controlled by at least 3 contributing factors as considered below:

[28] GI-XRD: Grazing incidence XRD. A 2-dimensional (2D) detector is significant measures a larger segment of the Debye-Scherrer rings as discussed in Section 3.2.2.

[29] A is a small organo-ammonium cation, and X is a halide as defined in Section 1.2.1.

(1) The mobility of A′ in the film, which controls the penetration depth, and thus A′ concentration distribution in the film. We relate this to literature in the case of Sutanto *et al.* where $PhEA^+$ mobility restricts the sample penetration depth, favouring the formation in the $PhEAI/MAPbI_3$ primarily to $n = 1$ with some $n = 2$ content, on annealing $PhEA^+$ diffuses through the film forming higher n structures.

(2) An energy barrier for expansion of a film through on the inclusion of A′ which favours larger n structures for their sparser large cation distribution. We consider the difference between phase formation for the 2-step $PABr/MAPbBr_3$ in which the 3D phase and $n = 3$ co-exist for the 0.1 and 0.2 M PABr solutions with the lower n phases only significant for the higher conc. 0.6 M variants. In the $PABr/MAPbBr_3$ of Section 9.4 we attribute the preferable formation of $n = 3$ to a higher PA^+ mobility, and a lower energy cost in reorganising the film compared to lower n phases. In the higher PABr dosages for these systems, the $MAPbBr_3$ is mostly consumed demanding structures which are more PA^+ rich with the $n = 2$ phase most prominent for the 0.6M, 40 μl sample, and $n = 1$ in the 0.6M, 40 μl sample.

(3) The relative stability between the layered phases favour lower n structure with respect to the 3D structure, as shown by Quan *et al.* [Quan et al., 2016]. When considering a system of a given stoichiometry, optimisation is expected between maximising the phase fraction of lower n phases, and minimising the phase fraction of the less energetically favourable higher n and/or 3D phases. In single solution deposition where a homogenous distribution of large cations is expected in the precursor solution, a *log-normal* distribution of n has been reported in literature as a function of composition [Quintero-Bermudez et al., 2018]. We relate this to the phase distribution of the thermodynamically controlled single step $(MABr)_{1-x}(PABr)_{2x}PbBr_2$ samples, where component mixing occurred in solution prior to deposition. Little overlap was observed between the low n layered and 3D phase, especially when considering that the peaks corresponding to a smaller $APbX_3$ (100) and (200) peaks for $x \geq 0.4$ most likely originate from a quasi-2D layered structure [30].

These contributing factors provide a consistent rationalisation for the considered systems eluding to the thermodynamically and kinetically relevant consideration which are hypothesised to dictate film formation.

[30] As discussed in Section 9.3.1

Strain

In the annealing of the PABr/$MAPbBr_3$, the lattice parameter shifts of Figure 9.12a corresponded to relative strain values reaching of -0.13, -0.10 and -0.73 % for the 0.1 M $n = 1$, 0.2 M $n = 3$ and 0.2 M $n = 1$ phases respectively [31]. These values are comparable to the 0.47 % compressive, out-of-plane strain observed in the work of Zhao *et al.* for $MAPbI_3$. Zhao *et al.* related the formation of strain to the thermal expansion mismatch between the glass substrate and $MAPbI_3$ thin-film, where cooling from 100 °C resulted in compressive out-of-plane strain and correlated tensile in-plane strain [Zhao et al., 2017]. This was compared to the PABr/$MAPbBr_3$ results in which the 0 min measurement presented layered phases formed at ambient temperature, which was thereafter annealed. The $MAPbBr_3$ phase showed no meaningful change in lattice parameter with annealing or between coated sample variants [32]. This was attributed to this film having been annealed prior to PABr deposition. As such no additional thermal expansion related strain would be expected. An out-of-plane lattice parameter decrease was observed for the layered phases on annealing, this is consistent with the introduction of compressive strain.

The micro-strain in this system is a result of inhomogeneous strain effects. This is suspected to occur as gradient in the film strain, which is suspected to occur as a function of distance from the substrate. This is rationalised by the substrate/film thermal expansion mismatch being the origin of the strain. The phase distribution within the film is not known so no assumptions are made regarding whether the layered phases directly contact the substrate or if the 3D phase is present as an interlayer.

In addition to the strain induced through annealing for the layered phases in the PABr/$MAPbBr_3$, we observed a lattice parameter change for the $n = 2$ phase from sample ageing of $(PABr)_{2x}(MABr)_{1-x}PbBr_2$, $x = 0.8$ in a desiccator, consistent with the relaxation of compressive out-of-plane strain expected from the sample annealing process, Section 9.4.3.

[31] Symmetric Bragg-Brentano measurements are utilised for this chapter, in which only the crystal planes parallel to the substrate contribute to the diffraction pattern. On this basis any strain or micro-strain observed is strictly out-of-plane.

[32] Figure E.9e shows the lattice parameter plotted for the various coated samples at 0 min annealing.

Wang *et al.* report strong strain relaxation effects ~ 0.6 % through the substitution of BA^+ into a $FA_{0.83}Cs_{0.17}Pb(I_{0.6}Br_{0.4})_3$ perovskite layer [Wang et al., 2017b]. In contrast we observe no such effect on the addition of PA^+ in to a $MAPbBr_3$ layers. The difference is suggested due to halide redistribution on the formation of new phases, facilitated by the mixed halide nature of the literature sample. At low substitution, 9 %, they observe a blueshift which is similar to what is observed in our $(PABr)_{2x}(MABr)_{1-x}PbBr_2$ data-set. At 50 % *BA* substitution a redshift is observed in the absorption peak, from 2.47 to 2.34 eV of Wang *et al.*, with a similar occurrence in their PL data. This is in strong contrast to our data, in which the lowest energy is the $x = 0$, $MAPbBr_3$ phase. This is suggested to be an indication of compositional inhomogeneity within their perovskite phase and charge carrier transfer between the regions due to its mixed halide composition [Motti et al., 2019, Wang et al., 2017b].

Zhao *et al.* established the detrimental effect of strain in $MAPbI_3$ hybrid-perovskites through its reduction of ion migration activation energies, related to accelerated degradation. We demonstrated structural observations of strain for layered $(PA)_2MA_{n-1}PbBr_{3n+1}$ phases with the additional consideration of micro-strain which was observed alongside strain. While layered hybrid-perovskite phases are established as more stable than the 3D structure, this provides an opportunity for the exploration of the effect of strain and micro-strain on stability as a topic of future work.

9.5.1 Conclusion and future work

The structure modelling of Section 9.2 was limited in part due to the broad peaks of mechanically prepared powder sample. The fabrication of $(PA)_2MA_{n-1}PbBr_{3n+1}$ single crystals could be leveraged to identify more accurate structural properties of pure phase layered structures, using single crystal XRD and the generation of high quality single phase optical data. Good reference data allows for the consideration of strain in thin-films against the ideally unstrained single crystal. Similarly with optical properties for consideration of defects and structural distortion on the electronic states and electronic structure of the material.

In Section 9.3, we evaluated the phases present as a function of composition for the $(PABr)_{2x}(MABr)_{1-x}PbBr_2$ system, using a diffractometer which measured scattering vectors perpendicular to the sample surface. This only allows the observation of crystallographic planes parallel to the substrate, the effects of which have been discussed previously in this chapter. Measurements using a 2D detector or a diffractometer with a goniometer arm capable of measuring out-of-plane could be used to assess the presence and orientation of additional phases in the systems studied.

The comparison between the single step deposition system of $(PABr)_{2x}$ $(MABr)_{1-x}PbBr_2$ and the $PABr/MAPbBr_3$ layer stack provided an interesting means of observing the difference between thermodynamic and kinetic control in film formation. We have hypothesised controlling factors using a limited data-set, and corroborated these using observations from similar systems in literature. These can be further refined and reconsidered with using *in-situ* annealing studies of multiple $A'X/APbX_3$ systems. The application of grazing-incidence XRD can be implemented to track structural changes in the sample as a function of depth. These measurements could be performed at a range of temperatures to infer information of the activation energy for A' to move through the $APbX_3$. With the application of these components in surface passivation, understanding the transport of larger A' cation in hybrid-perovskites can provide valuable information in relation to the long term stability of heterogeneous 2D/3D based devices. This type of device is exemplified by the graded quasi-2D photovoltaic device of Motti *et al.* [Motti et al., 2019].

Chapter 10

General conclusions

The fabrication of photoactive hybrid-perovskite type materials is achieved primarily using solution processing methods, such as spin coating. In this section, insights into the development of a novel gravity chuck spin coater for thin-film fabrication is presented. Additionally, significant results on the structure - property paradigm of these thin-film materials are highlighted. In this work, a range of hybrid-perovskite and hybrid-perovskite derivative materials have been fabricated and characterised, using *in-situ* and *ex-situ* X-ray diffraction, as well as optical absorption and photoluminescence spectroscopy. The temperature dependent structural characteristics of 3D perovskites, along with the composition and processing dependent effects in mixed 2D/3D hybrid-perovskites and layered derivative structures is summarised here.

The findings of this work provided insights into cation substitution and inclusion approaches which are prominent for improving the stability and performance of hybrid-perovskite based optoelectronic devices. This includes observations in XRD data on the composition dependence of decoupled signatures for pseudo-cubic to tetragonal, and $a^0a^0a^0$ to $a^0a^0a^+$ transitions in triple cation hybrid perovskites, indicative of structural heterogeneity. Further, the identification of phase formation and optical behaviour of mixed phase, hybrid-perovskite (3D) and hybrid-perovskite layered derivatives (2D), where

the thermodynamic and kinetic factors controlling phase formation were proposed. These finding have identified avenues for further investigation regarding the organic cations structural, bonding, and compositional configurations in triple cation systems, as well as the cation diffusion activation energies and relative phase stability within 2D/3D hybrid-perovskite systems.

Design of a novel gravity chuck spin coater

This work developed and relied upon the design and assembly of a spin coater utilising a novel gravity chuck. This sought to provide an alternative to the commercially available vacuum chuck based spin coaters, which are subject to many additional points of failure related to their vacuum system. This is exceptionally relevant to lead halide perovskites for which the lead halide salts require solvation in harsh chemicals such as dimethyl-formamide and dimethyl-sulfoxide, which can degrade rubber and plastic materials within equipment [MYKIN INC, 2019].

The gravity chuck design allows a simple means of accommodating new sample shapes using "sample masks", which can easily be cut from brass sheet metal using hand tools. The performance of this device in terms of thin-film quality, was shown by means of atomic force microscopy and X-ray reflectometry measurements, and the thermal performance was assessed through extended operation under both low and high PWM duty cycle conditions. The design have demonstrated it's utility with the 2nd version operating at the University of the Witwatersrand, South Africa since 2019, and the 3rd in Maseno University, Kenya since 2021.

The manuscript presented contains the novel aspects of the design. The further development of this concept can be improved through the use of existing technologies and knowledge present in the field. This includes the implementation of a motor with a built-in Hall sensor based tachometer, and the implementation of speed control algorithms.

The effect of cation substitution in 3D hybrid-perovskites

This work has explored the structural dependence of the $Cs_x(FA_{0.85}MA_{0.15})_{1-x}PbBr_{0.45}I_{2.55}$ based hybrid-perovskites on Cs, which includes $(FAPbI_3)_{0.85}(MAPbBr_3)_{0.15}$ corresponding to $x = 0$. The introduction of Cs in these materials has been related to a divergence between the onset temperatures of the cubic to tetragonal and $a^0a^0a^0$ to $a^0a^0c^+$ (Glazer notation) transitions, pertinent to the α and β phase transition in these systems. This is compared to the single cation $FAPbI_3$ system of Fabini *et al.*, where these critical temperatures for the transition were convergent [Fabini et al., 2016]. This effect has been proposed as due to the structural heterogeneity in mixed-cation, mixed-halide systems which has been established recently in the works of Barrier *et al.* and Mundt *et al.* [Barrier et al., 2021, Mundt et al., 2021].

The low temperature $\beta \rightarrow \gamma$ phase transition in these systems is substantially suppressed to lower temperatures at 80 to 90 K for $x = 0$ to $x = 0.08$, compared to $FAPbI_3$ in literature at 130 to 141 K [Kawachi et al., 2019]. This attributed to the inclusion of Br, based on observations in the works of Weller *et al.* and Lehmann *et al.*, in which a reduction of the transition temperature in $MAPb(I_{1-y}Br_y)_3$ systems from 165 to ∼125 K is established [Lehmann et al., 2019, Weller et al., 2015b]. A proposed explanation is the lower electronegativity of Br resulting in weaker hydrogen bonding between the organic cation and Pb-X framework, which is expected to allow a greater degree of cation rotation for a given temperature, as is associated with the phases changes in hybrid perovskite systems [Weller et al., 2015a, Weller et al., 2015b]. On this basis, the absence of a clear trend for $x = 0.1$ (Cs10) could either be attributed to noise in the data-set, or a greater concentration of Cs which does not have a dipole to form hydrogen bonds with the Pb−X framework. The latter has the potential to suppress the $\beta \rightarrow \gamma$ past the last collected data point, but does not explain why a larger discontinuity is observed in with increasing Cs for the axis ratio, or the larger discontinuity in the octahedral tilt of the $x = 0.08$ (Cs8) sample. This question could be probed using variable temperature X-ray diffraction with a larger sample volume to provide greater peak intensity, variable temperature neutron diffraction for its more pronounced scattering contrast between C, N, and H of the organic cation, and heat capacitance measurements to assess the energy transfer to the sample during such transitions [Castellanos et al.,

2017, Kawachi et al., 2019, Weller et al., 2015b]. Additionally, indications on the role of bond formation may be accessible through the modelling of NEXAFS data for the Cs L_3 edge [Honda et al., 2016], and Pb specific bond distances can be generated through a pair distribution function from EXAFS spectroscopy data of the Pb L_3 edge [Kluherz et al., 2022]. This can offer insights into local structure, and potentially structural heterogeneity when used in combination with complementary techniques such as XRD.

Phase composition and photophysical properties of the mixed PA/MA based lead bromide perovskites systems

Following the chapter forming mixed cation 3D perovskites, the effect of substituting the larger propyl-ammonium (PA) cation into the hybrid-perovskite system was studied. Much like the mixed cation systems, the inclusion of larger organic cations have shown promise in improving PV and luminescent device properties alongside device stability, as discussed in Section 1.4 [Blancon et al., 2018, Congreve et al., 2017, Grancini and Nazeeruddin, 2019, Motti et al., 2019, Wang et al., 2017b]

These larger cations are known to form $(A')_2A_{n-1}PbX_{3n+1}$ layered structures, which can be selected based on composition. Such phases were identified in the $(PABr)_{2x}(MABr)_{1-x}PbBr_2$, $0 \leq x \leq 1$ and $PABr/MAPbBr_3$ systems. Based on the structure database searches in the ICSD and COD of App. E.3, there is a gap in the literature for crystal structures of the $(PA)_2MA_{n-1}PbBr_{3n+1}$ phases. Structure determination was performed using the powder diffraction data for the $n = 1$, PA_2PbBr_4 composition. The details of the refined structure are provided in App. E.3.4. The $n = 2$ phase was only present as a mixed phase, with weak peaks preventing access to accurate details on the unit cell contents, as such only the space group and unit cell parameters for this structure were reported. In the $PABr/MAPbBr_3$ system prepared by a two step deposition, the $n = 3$ phase was identified. The identification of higher n phases was achieved through the interpretation of UV-Vis-NIR absorption and photoluminescence (PL) spectra. The Tauc band-gap of these materials has been identified for phases up to $n = 4$, and the PL derived band-gap has been identified up to $n = 6$. The highest n PL peaks of the $x = 0.4$ and $x = 0.5$ samples presented asymmetry, indicating

the possibility of the presence of higher n phases. These values are provided in Table 9.1 where values up to $n = 4$ were identified in literature supporting the phase assignment.

In the presence of the 3D phase ($n = \infty$), other phases observed from the diffraction or absorbance data, were not observed in the PL spectra. This was explained by charge carrier transfer to the 3D phase. The possibility of reabsorption of photons emitted by layered phases was also considered, although this effect is expected to occur on a slower time scale than conduction band to conduction band charge transfer, from layers phases to the 3D phase [Motti et al., 2019, Zou et al., 2018]. For samples where $n = 1$ was the highest intensity phase as determined by XRD, the higher n phases such as $n = 2$, were not observed in the PL data. This includes compositions where $n = 2$ was identified in XRD patterns and UV-Vis-NIR absorption spectra. This was consistent with an absence of charge carrier transfer from $n = 1$ to $n = 2$ phases, which was attributed to the high exciton binding energies for $n = 1$ layered phases reported in literature.

For the consideration of phase formation, the $(PABr)_{2x}(MABr)_{1-x}PbBr_2$ and $PABr/MAPbBr_3$ systems were examined. The difference in the kinetic and thermodynamic aspects of film formation were considered, where the former involved the homogenous mixing of the precursor components in solution prior to deposition, and the latter, post deposition of PABr onto annealed $MAPbBr_3$ films. These varied formation conditions were leveraged to propose a set of controlling factors responsible for the phase formation behaviour in these systems, in corroboration with the behaviour of similar systems observed in literature [Quan et al., 2016, Quintero-Bermudez et al., 2018, Sutanto et al., 2020]. The controlling factors were identified as (1) The mobility of the larger organic cations (A′) in the film, which controls the penetration depth and thus A′ concentration distribution in the film. (2) An energy barrier for expansion of a film on the inclusion of A′ which favours larger n structures for their sparser large cation distribution. (3) The relative stability between the layered phases favouring lower n structure with respect to the 3D structure, as shown by Quan *et al.* [Quan et al., 2016]. These factors were expanded on in Section 9.5 where each was explained relative to data within this thesis and/or in literature.

The structural and optical analysis of these systems can be improved via the production of single crystal samples, from which the crystal structure can be determined by single crystal XRD, and high quality optical data can be obtained, which is additionally useful for comparison to thin-film systems. The set of factors related with layered phase formation in these thin-films constitute a hypothesis which would benefit from expansion of this work to similar systems such as ethyl-, butyl-, and pentyl- ammonium cations. This work provided a basis for further studies of film formation and organic cation diffusion through a perovskite structure. This can be achieved using time resolved *in-situ* diffraction and optical techniques, including *in-situ* grazing incidence XRD (GI-XRD) using a 2-dimensional detector, which would provide additional orientation information of layered perovskites in thin-films, as is pertinent to their electrical transport properties due to their 2-dimensional (2D) or quasi-2D nature. GI-XRD can further be used to control the X-ray penetration depth into the samples to evaluate depth dependent structure and phase properties.

Bibliography

[Ahn et al., 2016] Ahn, N., Kwak, K., Jang, M. S., Yoon, H., Lee, B. Y., Lee, J.-K., Pikhitsa, P. V., Byun, J., and Choi, M. (2016). Trapped charge-driven degradation of perovskite solar cells. *Nature Communications*, 7(1):1–9.

[Altomare et al., 2018] Altomare, A., Cuocci, C., Moliterni, A., and Rizzi, R. (2018). *Indexing a powder diffraction pattern*, chapter 3.4, pages 270–281. John Wiley & Sons, Ltd.

[Amat et al., 2014] Amat, A., Mosconi, E., Ronca, E., Quarti, C., Umari, P., Nazeeruddin, M. K., Gratzel, M., and De Angelis, F. (2014). Cation-induced band-gap tuning in organohalide perovskites: Interplay of spin–orbit coupling and octahedra tilting. *Nano Letters*, 14(6):3608–3616.

[Ball and Petrozza, 2016] Ball, J. M. and Petrozza, A. (2016). Defects in perovskite-halides and their effects in solar cells. *Nature Energy*, 1(11):1–13.

[Barboni and De Souza, 2018] Barboni, D. and De Souza, R. A. (2018). The thermodynamics and kinetics of iodine vacancies in the hybrid perovskite methylammonium lead iodide. *Energy & Environmental Science*, 11(11):3266–3274.

[Barnes et al., 2006] Barnes, P., Jacques, S., and Vickers, M. (2006). Peak shapes. http://pd.chem.ucl.ac.uk/pdnn/peaks/peakindx.htm (accessed 10 Sept 2022).

[Barrier et al., 2021] Barrier, J., Beal, R. E., Gold-Parker, A., Vigil, J. A., Wolf, E., Waquier, L., Weadock, N. J., Zhang, Z., Schelhas, L. T., Nogueira, A. F., et al. (2021). Compositional heterogeneity in $Cs_yFA_{1-y}Pb(Br_xI_{1-x})_3$ perovskite films and its impact on phase behavior. *Energy & Environmental Science*, 14(12):6394–6405.

[Batmunkh et al., 2020] Batmunkh, M., Zhong, Y. L., and Zhao, H. (2020). Recent advances in perovskite-based building-integrated photovoltaics. *Advanced Materials*, 32(31):2000631.

[Becka and Cruickshank, 1961] Becka, L. and Cruickshank, D. (1961). The variation of apparent bond lengths with temperature in molecular crystals. *Acta Crystallographica*, 14(10):1092–1092.

[Berger, 1986] Berger, H. (1986). Study of the Kα emission spectrum of copper. *X-Ray Spectrometry*, 15(4):241–243.

[Bergmann et al., 2004] Bergmann, J., Le Bail, A., Shirley, R., and Zlokazov, V. (2004). Renewed interest in powder diffraction data indexing. *Zeitschrift für Kristallographie-Crystalline Materials*, 219(12):783–790.

[Binek et al., 2015] Binek, A., Hanusch, F. C., Docampo, P., and Bein, T. (2015). Stabilization of the trigonal high-temperature phase of formamidinium lead iodide. *The Journal of Physical Chemistry Letters*, 6(7):1249–1253. PMID: 26262982.

[Bisquert, 2017] Bisquert, J. (2017). *The physics of solar cells: perovskites, organics, and photovoltaic fundamentals*. CRC press.

[Black et al., 2020] Black, D. R., Mendenhall, M. H., Henins, A., Filliben, J., and Cline, J. P. (2020). Certification of SRM 640f line position and line shape standard for powder diffraction. *Powder Diffraction*, 35(3):156–159.

[Blancon et al., 2018] Blancon, J.-C., Stier, A. V., Tsai, H., Nie, W., Stoumpos, C. C., Traore, B., Pedesseau, L., Kepenekian, M., Katsutani, F., Noe, G., et al. (2018). Scaling law for excitons in 2D perovskite quantum wells. *Nature Communications*, 9(1):1–10.

[Boinapally, 2015] Boinapally, V. R. T. U. o. T. (2015). *Computational study of structural and electrical properties of methylammonium lead iodide perovskite*. PhD thesis, University of Toledo.

[Boyd et al., 2018] Boyd, C. C., Cheacharoen, R., Leijtens, T., and McGehee, M. D. (2018). Understanding degradation mechanisms and improving stability of perovskite photovoltaics. *Chemical Reviews*, 119(5):3418–3451.

[Braunger et al., 2018] Braunger, S., Mundt, L. E., Wolff, C. M., Mews, M., Rehermann, C., Jošst, M., Tejada, A., Eisenhauer, D., Becker, C., Guerra, J. A., et al. (2018). $Cs_xFA_{1-x}Pb(I_{1-y}Br_y)_3$ perovskite compositions: The appearance of wrinkled morphology and its impact on solar cell performance. *The Journal of Physical Chemistry C*, 122(30):17123–17135.

[Bruker, 2021] Bruker (2021). APEX4 version 2021.4-1 data collection software which includes SAINT version 8.40B, SADABS-2016/2 and XPREP version 2014/2. *Bruker AXS Inc., Madison, Wisconsin, USA.*

[Buin et al., 2014] Buin, A., Pietsch, P., Xu, J., Voznyy, O., Ip, A. H., Comin, R., and Sargent, E. H. (2014). Materials processing routes to trap-free halide perovskites. *Nano Letters*, 14(11):6281–6286.

[Byrnes, 2008] Byrnes, S. J. (2008). Basic theory and phenomenology of polarons. *Department of Physics, University of California at Berkeley, Berkeley, CA*, 94720.

[Castellanos et al., 2017] Castellanos, M. M., McAuley, A., and Curtis, J. E. (2017). Investigating structure and dynamics of proteins in amorphous phases using neutron scattering. *Computational and Structural Biotechnology Journal*, 15:117–130.

[Cheary and Coelho, 1992] Cheary, R. W. and Coelho, A. (1992). A fundamental parameters approach to X-ray line-profile fitting. *Journal of Applied Crystallography*, 25(2):109–121.

[Chen et al., 2015a] Chen, B., Yang, M., Zheng, X., Wu, C., Li, W., Yan, Y., Bisquert, J., Garcia-Belmonte, G., Zhu, K., and Priya, S. (2015a). Impact of capacitive effect and ion migration on the hysteretic behavior of perovskite solar cells. *The Journal of Physical Chemistry Letters*, 6(23):4693–4700. PMID: 26550850.

[Chen et al., 2018] Chen, C., Hu, X., Lu, W., Chang, S., Shi, L., Li, L., Zhong, H., and Han, J.-B. (2018). Elucidating the phase transitions and temperature-dependent photoluminescence of $MAPbBr_3$ single crystal. *Journal of Physics D: Applied Physics*, 51(4):045105.

[Chen et al., 2023] Chen, C.-H., Cheng, S.-N., Cheng, L., Wang, Z.-K., and Liao, L.-S. (2023). Toxicity, leakage, and recycling of lead in perovskite photovoltaics. *Advanced Energy Materials*, 13(14):2204144.

[Chen et al., 2021] Chen, H., Chen, Y., Zhang, T., Liu, X., Wang, X., and Zhao, Y. (2021). Advances to high-performance black-phase $FAPbI_3$ perovskite for efficient and stable photovoltaics. *Small Structures*, 2(5):2000130.

[Chen et al., 2015b] Chen, Q., De Marco, N., Yang, Y. M., Song, T.-B., Chen, C.-C., Zhao, H., Hong, Z., Zhou, H., and Yang, Y. (2015b). Under the spotlight: The organic–inorganic hybrid halide perovskite for optoelectronic applications. *Nano Today*, 10(3):355–396.

[Chen et al., 2020] Chen, S., Zhang, Y., Zhang, X., Zhao, J., Zhao, Z., Su, X., Hua, Z., Zhang, J., Cao, J., Feng, J., et al. (2020). General decomposition pathway of organic-inorganic hybrid perovskites through an intermediate superstructure and its suppression mechanism. *Advanced Materials*, 32(29):2001107.

[Chen et al., 2016] Chen, T., Foley, B. J., Park, C., Brown, C. M., Harriger, L. W., Lee, J., Ruff, J., Yoon, M., Choi, J. J., and Lee, S.-H. (2016). Entropy-driven structural transition and kinetic trapping in formamidinium lead iodide perovskite. *Science Advances*, 2(10):e1601650.

[Cho et al., 2018] Cho, K. T., Grancini, G., Lee, Y., Oveisi, E., Ryu, J., Almora, O., Tschumi, M., Schouwink, P. A., Seo, G., Heo, S., et al. (2018). Selective growth of layered perovskites for stable and efficient photovoltaics. *Energy & Environmental Science*, 11(4):952–959.

[Christians et al., 2015] Christians, J. A., Manser, J. S., and Kamat, P. V. (2015). Best practices in perovskite solar cell efficiency measurements. avoiding the error of making bad cells look good. *The Journal of Physical Chemistry Letters*, 6(5):852–857.

[Cline et al.,] Cline, J., Mendenhall, M., Black, D., Windover, D., and Henins, A. SRMs, instrumentation and data-collection procedures. *International Tables for Crystallography*, H:235–238.

[Cline et al., 2012] Cline, J. P., Black, D., Windover, D., and Henins, A. (2012). *The Calibration of Laboratory X-Ray Diffraction Equipment Using NIST Standard Reference Materials*, chapter 13, pages 399–438. John Wiley & Sons, Ltd.

[CNN, 2020] CNN (2020). Forget silicon. this material could be a game-changer for solar power. https://edition.cnn.com/2020/10/14/energy/solar-energy-perovskites-spc-intl/index.html (accessed: 2023-03-13).

[Coelho, 2020] Coelho, A. (2020). TOPAS-Academic version 7 technical reference 2020.

[Coelho, 2018] Coelho, A. A. (2018). TOPAS and TOPAS-Academic: an optimization program integrating computer algebra and crystallographic objects written in C++. *Journal of Applied Crystallography*, 51(1):210–218.

[Coelho and Rowles, 2017] Coelho, A. A. and Rowles, M. R. (2017). A capillary specimen aberration for describing X-ray powder diffraction line profiles for convergent, divergent and parallel beam geometries. *Journal of Applied Crystallography*, 50(5):1331–1340.

[Congreve et al., 2017] Congreve, D. N., Weidman, M. C., Seitz, M., Paritmongkol, W., Dahod, N. S., and Tisdale, W. A. (2017). Tunable light-emitting diodes utilizing quantum-confined layered perovskite emitters. *ACS Photonics*, 4(3):476–481.

[Cordero et al., 2021] Cordero, F., Trequattrini, F., Craciun, F., Paoletti, A., Pennesi, G., and Zanotti, G. (2021). Cation reorientation and octahedral tilting in the metal-organic perovskites MAPI and FAPI. *Journal of Alloys and Compounds*, 867:158210.

[Corsini and Griffini, 2020] Corsini, F. and Griffini, G. (2020). Recent progress in encapsulation strategies to enhance the stability of organometal halide perovskite solar cells. *Journal of Physics: Energy*, 2(3):031002.

[Cortecchia et al., 2017] Cortecchia, D., Neutzner, S., Srimath Kandada, A. R., Mosconi, E., Meggiolaro, D., De Angelis, F., Soci, C., and Petrozza, A. (2017). Broadband emission in two-dimensional hybrid perovskites: The role of structural deformation. *Journal of the American Chemical Society*, 139(1):39–42.

[Cromer and Liberman, 1970] Cromer, D. T. and Liberman, D. (1970). Relativistic calculation of anomalous scattering factors for X rays. *The Journal of Chemical Physics*, 53(5):1891–1898.

[Crothers et al., 2017] Crothers, T. W., Milot, R. L., Patel, J. B., Parrott, E. S., Schlipf, J., Müller-Buschbaum, P., Johnston, M. B., and Herz, L. M. (2017). Photon reabsorption masks intrinsic bimolecular charge-carrier recombination in $CH_3NH_3PbI_3$ perovskite. *Nano Letters*, 17(9):5782–5789.

[David et al., 2006] David, W. I., Shankland, K., McCusker, L. B., and Baerlocher, C. (2006). *Structure determination from powder diffraction data*, volume 13. OUP Oxford.

[De Boer et al., 2004] De Boer, R., Jochemsen, M., Klapwijk, T., Morpurgo, A., Niemax, J., Tripathi, A., and Pflaum, J. (2004). Space charge limited transport and time of flight measurements in tetracene single crystals: A comparative study. *Journal of Applied Physics*, 95(3):1196–1202.

[De Keijser et al., 1982] De Keijser, T. H., Langford, J., Mittemeijer, E. J., and Vogels, A. (1982). Use of the Voigt function in a single-line method for the analysis of X-ray diffraction line broadening. *Journal of Applied Crystallography*, 15(3):308–314.

[Delhez et al., 1982] Delhez, R., Keijser, T. H., and Mittemeijer, E. (1982). Determination of crystallite size and lattice distortions through X-ray diffraction line profile analysis. *Fresenius' Journal of Analytical Chemistry*, 312(1):1–16.

[deQuilettes et al., 2019] deQuilettes, D. W., Frohna, K., Emin, D., Kirchartz, T., Bulovic, V., Ginger, D. S., and Stranks, S. D. (2019). Charge-carrier recombination in halide perovskites: Focus review. *Chemical Reviews*, 119(20):11007–11019.

[Dhouib and Filali, 1990] Dhouib, A. and Filali, S. (1990). *Operating temperatures of photovoltaic panels*. Elsevier.

[Dinnebier et al., 2018] Dinnebier, R. E., Leineweber, A., and Evans, J. S. (2018). *Rietveld refinement: practical powder diffraction pattern analysis using TOPAS*. Walter de Gruyter GmbH & Co KG.

[Dohner et al., 2014] Dohner, E. R., Hoke, E. T., and Karunadasa, H. I. (2014). Self-assembly of broadband white-light emitters. *Journal of the American Chemical Society*, 136(5):1718–1721.

[Dollase, 1986] Dollase, W. (1986). Correction of intensities for preferred orientation in powder diffractometry: Application of the march model. *Journal of Applied Crystallography*, 19(4):267–272.

[Dolomanov et al., 2009] Dolomanov, O. V., Bourhis, L. J., Gildea, R. J., Howard, J. A., and Puschmann, H. (2009). OLEX2: a complete structure solution, refinement and analysis program. *Journal of Applied Crystallography*, 42(2):339–341.

[Du et al., 2017] Du, K.-z., Tu, Q., Zhang, X., Han, Q., Liu, J., Zauscher, S., and Mitzi, D. B. (2017). Two-dimensional lead (II) halide-based hybrid perovskites templated by acene alkylamines: Crystal structures, optical properties, and piezoelectricity. *Inorganic Chemistry*, 56(15):9291–9302.

[Elton and Salt, 1996] Elton, N. and Salt, P. (1996). Particle statistics in quantitative X-ray diffractometry. *Powder Diffraction*, 11(3):218–229.

[Eperon et al., 2016] Eperon, G. E., Leijtens, T., Bush, K. A., Prasanna, R., Green, T., Wang, J. T.-W., McMeekin, D. P., Volonakis, G., Milot, R. L., May, R., et al. (2016). Perovskite-perovskite tandem photovoltaics with optimized band gaps. *Science*, 354(6314):861–865.

[Etter et al., 2014] Etter, M., Mueller, M., Hanfland, M., and Dinnebier, R. E. (2014). Possibilities and limitations of parametric Rietveld refinement on high pressure data: The case study of $LaFeO_3$. *Zeitschrift für Kristallographie-Crystalline Materials*, 229(3):246–258.

[Fabini et al., 2017] Fabini, D. H., Siaw, T. A., Stoumpos, C. C., Laurita, G., Olds, D., Page, K., Hu, J. G., Kanatzidis, M. G., Han, S., and Seshadri, R. (2017). Universal dynamics of molecular reorientation in hybrid lead iodide perovskites. *Journal of the American Chemical Society*, 139(46):16875–16884. PMID: 29094934.

[Fabini et al., 2016] Fabini, D. H., Stoumpos, C. C., Laurita, G., Kaltzoglou, A., Kontos, A. G., Falaras, P., Kanatzidis, M. G., and Seshadri, R. (2016). Reentrant structural and optical properties and large positive thermal expansion in perovskite formamidinium lead iodide. *Angewandte Chemie*, 128(49):15618–15622.

[Faiman, 2008] Faiman, D. (2008). Assessing the outdoor operating temperature of photovoltaic modules. *Progress in Photovoltaics: Research and Applications*, 16(4):307–315.

[Filip et al., 2014] Filip, M. R., Eperon, G. E., Snaith, H. J., and Giustino, F. (2014). Steric engineering of metal-halide perovskites with tunable optical band gaps. *Nature communications*, 5(1):5757.

[Franchini et al., 2021] Franchini, C., Reticcioli, M., Setvin, M., and Diebold, U. (2021). Polarons in materials. *Nature Reviews Materials*, 6(7):560–586.

[Fu et al., 2021] Fu, P., Liu, Y., Yu, S., Yin, H., Yang, B., Ahmad, S., Guo, X., and Li, C. (2021). Dion-Jacobson and Ruddlesden-Popper double-phase 2D perovskites for solar cells. *Nano Energy*, 88:106249.

[Fu et al., 2017] Fu, Y., Wu, T., Wang, J., Zhai, J., Shearer, M. J., Zhao, Y., Hamers, R. J., Kan, E., Deng, K., Zhu, X.-Y., et al. (2017). Stabilization of the metastable lead iodide perovskite phase via surface functionalization. *Nano Letters*, 17(7):4405–4414.

[Futscher and Ehrler, 2016] Futscher, M. H. and Ehrler, B. (2016). Efficiency limit of perovskite/Si tandem solar cells. *ACS Energy Letters*, 1(4):863–868.

[Galkowski et al., 2016] Galkowski, K., Mitioglu, A., Miyata, A., Plochocka, P., Portugall, O., Eperon, G. E., Wang, J. T.-W., Stergiopoulos, T., Stranks, S. D., Snaith, H. J., et al. (2016). Determination of the exciton binding energy and effective masses for methylammonium and formamidinium lead tri-halide perovskite semiconductors. *Energy & Environmental Science*, 9(3):962–970.

[Game et al., 2017] Game, O. S., Buchsbaum, G. J., Zhou, Y., Padture, N. P., and Kingon, A. I. (2017). Ions matter: Description of the anomalous electronic behavior in methylammonium lead halide perovskite devices. *Advanced Functional Materials*, 27(16):1606584.

[García-Fernández et al., 2019] García-Fernández, A., Juarez-Perez, E. J., Bermúdez-García, J. M., Llamas-Saiz, A. L., Artiaga, R., López-Beceiro, J. J., Señarís-Rodríguez, M. A., Sánchez-Andújar, M., and Castro-García, S. (2019). Hybrid lead halide $[(CH_3)_2NH_2]PbX_3$ (X= Cl- and Br-) hexagonal perovskites with multiple functional properties. *Journal of Materials Chemistry C*, 7(32):10008–10018.

[Gebhardt and Rappe, 2019] Gebhardt, J. and Rappe, A. M. (2019). Mix and match: Organic and inorganic ions in the perovskite lattice. *Advanced Materials*, 31(47):1802697.

[Geisz et al., 2020] Geisz, J. F., France, R. M., Schulte, K. L., Steiner, M. A., Norman, A. G., Guthrey, H. L., Young, M. R., Song, T., and Moriarty, T. (2020). Six-junction III–V solar cells with 47.1 % conversion efficiency under 143 Suns concentration. *Nature Energy*, 5(4):326–335.

[Gholipour et al., 2017] Gholipour, S., Ali, A. M., Correa-Baena, J.-P., Turren-Cruz, S.-H., Tajabadi, F., Tress, W., Taghavinia, N., Grätzel, M., Abate, A., De Angelis, F., et al. (2017). Globularity-selected large molecules for a new generation of multication perovskites. *Advanced Materials*, 29(38):1702005.

[Glazer, 1972] Glazer, A. M. (1972). The classification of tilted octahedra in perovskites. *Acta Crystallographica Section B Structural Crystallography and Crystal Chemistry*, 28(11):3384–3392.

[Gommers et al., 2023] Gommers, R., Virtanen, P., Burovski, E., Haberland, M., Weckesser, W., Oliphant, T. E., Reddy, T., Cournapeau, D., alexbrc, Nelson, A., Peterson, P., Wilson, J., Roy, P., endolith, Polat, I., Mayorov, N., van der Walt, S., Brett, M., Laxalde, D., Larson, E., Millman, J., Sakai, A., Lars, peterbell10, van Mulbregt, P., Carey, C., eric jones, McKibben, N., Kai, and Kern, R. (2023). scipy/scipy: SciPy 1.10.1.

[Graf, 2014] Graf, J. (2014). Iμs for high resolution small molecule crystallography.

[Grancini and Nazeeruddin, 2019] Grancini, G. and Nazeeruddin, M. K. (2019). Dimensional tailoring of hybrid perovskites for photovoltaics. *Nature Reviews Materials*, 4(1):4–22.

[Grätzel, 2017] Grätzel, M. (2017). The rise of highly efficient and stable perovskite solar cells. *Accounts of Chemical Research*, 50(3):487–491.

[Gražulis et al., 2009] Gražulis, S., Chateigner, D., Downs, R. T., Yokochi, A., Quirós, M., Lutterotti, L., Manakova, E., Butkus, J., Moeck, P., and Le Bail, A. (2009). Crystallography open database–an open-access collection of crystal structures. *Journal of Applied Crystallography*, 42(4):726–729.

[Green, 2008] Green, M. A. (2008). Self-consistent optical parameters of intrinsic silicon at 300 K including temperature coefficients. *Solar Energy Materials and Solar Cells*, 92(11):1305–1310.

[Green et al., 2014] Green, M. A., Ho-Baillie, A., and Snaith, H. J. (2014). The emergence of perovskite solar cells. *Nature Photonics*, 8(7):506–514.

[Green et al., 2015] Green, M. A., Jiang, Y., Soufiani, A. M., and Ho-Baillie, A. (2015). Optical properties of photovoltaic organic–inorganic lead halide perovskites. *The Journal of Physical Chemistry Letters*, 6(23):4774–4785.

[Greenland et al., 2019] Greenland, C., Shnier, A., Rajendran, S. K., Smith, J. A., Game, O. S., Wamwangi, D., Turnbull, G. A., Samuel, I. D., Billing, D. G., and Lidzey, D. G. (2019). Correlating phase behavior with photophysical properties in mixed-cation mixed-halide perovskite thin films. *Advanced Energy Materials*, page 1901350.

[Guillemoles et al., 2019] Guillemoles, J.-F., Kirchartz, T., Cahen, D., and Rau, U. (2019). Guide for the perplexed to the Shockley–Queisser model for solar cells. *Nature Photonics*, 13(8):501–505.

[Gupta, 1998] Gupta, S. (1998). Peak decomposition using Pearson type VII function. *Journal of Applied Cystallography*, 31(3):474–476.

[Hellenbrandt, 2004] Hellenbrandt, M. (2004). The inorganic crystal structure database (ICSD)—present and future. *Crystallography Reviews*, 10(1):17–22.

[Henderson et al., 2014] Henderson, G. S., De Groot, F. M., and Moulton, B. J. (2014). X-ray absorption near-edge structure (XANES) spectroscopy. *Reviews in Mineralogy and Geochemistry*, 78(1):75–138.

[Hennig et al., 2001] Hennig, C., Reich, T., Funke, H., Rossberg, A., Rutsch, M., and Bernhard, G. (2001). EXAFS as a tool for bond-length determination in the environment of heavy atoms. *Journal of Synchrotron Radiation*, 8(2):695–697.

[Hoffman et al., 2019] Hoffman, J. M., Che, X., Sidhik, S., Li, X., Hadar, I., Blancon, J.-C., Yamaguchi, H., Kepenekian, M., Katan, C., Even, J., et al. (2019). From 2D to 1D electronic dimensionality in halide perovskites with stepped and flat layers using propylammonium as a spacer. *Journal of the American Chemical Society*, 141(27):10661–10676.

[Hölzer et al., 1997] Hölzer, G., Fritsch, M., Deutsch, M., Härtwig, J., and Förster, E. (1997). K$\alpha_{1,2}$ and K$\beta_{1,3}$ X-ray emission lines of the $3d$ transition metals. *Physical Review A*, 56(6):4554.

[Honda et al., 2016] Honda, M., Shimoyama, I., Okamoto, Y., Baba, Y., Suzuki, S., and Yaita, T. (2016). X-ray absorption fine structure at the cesium l_3 absorption edge for cesium sorbed in clay minerals. *The Journal of Physical Chemistry C*, 120(10):5534–5538.

[Hong et al., 1992] Hong, X., Ishihara, T., and Nurmikko, A. (1992). Photoconductivity and electroluminescence in lead iodide based natural quantum well structures. *Solid State Communications*, 84(6):657–661.

[Howard and Stokes, 1998] Howard, C. J. and Stokes, H. T. (1998). Group-theoretical analysis of octahedral tilting in perovskites. *Acta Crystallographica Section B: Structural Science*, 54(6):782–789.

[Howard and Stokes, 2002] Howard, C. J. and Stokes, H. T. (2002). Group-theoretical analysis of octahedral tilting in perovskites. Erratum. *Acta Crystallographica Section B Structural Science*, 58(3):565–565.

[Hui et al., 2021] Hui, Y., Tan, Y.-Y., Chen, L., Nan, Z.-A., Zhou, J.-Z., Yan, J.-W., and Mao, B.-W. (2021). Stability of perovskite thin films under working condition: bias-dependent degradation and grain boundary effects. *Advanced Functional Materials*, 31(36):2103894.

[Hunter, 2007] Hunter, J. D. (2007). Matplotlib: A 2D graphics environment. *Computing in science & engineering*, 9(3):90–95.

[Inkscape Project, 2021] Inkscape Project (2021). Inkscape.

[Ishihara, 1994] Ishihara, T. (1994). Optical properties of PbI-based perovskite structures. *Journal of Luminescence*, 60:269–274.

[Ishihara et al., 1989] Ishihara, T., Takahashi, J., and Goto, T. (1989). Exciton state in two-dimensional perovskite semiconductor $(C_{10}H_{21}NH_3)_2PbI_4$. *Solid State Communications*, 69(9):933–936.

[James et al., 2001] James, J., Spittle, J., Brown, S., and Evans, R. (2001). A review of measurement techniques for the thermal expansion coefficient of metals and alloys at elevated temperatures. *Measurement Science and Technology*, 12(3):R1.

[Jang et al., 2021] Jang, Y.-W., Lee, S., Yeom, K. M., Jeong, K., Choi, K., Choi, M., and Noh, J. H. (2021). Intact 2D/3D halide junction perovskite solar cells via solid-phase in-plane growth. *Nature Energy*, 6(1):63–71.

[Järvinen, 1993] Järvinen, M. (1993). Application of symmetrized harmonics expansion to correction of the preferred orientation effect. *Journal of Applied Crystallography*, 26(4):525–531.

[Jeon et al., 2015] Jeon, N. J., Noh, J. H., Yang, W. S., Kim, Y. C., Ryu, S., Seo, J., and Seok, S. I. (2015). Compositional engineering of perovskite materials for high-performance solar cells. *Nature*, 517(7535):476–480.

[Jeong et al., 2020] Jeong, M., Choi, I. W., Go, E. M., Cho, Y., Kim, M., Lee, B., Jeong, S., Jo, Y., Choi, H. W., Lee, J., et al. (2020). Stable perovskite solar cells with efficiency exceeding 24.8 % and 0.3 V voltage loss. *Science*, 369(6511):1615–1620.

[Jesper Jacobsson et al., 2016] Jesper Jacobsson, T., Correa-Baena, J.-P., Pazoki, M., Saliba, M., Schenk, K., Grätzel, M., and Hagfeldt, A. (2016). Exploration of the compositional space for mixed lead halogen perovskites for high efficiency solar cells. *Energy Environ. Sci.*, 9:1706–1724.

[Jiang et al., 2019] Jiang, Q., Zhao, Y., Zhang, X., Yang, X., Chen, Y., Chu, Z., Ye, Q., Li, X., Yin, Z., and You, J. (2019). Surface passivation of perovskite film for efficient solar cells. *Nature Photonics*, 13(7):460–466.

[Jung and Park, 2015] Jung, H. S. and Park, N.-G. (2015). Perovskite solar cells: From materials to devices. *Small*, 11(1):10–25.

[Kang and Park, 2019] Kang, D.-H. and Park, N.-G. (2019). On the current–voltage hysteresis in perovskite solar cells: Dependence on perovskite composition and methods to remove hysteresis. *Advanced Materials*, 31(34):1805214.

[Katan et al., 2019] Katan, C., Mercier, N., and Even, J. (2019). Quantum and dielectric confinement effects in lower-dimensional hybrid perovskite semiconductors. *Chemical Reviews*, 119(5):3140–3192.

[Kawachi et al., 2019] Kawachi, S., Atsumi, M., Saito, N., Ohashi, N., Murakami, Y., and Yamaura, J.-i. (2019). Structural and thermal properties in formamidinium and Cs-mixed lead halides. *The Journal of Physical Chemistry Letters*, 10(22):6967–6972.

[Kawamura et al., 2002] Kawamura, Y., Mashiyama, H., and Hasebe, K. (2002). Structural study on cubic-tetragonal transition of $CH_3NH_3PbI_3$. *Journal of the Physical Society of Japan*, 71(7):1694–1697.

[Kieslich et al., 2018] Kieslich, G., Skelton, J. M., Armstrong, J., Wu, Y., Wei, F., Svane, K. L., Walsh, A., and Butler, K. T. (2018). Hydrogen bonding versus entropy: revealing the underlying thermodynamics of the hybrid organic–inorganic perovskite $[CH_3NH_3]PbBr_3$. *Chemistry of Materials*, 30(24):8782–8788.

[Kitazawa, 1997] Kitazawa, N. K. N. (1997). Optical absorption and photoluminescence properties of Pb(I, Br)-based two-dimensional layered perovskite. *Japanese Journal of Applied Physics*, 36(4R):2272.

[Kluherz et al., 2022] Kluherz, K. T., Mergelsberg, S. T., Sommer, D. E., Roh, J. Y. D., Saslow, S. A., Biner, D., Krämer, K. W., Dunham, S. T., De Yoreo, J. J., and Gamelin, D. R. (2022). Defect structure in quantum-cutting Yb^{3+}-doped $CsPbCl_3$ perovskites probed by X-ray absorption and atomic pair distribution function analysis. *Physical Review Materials*, 6(7):074601.

[Koo et al., 2020] Koo, D., Cho, Y., Kim, U., Jeong, G., Lee, J., Seo, J., Yang, C., and Park, H. (2020). High-performance inverted perovskite solar cells with operational stability via n-type small molecule additive-assisted defect passivation. *Advanced Energy Materials*, 10(46):2001920.

[Kuciauskas et al., 2021] Kuciauskas, D., Moseley, J., and Lee, C. (2021). Identification of recombination losses in CdSe/CdTe solar cells from spectroscopic and microscopic time-resolved photoluminescence. *Solar RRL*, 5(4):2000775.

[Langford and Wilson, 1978] Langford, J. I. and Wilson, A. (1978). Scherrer after sixty years: A survey and some new results in the determination of crystallite size. *Journal of Applied Crystallography*, 11(2):102–113.

[Le Bail, 2005] Le Bail, A. (2005). Whole powder pattern decomposition methods and applications: A retrospection. *Powder Diffraction*, 20(4):316–326.

[Le Bail et al., 2008] Le Bail, A., Cranswick, L. M., Madsen, I., Fitch, A., Allmann, R., Giacovazzo, C., Altomare, A., Cockcroft, J. K., Caliandro, R., Norby, P., et al. (2008). *Powder diffraction: Theory and practice*. Royal Society of Chemistry.

[Lee et al., 2021] Lee, J.-W., Seo, S., Nandi, P., Jung, H. S., Park, N.-G., and Shin, H. (2021). Dynamic structural property of organic-inorganic metal halide perovskite. *iScience*, 24(1):101959.

[Lehmann et al., 2019] Lehmann, F., Franz, A., Többens, D. M., Levcenco, S., Unold, T., Taubert, A., and Schorr, S. (2019). The phase diagram of a mixed halide (Br, I) hybrid perovskite obtained by synchrotron X-ray diffraction. *RSC Advances*, 9(20):11151–11159.

[Lei et al., 2021] Lei, Y., Xu, Y., Wang, M., Zhu, G., and Jin, Z. (2021). Origin, influence, and countermeasures of defects in perovskite solar cells. *Small*, 17(26):2005495.

[Leoni, 2019] Leoni, M. (2019). The Scherrer formula and integral-breadth methods. *International Tables for Crystallography*, H:524.

[Li et al., 2008] Li, C., Lu, X., Ding, W., Feng, L., Gao, Y., and Guo, Z. (2008). Formability of ABX_3 (X= F, Cl, Br, I) halide perovskites. *Acta Crystallographica Section B: Structural Science*, 64(6):702–707.

[Li et al., 2016] Li, Z., Yang, M., Park, J.-S., Wei, S.-H., Berry, J. J., and Zhu, K. (2016). Stabilizing perovskite structures by tuning tolerance factor: formation of formamidinium and cesium lead iodide solid-state alloys. *Chemistry of Materials*, 28(1):284–292.

[Liu et al., 2020] Liu, G., Zheng, H., Xu, H., Zhang, L., Xu, X., Xu, S., and Pan, X. (2020). Interface passivation treatment by halogenated low-dimensional perovskites for high-performance and stable perovskite photovoltaics. *Nano Energy*, 73:104753.

[Luo et al., 2018] Luo, D., Yang, W., Wang, Z., Sadhanala, A., Hu, Q., Su, R., Shivanna, R., Trindade, G. F., Watts, J. F., Xu, Z., et al. (2018). Enhanced photovoltage for inverted planar heterojunction perovskite solar cells. *Science*, 360(6396):1442–1446.

[Ma et al., 2022] Ma, D., Qin, X., Dai, N., and Cao, X. (2022). Tunable photoluminescence and enhanced stability in two-dimensional $(C_3H_7NH_3)_2(MA)_{n-1}Pb_nBr_{3n+1}$ perovskite colloidal nanocrystals. *Optical Materials*, 133:113072.

[Ma et al., 2017] Ma, F., Li, J., Li, W., Lin, N., Wang, L., and Qiao, J. (2017). Stable α/δ phase junction of formamidinium lead iodide perovskites for enhanced near-infrared emission. *Chemical Science*, 8(1):800–805.

[Mahata et al., 2019] Mahata, A., Meggiolaro, D., and De Angelis, F. (2019). From large to small polarons in lead, tin, and mixed lead–tin halide perovskites. *The Journal of Physical Chemistry Letters*, 10(8):1790–1798.

[Makuła et al., 2018] Makuła, P., Pacia, M., and Macyk, W. (2018). How to correctly determine the band gap energy of modified semiconductor photocatalysts based on UV–Vis spectra.

[Mannino et al., 2020] Mannino, G., Deretzis, I., Smecca, E., La Magna, A., Alberti, A., Ceratti, D., and Cahen, D. (2020). Temperature-dependent optical band gap in $CsPbBr_3$, $MAPbBr_3$, and $FAPbBr_3$ single crystals. *The Journal of Physical Chemistry Letters*, 11(7):2490–2496. PMID: 32148047.

[Marchenko et al., 2022] Marchenko, E. I., Fateev, S. A., Korolev, V. V., Buchinskiy, V., Eremin, N., Goodilin, E. A., and Tarasov, A. B. (2022). Structure-related bandgap of hybrid lead halide perovskites and close-packed $APbX_3$ family of phases. *Journal of Materials Chemistry C*, 10(44):16838–16846.

[Marti and Araújo, 1996] Marti, A. and Araújo, G. L. (1996). Limiting efficiencies for photovoltaic energy conversion in multigap systems. *Solar Energy Materials and Solar Cells*, 43(2):203–222.

[Masson et al., 1996] Masson, O., Guinebretière, R., and Dauger, A. (1996). Reflection asymmetric powder diffraction with flat-plate sample using a curved position-sensitive detector (inel cps 120). *Journal of Applied Crystallography*, 29(5):540–546.

[Mattoni et al., 2015] Mattoni, A., Filippetti, A., Saba, M., and Delugas, P. (2015). Methylammonium rotational dynamics in lead halide perovskite by classical molecular dynamics: The role of temperature. *The Journal of Physical Chemistry C*, 119(30):17421–17428.

[Mercier et al., 2004] Mercier, N., Poiroux, S., Riou, A., and Batail, P. (2004). Unique hydrogen bonding correlating with a reduced band gap and phase transition in the hybrid perovskites $(HO(CH_2)_2NH_3)_2PbX_4$ (X= I, Br). *Inorganic Chemistry*, 43(26):8361–8366.

[Meresse and Daoud, 1989] Meresse, A. and Daoud, A. (1989). Bis(n-propylammonium) tetrachloroplumbate. *Acta Crystallographica Section C: Crystal Structure Communications*, 45(2):194–196.

[Ming et al., 2018] Ming, W., Yang, D., Li, T., Zhang, L., and Du, M.-H. (2018). Formation and diffusion of metal impurities in perovskite solar cell material $CH_3NH_3PbI_3$: implications on solar cell degradation and choice of electrode. *Advanced Science*, 5(2):1700662.

[Mittemeijer and Welzel, 2008] Mittemeijer, E. J. and Welzel, U. (2008). The "state of the art" of the diffraction analysis of crystallite size and lattice strain. *Zeitschrift für Kristallographie*, 223(9):552–560.

[Miyasaka, 2018] Miyasaka, T. (2018). Lead halide perovskites in thin film photovoltaics: Background and perspectives. *Bulletin of the Chemical Society of Japan*, 91(7):1058–1068.

[Miyata and Zhu, 2018] Miyata, K. and Zhu, X.-Y. (2018). Ferroelectric large polarons. *Nature Materials*, 17(5):379–381.

[Motti et al., 2019] Motti, S. G., Crothers, T., Yang, R., Cao, Y., Li, R., Johnston, M. B., Wang, J., and Herz, L. M. (2019). Heterogeneous photon recycling and charge diffusion enhance charge transport in quasi-2D lead-halide perovskite films. *Nano Letters*, 19(6):3953–3960.

[Müller et al., 2009] Müller, M., Dinnebier, R. E., Jansen, M., Wiedemann, S., and Plüg, C. (2009). Kinetic analysis of the phase transformation from α-to β-copper phthalocyanine: A case study for sequential and parametric Rietveld refinements. *Powder Diffraction*, 24(3):191–199.

[Mundt et al., 2021] Mundt, L. E., Zhang, F., Palmstrom, A. F., Xu, J., Tirawat, R., Kelly, L. L., Stone, K. H., Zhu, K., Berry, J. J., Toney, M. F., et al. (2021). Mixing matters: Nanoscale heterogeneity and stability in metal halide perovskite solar cells. *ACS Energy Letters*, 7(1):471–480.

[Nasdaq, 2015] Nasdaq (2015). Solar energy will perovskite cells live their promise. https://www.nasdaq.com/articles/solar-energy-will-perovskite-cells-live-their-promise-2015-06-12 (accessed: 2023-03-13).

[Näsström et al., 2020] Näsström, H., Becker, P., Márquez, J., Shargaieva, O., Mainz, R., Unger, E., and Unold, T. (2020). Dependence of phase transitions on halide ratio in inorganic $CsPb(Br_xI_{1-x})_3$ perovskite thin films obtained from high-throughput experimentation. *Journal of Materials Chemistry A*, 8(43):22626–22631.

[Nelson et al., 2001] Nelson, C., Zimmermann, M. v., Hill, J., Gibbs, D., Kiryukhin, V., Koo, T., and Cheong, S. (2001). X-ray scattering studies of correlated polarons in $La_{0.7}Ca_{0.3}MnO_3$. In *Vibronic Interactions: Jahn-Teller Effect in Crystals and Molecules*, pages 209–213. Springer.

[Newville et al., 2014] Newville, M., Stensitzki, T., Allen, D. B., and Ingargiola, A. (2014). LMFIT: Non-linear least-square minimization and curve-fitting for Python.

[Noffsinger et al., 2012] Noffsinger, J., Kioupakis, E., Van de Walle, C. G., Louie, S. G., and Cohen, M. L. (2012). Phonon-assisted optical absorption in silicon from first principles. *Physical Review Letters*, 108(16):167402.

[NREL, 2023] NREL (2023). Best research-cell efficiency chart. https://www.nrel.gov/pv/assets/docs/cell-efficiency-data-table.xlsx (accessed: 2023-03-13).

[Paritmongkol et al., 2020] Paritmongkol, W., Powers, E. R., Dahod, N. S., and Tisdale, W. A. (2020). Two origins of broadband emission in multilayered 2D lead iodide perovskites. *The Journal of Physical Chemistry Letters*, 11(20):8565–8572.

[Park et al., 2018] Park, J. S., Kim, S., Xie, Z., and Walsh, A. (2018). Point defect engineering in thin-film solar cells. *Nature Reviews Materials*, 3(7):194–210.

[Pazos-Outon et al., 2017] Pazos-Outon, L. M., Lee, J. M., Futscher, M. H., Kirch, A., Tabachnyk, M., Friend, R. H., and Ehrler, B. (2017). A silicon-singlet fission tandem solar cell exceeding 100 % external quantum efficiency with high spectral stability. *ACS Energy Letters*, 2(2):476–480.

[Pecharsky and Zavalij, 2005] Pecharsky, V. and Zavalij, P. (2005). *Fundamentals of Powder Diffraction and Structural characterization of Materials*. Springer Science+Business Media.

[Peterson, 2005] Peterson, V. (2005). Lattice parameter measurement using Le Bail versus structural (Rietveld) refinement: A caution for complex, low symmetry systems. *Powder Diffraction*, 20(1):14–17.

[Petrov et al., 2017] Petrov, A. A., Goodilin, E. A., Tarasov, A. B., Lazarenko, V. A., Dorovatovskii, P. V., and Khrustalev, V. N. (2017). Formamidinium iodide: crystal structure and phase transitions. *Acta Crystallographica Section E: Crystallographic Communications*, 73(4):569–572.

[Quan et al., 2016] Quan, L. N., Yuan, M., Comin, R., Voznyy, O., Beauregard, E. M., Hoogland, S., Buin, A., Kirmani, A. R., Zhao, K., Amassian, A., et al. (2016). Ligand-stabilized reduced-dimensionality perovskites. *Journal of the American Chemical Society*, 138(8):2649–2655.

[Queisser, 2009] Queisser, H. J. (2009). Detailed balance limit for solar cell efficiency. *Materials Science and Engineering: B*, 159:322–328.

[Quintero-Bermudez et al., 2018] Quintero-Bermudez, R., Gold-Parker, A., Proppe, A. H., Munir, R., Yang, Z., Kelley, S. O., Amassian, A., Toney, M. F., and Sargent, E. H. (2018). Compositional and orientational control in metal halide perovskites of reduced dimensionality. *Nature Materials*, 17(10):900–907.

[Ramirez et al., 2018] Ramirez, D., Montoya, J. F., Uribe, J. I., and Jaramillo, F. (2018). Study of the crystallization of metal halide perovskites containing additives via differential scanning calorimetry. *Journal of Electronic Materials*, 47(10):6319–6327.

[Rao et al., 1996] Rao, G. N., Sastry, V. S., Murthy, H. G. K., Seshagiri, V., and Radhakrishnan, T. (1996). Toward development of an ideal X-ray diffractometer sample holder. *Powder Diffraction*, 11(3):200–203.

[MYKIN INC, 2019] MYKIN INC (2019). Rubber chemical resistance chart. (accessed: 2023-03-21).

[Rietveld, 1969] Rietveld, H. M. (1969). A profile refinement method for nuclear and magnetic structures. *Journal of Applied Crystallography*, 2(2):65–71.

[Romande Energie and Mediacom, 2013] Romande Energie and Mediacom (2013). Accessed: 2022-02-21, https://actu.epfl.ch/news/epfl-s-campus-has-the-world-s-first-solar-window/.

[Rowles, 2021] Rowles, M. (2021). Accessed: 2022-04-21, http://TOPAS.dur.ac.uk/TOPASwiki/doku.php?id=sequential_refinements.

[Rühle, 2016] Rühle, S. (2016). Tabulated values of the Shockley–Queisser limit for single junction solar cells. *Solar Energy*, 130:139–147.

[Sabine et al., 1998] Sabine, T., Hunter, B., Sabine, W., and Ball, C. (1998). Analytical expressions for the transmission factor and peak shift in absorbing cylindrical specimens. *Journal of Applied Crystallography*, 31(1):47–51.

[Saliba et al., 2016] Saliba, M., Matsui, T., Seo, J.-Y., Domanski, K., Correa-Baena, J.-P., Nazeeruddin, M. K., Zakeeruddin, S. M., Tress, W., Abate, A., Hagfeldt, A., et al. (2016). Cesium-containing triple cation perovskite solar cells: Improved stability, reproducibility and high efficiency. *Energy & Environmental Science*, 9(6):1989–1997.

[Scardi, 2008] Scardi, P. (2008). Microstructural properties: Lattice defects and domain size effects. In *Powder Diffraction: Theory and Practice*, pages 376–413. Royal society of chemistry.

[Schileo and Grancini, 2021] Schileo, G. and Grancini, G. (2021). Lead or no lead? availability, toxicity, sustainability and environmental impact of lead-free perovskite solar cells. *Journal of Materials Chemistry C*, 9(1):67–76.

[Schueller et al., 2018] Schueller, E. C., Laurita, G., Fabini, D. H., Stoumpos, C. C., Kanatzidis, M. G., and Seshadri, R. (2018). Crystal structure evolution and notable thermal expansion in hybrid perovskites formamidinium tin iodide and formamidinium lead bromide. *Inorganic chemistry*, 57(2):695–701.

[Sheldrick, 2015a] Sheldrick, G. M. (2015a). Crystal structure refinement with SHELXL. *Acta Crystallographica Section C: Structural Chemistry*, 71(1):3–8.

[Sheldrick, 2015b] Sheldrick, G. M. (2015b). SHELXT–integrated space-group and crystal-structure determination. *Acta Crystallographica Section A: Foundations and Advances*, 71(1):3–8.

[Shen et al., 2020] Shen, P., Vogt, T., and Lee, Y. (2020). Pressure-induced enhancement of broad-band white light emission in butylammonium lead bromide. *The Journal of Physical Chemistry Letters*, 11(10):4131–4137.

[Sherkar et al., 2017] Sherkar, T. S., Momblona, C., Gil-Escrig, L., Ávila, J., Sessolo, M., Bolink, H. J., and Koster, L. J. A. (2017). Recombination in perovskite solar cells: significance of grain boundaries, interface traps, and defect ions. *ACS Energy Letters*, 2(5):1214–1222.

[Shin et al., 2021] Shin, Y., Choi, H., Park, C., Park, D., Jeong, M., Nojiri, H., Yang, Z., Kohama, Y., and Kim, Y. (2021). Combination of optical transitions of polarons with Rashba effect in methylammonium lead trihalide perovskites under high magnetic fields. *Physical Review B*, 104(3):035205.

[Shirley, 1980] Shirley, R. (1980). Data accuracy for powder indexing. *National Bureau of Standards (US) Special Publication*, (567):361–382.

[Shnier, 2019] Shnier, A. (2019). Spin coater V1 (almost analog). https://www.instructables.com/Spin-Coater-V1-almost-Analog/ (accessed: 2021-11-23).

[Shockley and Queisser, 1961] Shockley, W. and Queisser, H. J. (1961). Detailed balance limit of efficiency of p-n junction solar cells. *Journal of Applied Physics*, 32(3):510–519.

[Singh and Parashar, 2020] Singh, R. and Parashar, M. (2020). Origin of hysteresis in perovskite solar cells. In *Soft-matter thin film solar cells: Physical processes and device simulation*, pages 1–1. AIP Publishing LLC Melville, New York.

[Skoplaki and Palyvos, 2009] Skoplaki, E. and Palyvos, J. A. (2009). Operating temperature of photovoltaic modules: A survey of pertinent correlations. *Renewable Energy*, 34(1):23–29.

[Smets et al., 2015] Smets, A. H., Jäger, K., Isabella, O., Swaaij, R. A., and Zeman, M. (2015). *Solar Energy: The physics and engineering of photovoltaic conversion, technologies and systems*. UIT Cambridge.

[Smith, 2001] Smith, D. K. (2001). Particle statistics and whole-pattern methods in quantitative X-ray powder diffraction analysisa. *Powder Diffraction*, 16(4):186–191.

[Smith et al., 2014] Smith, I. C., Hoke, E. T., Solis-Ibarra, D., McGehee, M. D., and Karunadasa, H. I. (2014). A layered hybrid perovskite solar-cell absorber with enhanced moisture stability. *Angewandte Chemie International Edition*, 53(42):11232–11235.

[Smith et al., 2019] Smith, M. D., Connor, B. A., and Karunadasa, H. I. (2019). Tuning the luminescence of layered halide perovskites. *Chemical Reviews*, 119(5):3104–3139.

[Smith et al., 2017] Smith, M. D., Jaffe, A., Dohner, E. R., Lindenberg, A. M., and Karunadasa, H. I. (2017). Structural origins of broadband emission from layered Pb–Br hybrid perovskites. *Chemical Science*, 8(6):4497–4504.

[Speakman, 2014] Speakman, S. A. (2014). Estimating crystallite size using XRD. *MIT Center for Materials Science and Engineering*, 2:14.

[Steirer et al., 2016] Steirer, K. X., Schulz, P., Teeter, G., Stevanovic, V., Yang, M., Zhu, K., and Berry, J. J. (2016). Defect tolerance in methylammonium lead triiodide perovskite. *ACS Energy Letters*, 1(2):360–366.

[Stinton and Evans, 2007] Stinton, G. W. and Evans, J. S. (2007). Parametric Rietveld refinement. *Journal of Applied Crystallography*, 40(1):87–95.

[Stokes et al., 2017] Stokes, H. T., Hatch, D., and Campbell, B. (2017). ISODISTORT. *ISOTROPY Software Suite, iso.byu.edu*.

[Stokes et al., 2006] Stokes, H. T., Hatch, D. M., Campbell, B. J., and Tanner, D. E. (2006). ISODISPLACE: a web-based tool for exploring structural distortions. *Journal of Applied Crystallography*, 39(4):607–614.

[Stokes et al., 2002] Stokes, H. T., Kisi, E. H., Hatch, D. M., and Howard, C. J. (2002). Group-theoretical analysis of octahedral tilting in ferroelectric perovskites. *Acta Crystallographica Section B: Structural Science*, 58(6):934–938.

[Stoumpos et al., 2016] Stoumpos, C. C., Cao, D. H., Clark, D. J., Young, J., Rondinelli, J. M., Jang, J. I., Hupp, J. T., and Kanatzidis, M. G. (2016). Ruddlesden–Popper hybrid lead iodide perovskite 2D homologous semiconductors. *Chemistry of Materials*, 28(8):2852–2867.

[Stoumpos et al., 2017] Stoumpos, C. C., Soe, C. M. M., Tsai, H., Nie, W., Blancon, J.-C., Cao, D. H., Liu, F., Traoré, B., Katan, C., Even, J., et al. (2017). High members of the 2D Ruddlesden-Popper halide perovskites: Synthesis, optical properties, and solar cells of $(CH_3(CH_2)_3NH_3)_2(CH_3NH_3)_4Pb_5I_{16}$. *Chem*, 2(3):427–440.

[Sun et al., 2017] Sun, S., Deng, Z., Wu, Y., Wei, F., Isikgor, F. H., Brivio, F., Gaultois, M. W., Ouyang, J., Bristowe, P. D., Cheetham, A. K., et al. (2017). Variable temperature and high-pressure crystal chemistry of perovskite formamidinium lead iodide: a single crystal X-ray diffraction and computational study. *Chemical Communications*, 53(54):7537–7540.

[Sutanto et al., 2020] Sutanto, A. A., Szostak, R., Drigo, N., Queloz, V. I., Marchezi, P., Germino, J., Tolentino, H. C., Nazeeruddin, M. K., Nogueira, A. F., and Grancini, G. (2020). In situ analysis reveals the role of 2D perovskite in preventing thermal-induced degradation in 2D/3D perovskite interfaces. *Nano Letters*, 20(5):3992–3998.

[Syzgantseva et al., 2017] Syzgantseva, O. A., Saliba, M., Graätzel, M., and Rothlisberger, U. (2017). Stabilization of the perovskite phase of formamidinium lead triiodide by methylammonium, Cs, and/or Rb doping. *The Journal of Physical Chemistry Letters*, 8(6):1191–1196.

[Tanaka et al., 2003] Tanaka, K., Takahashi, T., Ban, T., Kondo, T., Uchida, K., and Miura, N. (2003). Comparative study on the excitons in lead-halide-based perovskite-type crystals $CH_3NH_3PbBr_3$ $CH_3NH_3PbI_3$. *Solid State Communications*, 127(9-10):619–623.

[Tanaka et al., 2005] Tanaka, K., Takahashi, T., Kondo, T., Umeda, K., Ema, K., Umebayashi, T., Asai, K., Uchida, K., and Miura, N. (2005). Electronic and excitonic structures of inorganic–organic perovskite-type quantum-well crystal $(C_4H_9NH_3)_2PbBr_4$. *Japanese Journal of Applied Physics*, 44(8R):5923.

[Tao et al., 2017] Tao, S. X., Cao, X., and Bobbert, P. A. (2017). Accurate and efficient band gap predictions of metal halide perovskites using the DFT-1/2 method: GW accuracy with DFT expense. *Scientific Reports*, 7(1):14386.

[Taufique et al., 2018] Taufique, M., Khanal, R., Choudhury, S., and Banerjee, S. (2018). Impact of iodine antisite (I_{Pb}) defects on the electronic properties of the (110) $CH_3NH_3PbI_3$ surface. *The Journal of Chemical Physics*, 149(16):164704.

[Toby, 2006] Toby, B. H. (2006). R factors in Rietveld analysis: How good is good enough? *Powder Diffraction*, 21(1):67–70.

[Toby and Von Dreele, 2013] Toby, B. H. and Von Dreele, R. B. (2013). GSAS-II: The genesis of a modern open-source all purpose crystallography software package. *Journal of Applied Crystallography*, 46(2):544–549.

[Tremblay et al., 2019] Tremblay, M.-H., Bacsa, J., Zhao, B., Pulvirenti, F., Barlow, S., and Marder, S. R. (2019). Structures of $(4\text{-}Y{-}C_6H_4CH_2NH_3)_2PbI_4$ {Y= H, F, Cl, Br, I}: tuning of hybrid organic inorganic perovskite structures from Ruddlesden–Popper to Dion–Jacobson limits. *Chemistry of Materials*, 31(16):6145–6153.

[Trots and Myagkota, 2008] Trots, D. and Myagkota, S. (2008). High-temperature structural evolution of caesium and rubidium triiodoplumbates. *Journal of Physics and Chemistry of Solids*, 69(10):2520–2526.

[Umebayashi et al., 2003] Umebayashi, T., Asai, K., Kondo, T., and Nakao, A. (2003). Electronic structures of lead iodide based low-dimensional crystals. *Physical Review B*, 67(15):155405.

[Van Rossum and Drake, 2009] Van Rossum, G. and Drake, F. L. (2009). *Python 3 reference manual*. CreateSpace, Scotts Valley, CA.

[Von Dreele and Rodriguez-Carvajal, 2008] Von Dreele, R. and Rodriguez-Carvajal, J. (2008). The intensity of a Bragg reflection. In *Powder Diffraction*, pages 58–88. RSCPublishing: Cambridge.

[Vonk and Graafsma, 2014] Vonk, V. and Graafsma, H. (2014). *In-situ* X-ray diffraction at synchrotrons and free-electron laser sources. In *In-situ Materials Characterization*, pages 39–58. Springer.

[Walsh et al., 2015] Walsh, A., Scanlon, D. O., Chen, S., Gong, X., and Wei, S.-H. (2015). Self-regulation mechanism for charged point defects in hybrid halide perovskites. *Angewandte Chemie*, 127(6):1811–1814.

[Wang et al., 2020] Wang, J., Li, W., and Yin, W.-J. (2020). Passivating detrimental DX centers in $CH_3NH_3PbI_3$ for reducing nonradiative recombination and elongating carrier lifetime. *Advanced Materials*, 32(6):1906115.

[Wang et al., 2017a] Wang, Q., Chen, B., Liu, Y., Deng, Y., Bai, Y., Dong, Q., and Huang, J. (2017a). Scaling behavior of moisture-induced grain degradation in polycrystalline hybrid perovskite thin films. *Energy & Environmental Science*, 10(2):516–522.

[Wang et al., 2019] Wang, R., Xue, J., Meng, L., Lee, J.-W., Zhao, Z., Sun, P., Cai, L., Huang, T., Wang, Z., Wang, Z.-K., et al. (2019). Caffeine improves the performance and thermal stability of perovskite solar cells. *Joule*, 3(6):1464–1477.

[Wang et al., 2017b] Wang, Z., Lin, Q., Chmiel, F. P., Sakai, N., Herz, L. M., and Snaith, H. J. (2017b). Efficient ambient-air-stable solar cells with 2D–3D heterostructured butylammonium-caesium-formamidinium lead halide perovskites. *Nature Energy*, 2(9):1–10.

[Weber et al., 2016] Weber, O., Charles, B., and Weller, M. (2016). Phase behaviour and composition in the formamidinium–methylammonium hybrid lead iodide perovskite solid solution. *Journal of Materials Chemistry A*, 4(40):15375–15382.

[Weber et al., 2018] Weber, O. J., Ghosh, D., Gaines, S., Henry, P. F., Walker, A. B., Islam, M. S., and Weller, M. T. (2018). Phase behavior and polymorphism of formamidinium lead iodide. *Chemistry of Materials*, 30(11):3768–3778.

[Weller et al., 2015a] Weller, M. T., Weber, O. J., Frost, J. M., and Walsh, A. (2015a). Cubic perovskite structure of black formamidinium lead iodide, α-[HC $(NH_2)_2$] PbI_3, at 298 K. *The Journal of Physical Chemistry Letters*, 6(16):3209–3212.

[Weller et al., 2015b] Weller, M. T., Weber, O. J., Henry, P. F., Di Pumpo, A. M., and Hansen, T. C. (2015b). Complete structure and cation orientation in the perovskite photovoltaic methylammonium lead iodide between 100 and 352 K. *Chemical Communications*, 51(20):4180–4183.

[Whitfield et al., 2016] Whitfield, P., Herron, N., Guise, W., Page, K., Cheng, Y., Milas, I., and Crawford, M. (2016). Structures, phase transitions and tricritical behavior of the hybrid perovskite methyl ammonium lead iodide. *Scientific Reports*, 6(1):35685.

[Wu et al., 2022] Wu, G., Liang, R., Ge, M., Sun, G., Zhang, Y., and Xing, G. (2022). Surface passivation using 2D perovskites toward efficient and stable perovskite solar cells. *Advanced Materials*, 34(8):2105635.

[Xi et al., 2019] Xi, J., Xi, K., Sadhanala, A., Zhang, K. H., Li, G., Dong, H., Lei, T., Yuan, F., Ran, C., Jiao, B., et al. (2019). Chemical sintering reduced grain boundary defects for stable planar perovskite solar cells. *Nano Energy*, 56:741–750.

[Xia et al., 2023] Xia, J., Liang, C., Gu, H., Mei, S., Li, S., Zhang, N., Chen, S., Cai, Y., and Xing, G. (2023). Surface passivation toward efficient and stable perovskite solar cells. *Energy & Environmental Materials*.

[Xiao et al., 2016] Xiao, Z., Meng, W., Saparov, B., Duan, H.-S., Wang, C., Feng, C., Liao, W., Ke, W., Zhao, D., Wang, J., et al. (2016). Photovoltaic properties of two-dimensional $(CH_3NH_3)_2Pb(SCN)_2I_2$ perovskite: A combined experimental and density functional theory study. *The Journal of Physical Chemistry Letters*, 7(7):1213–1218.

[Xie et al., 2020] Xie, Y., Peng, B., Bravić, I., Yu, Y., Dong, Y., Liang, R., Ou, Q., Monserrat, B., and Zhang, S. (2020). Highly efficient blue-emitting $CsPbBr_3$ perovskite nanocrystals through neodymium doping. *Advanced Science*, 7(20):2001698.

[Yamamoto et al., 2012] Yamamoto, Y., Oohata, G., Mizoguchi, K., Ichida, H., and Kanematsu, Y. (2012). Photoluminescence of excitons and biexcitons in $(C_4H_9NH_3)_2PbBr_4$ crystals under high excitation density. *Physica Status Solidi (c)*, 9(12):2501–2504.

[Yang et al., 2018a] Yang, B., Ming, W., Du, M.-H., Keum, J. K., Puretzky, A. A., Rouleau, C. M., Huang, J., Geohegan, D. B., Wang, X., and Xiao, K. (2018a). Real-time observation of order-disorder transformation of organic cations induced phase transition and anomalous photoluminescence in hybrid perovskites. *Advanced Materials*, 30(22):1705801.

[Yang et al., 2018b] Yang, S., Wu, D., Gong, W., Huang, Q., Zhen, H., Ling, Q., and Lin, Z. (2018b). Highly efficient room-temperature phosphorescence and afterglow luminescence from common organic fluorophores in 2D hybrid perovskites. *Chemical Science*, 9(48):8975–8981.

[Yang et al., 2015] Yang, Y., Yang, M., Li, Z., Crisp, R., Zhu, K., and Beard, M. C. (2015). Comparison of recombination dynamics in $CH_3NH_3PbBr_3$ and $CH_3NH_3PbI_3$ perovskite films: Influence of exciton binding energy. *The Journal of Physical Chemistry Letters*, 6(23):4688–4692.

[Yin et al., 2014] Yin, W.-J., Shi, T., and Yan, Y. (2014). Unusual defect physics in $CH_3NH_3PbI_3$ perovskite solar cell absorber. *Applied Physics Letters*, 104(6):063903.

[Yin et al., 2015] Yin, W. J., Yang, J. H., Kang, J., Yan, Y., and Wei, S. H. (2015). Halide perovskite materials for solar cells: A theoretical review. *Journal of Materials Chemistry A*, 3(17):8926–8942.

[Yoshikawa et al., 2017] Yoshikawa, K., Kawasaki, H., Yoshida, W., Irie, T., Konishi, K., Nakano, K., Uto, T., Adachi, D., Kanematsu, M., Uzu, H., et al. (2017). Silicon heterojunction solar cell with interdigitated back contacts for a photoconversion efficiency over 26 %. *Nature Energy*, 2(5):1–8.

[Young, 1993] Young, R. (1993). *The Rietveld Method*, volume 5. International union of crystallography.

[Yue et al., 2014] Yue, D., You, F., and Darling, S. B. (2014). Domestic and overseas manufacturing scenarios of silicon-based photovoltaics: Life cycle energy and environmental comparative analysis. *Solar Energy*, 105:669–678.

[Yukta et al., 2021] Yukta, Chini, M. K., Ranjan, R., and Satapathi, S. (2021). Lewis base passivation of quasi-2D Ruddlesden–Popper perovskite for order of magnitude photoluminescence enhancement and improved stability. *ACS Applied Electronic Materials*, 3(4):1572–1582.

[Zhao et al., 2017] Zhao, J., Deng, Y., Wei, H., Zheng, X., Yu, Z., Shao, Y., Shield, J. E., and Huang, J. (2017). Strained hybrid perovskite thin films and their impact on the intrinsic stability of perovskite solar cells. *Science Advances*, 3(11):eaao5616.

[Zheng et al., 2017] Zheng, X., Chen, B., Dai, J., Fang, Y., Bai, Y., Lin, Y., Wei, H., Zeng, X. C., and Huang, J. (2017). Defect passivation in hybrid perovskite solar cells using quaternary ammonium halide anions and cations. *Nature Energy*, 2(7):1–9.

[Zhenyi et al., 2020] Zhenyi, N., Bao, C., Lui, Y., Jiang, Q., Wi, W.-Q., Chen, S., Dai, X., Chen, B., Hartweg, B., Yu, Z., Holman, Z., and Huang, J. (2020). Resolving spatial and energetic distributions of trap states in metal halide perovskite solar cells. *Science*, 1358(March):1352–1358.

[Zhu et al., 2018] Zhu, Z., Sun, Q., Zhang, Z., Dai, J., Xing, G., Li, S., Huang, X., and Huang, W. (2018). Metal halide perovskites: stability and sensing-ability. *Journal of Materials Chemistry C*, 6(38):10121–10137.

[Zou et al., 2018] Zou, W., Li, R., Zhang, S., Liu, Y., Wang, N., Cao, Y., Miao, Y., Xu, M., Guo, Q., Di, D., et al. (2018). Minimising efficiency roll-off in high-brightness perovskite light-emitting diodes. *Nature Communications*, 9(1):608.

Appendices

Appendix A

Appendix for Chapter 5

Supplementary information for: Robust Arduino controlled spin coater using a novel and simple gravity chuck design

(Version 13 Sept 2022)

Contents

1 Electronics for hV2 **2**
1.1 Assembled circuit . . . 3

2 Software flow diagram for hardware versions 2 and 3 (software versions 1.4 and 2.3) **4**

3 Variations on sample chuck design **5**
3.1 Sample chuck using drill press and hand tools . . . 6

4 Sample masks **9**

5 NOT Gate for the Tachometer **10**

6 Tachometer **11**

7 Calibration **12**

8 Temperature on cycling of hV2 at 31% duty cycle (~5000 RPM): With MOSFET-Low trace **12**

9 PBDB-T:PC71BM: additional detail on AFM for 3000 RPM, 60 s deposition **13**

10 Additional DIY health & safety **14**

11 Spin coating best practices **15**

12 Useful resources **15**

13 Existing spin coaters **15**
13.1 Open-source designs . . . 15
13.2 Commercial spin coaters . . . 16

14 After-market chucks **17**

1. Electronics for hV2

Figure 1 shows the circuit diagram for spin coater hardware version 2 (hV2). The circuit diagram for hV3 is included in the main manuscript. The primary development between these versions is of the input peripherals. hV2 uses potentiometers and buttons for operation while hV3 makes use of an incremental type rotary encoder.

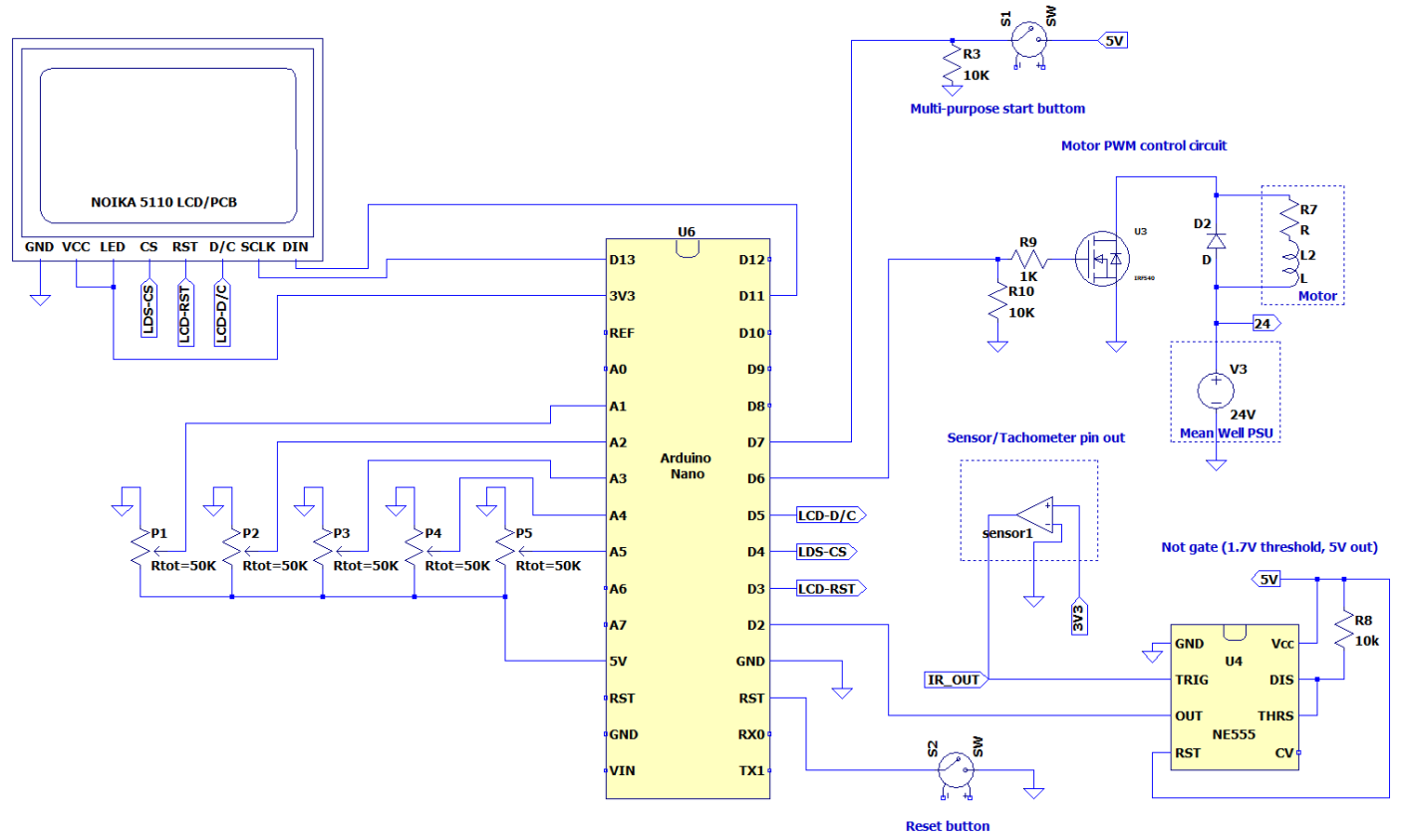

Figure 1: Circuit diagram for hardware Version 2

1.1 Assembled circuit

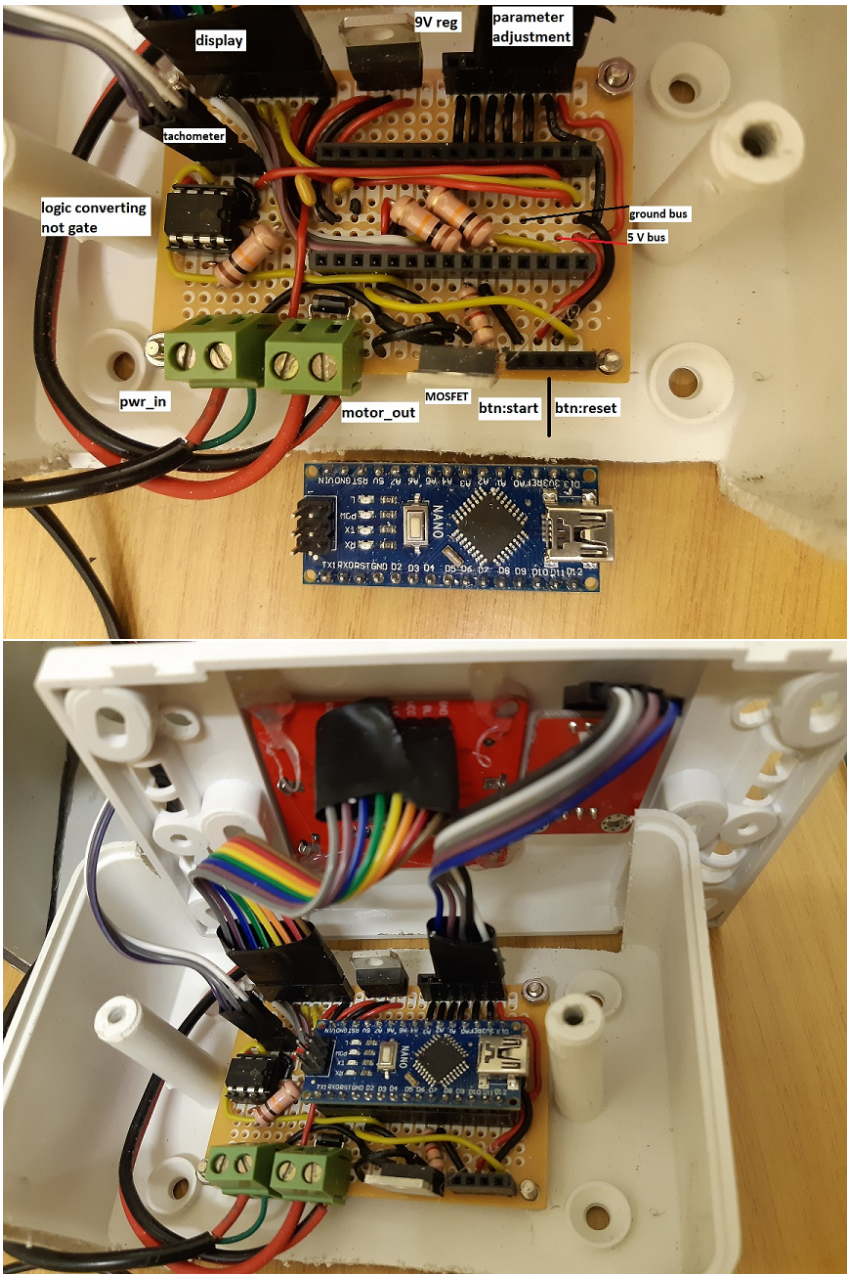

Figure 2: Electronics circuit board as assembled for hV3.

Figure 2 shows a labelled circuit board for hV3, including the unused ”btn:start” and ”btn:reset” header inherited from the design of hV2. The rotary encoder is connected to the ”parameter adjustment” header. The mounting of the electronics board for hV2 is detailed in the hV2 assembly SI document.

For the parameter adjustment header, in hV2 the inputs consist of 5 potentiometers each connected to an analogue read pin (A2 to A6). In hV3 pins A0 to A2 are used for digital signals from the rotary encoder. The choice of pins is convenience based and requires consistency with the corresponding *pin* variables in the Arduino code. The power delivery in hV2 and hV3 differ, the Nano microcontroller in hV2 is powered through the USB cable by a 5.2 V step-down converter, while hV3 has an on-board 9V regulator as visible in Figure 2 and as described in the main manuscript.

2. Software flow diagram for hardware versions 2 and 3 (software versions 1.4 and 2.3)

The Arduino code written for hV2 (software 1.4) and hV3 (software 2.3) differ primarily in the handling of inputs used to program the run parameters as shown diagrammatically in Figure 3.

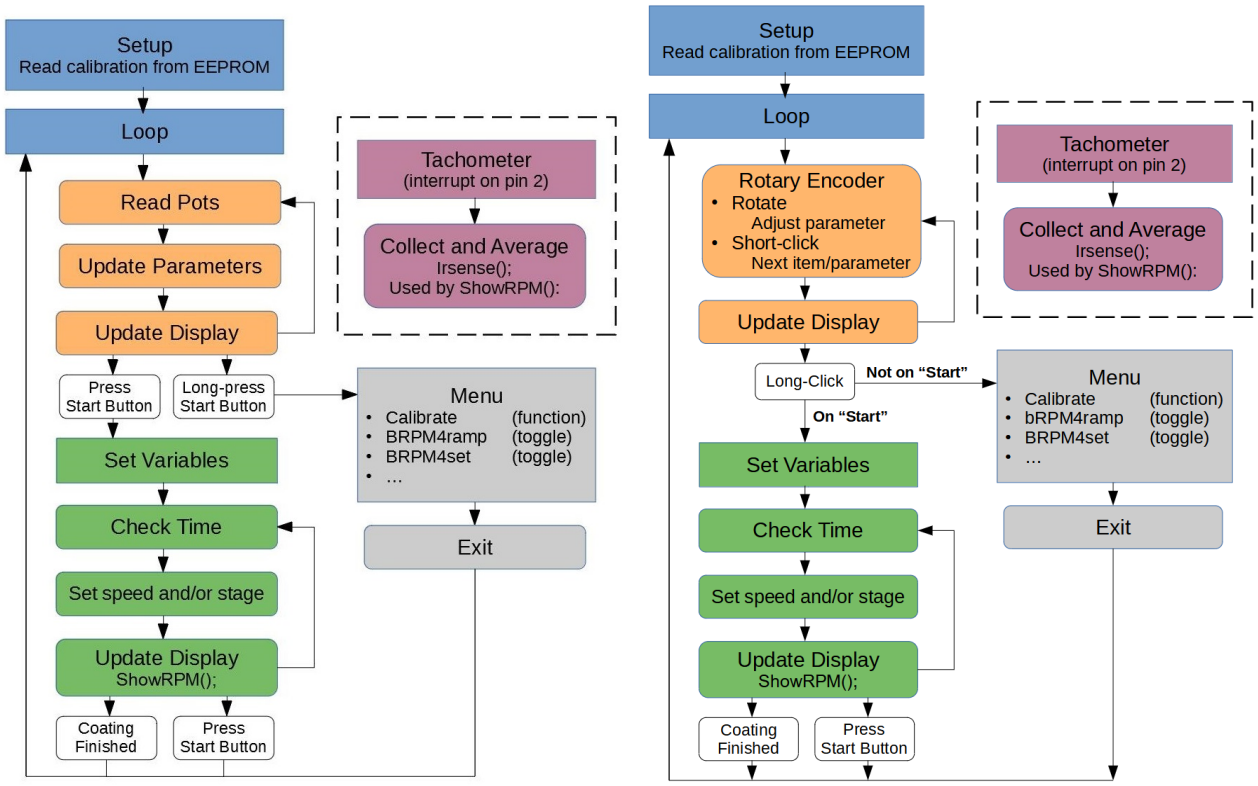

(a) Software version 1.4 (hV2)

(b) Software version 2.3 (hV3)

Figure 3: Flow diagrams of software versions 1.4 and 2.3 operation as used in hV2 and hV3 respectively.

3. Variations on sample chuck design



(a) (b)

Figure 4: Final sample chuck design used for hV2 employed smooth pins machined out of the same block of aluminium as the chuck itself. (a) Chuck with the sample mask and a glass substrate in place, (b) Chuck with the sample mask removed.

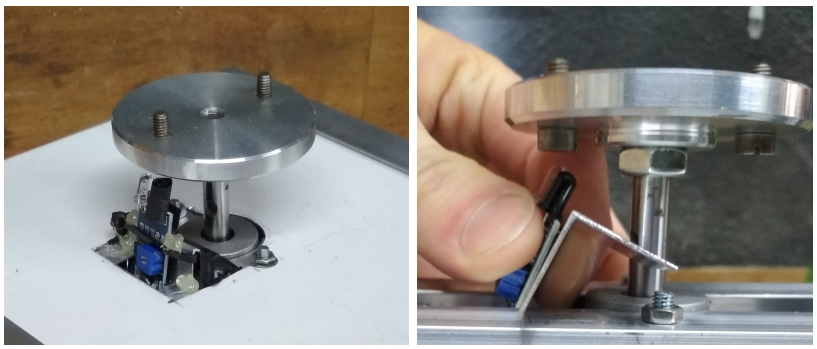

Figure 5: An earlier prototype of the sample chuck; threads were tapped into the aluminium chuck which held threaded bolts. These bolts acted as pins to hold the brass masks. To complete such a design the thread above the chuck surface needed to be machined off the bolts for easy placement and removal of the sample masks.

3.1 Sample chuck using drill press and hand tools

A more accessible alternative to a machined aluminium chuck was also considered. A sample chuck was produced from recycled plastic from a plasterers float, bending wire, and a 3mm drill bit using a drill press, hole saw bit, mini rotary tool, utility knife blade and sandpaper as detailed below. A plastic plasterers float can be purchased new for approximately $ 2-3.

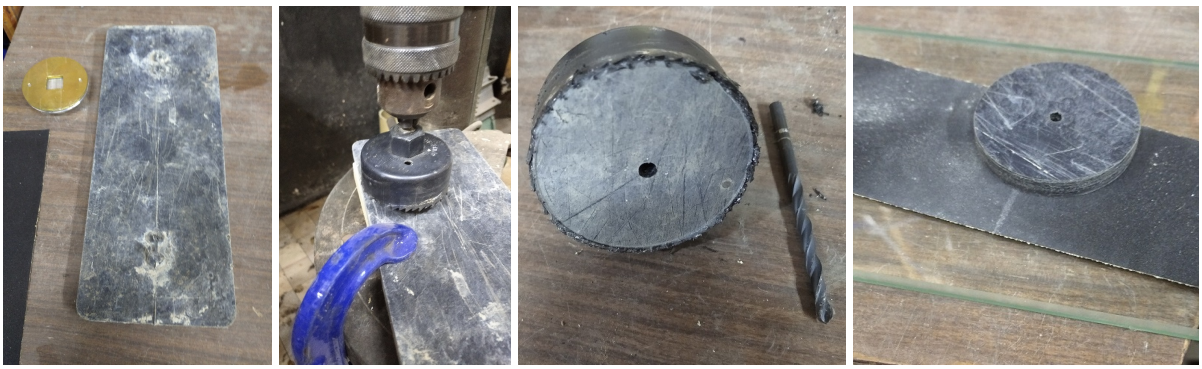

(a) (b) (c) (d)

Figure 6: Cutting a disk from a (broken) plasterers' float for a spin coater chuck.

- Figure 6b, The chuck was cut from the recycled plastic using a hole saw in a drill press. The plastic was tightly clamped to avoid it shifting during the cutting process.
- Figure 6c, For the case that the guiding bit of the hole saw arbour had a larger diameter than the shaft of the intended motor, a hole the intended size was first drilled with the drill press. After this, the guiding bit of the hole saw arbour was removed without shifting the drill press or plastic. The hole saw was then mounted in the drill press without its guiding drill bit (Figure 6b), and the plastic was slowly cut using the drill press.
  - For threaded motor shafts, an appropriate pilot hole is drilled. Thereafter a thread is tapped with a *tap* corresponding to the thread on the motor shaft.
- Figure 6d, Once cut the plastic disk was cleaned up with sandpaper. The sandpaper was placed on a sheet of glass which provides a reliably flat and smooth surface. [1] The plastic disk was rotated a few degrees at a time as it was worked across the sandpaper.



(a) (b) (c) (d)

Figure 7: Adding pins to the spin coater chuck to support the sample masks.

- Figure 7a, A paper template was prepared to mark the placement of the pins for the sample mask, the centre hole was 5 mm, and the pin spacing 45 mm centre to centre. Based on this, a vernier caliper was set to 20 mm and the pin positions were marked relative to the edge of the motor shaft hole.
- Figure 7b, The drill press was set up with a 3 mm bit and the intended depth was marked on the drill bit using red electrical tape.
- Figure 7c, These holes were "deburred" using a sharp blade.

[1] Glass does have a degree of flexibility as such is requires support. In the glass manufacturer links referenced, their float glass 4 to 6 mm has a manufacturing thickness tolerance of ± 0.2 mm. [supplier specification, archived-link (accessed 2022Jun25)]

- Figure 7d, The sample mask fit was tested by placing 2 x 3 mm drill bits in these holes.

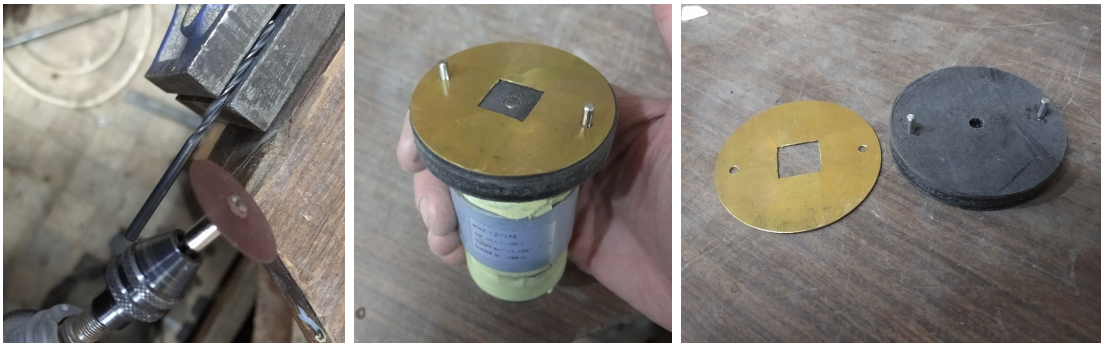

(a) (b) (c)

Figure 8: Adding pins to the spin coater chuck to support the sample masks.

- Figure 8a, The smooth shaft section of a 3 mm drill bit was cut into 2 pins using a mini grinder tool.
  - Drill bits offer a widely available source of steel pins in specific diameters.
- Figure 8b, The portion of these that was exposed when fitted into their holes was lightly ground down with the mini rotary tool grinding disk.
  - This increased the clearance between the pins and the sample mask for a looser fit. An alternative to this would be to use a slightly larger drill bit for the mask holes than used for the pin (i.e. 3.0 mm hole and 2.8 mm pins).

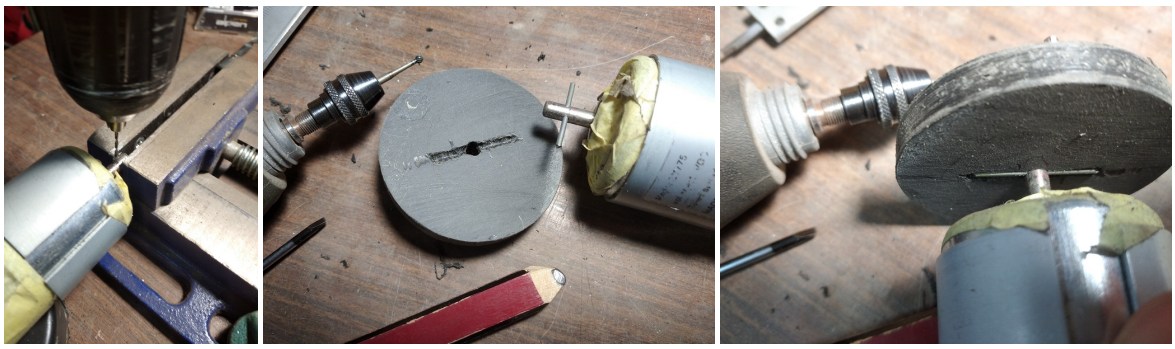

(a) (b) (c)

Figure 9: Making a seating, rotation locking mechanism for the chuck.

While the chuck fitted tightly on the motor shaft, for additional security a rotation locking mechanism was prepared as shown in Figure 9.

- Figure 9a, A 2 mm hole was drilled through the motor shaft, this should be performed at low speed with a drill press.
  - The low speed is suggested to reduce heat generation and prevent work hardening of the steel.
  - A drill press is a necessity to avoid a skew hole.
- Figure 9b, A bar shape was marked out on the chuck and a channel was cut into the chuck using a round bur in a mini rotary tool.
- Figure 9b, Bending wire ($\phi \approx 2$ mm) with a length corresponding to the length of the channel cut previously was placed though the motor shaft.



Figure 10: The spin coater chuck with rotation lock and sample mask pins rotating on a motor (photo).

The finished chuck was placed on the motor and a photo was taken during motor operation. The photo of the rotating chuck in Figure 10 shows very little precession, which would be due to miss-alignment of the chuck w.r.t the motor shaft. A large precession would be evident as a blur or transparency effect in the photo. This is by no means a quantitative test yet it shows that a reasonably useful spin coater chuck can be made with a drill press and hand tools.

A slight degree of miss-alignment between that chuck and motor shaft which was primarily attributed to the precession in the drill press and its stage being less than perfectly perpendicular to the drill bit *(The drill press in use was a repaired machine from 1986)*.

4. Sample masks

The sample masks were cut from 0.7 mm brass sheet using a CNC router (Figure 11). The brass sheet was fastened onto a wooden board for support during machining. The 3 mm holes were drilled followed by the centre opening, and lastly the perimeter was machined. The CNC router bits could only produce rounded corners for the centre hole, these inner corners were squared with a triangular jewellers file.

Similar brass work has been done by the author using a standard drill to make holes, followed by a jewellers saw to cut the centre shape and the perimeter.

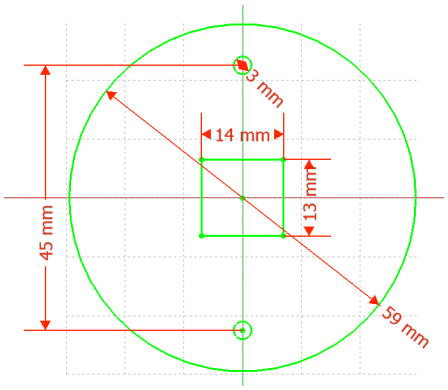

(a) A sample mask for hand-cut 12.5 x 12.5 mm samples.

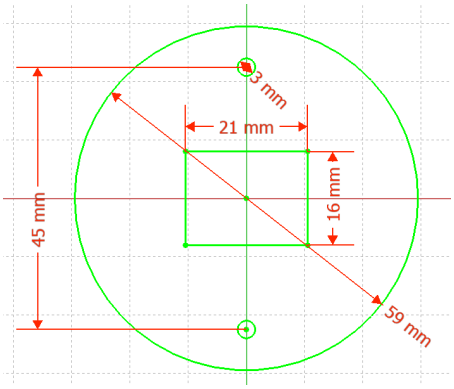

(b) A sample mask for 20 x 15 mm samples.

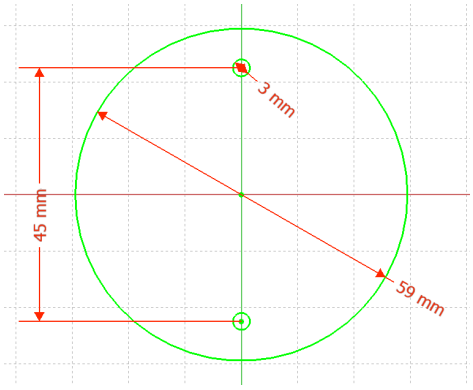

(c) A blank sample mask for later machining to accommodate an unaccounted for sample size.

Figure 11: Sample masks measurements, the sizes of the openings are larger than the intended samples for accommodation of any inaccuracies when using hand cut samples.

5. NOT Gate for the Tachometer

The NOT gate used alongside the tachometer originates from the availability of NE555 chips at the time and their ability to respond to relatively low ”trigger” voltages with short response times. Figure 12 shows the simulated response of the NOT gate on a millisecond timescale. The ”trigger” threshold voltage of the NOT gate is 1.67 V with the circuit using at most 2.1 mA during its operation. The LM1117 voltage regulator of the Arduino Nano compatible microcontroller has a maximum current draw specification of 800 mA making this a marginal power consumption compared to the supply capacity. These properties were found to be well suited to the application. An alternative is a MOSFET based logic level converter which consists of a MOSFET and two resistors.

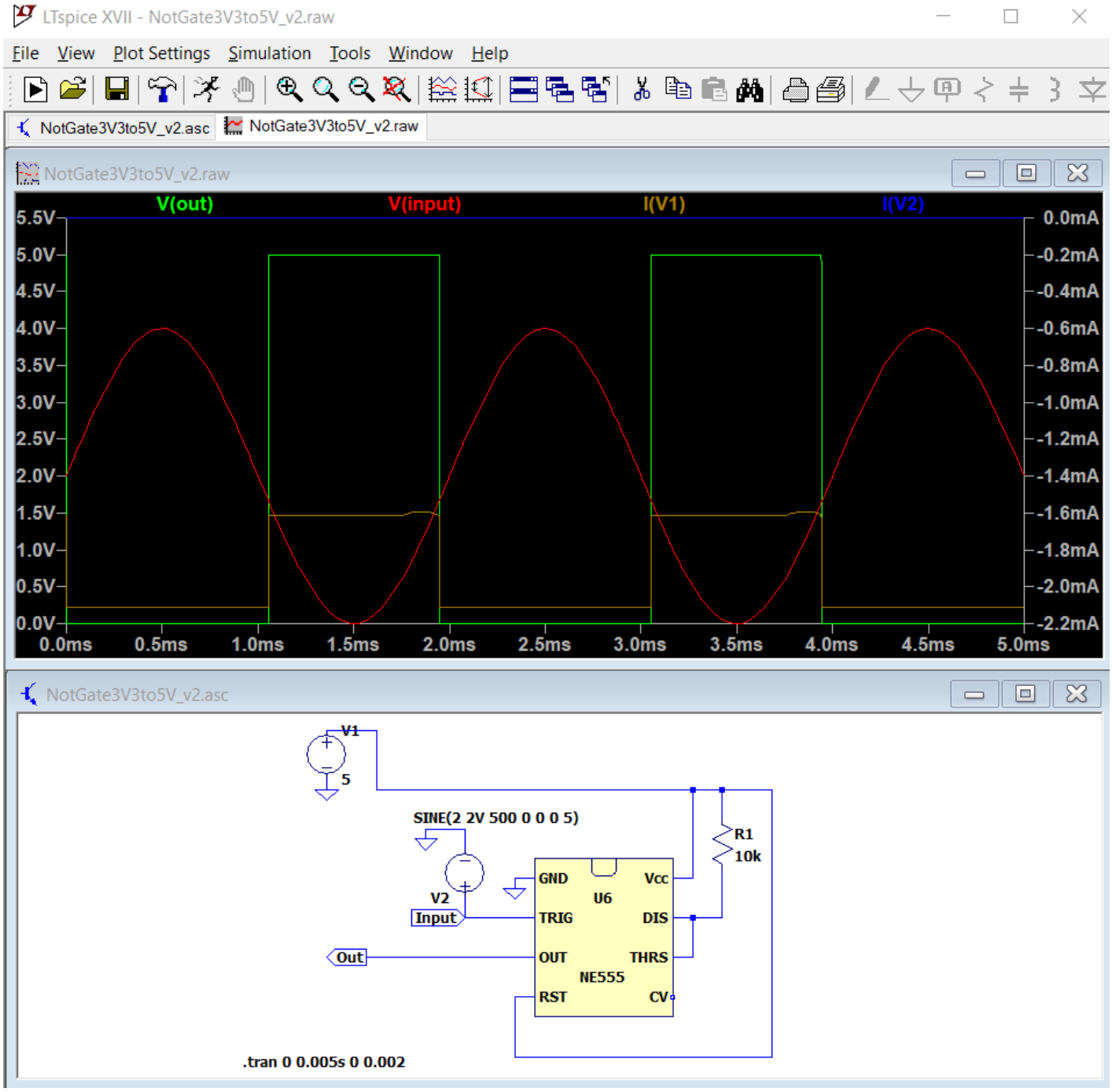

Figure 12: LTspice simulation of the NE555 based NOT gate with an input sine wave of 500 Hz (30000 cycles/min).

6. Tachometer

The tachometer was based around an "Infrared Obstacle Avoidance Sensor" [link, archived-link] as per Figure 13. hV2 used an infra-red sensor, the light emitted by this sensor is reflected off aluminium or is diffused and absorbed by sandpaper on the underside of the chuck. hV3 uses a brass reflector attached to the motor shaft on its rear end. The brass reflector was painted black on the inner-side and covered with aluminium tape on the outer-side for reflectivity contrast.

The conditions of a signal to be read as a "guaranteed" digital high requires a voltage between $0.6V_{CC}$ and $V_{CC}+0.5V$ for the ATmega328P chip in the Nano, where V_{CC} is the ATmega328P's supply voltage of 5.0 V for this system. This translates to a signal between 3.0 and 5.5 V. For a digital low this value is between $-0.5V$ and $0.3V_{CC}$ $(1.5V)$. [ATmega328P_Datasheet, archived-link]

The tachometer was powered with 3.3 V and the output signal was measured as 3.2 V. Considering the digital logic level voltage windows of an ATmega32P microcontroller this should have been sufficient for reliable operation, but was found to not be the case during early experimentation. The use of NE555 chip to make a logic converting NOT gate as per Figure 12 improved reliability of the tachometer reading.



(a) Infra-red (IR) proximity sensor used in both hV2 and hV3.



(b) IR proximity sensor in hV2.



(c) Absorber/reflector pattern under the chuck in hV2.

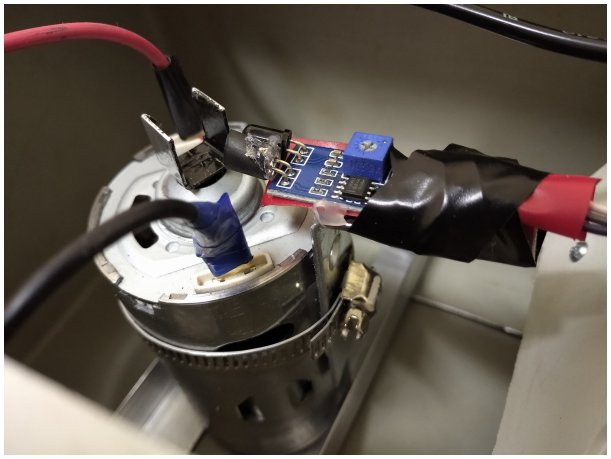

(d) IR sensor and reflector in hV3.

Figure 13: Tachometer sensor and its placement

7. Calibration

The calibration data for hV2 was fitted with a 6th order polynomial as shown in Figure 14, $R^2 = 0.9997$. The spin coater uses the raw calibration data for its operation while the calibration was fitted for the purpose of calculating a residual standard error, σ. σ was calculated to a value of 31.3 RPM as used in the *Validation and characterization* section of the main paper, using $\sigma = \sqrt{\frac{\sum(X_{Raw} - X_{Fitted})^2}{n-2}}$ where X refers to the RPM values and n is the number of collected data points.

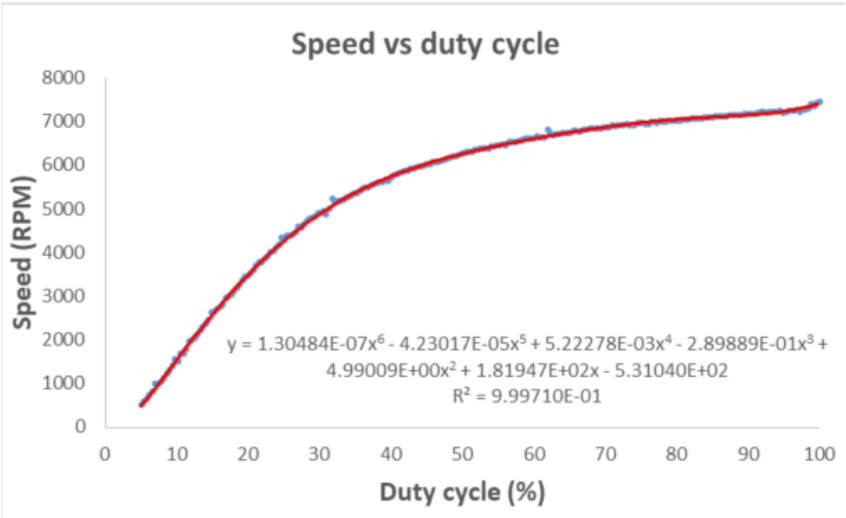

Figure 14: The relationship between motor speed and duty cycle at room temperature for the 24V DC motor controlled through a n-channel MOSFET with an Arduino Nano compatible microcontroller as used in hV2. (blue) Collected data, (Red) Fitted 6th order polynomial.

8. Temperature on cycling of hV2 at 31% duty cycle (~5000 RPM): With MOSFET-Low trace

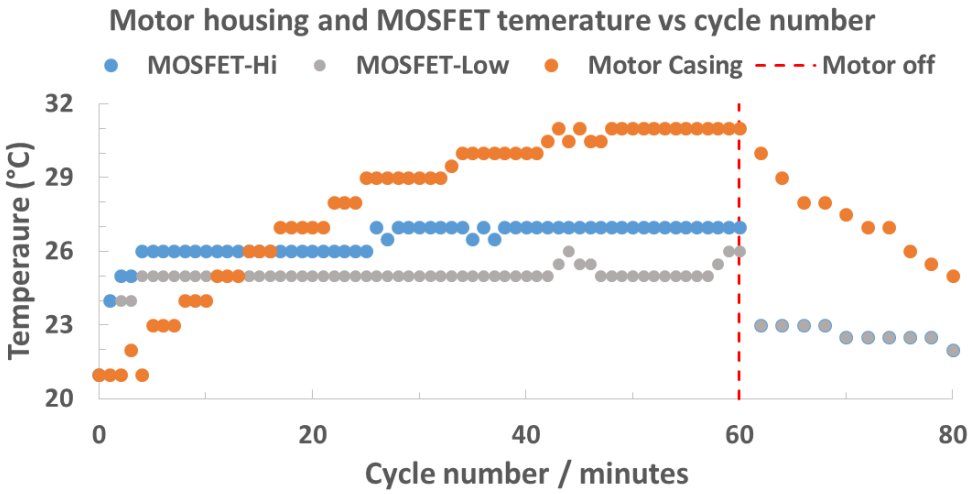

Figure 15: Motor housing and MOSFET temperature as a function of cycle number with the additional MOSFET-Low trace.

The MOSFET-Low trace in Figure 15 rapidly reaches 25 ° C. At cycles 44, 59 and 60 the temperature reaches 26 ° with nearby values of 25.5 ° C representing instability between a reading of 25 and 26 during the cycle ° C. This is with consideration of a temperature measurement resolution of 1 ° C.

9. PBDB-T:PC71BM: additional detail on AFM for 3000 RPM, 60 s deposition

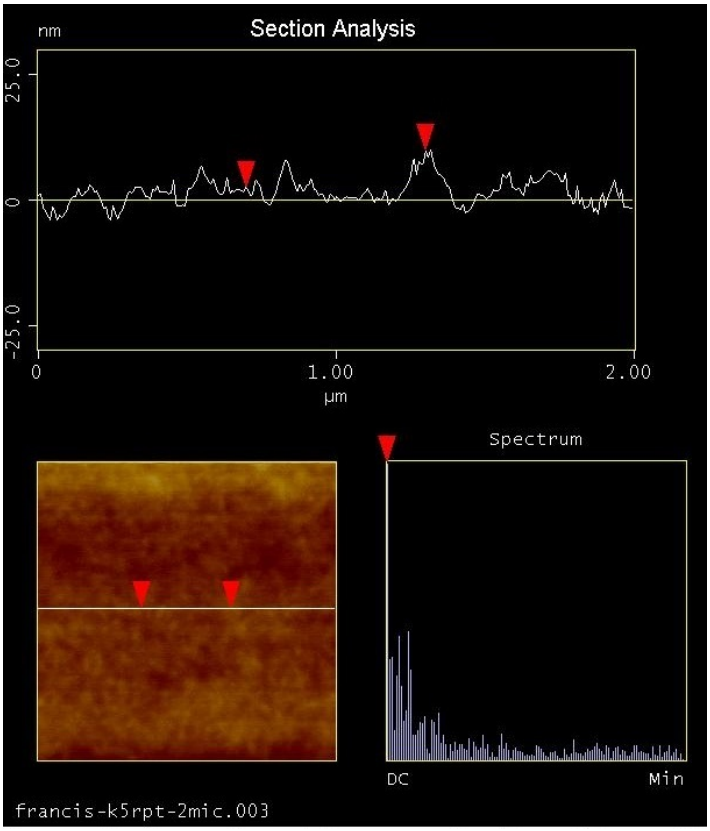

Parameter	Value
L	601.56 nm
RMS	2.515 nm
lc	DC
Ra(lc)	1.910 nm
Rmax	10.887 nm
Rz	5.739 nm
Rz Cnt	valid
Radius	2.473 μm
Sigma	5.039 nm

Figure 16: Tapping mode AFM of PBDB-T:PC71BM (1:1) thin films, spin coated for 60 s at 3000 rpm showing a 3 μm line trace.

Figure 16 shows a AFM line trace in the top left corner with parameters from this trace on the right. Here we see a difference between the maximum and minimum points of *Rmax*, 10.887 nm $\approx$ 11 nm.

10. Additional DIY health & safety

The following precautions provide **some** of the most important relevant hazards and precautions. Some points are derived from sources including [1].

Electrical hazards

- Check the wiring on all tool and equipment for damage or bad insulation. Do not use equipment with hazardous wiring.
- Do not use damages tools and equipments.
- Do not work with electricity in wet areas.

Safety practices

- For any work with or around potentially dangerous equipment, minimise the potential dangers, ensure a clean and clear workspace and ensure you have stable footing, especially when working with power tools such as angle grinders.
- Any materials being cut or worked on should be well secured to a sturdy surface.
- Work with a colleague present in the area.
- Remove jewellery and metal objects when working with motorised tools or electricity.

Personal Protective Equipment (PPE)

- Wear safety glasses.
- Don't wear loose clothing.
- Secure long hair.
- Wear protective footwear.
- Use hearing protection where appropriate such as for angle grinders.

Chemical Safety

- Read the material safety data sheets (MSDS) for all chemicals used during spin coating and follow the appropriate safety precautions.
- Operate the spin coater in a well ventilated area, glove-box or fume-hood as appropriate for the chemicals in use.
- Wear appropriate PPE including gloves, safety glasses, lab coat, etc.

Rotary motor safety

- Keep the sample chamber clear of obstructions.
- Do not touch the chuck or any moving parts while they are in motion.
- Wear appropriate PPE including gloves, safety glasses, lab coat, etc.
- The spin coater should not be operated in the presence of loose hair, loose clothing, loose jewellery or anything that could get caught in and/or wrapped around moving parts.

11. Spin coating best practices

- When using **vacuum chucks** on commercial spin coaters. the precursor solution can leave behind residues, and any such precursor solution drawn by the vacuum chuck has the potential to gradually build up a residue *gluing* the chuck to the motor shaft. As such it was found best to remove and clean the chuck after every use. This was especially critical for solutes such as lead halides in dimethylformamide where the low solubility of the lead salt readily causes residue deposits that require harsh solvents to remove.
- In glove boxes or other closed off environments where research involving multiple chemistries take place, contamination from the spin coating process can be deleterious as such these environments should be closely monitored when introducing spin coating for potential impacts on adjacent works.
- The precursor solutions can be passed through a sub micrometer syringe filter to remove undissolved particles or contaminants from the solution which could be the source of "comet" film defects. [2]
- When applying precursor solution, a micropipette allows the application of a reliable, reproducible quantity which can be finely tuned to reduce wasting of precursor solution. An example of an open-source micropipette build can be found at [3]

12. Useful resources

- *Ossila's spin coating guide,*
  Ossila provides a spin coating guide which covers wide range of concepts and considerations including spin coating theory, practical considerations and handling defects. Among this information they mention vacuum warping of thin substrates and the additional maintenance required with vacuum chucks as the vacuum often draws in the precursor ink/solution. [Ossila spin-coating, archived-link (accessed 8 Nov 2021)]
- *Spin coating: art and science,*
  Birnie lays out the dominant physics in spin-coating, coating defects and the causes of in the chapter "Spin coating: art and science" of the book "Chemical Solution Deposition of Functional Oxide Thin Films". This includes the work of Emslie, Bonner and Peck where *flow* was described as a primary to the evolution of film thickness, determined by viscous forces, density and rotational speed. Meyerhofer expanded this work by including evaporation effects into the equations which become dominant after the rate of flow dominated change in thickness declines. In the section where defects are discussed, these include defects related to solvent evaporation, surface tension, viscosity and contaminants. The causes of these defects are discussed with direct or indirect implementations of how to address them. [2, 4, 5].

13. Existing spin coaters

13.1 Open-source designs

- Sadegh-cheri's spin coater [6]
  Double sided tape sample mounting
  1000-9000 rpm
  Brushless DC motor from a computer hard
  https://pubs.acs.org/doi/full/10.1021/acs.jchemed.9b00013 (accessed 2021Nov08)

- Bianchi *et al.* [7]
  Spin coater based on brushless dc motor of hard disk drivers
  Vacuum sample mount
  0-10000 rpm
  Brushless DC motor from a computer hard

- Yetkin Akyüz Electrical Electronics Engineer - Düzce University [8]
  Gravity chuck, 4 steel flat bar sections with a slide channel in which a screw fixed the slides to the chuck. This allows sample size adjustment using a screwdriver with the minimum size defined by the width of

the flat bar.
Programmable up to 10 stages
24 V 9000 rpm DC motor [project page link, archived-link (accessed 2021Nov08)]

- Segura *et al.* Mechanical and Electronic Systems of an Open Source Based Spin and Dip Coater [9]
  Double sided tape sample mounting
  300 - 10000 rpm speed control by Arduino Uno hardware PWM signal (byte value of 0-255)
  24 V, 12 W DC motor
  https://revistapolitecnica.epn.edu.ec/ojs2/index.php/revista_politecnica2/article/view/561 (accessed 8Nov2021)

- Ben Krasnow photoresist spin coater [10]
  Mounting set for microscope slides, flat chuck with 5 flat-head screws, 4 fixed and one removed and replaced for sample mounting.
  Quad-copter motor driven through an ESC controller. These types of motors and controller combinations can offer control over the motor acceleration and deceleration rate as well as speed readings either by monitoring the motor windings during rotation or through the hall sensor in variants which have one included. Quad-copter motors frequently run at a few 10 000's rpm. As such care needs to be taken to ensure the motor can go slow enough. A speed rage from a few hundred to a few thousand rpm is often required for a spin coater.
  https://benkrasnow.blogspot.com/2016/02/design-and-build-spin-coater.html (accessed 8Nov2021)

13.2 Commercial spin coaters

Supplier	**Model**	**Chuck type**	**Speed RPM**	**Price**	**Additional**
SETCAS [11]	SETCAS KW-4A	Vacuum	500 - 8500	$ 2000 (Nov2021) Cheapest of their range	• Substrate size ϕ 5- 100 mm • Two-stage • Includes Vacuum pump • Includes 3 chucks • Motor speed stability ± 1%, Tachometer ± 10 rpm • 2 Year warrantee
	https://www.setcas.online/product-page/kw-4a (accessed 8Nov2021)				
SPI [12]	SPI KW-4A 220V	Vacuum	500 - 8000	$ 5505.79 (Nov2021)	• Two-stage • Substrate size up to 152 mm (6") • Speed stability ¡ 1% • (A diaphragm pump is recommended for operation)
	https://www.2spi.com/item/12170-ax/spin-coater/ (accessed 8Nov2021)				
MTI Corporation [13]	Compact Spin Coater VTC-100A 220V	Vacuum	500 - 8000	$ 3988.00 + $ 598.20 not in USA warrantee surcharge (Nov2021)	• Two-stage • 1,2 and 4" vacuum chucks included • 24 V DC motor rated 150 W Max • 1 Year warranty with lifetime support
	https://www.mtixtl.com/ProgrammableCompact SpinCoater0-8000rpm4waferMax-VTC-100A.aspx (accessed 8Nov2021)				
Ossila [14]	Ossila Spin Coater	Gravity	120 - 6000	£1900 (Nov2021)	• Digitally stored step profiles up to 50 steps each • Built in spirit level • Includes a chuck • 2 year warrantee
	https://www.ossila.com/products/spin-coater (accessed 8Nov2021) https://web.archive.org/web/20210428130823/https://www.ossila.com/products/spin-coater				

14. After-market chucks

- Vacuum chucks for SETCAS KW series starting at $ 100 (21 Oct2021, archived-link). Their website reported the starting price as $ 130 in Nov2021 and $ 300 in Aug 2022 archived-link, it is suspected the difference was related to stock availability of their lower cost options.
  https://www.setcas.online/product-page/vacuum-chuck (accessed 8Nov2021)

- Vacuum chucks for SPI KW-4A
  From SPI starting at $91.80 for aluminium and $153.00 for PTFE (Nov2021)
  https://www.2spi.com/item/z12173/
  https://www.2spi.com/item/z12173t/

- Anti-corrosive vacuum chucks with O-Rings of different sizes FOR VTC-100PA - MTI-VTC100PA
  Price not specified but adding an extra O-Ring for the ϕ 10 mm chuck is marked as $ 25.95, it is unspecified what advanced material this $ 25.95 O-Ring is made from.
  https://www.mtixtl.com/VacuumchuckswithdifferentsizesFORVTC-100PAMTI-VTC100PA.aspx (accessed 8Nov2021)

- Ossila spin coater chucks
  £199 for standard or £249 for a custom chuck Nov2021. Ossila also provides *.STL* and *.SLDPRT* files to allow their customers to produce their own chucks.
  https://www.ossila.com/products/spin-coater-chucks (accessed 8Nov2021)

References

[1] J. Ojeme, E. Raymond, Occupational safety and health practices required by electrical/electronics technology graduates in north central nigeria (2021).

[2] D. P. Birnie, Spin coating: art and science, in: Chemical Solution Deposition of Functional Oxide Thin Films, Springer, 2013, pp. 263–274.

[3] M. D. Brennan, F. F. Bokhari, D. T. Eddington, Open design 3d-printable adjustable micropipette that meets the iso standard for accuracy, Micromachines 9 (4) (2018) 191.

[4] A. G. Emslie, F. T. Bonner, L. G. Peck, Flow of a viscous liquid on a rotating disk, Journal of Applied Physics 29 (5) (1958) 858–862.

[5] D. Meyerhofer, Characteristics of resist films produced by spinning, Journal of Applied Physics 49 (7) (1978) 3993–3997.

[6] M. Sadegh-cheri, Design, fabrication, and optical characterization of a low-cost and open-source spin coater, J. Chem. Educ. 96 (6) (2019) 1268–1272. doi:https://doi.org/10.1021/acs.jchemed.9b00013.

[7] R. F. Bianchi, M. Panssiera, J. Lima, L. Yagura, A. Andrade, R. M. Faria, Spin coater based on brushless dc motor of hard disk drivers, Prog. Org. Coat. 57 (1) (2006) 33–36. doi:https://doi.org/10.1016/j.porgcoat.2006.05.004.

[8] Y. Akyüz, Design and fabrication of a cost-effective spin coater, (accessed: 2021-11-08) (2020).
URL https://github.com/yetkinakyz/SpinCoater

[9] R. Dabirian, V. H. Guerrero, D. C. L. Matovelle, L. J. Segura, Mechanical and electronic systems of an open source based spin and dip coater, Revista Politécnica 37 (2) (2016) 53–53.

[10] Y. Akyüz, Design and build a spin coater, (accessed: 2021-11-08) (2016).
URL https://benkrasnow.blogspot.com/2016/02/design-and-build-spin-coater.html

[11] SETCAS LLC, Setcas llc — kw-4a spin coater, (accessed: 2021-11-08).
URL https://www.setcas.online/product-page/kw-4a

[12] SPI KW-4A, Setcas llc — kw-4a spin coater, (accessed: 2021-11-08).
URL https://www.setcas.online/product-page/kw-4a

[13] MTI Corporation, Compact spin coater - vtc-100a, (accessed: 2021-11-08).
URL https://www.mtixtl.com/ProgrammableCompactSpinCoater0-8000rpm4waferMax-VTC-100A.aspx

[14] Ossila Limited, Spin coater — low price compact spin coating system, (accessed: 2020-02-04).
URL https://www.ossila.com/products/spin-coater?variant=1200242585

Appendix B

Appendix for Section 6.4 and 6.5

Contents

B.1 Additional literature structure refinements on $(FAPbI_3)_{0.85}(MAPbBr_3)_{0.15}$ **277**

B.2 Le Bail fits on $(FAPbI_3)_{0.85}(MAPbBr_3)_{0.15}$ for pattern indexing **282**

B.1 Additional literature structure refinements on $(FAPbI_3)_{0.85}(MAPbBr_3)_{0.15}$

In this Appendix discuss refinements of structures included in Table 6.1 which were briefly mentioned in Section 6.4. This includes the typical $MAPbI_3$ β and γ phase as well as the P4/mbm β phase of $FAPbI_3$ provide very poor fits against the 1-315K and 22-150K patterns of the $(FAPbI_3)_{0.85}(MAPbBr_3)_{0.15}$ data set. The same means of assessment was applied to the 8-280K and 29-80K patterns leading to equivalent results (available on request).

Refinements were accompanied with lattice parameters modified by refined scaling factor, for tetragonal unit cells 2 of the unit cell parameters were constrained to be equal, below is an example of the orthorhombic unit cell parameters from the refinement of a $MAPbI_3$ *Pnma* unit cell on the 22-150K diffraction pattern. Further the halides were replaced with the stoichiometric mix of the sample of interest.

```
prm r1  1.00815913 min 0.95 max 1.05
prm r2  0.99850147 min 0.95 max 1.05
prm r3  1.03279691 min 0.95 max 1.05
a = 8.86574 * r1;:8.938077
b = 12.6293 * r2;:12.610375
c = 8.57689 * r3;:8.858185
```

In the Figures B.1 and B.2, (a) the $FAPbI_3$ β structure ($P4/mbm$, ICSD 230492) is refined against the collected data. Additional peaks are present in the simulated data which are not present in the 315 K data while there is a near perfect alignment of peak positions. For the 150 K refinement, the literature values $a = b = 8.29312$ Å, $c = 6.3222$ Å refined to $a = b = 8.83300 \pm 0.00053$ Å, $c = 6.20225 \pm 0.00062$ Å. The a and b unit cell parameters deviated drastically from the literature values, the literature data was collected at a slightly higher temperature of 200 K compared to the data collected at 150 K, such a temperature difference is not expected to be significant enough to account for the differences in lattice parameter. The relative peak intensities for this phase provided a mediocre fit to the data even with the refinement of thermal parameters to the unlikely values below. [1]

```
# Thermal paramters in the refinement of $FAPbI_3 \beta$ (P4/mbm, ICSD 230492) against 22-150K
# Pb:b1, I/Br:b2, C/N/H:b3
prm b1  3 min 0.1 max 3
prm b2  8.2374‘_0.3777 min 1 max =b3;
prm b3  8.2374‘_7.2769 min =b2; max 20
```

[1] This refinement was performed after a $P4/mbm$ based phase had shown to be of interest in subsequent sections

In sub-figures (b) representing the $MAPbI_3$ β phase (I4/mcm, ICSD428899) There are only a few additional peaks not present in the collected data such as near 20.4 ° with intensities poorly described in the 315 K pattern and multiple peaks not accounted such as near 22.5 and 27 ° 2θ for in the 150K pattern. The $MAPbI_3$ γ phase (*Pnma*, ICSD428898) in sub-figures (c) accounts for a few additional peak positions in the 150K pattern while still having additional peaks such as near 24 ° and poorly describing the relative peak intensities.

The relative peak intensities in these comparisons is not definitive considering the replacement of the halide I with $I_{0.85}Br_{0.15}$ and that the thermal parameters were not refined. The presence of additional and failure to account for certain peaks indicates these literature structures as tested are not suitable to represent the $(FAPbI_3)_{0.85}(MAPbBr_3)_{0.15}$ data.

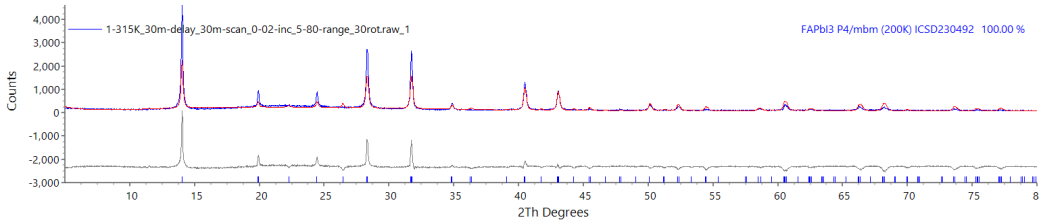

(a) $P4/mbm$-$FAPbI_3$ refined against $(FAPbI_3)_{0.85}(MAPbBr_3)_{0.15}$ data at 315 K, with the halide represented by $I_{0.85}Br_{0.15}$

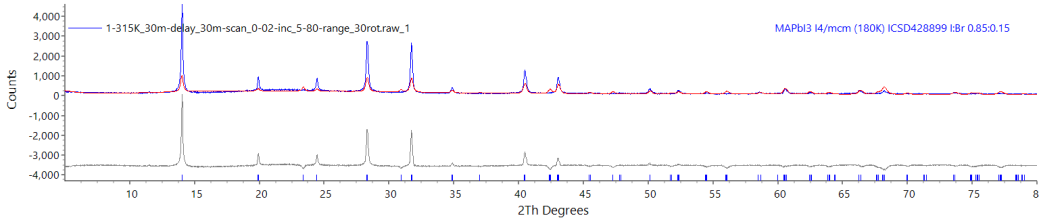

(b) $I4/mcm$-$MAPbI_3$ refined against $(FAPbI_3)_{0.85}(MAPbBr_3)_{0.15}$ data at 315 K, with the halide represented by $I_{0.85}Br_{0.15}$

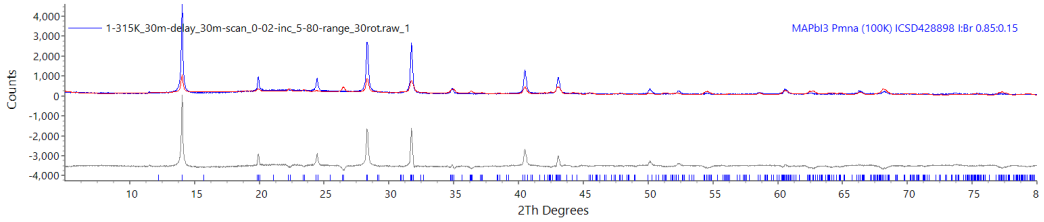

(c) $Pnma$-$MAPbI_3$ refined against $(FAPbI_3)_{0.85}(MAPbBr_3)_{0.15}$ data at 315 K, with the halide represented by $I_{0.85}Br_{0.15}$

Figure B.1: Investigative structure fits on 1-315K. These use fundamental parameter peak profile described in Section 4.8.1.

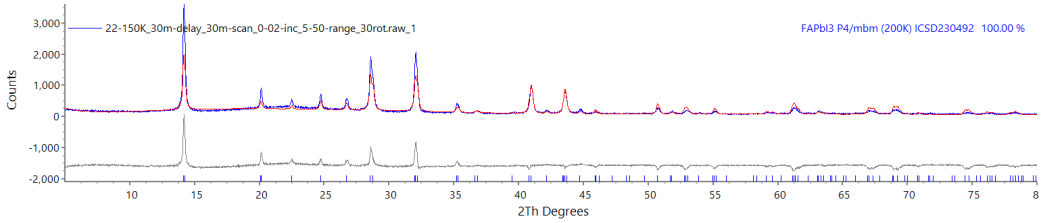

(a) $P4/mbm$-$FAPbI_3$ refined against $(FAPbI_3)_{0.85}(MAPbBr_3)_{0.15}$ data at 150 K, with the halide represented by $I_{0.85}Br_{0.15}$

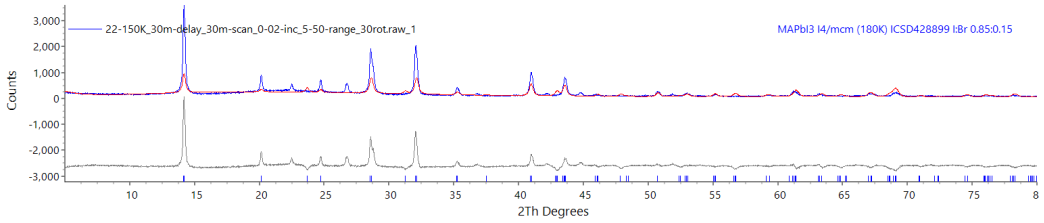

(b) $I4/mcm$-$MAPbI_3$ refined against $(FAPbI_3)_{0.85}(MAPbBr_3)_{0.15}$ data at 150 K, with the halide represented by $I_{0.85}Br_{0.15}$

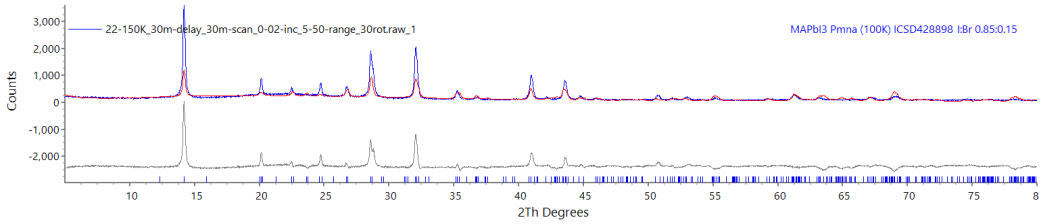

(c) $Pnma$-$MAPbI_3$ refined against $(FAPbI_3)_{0.85}(MAPbBr_3)_{0.15}$ data at 150 K, with the halide represented by $I_{0.85}Br_{0.15}$

Figure B.2: Investigative structure fits on 22-150K. These use fundamental parameter peak profile described in Section 4.8.1.

B.2 Le Bail fits on $(FAPbI_3)_{0.85}(MAPbBr_3)_{0.15}$ for pattern indexing

The refinements using the Le Bail method in Section 6.5 were based on space group and lattice parameter combinations derived from indexing methods in TOPAS. For indexing, individual peaks were fitted using the fundamental parameters instrument profile described in Section 4.8.1. Sample broadening across the individual peaks was accounted for by a common Lorentzian based convolution relating to crystallite size broadening. Indexing was performed across various crystal systems. Crystal systems were excluded from the indexing runs as needed to prevent results from a single system eclipsing candidates from other systems. The choice of candidates for Le Bail refinements were based on indexing candidates with the best goodness of fit parameter and fewest missing/additional peaks. An example of a TOPAS indexing script is provided below.

```
' Indexing paramters, peak positions fitted to 29-80K
index_range "Indexing"
index_lam  1.540596
index_zero_error
index_max_zero_error  0.1
index_max_th2_error  0.05
index_max_Nc_on_No  5
index_max_number_of_solutions 3000
try_space_groups ""
' Crystal systems (commented out as needed)
'Cubic_F
'Cubic_I
'Cubic_P
'Trigonal_Hexagonal_R
'Trigonal_Hexagonal_P
Tetragonal_I
Tetragonal_P
Orthorhombic_F
Orthorhombic_I
Orthorhombic_C
Orthorhombic_P
'Monoclinic_C
'Monoclinic_P
load index_th2 index_I {
    14.19357668   22.2228454
    20.15553282   7.607553321
    22.52357947   4.235363442
    24.75822114   7.85444451
    26.78071187   11.65582009
    28.67235363   65.24864836
    32.12763043   86.97942465
    35.33496308   20.58269758
    36.85621209   6.756761854
}
```

Appendix C

FAMA sequential refinement sets

Contents

C.1 Diffraction patterns list for Chapter 6 . . . . . **285**

C.2 Raw data visualisation **286**

C.3 Rigid body models **287**

C.3.1 Rigid body model for Pb-X octahedra 287

C.3.2 Rigid body model for FA 288

C.4 Structure model refinements on representative diffraction patterns **288**

C.5 Least-square Rietveld refinement based sets **292**

C.5.1 Set 1: $a = b$ 292

C.5.2 Set 2: lattice parameters from projections 293

C.5.3 Set 3: distorted octahedra 294

C.5.4 Set 4: a!=b 294

C.5.5 Set 5: a=b, Pb-Oh offset 294

C.5.6 Set 6:: a!=b, Pb-Oh offset 295

C.5.7 Set 7:: a=b, Pb-Oh offset 295

C.5.8 Set 8: repetition of Set 1 296

C.5.9 Set 8b: repetition of Set 1, rotation limits adjusted 296
C.6 Monte-Carlo assisted least-square Rietveld refinement based sets **299**
C.6.1 Set 9: Based on Set 3, Distorted Oh 299
C.6.2 Set 10: a=b, Pb-Oh offset 300
C.6.3 Set 11 and 12: a=b, Pb-Oh offset, fixed Pb-X bond length 302
C.6.4 Set 13: a,b,c fixed, Pb-Oh offset, fixed Pb-X bond length 302
C.6.5 Set 14, 14b and 15b: a,b,c fixed, Pb-Oh offset . . 303
C.6.6 Set 15: a,b,c fixed, Pb-Oh offset 304
C.6.7 Set 16: a,b,c fixed, Pb-Oh offset 305
C.6.8 Set 17: a,b,c fixed, Pb-Oh offset, halide in $P4$ symmetry 305
C.6.9 Set 18: a=b, Pb-Oh offset, halide in $P4$ symmetry 306
C.6.10 Set 19: a=b, Pb-Oh offset, halide in $P4$ symmetry 306
C.6.11 Set 20: a=b, Pb-Oh offset, halide in $P4$ symmetry 307
C.6.12 Set 21: a,b,c fixed, Pb-Oh offset, halide in $P4$ symmetry 310
C.6.13 Set 22: a,b,c fixed, Pb-Oh offset and halide in $P4$ symmetry 310
C.6.14 Set 23: a=b, Pb-Oh offset and halide in $P4$ symmetry 312
C.6.15 Set 26: a=b, Pb-Oh offset and halide in $P4$ symmetry 315
C.6.16 Additional literature data 316
C.6.17 Selected correlation tables 317

C.1 Diffraction patterns list for Chapter 6

Table C.1: Literature structures of similar systems

Scan number	Temperature (K)	Range (° 2θ)	Equilibration time
1	315	5–50	30 min
14	150	5–50	30 min
16	100	5–50	30 min

Table C.2: Dataset 201810 of in-situ XRD diffraction patterns.

Cooling - 201810				**Heating - 201810**				**Additional scans - 201810**			
Scan number	Temp (K)	Range (2θ)	Equilibration time	Scan number	Temp (K)	Range (2θ)	Equilibration time	Scan number	Temp (K)	Range (2θ)	Equilibration time
1	315	5-80	30 min	30	90	5-50	30 min				
2	310	5-50	30 min	31	100	5-50	30 min	58	315	5-80	60 min
3	305	5-50	30 min	32	110	5-50	30 min	59	315	5-80	60 min
4	300	5-50	30 min	33	120	5-50	30 min	60	315	5-80	60 min
5	295	5-50	30 min	34	130	5-50	30 min	63	320	5-80	60 min
6	290	5-50	30 min	35	140	5-50	30 min	64	330	5-80	60 min
7	285	5-50	30 min	36	150	5-80	30 min	65	240	5-80	60 min
8	280	5-80	30 min	37	160	5-50	30 min	66	350	5-80	60 min
9	275	5-50	30 min	38	170	5-50	30 min				
10	270	5-50	30 min	39	180	5-50	30 min				
11	260	5-50	30 min	40	190	5-50	30 min				
12	250	5-50	30 min	41	200	5-50	30 min				
13	240	5-50	30 min	42	210	5-50	30 min				
14	230	5-50	30 min	43	220	5-50	30 min				
15	220	5-50	30 min	44	230	5-50	30 min				
16	210	5-50	30 min	45	240	5-50	30 min				
17	200	5-50	30 min	46	250	5-50	30 min				
18	190	5-50	30 min	47	260	5-50	30 min				
19	180	5-50	30 min	48	270	5-50	30 min				
20	170	5-50	30 min	49	275	5-50	30 min				
21	160	5-50	30 min	50	280	5-80	30 min				
22	150	5-80	30 min	51	285	5-50	30 min				
23	140	5-50	30 min	52	290	5-50	30 min				
24	130	5-50	30 min	53	295	5-50	30 min				
25	120	5-50	30 min	54	300	5-50	30 min				
26	110	5-50	30 min	55	305	5-50	30 min				
27	100	5-50	30 min	56	310	5-50	30 min				
28	90	5-50	30 min	57	315	5-80	30 min				
29	80	5-80	30 min								

C.2 Raw data visualisation

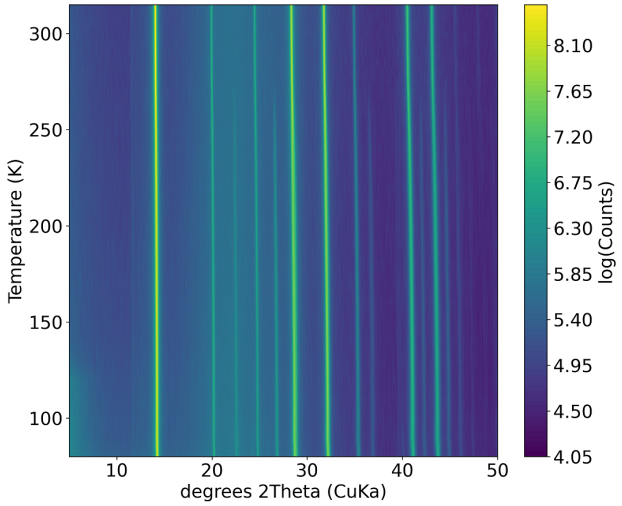

(a) Cooling

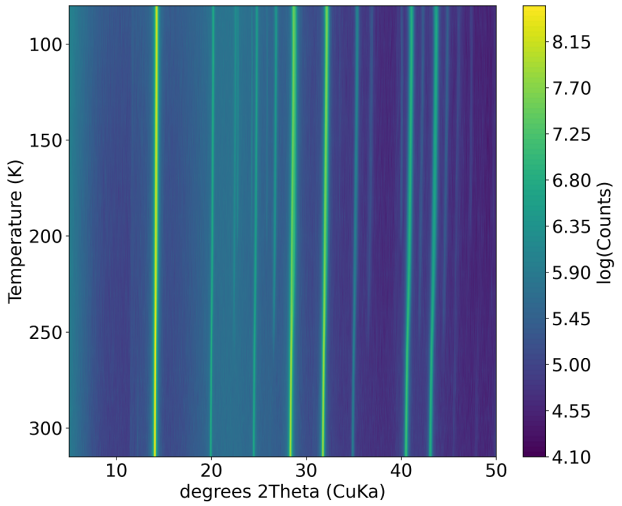

(b) Heating

Figure C.1: PXRD measurements of $(FAPbI_3)_{0.85}(MAPbBr_3)_{0.15}$ showing the log() of diffraction intensity as a function of temperature. Measurements were taken on cooling followed by heating ordered in the figures chronologically from the top down.

Both cooling and heating directions in Figure C.1 present common sets of peaks in bound by similar transition point for the higher temperature transition near 260/270 K. The additional peaks on cooling from 90 to 80 K remain present past 200 K on heating. The origin of these peaks is unclear and were tested a $P1$ symmetry structure agnostic refinement to exclude the possibility of the peaks being related to a lower symmetry perovskite phase. Various literature structures of possible phase separation/decomposition and non-perovskite phases were compared to the unidentified peaks providing a close match.

C.3 Rigid body models

C.3.1 Rigid body model for Pb-X octahedra

The following is a snippet of TOPAS code used for the rigid body description of the Pb-X octahedra. In cases where the octahedra were offset from a stationary Pb atom, Pb1 in the model below was substitute by a placeholder atom which had an occupancy of 0. In some models the bond length "r" was replaced with multiple parameters with absolute or relative limits to keep "r" within some form of constraints.

```
prm r  3.15577‘_0.37578 min 2.9 max 3.5
rigid
point_for_site Pb1
point_for_site I1 ux = r;
point_for_site I2 uy = r;
point_for_site I3 uz = r;
Rotate_about_axies( @ 0 min -10 max 10, @ 0 min -10 max 10, @  45 min 35 max 55)
Translate( 0, 0, 0)
```

C.3.2 Rigid body model for FA

The structure of the FA rigid body was based on [Petrov 2017 Formamidinium iodide: crystal structure and phase transitions] [Petrov et al., 2017]

```
prm r2  1.297 min 1.2 max 1.35
rigid
z_matrix C1
z_matrix N1 C1 = r2;
z_matrix N2 C1 = r2;  N1 @  129.98 min 121 max 132
Rotate_about_axies( @  173.80 min -10 max 190, @ -2.49 min -10 max 190, @  20.50 min -10 max 190)
Translate(@  0.107 min -0.15 max 0.15 , @  0.492 min 0.4 max 0.6 , @  0.587 min 0.35 max 0.65 )
```

C.4 Structure model refinements on representative diffraction patterns

Additional refinements are provided for Section 6.6. Additional refinements are provided for 8-280K and 22-150K patterns collected at 280 and 150 K respectively on cooling in the VT-XRD measurement set. For these additional scans in Table C.3 it is noted that the additional R_{wp} values are supportive of the discussion in Section 6.6 supporting Set D as the favoured model.

Table C.3: Expanded summary of fit parameters

Set	R_{wp}**(80 K)**	R_{wp}**(150 K)**	R_{wp}**(280 K)**	R_{wp}**(315 K)**	**Location**	Model basis
Set C	13.01	10.41	10.93	10.96	FigureC.2	$P4$ symmetry
Set A	10.90	10.50	10.06	9.94	FigureC.3	4 Octahedra
Set D	8.74	9.58	10.52	10.23	FigureC.4	2 Octahedra

Note: R_{exp} is 6.87, 7.22, 7.32 and 7.33 for 80, 150, 280 and 315 K respectively.

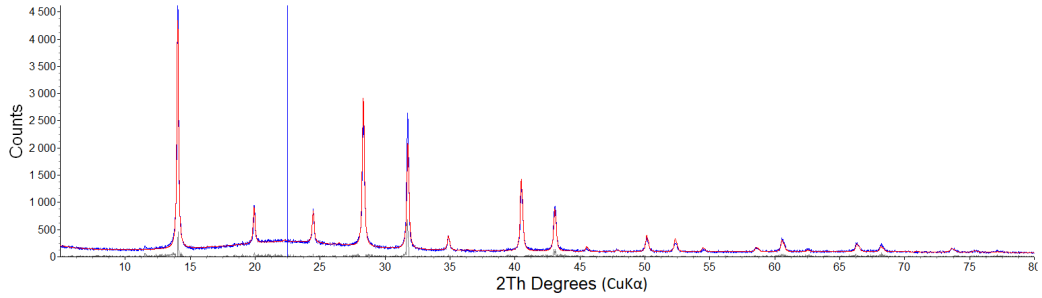

(a) Cs0-setC-315K

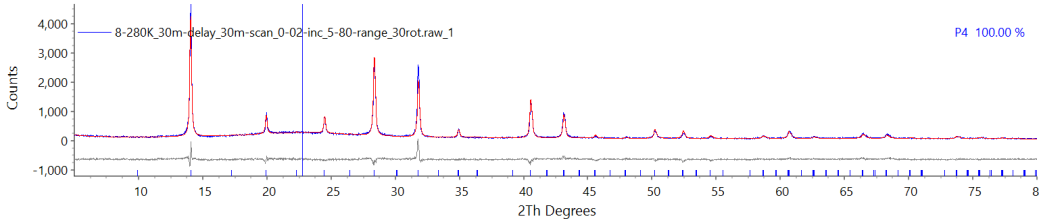

(b) Cs0-setC-280K

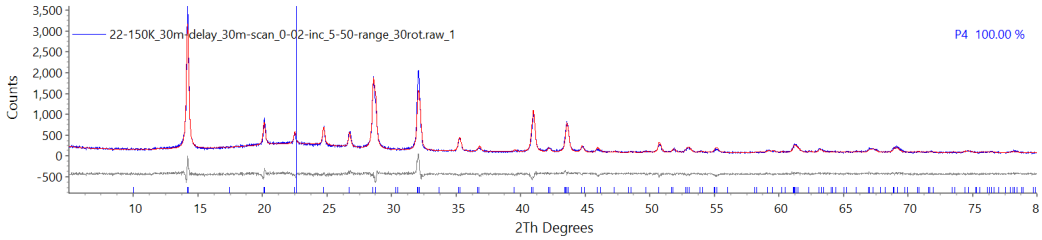

(c) Cs0-setC-150K

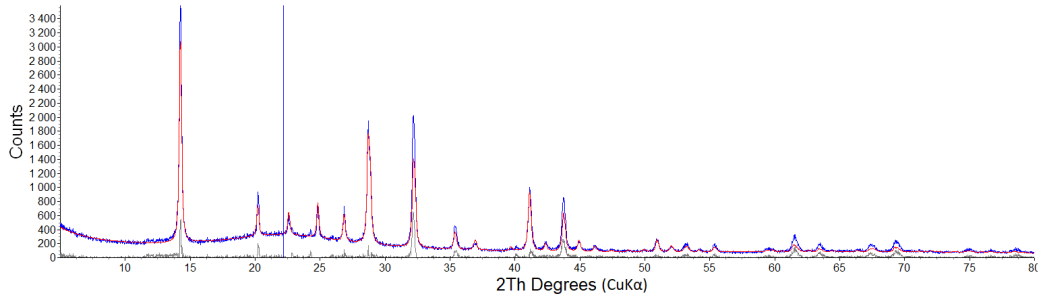

(d) Cs0-setC-80K

Figure C.2: Set C (Cs0-setC): Rietveld refinements using a $P4$ space group to impart it's symmetry to the Pb-X octahedra.

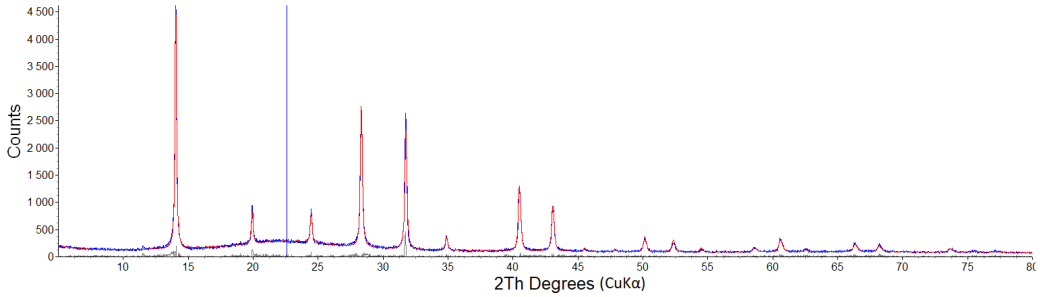

(a) Cs0-setA-315K

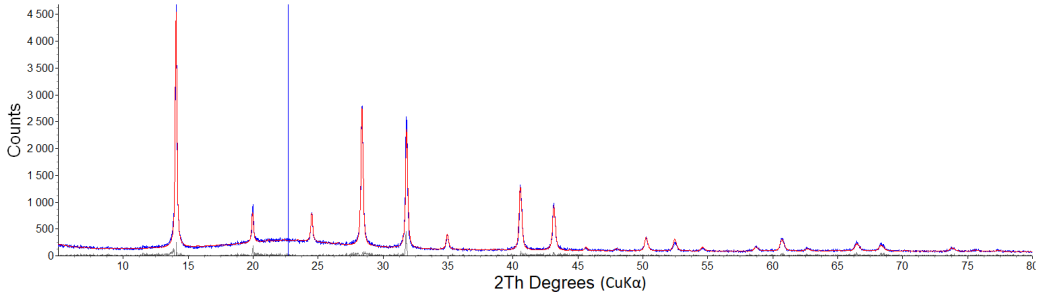

(b) Cs0-setA-280K

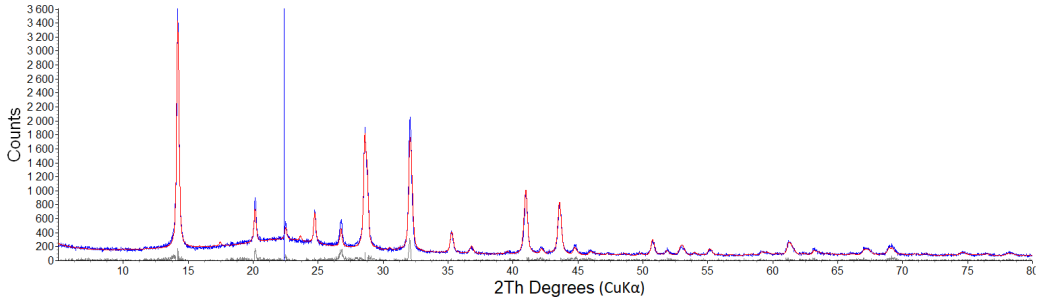

(c) Cs0-setA-150K

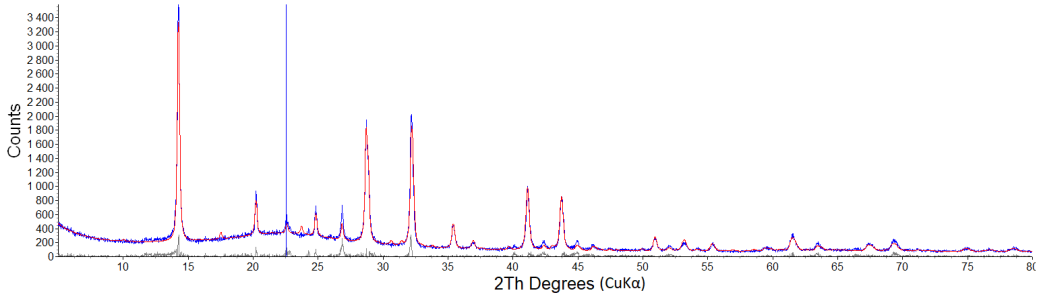

(d) Cs0-setA-80K

Figure C.3: Set A (Cs0-setA): Rietveld refinements using a structure model with 4 octahedra with free rotation and lattice parameters determined by projections of Pb-X bonds.

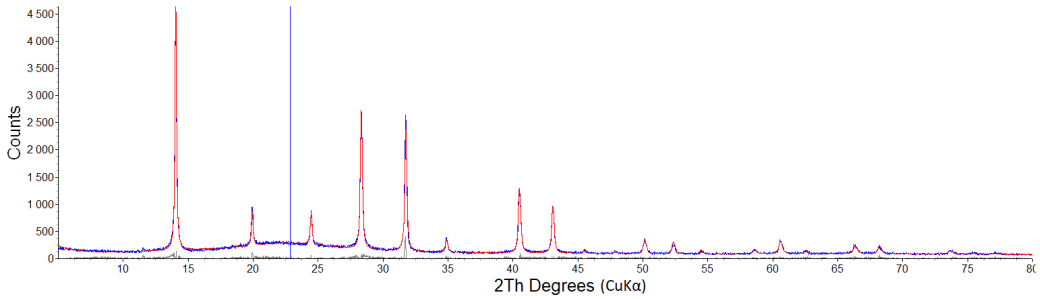

(a) Cs0-setD-315K

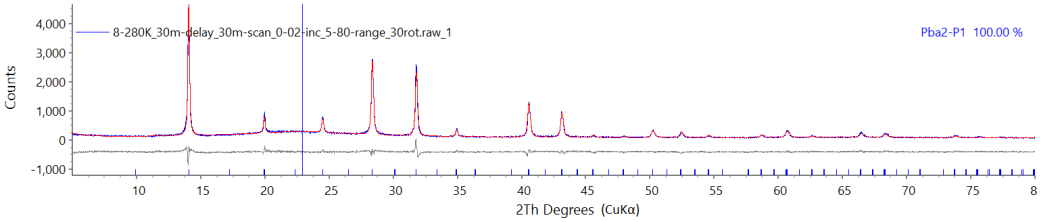

(b) Cs0-setD-280K

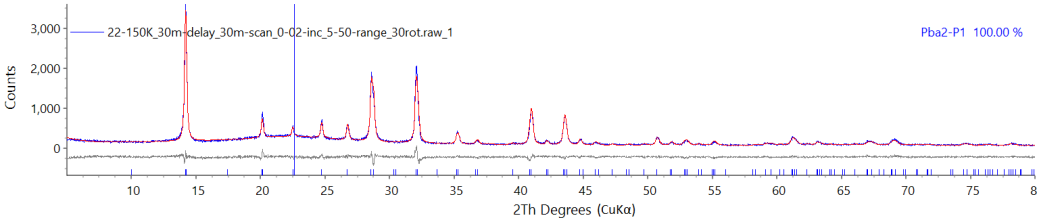

(c) Cs0-setD-150K

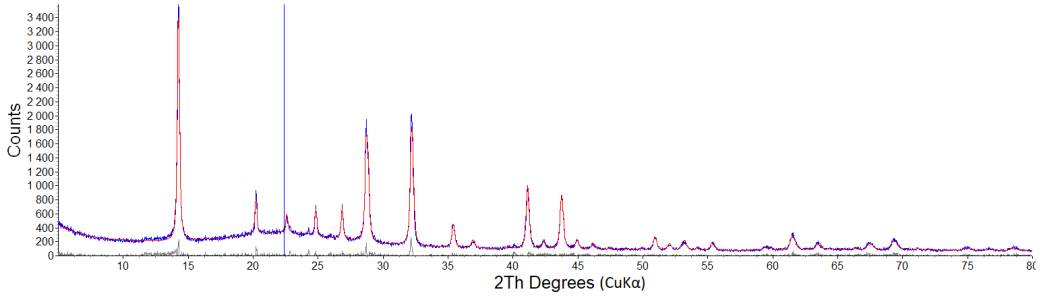

(d) Cs0-setD-80K

Figure C.4: Set D (Cs0-setD): Rietveld refinements using a structure model with 2 octahedra with free rotation and lattice parameters constraints $a = b$, c is free.

C.5 Least-square Rietveld refinement based sets

Sets 1 - 8b made use of 2 runs of sequential refinement, each starting from the opposite end of the data set. The results of the set were the the refinements with the lower R_{Bragg} value. This was to reduce the impact of sudden changes in the structure on the quality of the refinement.

Parameters referred to as free are typically refined within reasonable limits to reduce the size of the solution space.

C.5.1 Set 1: $a = b$

- Lattice parameters, refined $a = b$ and c.
- Pb fixed position
- Octahedra rotation : Rotate_about_axies(@ 0 min -10 max 10, @ 0 min -10 max 10, @ 45 min 35 max 55)
- Organic as a rigid body CN_2 with free translation and rotation
- A single Pb-X bond distance parameter was defined for the rigid bodies
- Average R_{Bragg}: 2.052, σ: 0.531

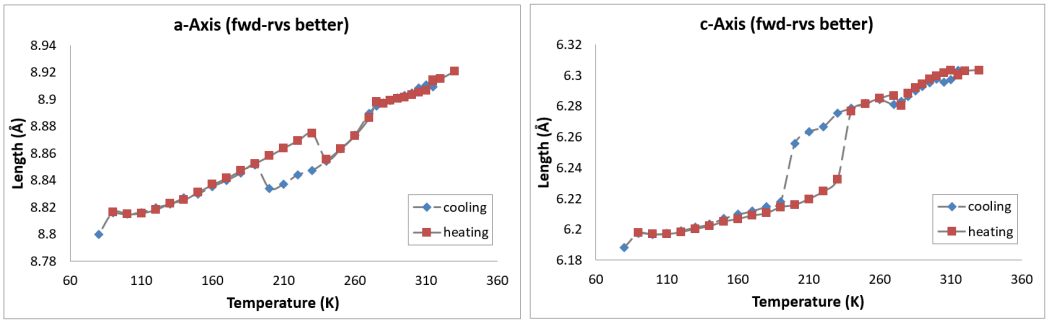

Figure C.5: Set 1

C.5.2 Set 2: lattice parameters from projections

- Lattice parameter defined by projection with respect to the Pb-X bond length.
- Octahedra rotation : Rotate_about_axies(@ 0 min -10 max 10, @ 0 min -10 max 10, @ 45 min 35 max 55)
- Organic as a rigid body CN_2 with free translation and rotation
- A Pb-X bond distance distance parameter was defined the bond in the ab plane and the bond in the c-direction separately for the rigid bodies
- Average R_{Bragg}: 2.681, σ: 0.648

```
Snippet of a TOPAS input file from Set 2
      ' Octahedra rotation angles
      prm Oh1 -2.63458‘_1.73840 min -10 max 10
      prm Oh2  2.00382‘_2.95493 min -10 max 10
      prm Oh3  44.65999‘_2.25551 min 35 max 55
      prm Oh4 -0.47763‘_2.37428 min -10 max 10
      prm Oh5  2.88194‘_2.11261 min -10 max 10
      prm Oh6  45.27340‘_2.17872 min 35 max 55

      ' Projection of Pb-X bonds onto a-axis
      ' Rotation angle have to be in degree and trig angles in radians
      prm !a1 = 2*r*(Cos(Oh2*Pi/180)*Cos(Oh3*Pi/180)+Cos(Oh5*Pi/180)*Cos(Oh6*Pi/180));
      prm !a2 = 2*r*(Cos(Oh1*Pi/180)*Cos(Oh3*Pi/180)+Cos(Oh4*Pi/180)*Cos(Oh6*Pi/180));
      prm !a3 = 2*r1b*(Cos(Oh1*Pi/180)*Cos(Oh2*Pi/180));

      a = a1;
      b = a2;
      c = a3;
      al = 90;
      be = 90;
      ga = 90;
```

In the above code snippet Oh1 and Oh4 are the the octahedral rotation about the a-axis, Oh2 and Oh5 the b-axis and Oh3 and Oh6 the c-axis. For the projections used a separate bond length is used for the bonds in the ab plane and those along the c-direction. This allows elongation or contraction of the unit cell in the c-direction beyond the effect of rotation about the a and b-axis.

The restraint of the lattice parameters by projections prevented distortion of the octahedra. This unfavourably increased the average R_{Bragg} and the standard deviation σ. The loss in fit quality was primarily below 240 K with the majority if Refinements having an R_{Bragg} greater than 3.

C.5.3 Set 3: distorted octahedra

- Lattice parameters, refined $a = b$ and c.
- Pb fixed position
- Octahedra rotation : Rotate_about_axies(@ 0 min -10 max 10, @ 0 min -10 max 10, @ 45 min 35 max 55)
- Octahedra (Oh) defined about a place-holder atom with no electron density. The Oh were allowed to translate across the unit cell by 15 % of the unit cell in any direction, subsequent sets used tighter limits.
- Organic as a rigid body CN_2 with free translation and rotation
- A Pb-X bond distance parameter was defined for each direction in the rigid bodies
- Average R_{Bragg}: Not processed

This set was included for completeness and will not be discussed in detail. It was evaluated to the extent needed to continue onto other sets. Set 5 and 6 are similar with only 2 and 1 bond length parameters respectively in the rigid body model. This is compared to the 3 here in Set 3.

C.5.4 Set 4: a!=b

- Lattice parameters, refined a, b and c individually.
- Pb fixed position
- Octahedra rotation : Rotate_about_axies(@ 0 min -10 max 10, @ 0 min -10 max 10, @ 45 min 35 max 55)
- Organic as a rigid body CN_2 with free translation and rotation
- A single Pb-X bond distance parameter was defined for the rigid bodies
- Average R_{Bragg}: Not processed

This set was included for completeness and will not be discussed in detail. It was evaluated to the extent needed to continue onto other sets.

C.5.5 Set 5: a=b, Pb-Oh offset

- Lattice parameters, refined $a = b$ and c.
- Pb fixed position

- Octahedra rotation : Rotate_about_axies(@ 0 min -10 max 10, @ 0 min -10 max 10, @ 45 min 35 max 55)
- Octahedra (Oh) defined about a place-holder atom with no electron density. The Oh were allowed to translate across the unit cell by 10 % of the unit cell in any direction.
- Organic as a rigid body CN_2 with free translation and rotation
- A Pb-X bond distance distance parameter was defined the bond in the ab plane and the bond in the c-direction separately for the rigid bodies
- Average R_{Bragg}: 2.377, σ: 0.623 (processed in a single direction).

This set was included for completeness and will not be discussed in detail. It was evaluated to the extent needed to continue onto other sets.

C.5.6 Set 6:: a!=b, Pb-Oh offset

- Lattice parameters, refined a, b and c individually.
- Pb fixed position
- Octahedra rotation : Rotate_about_axies(@ 0 min -10 max 10, @ 0 min -10 max 10, @ 45 min 35 max 55)
- Octahedra (Oh) defined about a place-holder atom with no electron density. The Oh were allowed to translate across the unit cell by less than 10 % of the unit cell.
- Organic as a rigid body CN_2 with free translation and rotation
- A single Pb-X bond distance parameter was defined for the rigid bodies
- Average R_{Bragg}: 2.217, σ: 0.452 (processed in a single direction).

This set was included for completeness and will not be discussed in detail. It was evaluated to the extent needed to continue onto other sets.

C.5.7 Set 7:: a=b, Pb-Oh offset

- Lattice parameters, refined $a = b$ and c.
- Pb fixed position
- Octahedra rotation : Rotate_about_axies(@ 0 min -10 max 10, @ 0 min -10 max 10, @ 45 min 35 max 55)

- Octahedra (Oh) defined about a place-holder atom with no electron density. The Oh were allowed to translate across the unit cell by less than 5 % of the unit cell.
- Organic as a rigid body CN_2 with free translation and rotation
- A single Pb-X bond distance parameter was defined for the rigid bodies
- Average R_{Bragg}: 2.229, σ: 0.493

This set was included for completeness and will not be discussed in detail. It was evaluated to the extent needed to continue onto other sets.

C.5.8 Set 8: repetition of Set 1

- Lattice parameters, refined $a = b$ and c.
- Pb fixed position
- Octahedra rotation : Rotate_about_axies(@ 0 min -10 max 10, @ 0 min -10 max 10, @ 45 min 35 max 55)
- Organic as a rigid body CN_2 with free translation and rotation
- A single Pb-X bond distance parameter was defined for the rigid bodies
- Average R_{Bragg}: 2.088, σ: 0.632

C.5.9 Set 8b: repetition of Set 1, rotation limits adjusted

- Lattice parameters, refined $a = b$ and c.
- Pb fixed position
- Octahedra rotation:

```
' First octahedra
  prm Oh1 0 min -12 max 12 '
  prm Oh2 0 min -12 max 12
  prm Oh3 45 min 33 max 45.1
' Second octahedra
  prm Oh4 0 min -12 max 12
  prm Oh5 0 min -12 max 12
  prm Oh6 45 min 44.9 max 57
```

- Organic as a rigid body CN_2 with free translation and rotation
- A single Pb-X bond distance parameter was defined for the rigid bodies
- Average R_{Bragg}: 2.098, σ: 0.627

In Set 1 the Oh can rotate about the c-axis in both the clockwise and anti-clockwise directions independently. Here in Set 8b the rotation was limited to only clockwise for one Oh and anti-clockwise for the second Oh bringing the constraints closer to that of the symmetric $a^0b^0c^+$ rotation. There was no significant increase in the average R_{Bragg} resulting from this constraint.

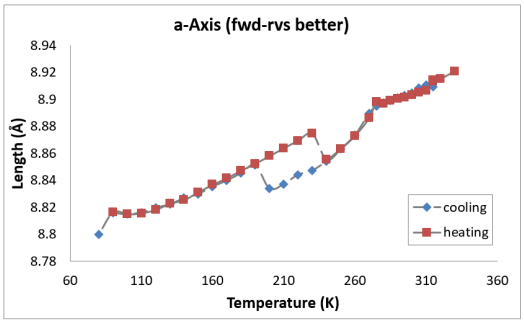

(a) Set 1: a-axis

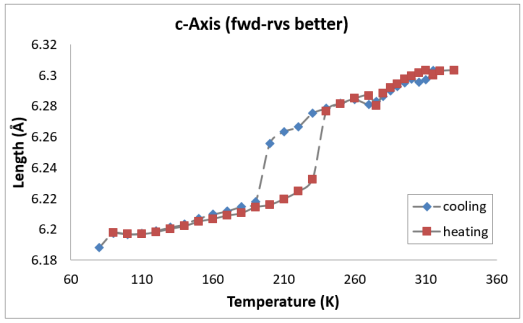

(b) Set 1: c-axis

Figure C.6: Set 1 in $(FAPbI_3)_{0.85}(MAPbBr_3)_{0.15}$ analysis

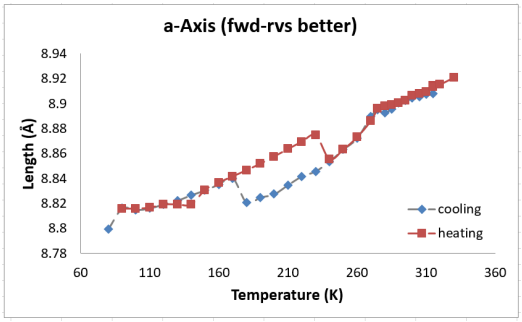

(a) Set 8: a-axis

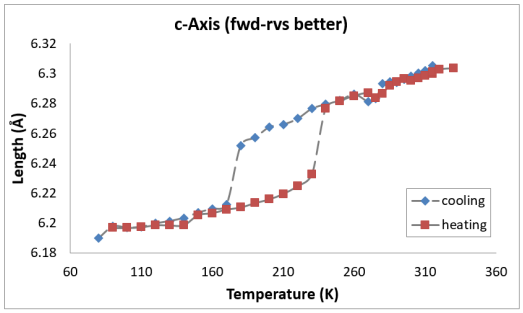

(b) Set 8: c-axis

Figure C.7: Set 8 in $(FAPbI_3)_{0.85}(MAPbBr_3)_{0.15}$ analysis

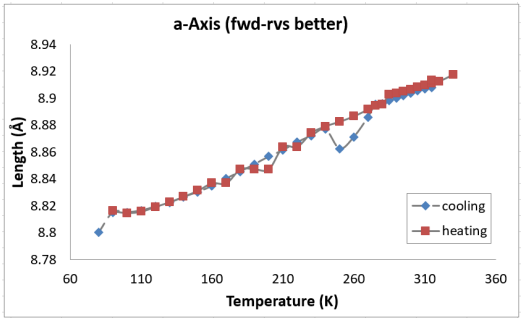

(a) Set 8b: a-axis

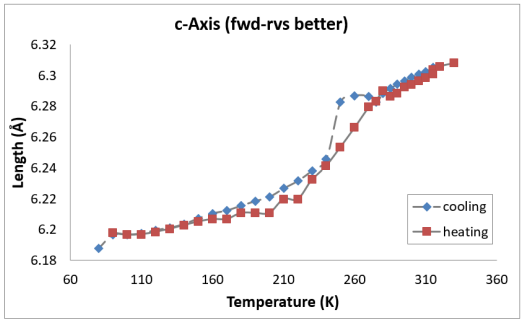

(b) Set 8b: c-axis

Figure C.8: Set 8b in $(FAPbI_3)_{0.85}(MAPbBr_3)_{0.15}$ analysis

C.6 Monte-Carlo assisted least-square Rietveld refinement based sets

These sets were refined using sequential refinement as the base with a Monte-Carlo randomisation based on errors for the purpose of overcoming local minima in the solution space of the refinements.

C.6.1 Set 9: Based on Set 3, Distorted Oh

- Lattice parameters, refined $a = b$ and c.
- Pb fixed position
- Octahedra rotation : Rotate_about_axies(=Oh4;, =Oh5;, =Oh6;)

```
' Octahedra rotation angles
prm Oh1 -3.0612  min -12 max 12
prm Oh2  6.8458  min -12 max 12
prm Oh3  46.4236 min 33 max 57
prm Oh4 -1.4102  min -12 max 12
prm Oh5  2.8812  min -12 max 12
prm Oh6  46.1800 min 33 max 57
```

- Octahedra (Oh) defined about a place-holder atom with no electron density. The Oh were allowed to translate across the unit cell by less than 10 % of the unit cell.
- Organic as a rigid body CN_2 with free rotation and translation as follows:

```
Translate(@ 0 min -0.05 max 0.05 , @  0.5 min 0.48 max 0.52 , 0.5 )
Translate(@ 0.5 min 0.45 max 0.55 , @ 0 min -0.02 max 0.02 , 0.5 )
```

- A Pb-X bond distance parameter was defined for each direction in the rigid bodies
- Directly from Monte-Carlo R_{Bragg}: 7.390, σ: 4.415
- With follow up reprocessing Average R_{Bragg}: 2.162, σ: 0.480

Once processed this set produced very unfavourable R_{Bragg} values and to deal with this a *Python* script was used to create new TOPAS input files from the result files with the code which called for the Monte-Carlo optimisation removed. This was processed in TOPAS using a Windows batch file which was generated under the same *Python* script.

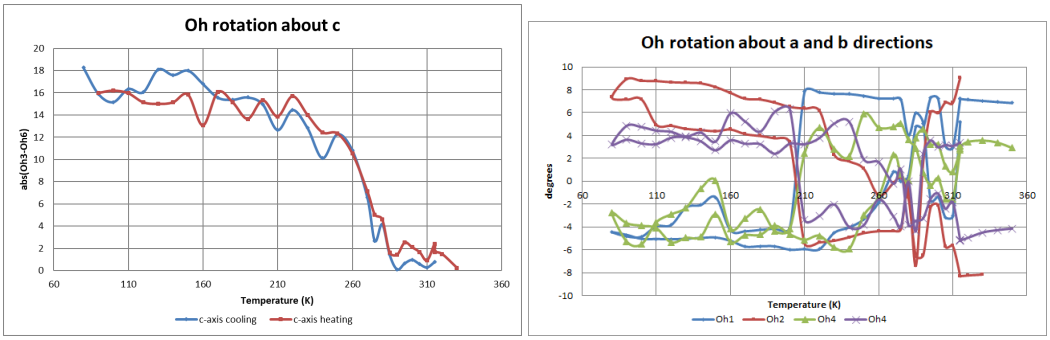

Figure C.9: Set 9: (left) Effective octahedral rotation about the c-axis. This was evaluated by taking the absolute value of the difference in rotation about the c-axis of the 2 Oh in the unit cell. (right) noisy rotation about the a and b axes

C.6.2 Set 10: a=b, Pb-Oh offset

- Lattice parameters, refined $a = b$ and c.
- Pb fixed position
- Octahedra rotation:

```
prm Oh1 0 min -12 max 12
prm Oh2 0 min -12 max 12
prm Oh3 45 min 33 max 45.1
prm Oh4 0 min -12 max 12
prm Oh5 0 min -12 max 12
prm Oh6 45 min 44.9 max 57
```

- Octahedra (Oh) defined about a place-holder atom with no electron density. The Oh were allowed to translate across the unit cell by a percentage of the unit cell.
- Organic as a rigid body CN_2 with free rotation and translation as follows:

```
Translate(@ 0 min -0.05 max 0.05 , @  0.5 min 0.48 max 0.52 , 0.5 )
Translate(@ 0.5 min 0.45 max 0.55 , @ 0 min -0.02 max 0.02 , 0.5 )
```

- A single Pb-X bond distance parameter was defined for the rigid bodies
- Average R_{Bragg}: 2.209, σ: 0.555

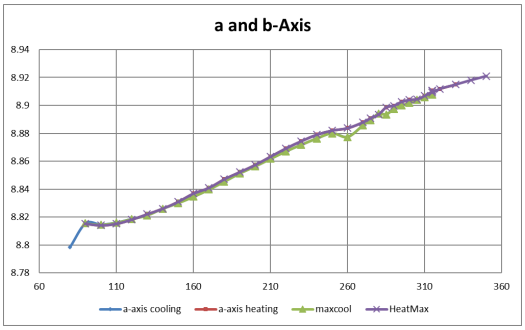

(a) Set 10: c-axis

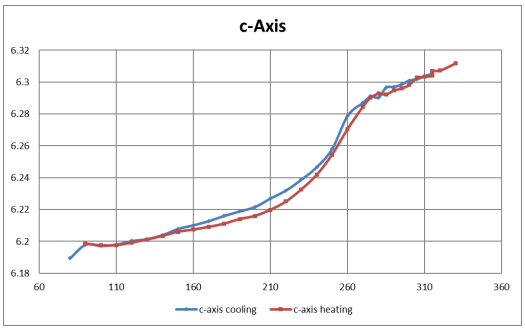

(b) Set 10: c-axis

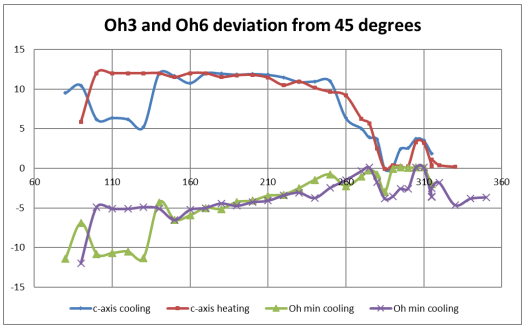

(c) Set 10

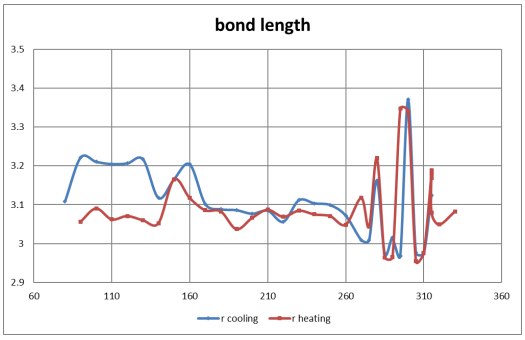

(d) Set 10: Pb-X bond length

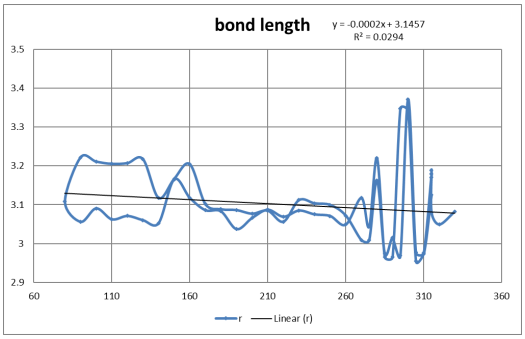

(e) Set 10: Pb-X bond length with a fitted trend line

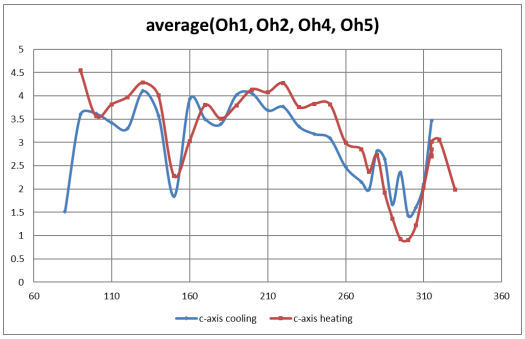

(f) Set 10: Rotation about the x and y axes of the Pb-X octahedra.

Figure C.10: Set 10 in $(FAPbI_3)_{0.85}(MAPbBr_3)_{0.15}$ analysis

C.6.3 Set 11 and 12: a=b, Pb-Oh offset, fixed Pb-X bond length

- Lattice parameters, refined $a = b$ and c.
- Pb fixed position
- Octahedra rotation:

```
prm Oh1 0 min -12 max 12
prm Oh2 0 min -12 max 12
prm Oh3 45 min 33 max 45.1
prm Oh4 0 min -12 max 12
prm Oh5 0 min -12 max 12
prm Oh6 45 min 44.9 max 57
```

- Octahedra (Oh) defined about a place-holder atom with no electron density. The Oh were allowed to translate across the unit cell by a percentage of the unit cell.
- Organic as a rigid body CN_2 with free rotation and translation as follows:

```
Translate(@ 0 min -0.05 max 0.05 , @  0.5 min 0.48 max 0.52 , 0.5 )
Translate(@ 0.5 min 0.45 max 0.55 , @ 0 min -0.02 max 0.02 , 0.5 )
```

- A single Pb-X bond distance parameter **fixed** for the rigid bodies as the average from Set 10: 3.099 Å
- Set 11: Oh rotation limits hit: Average R_{Bragg}: 2.268, σ: 0.534
- Set 11f: Oh rotation limits relaxed shortened Monte-Carlo step: Average R_{Bragg}: 2.258, σ: 0.514
- Set 12: Oh rotation limits relaxed, 300 iterations per scan Monte-Carlo step: Average R_{Bragg}: 1.844, σ: 0.316

C.6.4 Set 13: a,b,c fixed, Pb-Oh offset, fixed Pb-X bond length

- Lattice parameters, fixed to values from Le Bail fits which used a $Pba2$ space group.
- Pb fixed position
- Octahedra rotation:

```
prm Oh1 0 min -12 max 12
prm Oh2 0 min -12 max 12
prm Oh3 45 min 28 max 48
prm Oh4 0 min -12 max 12
prm Oh5 0 min -12 max 12
prm Oh6 45 min = Oh3; max = 62;
```

- Octahedra (Oh) defined about a place-holder atom with no electron density. The Oh were allowed to translate across the unit cell by a percentage of the unit cell.
- Organic as a rigid body CN_2 with free rotation and translation as follows:

```
Translate(@ 0 min -0.05 max 0.05 , @  0.5 min 0.48 max 0.52 , 0.5 )
Translate(@ 0.5 min 0.45 max 0.55 , @ 0 min -0.02 max 0.02 , 0.5 )
```

- A single Pb-X bond distance parameter **fixed** for the rigid bodies as the average from Set 10: 3.099 Å
- 300 iterations per scan Monte-Carlo step
- Average R_{Bragg}: 1.894, σ: 0.325

C.6.5 Set 14, 14b and 15b: a,b,c fixed, Pb-Oh offset

- Lattice parameters, fixed to values from Le Bail fits which used a $Pba2$ space group.
- Pb fixed position
- Octahedra rotation:

```
prm Oh1 0 min -12 max 12
prm Oh2 0 min -12 max 12
prm Oh3 45 min 28 max 48
prm Oh4 0 min -12 max 12
prm Oh5 0 min -12 max 12
prm Oh6 45 min = Oh3; max = 62;
```

- Octahedra (Oh) defined about a place-holder atom with no electron density. The Oh were allowed to translate across the unit cell by a percentage of the unit cell.
- Organic as a rigid body CN_2 with free rotation and translation as follows:

```
Translate(@ 0 min -0.05 max 0.05 , @  0.5 min 0.48 max 0.52 , 0.5 )
Translate(@ 0.5 min 0.45 max 0.55 , @ 0 min -0.02 max 0.02 , 0.5 )
```

- A single Pb-X bond distance parameter was defined for the rigid bodies
- 300 iterations per scan Monte-Carlo step
- Set 14: 300 iterations per scan Monte-Carlo step, Average R_{Bragg}: 1.856, σ: 0.287
- Set 14b: 200 iterations per scan Monte-Carlo step, Average R_{Bragg}: 1.938, σ: 0.383

- Set 15b: 200 iterations per scan Monte-Carlo step, Average R_{Bragg}: 1.939, σ: 0.347

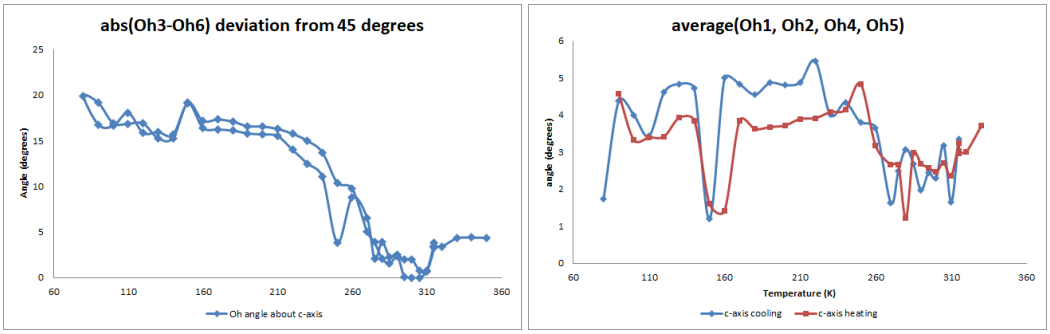

Figure C.11: Set 14: (left) Effective octahedral rotation about the c-axis. This was evaluated by taking the absolute value of the difference in rotation about the c-axis of the 2 Oh in the unit cell. (right) noisy rotation about the a and b axes

C.6.6 Set 15: a,b,c fixed, Pb-Oh offset

- Lattice parameters, fixed to values from Le Bail fits which used a $Pba2$ space group.
- Pb fixed position
- Octahedra rotation:

```
prm Oh1 0 min -12 max 12
prm Oh2 0 min -12 max 12
prm Oh3 45 min 28 max 48
prm Oh4 0 min -12 max 12
prm Oh5 0 min -12 max 12
prm Oh6 45 min = Oh3; max = 62;
```

- Octahedra (Oh) defined about a place-holder atom with no electron density. The Oh were allowed to translate across the unit cell by a percentage of the unit cell.
- Organic as a rigid body CN_2 with free rotation and translation as follows:

```
Translate(@ 0 min -0.05 max 0.05 , @  0.5 min 0.48 max 0.52 , 0.5 )
Translate(@ 0.5 min 0.45 max 0.55 , @ 0 min -0.02 max 0.02 , 0.5 )
```

- A single Pb-X bond distance parameter **fixed** for the rigid bodies as the average from Set 14: 3.179 Å

- 200 iterations per scan Monte-Carlo step
- Average R_{Bragg}: 1.913, σ: 0.300

C.6.7 Set 16: a,b,c fixed, Pb-Oh offset

Like Set 15, with the exception that it uses 3 parameters for the Pb-I bond lengths in the rigid bodies defined.

C.6.8 Set 17: a,b,c fixed, Pb-Oh offset, halide in $P4$ symmetry

- Lattice parameters, fixed to values from Le Bail fits which used a $Pba2$ space group.
- Pb position refined.
- Octahedra rotation in the ab plane defined by parameter p1 as follows, the halide in the c-direction was free to move 10 % of the unit cell in any direction:

```
prm p1  0.00850‘_0.00404 min -0.05 max 0.15

    site I1 occ I-1  0.85 beq = b2; occ Br-1  0.15 beq = b3; x = 0.25 + p1;
                                                  y = 0.25 - p1; z = 0;
    site I2 occ I-1  0.85 beq = b2; occ Br-1  0.15 beq = b3; x = 0.75 + p1;
                                                  y = 0.25 + p1; z = 0;
            site I3 occ I-1  0.85 beq = b2; occ Br-1  0.15 beq = b3; x @ 0 min -0.1 max 0.1
                                      y @ 0 min -0.1 max 0.1 z @  0.5 min 0.4 max 0.6
```

- Octahedra (Oh) defined about a place-holder atom with no electron density. The Oh were allowed to translate across the unit cell by a percentage of the unit cell.
- Organic as a rigid body CN_2 with free rotation and translation as follows:

```
Translate(@ 0 min -0.05 max 0.05 , @  0.5 min 0.48 max 0.52 , 0.5 )
Translate(@ 0.5 min 0.45 max 0.55 , @ 0 min -0.02 max 0.02 , 0.5 )
```

- 200 iterations per scan Monte-Carlo step
- Average R_{Bragg}: 1.939, σ: 0.347

C.6.9 Set 18: a=b, Pb-Oh offset, halide in $P4$ symmetry

- Lattice parameters, refined a, b and c individually.
- Pb position refined using 2 sites.
- Octahedra rotation in the ab plane defined by parameter p1 as follows, the halide in the c-direction was free to move 10 % of the unit cell in any direction:

```
prm p1  0.00850‘_0.00404 min -0.05 max 0.15

    site I1 occ I-1  0.85 beq = b2; occ Br-1  0.15 beq = b3; x = 0.25 + p1;
                                                y = 0.25 - p1; z = 0;
    site I2 occ I-1  0.85 beq = b2; occ Br-1  0.15 beq = b3; x = 0.75 + p1;
                                                y = 0.25 + p1; z = 0;
site I3 occ I-1  0.85 beq = b2; occ Br-1  0.15 beq = b3; x @ 0 min -0.1 max 0.1
                              y @ 0 min -0.1 max 0.1 z @  0.5 min 0.4 max 0.6
```

- Organic as a rigid body CN_2 with free rotation and translation as follows:

```
Translate(@ 0 min -0.05 max 0.05 , @  0.5 min 0.48 max 0.52 , 0.5 )
Translate(@ 0.5 min 0.45 max 0.55 , @ 0 min -0.02 max 0.02 , 0.5 )
```

- 200 iterations per scan Monte-Carlo step
- Average R_{Bragg}: 1.871, σ: 0.277

C.6.10 Set 19: a=b, Pb-Oh offset, halide in $P4$ symmetry

- Lattice parameters, refined $a = b$ and c.
- Pb position refined using 2 independent sites, one for each of the 2 octahedra in the unit cell.
- Octahedra rotation in the ab plane defined by parameter p1 as follows, the halide in the c-direction was free to move 10 % of the unit cell in any direction:

```
prm p1  0.00850‘_0.00404 min -0.05 max 0.15

    site I1 occ I-1  0.85 beq = b2; occ Br-1  0.15 beq = b3; x = 0.25 + p1;
                                                y = 0.25 - p1; z = 0;
    site I2 occ I-1  0.85 beq = b2; occ Br-1  0.15 beq = b3; x = 0.75 + p1;
                                                y = 0.25 + p1; z = 0;
            site I3 occ I-1  0.85 beq = b2; occ Br-1  0.15 beq = b3; x @ 0 min -0.1 max 0.1
                                  y @ 0 min -0.1 max 0.1 z @  0.5 min 0.4 max 0.6
```

- Organic as a rigid body CN_2 with free rotation and translation as follows:

```
Translate(@ 0 min -0.05 max 0.05 , @  0.5 min 0.48 max 0.52 , 0.5 )
Translate(@ 0.5 min 0.45 max 0.55 , @ 0 min -0.02 max 0.02 , 0.5 )
```

- 200 iterations per scan Monte-Carlo step
- Average R_{Bragg}: 1.921, σ: 0.319

C.6.11 Set 20: a=b, Pb-Oh offset, halide in $P4$ symmetry

- Lattice parameters, refined $a = b$ and c.
- Pb position refined using 2 independent sites, one for each of the 2 octahedra in the unit cell.
- Octahedra rotation in the ab plane defined by parameter p1, and the halide in the c-direction was **fixed** as follows:

```
prm p1  0.00850‘_0.00404 min -0.05 max 0.15

site I1 occ I-1  0.85 beq = b2; occ Br-1  0.15 beq = b3; x = 0.25 + p1; y = 0.25 - p1; z = 0;
site I2 occ I-1  0.85 beq = b2; occ Br-1  0.15 beq = b3; x = 0.75 + p1; y = 0.25 + p1; z = 0;
site I3 occ I-1  0.85 beq = b2; occ Br-1  0.15 beq = b3; x 0 y 0 z 0.5
```

- Organic as a rigid body CN_2 with free rotation and translation as follows:

```
Translate(@ 0 min -0.05 max 0.05 , @  0.5 min 0.48 max 0.52 , 0.5 )
Translate(@ 0.5 min 0.45 max 0.55 , @ 0 min -0.02 max 0.02 , 0.5 )
```

- A single Pb-X bond distance parameter **fixed** for the rigid bodies as the average from Set 14: 3.179 Å
- 200 iterations per scan Monte-Carlo step
- Average R_{Bragg}: 2.229, σ: 0.299

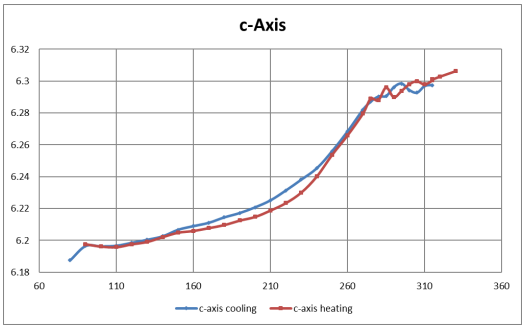

(a) Set 19: c-axis

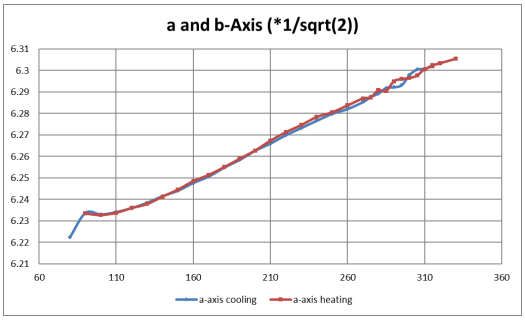

(b) Set 19: a axis (a=b) scaled by $\frac{1}{\sqrt{2}}$

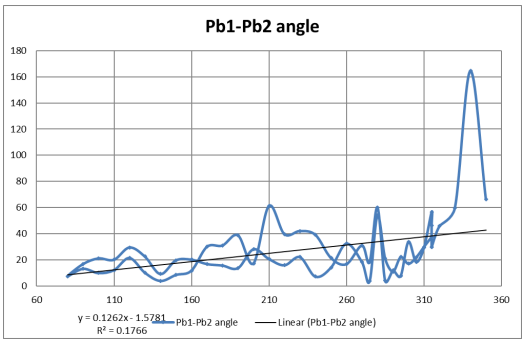

(c) Set 19: $\frac{c\sqrt{2}}{a}$

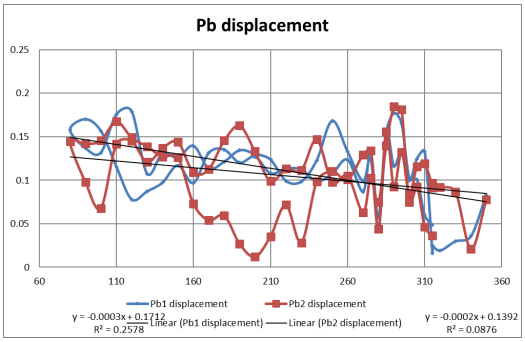

(d) Set 19

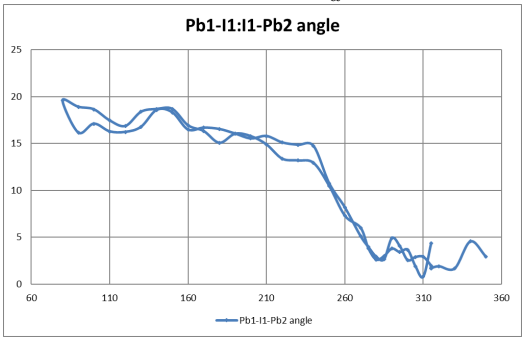

(e) Set 19

Figure C.12: Set 19 in $(FAPbI_3)_{0.85}(MAPbBr_3)_{0.15}$ analysis

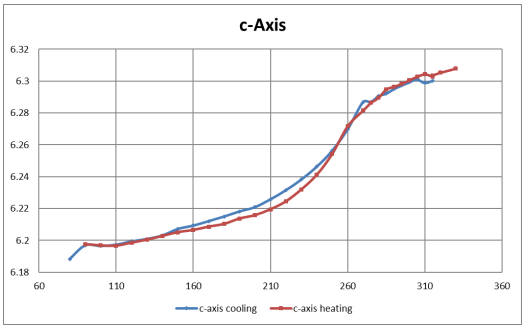

(a) Set 20: c-axis

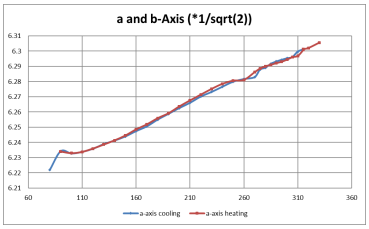

(b) Set 20: a axis (a=b) scaled by $\frac{1}{\sqrt{2}}$

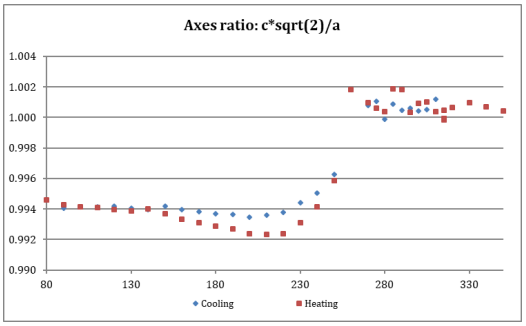

(c) Set 23: $\frac{c\sqrt{2}}{a}$

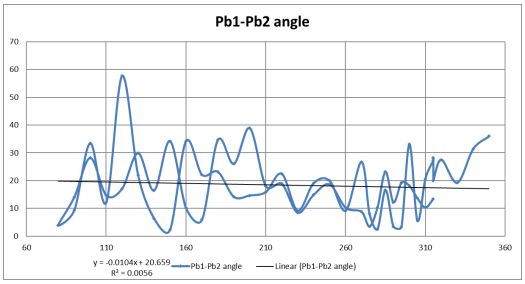

(d) Set 20

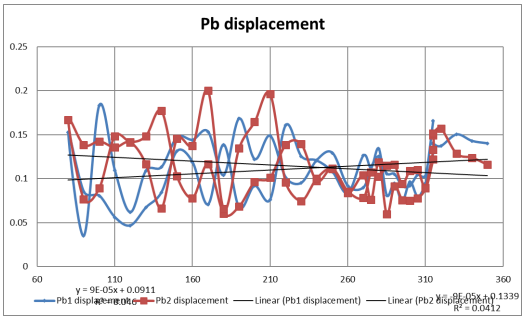

(e) Set 20

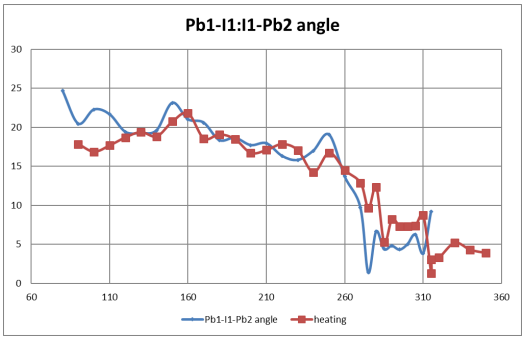

(f) Set 20

Figure C.13: Set 20 in $(FAPbI_3)_{0.85}(MAPbBr_3)_{0.15}$ analysis

C.6.12 Set 21: a,b,c fixed, Pb-Oh offset, halide in $P4$ symmetry

- Lattice parameters, fixed to values from Le Bail fits which used a $Pba2$ space group.
- Pb position refined.
- Octahedra rotation in the ab plane defined by parameter p1, and the halide in the c-direction was **fixed** as follows:

```
prm p1  0.00850‘_0.00404 min -0.05 max 0.15

site I1 occ I-1  0.85 beq = b2; occ Br-1  0.15 beq = b3; x = 0.25 + p1;
                                                  y = 0.25 - p1; z = 0;
site I2 occ I-1  0.85 beq = b2; occ Br-1  0.15 beq = b3; x = 0.75 + p1;
                                                  y = 0.25 + p1; z = 0;
site I3 occ I-1  0.85 beq = b2; occ Br-1  0.15 beq = b3; x 0 y 0 z 0.5
```

- Octahedra (Oh) defined about a place-holder atom with no electron density. The Oh were allowed to translate across the unit cell by a percentage of the unit cell.
- Organic as a rigid body CN_2 with free rotation and translation as follows:

```
Translate(@ 0 min -0.05 max 0.05 , @  0.5 min 0.48 max 0.52 , 0.5 )
Translate(@ 0.5 min 0.45 max 0.55 , @ 0 min -0.02 max 0.02 , 0.5 )
```

- 200 iterations per scan Monte-Carlo step
- Average R_{Bragg}: 2.229, σ: 0.299

C.6.13 Set 22: a,b,c fixed, Pb-Oh offset and halide in $P4$ symmetry

- Lattice parameters, fixed to values from Le Bail fits which used a $Pba2$ space group.
- Pb position refined in a $P4$ symmetry confined to the ab plane.

```
prm p2  0.01300‘_1.16512 min -0.1 max 0.1
prm p3  0.02270‘_0.66505 min -0.1 max 0.1

site Pb1a occ Pb+2  0.25 beq = b1; x = 0+p2; y = 0+p3; z = 0;
site Pb1b occ Pb+2  0.25 beq = b1; x = 0-p2; y = 0-p3; z = 0;
site Pb1c occ Pb+2  0.25 beq = b1; x = 0-p3; y = 0+p2; z = 0;
site Pb1d occ Pb+2  0.25 beq = b1; x = 0+p3; y = 0-p2; z = 0;
```

- Octahedra rotation in the ab plane defined by parameter p1, and the halide in the c-direction was **fixed** as follows:

```
prm p1  0.00850‘_0.00404 min -0.05 max 0.15

site I1 occ I-1  0.85 beq = b2; occ Br-1  0.15 beq = b3; x = 0.25 + p1;
                                                    y = 0.25 - p1; z = 0;
site I2 occ I-1  0.85 beq = b2; occ Br-1  0.15 beq = b3; x = 0.75 + p1;
                                                    y = 0.25 + p1; z = 0;
site I3 occ I-1  0.85 beq = b2; occ Br-1  0.15 beq = b3; x 0 y 0 z 0.5
```

- Octahedra (Oh) defined about a place-holder atom with no electron density. The Oh were allowed to translate across the unit cell by a percentage of the unit cell.
- Organic as a rigid body CN_2 with free rotation and translation as follows:

```
Translate(@ 0 min -0.05 max 0.05 , @  0.5 min 0.48 max 0.52 , 0.5 )
Translate(@ 0.5 min 0.45 max 0.55 , @ 0 min -0.02 max 0.02 , 0.5 )
```

- 200 iterations per scan Monte-Carlo step
- Average R_{Bragg}: 2.368, σ: 0.312

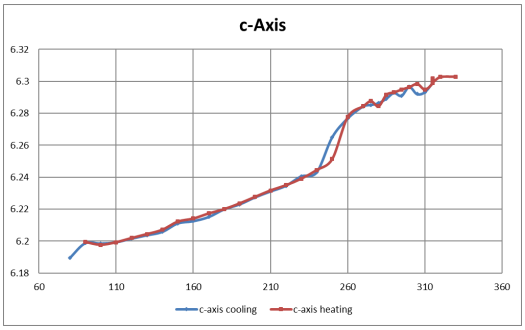

(a) Set 22: c-axis

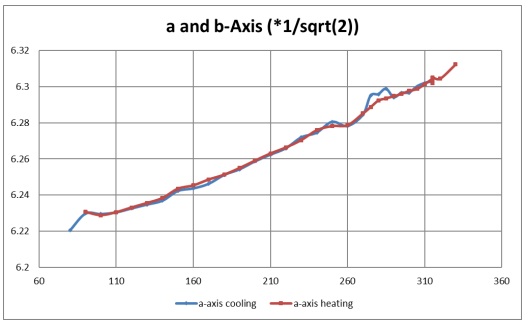

(b) Set 22: a axis (a=b) scaled by $\frac{1}{\sqrt{2}}$

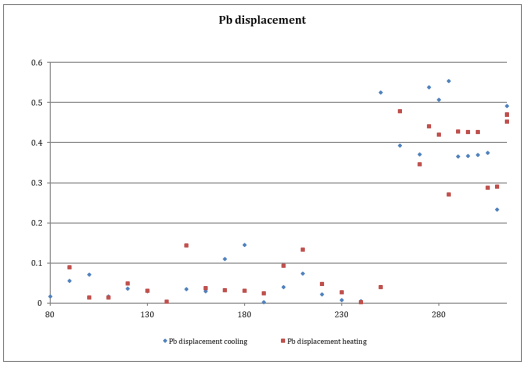

(c) Set 22

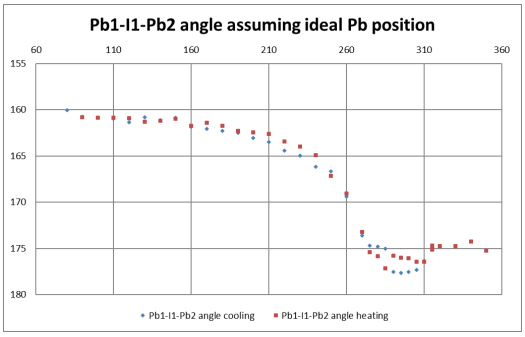

(d) Set 22

Figure C.14: Set 22 in $(FAPbI_3)_{0.85}(MAPbBr_3)_{0.15}$ analysis

C.6.14 Set 23: a=b, Pb-Oh offset and halide in $P4$ symmetry

- Lattice parameters, refined $a = b$ and c.
- Pb position refined in a $P4$ symmetry confined to the ab plane.
- Octahedra rotation in the ab plane defined by parameter p1, and the halide in the c-direction was **fixed** as follows:

```
prm p1  0.00850‘_0.00404 min -0.05 max 0.15

    site I1 occ I-1  0.85 beq = b2; occ Br-1  0.15 beq = b3; x = 0.25 + p1; y = 0.25 - p1; z = 0;
    site I2 occ I-1  0.85 beq = b2; occ Br-1  0.15 beq = b3; x = 0.75 + p1; y = 0.25 + p1; z = 0;
    site I3 occ I-1  0.85 beq = b2; occ Br-1  0.15 beq = b3; x 0 y 0 z 0.5
```

- Octahedra (Oh) defined about a place-holder atom with no electron density. The Oh were allowed to translate across the unit cell by a percentage of the unit cell.
- Organic as a rigid body CN_2 with free rotation and translation as follows:

```
Translate(@ 0 min -0.05 max 0.05 , @  0.5 min 0.48 max 0.52 , 0.5 )
Translate(@ 0.5 min 0.45 max 0.55 , @ 0 min -0.02 max 0.02 , 0.5 )
```

- 200 iterations per scan Monte-Carlo step
- Average R_{Bragg}: 2.258, σ: 0.332

Table C.4 provides an overview of volumetric thermal expansion values calculated from Set23. The volumetric thermal expansion coefficients are calculated by $\alpha_V = \frac{1}{V}(\frac{\delta V}{\delta T})$ ([James et al., 2001]) and the equations provided in Figure C.16b. These can be compared to the literature values of Table C.6 where we see values between 98.6 and 206 for lead iodide based perovskites.

Table C.4: Set 23: Volume thermal expansion coefficients (α_V)

Phase	Temp (K)	Vol Å^3	α_V (x10^{-6} K^{-1})
α	275	248.66	155.01
α	315	250.20	154.05
α	350	251.55	153.23
β	100	240.70	73.63
β	175	242.86	163.98
β	250	246.67	251.03

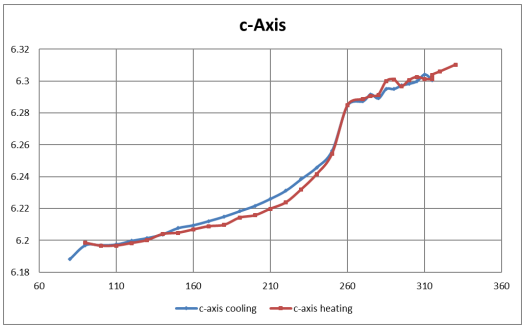

(a) Set 23: c-axis

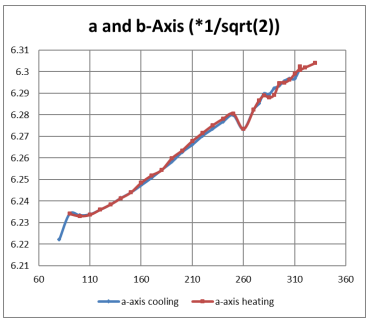

(b) Set 23: a axis (a=b) scaled by $\frac{1}{\sqrt{2}}$

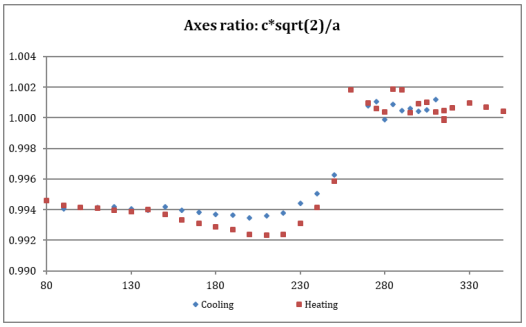

(c) Set 23: $\frac{c\sqrt{2}}{a}$

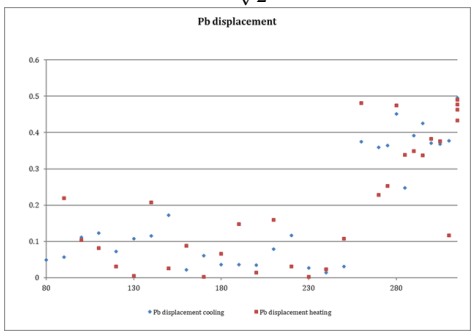

(d) Set 23: Displacement of Pb from the ideal position

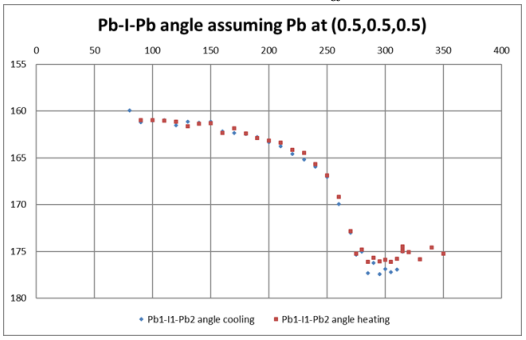

(e) Set 23

Figure C.15: Set 23 in $(FAPbI_3)_{0.85}(MAPbBr_3)_{0.15}$ analysis

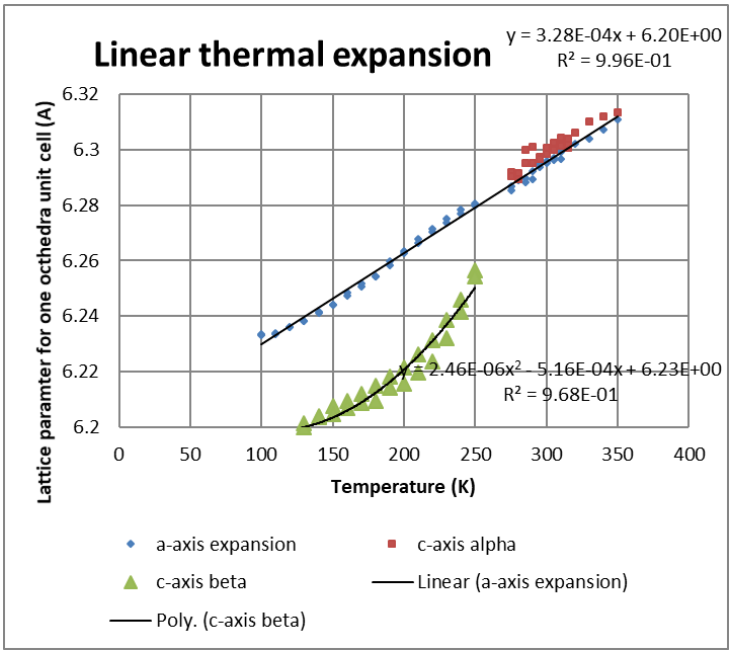

(a) Set 23: Linear thermal expansion.

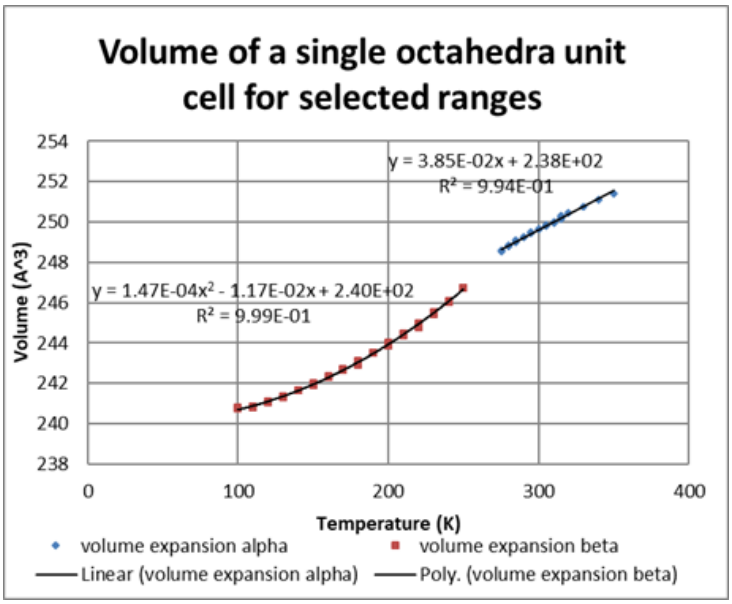

(b) Set 23: Volumetric thermal expansion.

Figure C.16: Set 23: Thermal expansion in $(FAPbI_3)_{0.85}(MAPbBr_3)_{0.15}$

C.6.15 Set 26: a=b, Pb-Oh offset and halide in $P4$ symmetry

- Lattice parameters, refined $a = b$ and c.
- Pb position refined in a $P4$ symmetry confined to the ab plane.
- Octahedra rotation in the ab plane defined by parameter p1, and the halide in the c-direction was **fixed** as follows:

```
prm p1  0.00850‘_0.00404 min -0.05 max 0.15

site I1 occ I-1  0.85 beq = b2; occ Br-1  0.15 beq = b3; x = 0.25 + p1; y = 0.25 - p1; z = 0;
site I2 occ I-1  0.85 beq = b2; occ Br-1  0.15 beq = b3; x = 0.75 + p1; y = 0.25 + p1; z = 0;
site I3 occ I-1  0.85 beq = b2; occ Br-1  0.15 beq = b3; x 0 y 0 z 0.5
```

- Octahedra (Oh) defined about a place-holder atom with no electron density. The Oh were allowed to translate across the unit cell by a percentage of the unit cell.
- Organic was substituted to be a single Mn atom which has 25 electrons which is the same as FA prior to ionisation, occupancy was not adjusted for the 15 % of MA content (19 e^- before ionisation).
- 200 iterations per scan Monte-Carlo step
- Average R_{Bragg}: 2.703, σ: 0.377 The R_{Bragg} of this set was high compared to the previous Sets as such the model was not considered.

C.6.16 Additional literature data

Table C.5: Table of selected lead halide bond lengths

Source	Ref	Bond	Length Å	Temp (K)	Composition	Space group
COD	7225287	Pb-I	3.13615	293	$MAPbI_3$	$Pm\bar{3}m$
ICSD	238610	Pb-I (ab)	3.1736	253	$MAPbI_3$	$I4/mcm$
		Pb-I (c)	3.1737			
ICSD	428899	Pb-I (ab)	3.1720	180	$MAPbI_3$	$I4/mcm$
		Pb-I (c)	3.1782			
ICSD	428898	Pb-I (ab)	3.1870	100	$MAPbI_3$	$Pmna$
		Pb-I (c)	3.1970			
COD	1545319	Pb-Br	2.98488	300	$MAPbBr_3$	$Pm\bar{3}m$
ICSD	230492	Pb-I (ab)	2.962	200	$FAPbI_3$	$P4/mbm$
		Pb-I (c)	3.161			
COD	4127358	Pb-I (1)	3.2646	295	$CsPbI_3$	$Pnma$
		Pb-I (2)	3.4101			
		Pb-I (3)	3.2288			
		Pb-I (4)	3.0456			
		Pb-I (5)	3.2288			
		Pb-I (6)	3.2288			
		Ave	3.23445			
		Min	3.0456			
		Max	3.4101			

Table C.6: Literature volume thermal expansion coefficients (α_V) for contrast against Table C.4

Composition	Phase	T (K)	a_V (10^{-6} K^{-1}	Reference
$FAPbI_3$	α	348-489	100-98.6	[Fabini et al., 2016]
$FAPbI_3$	β	200-299	206-202	[Fabini et al., 2016]
$MAPbI_3$	β	280	132	[Fabini et al., 2016]

C.6.17 Selected correlation tables

Set 23 monte Correlation table: 1-315K_30m-delay_30m-scan_0-02-inc_5-80-range_30rot.out												
Parameter	**Descrption**		**19**	**21**	**22**	**23**	**24**	**25**	**26**	**29**	**30**	**31**
b1	Pb thermal parameter	**19**	100	-8	-17	-6	1	6	-26	18	0	0
b3	I thermal parameter	**21**	-8	100	19	-3	-36	13	-17	-45	-2	2
b4	C thermal parameter	**22**	-17	19	100	-2	-22	10	-8	27	0	0
b5	N thermal parameter	**23**	-6	-3	-2	100	13	-28	26	-4	0	1
p1	I position	**24**	1	-36	-22	13	100	-19	24	8	1	-1
p2	Pb1 position	**25**	6	13	10	-28	-19	100	-97	-5	2	-1
p3	Pb2 position	**26**	-26	-17	-8	26	24	-97	100	7	-1	1
scale30337b8_	Scale parameter	**29**	18	-45	27	-4	8	-5	7	100	0	0
a1	a=b axis	**30**	0	-2	0	0	1	2	-1	0	100	-94
c3017bc8_	c-axis	**31**	0	2	0	1	-1	-1	1	0	-94	100

(a) Set 23 correlation table for 315K

Set 23 monte Correlation table: 29-80K_30m-delay_30m-scan_0-02-inc_5-80-range_30rot.out												
Parameter	**Descrption**		**19**	**21**	**22**	**23**	**24**	**25**	**26**	**29**	**30**	**31**
b1	Pb thermal parameter	**19**	100	18	4	-1	-6	-13	13	23	-40	-26
b3	I thermal parameter	**21**	18	100	-9	2	-5	-26	26	55	1	-4
b4	C thermal parameter	**22**	4	-9	100	-25	-3	-24	24	1	0	-5
b5	N thermal parameter	**23**	-1	2	-25	100	20	9	-9	3	-5	-2
p1	I position	**24**	-6	-5	-3	20	100	-5	5	12	-6	20
p2	Pb1 position	**25**	-13	-26	-24	9	-5	100	-100	-15	10	2
p3	Pb2 position	**26**	13	26	24	-9	5	-100	100	15	-10	-2
scale38071d8_	Scale parameter	**29**	23	55	1	3	12	-15	15	100	-9	10
a1	a=b axis	**30**	-40	1	0	-5	-6	10	-10	-9	100	-27
c37ff2c8_	c-axis	**31**	-26	-4	-5	-2	20	2	-2	10	-27	100

(b) Set 23 correlation table for 80K

Figure C.17: Set 23 correlation tables for 315 and 80 K

Set 10 Correlation table: 1-315K_30m-delay_30m-scan_0-02-inc_5-80-range_30rot2.out																							
Parameter	**Descrption**		**19**	**20**	**21**	**22**	**23**	**24**	**25**	**26**	**27**	**28**	**35**	**36**	**37**	**38**	**39**	**40**	**41**	**42**	**43**
r	Pb-X bond length	**19**	100	-36	49	-29	-17	14	-13	-62	55	27	19	9	-12	-22	-22	50	-4	-22	8
Oh1	Octahedra rotation	**20**	-36	100	-19	-58	-38	-33	66	25	-17	-6	-9	-15	17	-56	5	-64	66	-8	33
Oh2	Octahedra rotation	**21**	49	-19	100	-65	-59	-4	50	-37	39	14	20	0	-2	-65	-27	50	55	-30	23
Oh3	Octahedra rotation	**22**	-29	-58	-65	100	76	21	-84	17	-25	-8	-12	7	-7	96	23	4	-89	34	-45
Oh4	Octahedra rotation	**23**	-17	-38	-59	76	100	-37	-79	24	-27	-23	-7	8	-7	79	19	3	-75	38	-82
Oh5	Octahedra rotation	**24**	14	-33	-4	21	-37	100	-22	-1	-2	9	-7	13	-15	18	-9	5	-30	-18	55
Oh6	Octahedra rotation	**25**	-13	66	50	-84	-79	-22	100	-13	17	16	6	-19	20	-88	-8	-16	97	-22	52
b1	Pb thermal parameter	**26**	-62	25	-37	17	24	-1	-13	100	-81	-59	-24	13	-11	17	-4	-48	-13	4	-17
b2	I thermal parameter	**27**	55	-17	39	-25	-27	-2	17	-81	100	10	68	-14	12	-23	-6	42	20	-11	17
b3	I thermal parameter	**28**	27	-6	14	-8	-23	9	16	-59	10	100	-36	-9	9	-14	13	17	11	3	24
scale386eff0_	Scale parameter	**35**	19	-9	20	-12	-7	-7	6	-24	68	-36	100	3	-3	-4	-20	22	12	-21	-1
a1	a=b axis	**36**	9	-15	0	7	8	13	-19	13	-14	-9	3	100	-96	11	-10	4	-16	-9	-6
c3853400_	c-axis	**37**	-12	17	-2	-7	-7	-15	20	-11	12	9	-3	-96	100	-11	10	-6	17	8	6
rx386f608_	Octahedra translation	**38**	-22	-56	-65	96	79	18	-88	17	-23	-14	-4	11	-11	100	4	6	-87	17	-51
ry386f680_	Octahedra translation	**39**	-22	5	-27	23	19	-9	-8	-4	-6	13	-20	-10	10	4	100	-40	-22	86	-18
rz386f6f8_	Octahedra translation	**40**	50	-64	50	4	3	5	-16	-48	42	17	22	4	-6	6	-40	100	-14	-29	-15
rx386fd10_	Octahedra translation	**41**	-4	66	55	-89	-75	-30	97	-13	20	11	12	-16	17	-87	-22	-14	100	-36	45
ry386fd88_	Octahedra translation	**42**	-22	-8	-30	34	38	-18	-22	4	-11	3	-21	-9	8	17	86	-29	-36	100	-42
rz386fe00_	Octahedra translation	**43**	8	33	23	-45	-82	55	52	-17	17	24	-1	-6	6	-51	-18	-15	45	-42	100

(a) Set 10 correlation table for 315 K

Set 10 Correlation table: 28-90K_30m-delay_30m-scan_0-02-inc_5-50-range_30rot2.out																							
			19	**20**	**21**	**22**	**23**	**24**	**25**	**26**	**27**	**28**	**29**	**30**	**35**	**36**	**37**	**38**	**39**	**40**	**41**	**42**	**43**
r	Pb-X bond length	**19:**	100	2	-43	-14	8	-33	-24	2	6	-6	-37	13	-9	-23	-6	-32	-1	-23	-37	8	-46
Oh1	Octahedra rotation	**20:**	2	100	74	-53	18	60	73	11	-69	69	37	68	-62	-32	-28	-67	73	-75	48	-51	54
Oh2	Octahedra rotation	**21:**	-43	74	100	-24	29	58	61	34	-63	61	58	63	-48	-20	-21	-28	61	-48	45	-41	60
Oh3	Octahedra rotation	**22:**	-14	-53	-24	100	53	6	-38	49	41	-43	-11	-19	20	15	20	81	-1	73	-43	-19	-65
Oh4	Octahedra rotation	**23:**	8	18	29	53	100	53	13	76	-15	12	17	51	-25	-12	-8	22	64	19	-16	-57	-48
Oh5	Octahedra rotation	**24:**	-33	60	58	6	53	100	53	39	-58	56	57	62	-44	-7	-20	-17	75	-2	27	-67	19
Oh6	Octahedra rotation	**25:**	-24	73	61	-38	13	53	100	1	-51	50	29	32	-54	-15	-9	-40	64	-46	85	-60	50
b1	Pb thermal parameter	**26:**	2	11	34	49	76	39	1	100	-9	5	18	50	-9	-13	-10	16	48	19	-28	-42	-37
b2	I thermal parameter	**27:**	6	-69	-63	41	-15	-58	-51	-9	100	-100	-66	-74	59	21	23	66	-65	53	-18	39	-54
b3	I thermal parameter	**28:**	-6	69	61	-43	12	56	50	5-10	100	66	72	40	-20	-23	-67	63	-54	19	-36	56	-56
b4	FA thermal parameter	**29:**	-37	37	58	-11	17	57	29	18	-66	66	100	54	-10	8	-2	-27	41	-15	10	-21	42
b5	FA thermal parameter	**30:**	13	68	63	-19	51	62	32	50	-74	72	54	100	-53	-30	-33	-53	70	-42	-6	-38	17
scale2dd17b0_	Scale parameter	**35:**	-9	-62	-48	20	-25	-44	-54	-9	59	-57	-10	-53	100	36	23	37	-62	41	-30	58	-25
a1	a=b axis	**36:**	-23	-32	-20	15	-12	-7	-15	-13	21	-20	8	-30	36	100	-8	26	-27	32	-2	19	-9
c2db7bc8_	c-axis	**37:**	-6	-28	-21	20	-8	-20	-9	-10	23	-23	-2	-33	23	-8	100	23	-19	21	-3	5	-13
rx2dd1dc8_	Octahedra translation	**38:**	-32	-67	-28	81	22	-17	-40	16	66	-67	-27	-53	37	26	23	100	-34	73	-13	6	-50
ry2dd1e40_	Octahedra translation	**39:**	-1	73	61	-1	64	75	64	48	-65	63	41	70	-62	-27	-19	-34	100	-35	24	-87	16
rz2dd1eb8_	Octahedra translation	**40:**	-23	-75	-48	73	19	-2	-46	19	53	-54	-15	-42	41	32	21	73	-35	100	-33	10	-66
rx2dd24d0_	Octahedra translation	**41:**	-37	48	45	-43	-16	27	85	-28	-18	19	10	-6	-30	-2	-3	-13	24	-33	100	-30	52
ry2dd2548_	Octahedra translation	**42:**	8	-51	-41	-19	-57	-67	-60	-42	39	-36	-21	-38	58	19	5	6	-87	10	-30	100	-3
rz2dd25c0_	Octahedra translation	**43:**	-46	54	60	-65	-48	19	50	-37	-54	56	42	17	-25	-9	-13	-50	16	-66	52	-3	100

(b) Set 10 correlation table for 90 K

Set 10 Correlation table: 29-80K_30m-delay_30m-scan_0-02-inc_5-80-range_30rot2.out																							
Parameter	**Descrption**		**19**	**20**	**21**	**22**	**23**	**24**	**25**	**26**	**27**	**28**	**29**	**30**	**35**	**36**	**37**	**38**	**39**	**40**	**41**	**42**	**43**
r	Pb-X bond length	**19**	100	4	-1	-4	0	1	0	-3	20	-7	-4	0	29	9	-3	-15	2	-6	4	-7	-6
Oh1	Octahedra rotation	**20**	4	100	-68	-46	-92	75	30	33	-11	-9	22	26	-12	-4	-15	-47	73	-53	31	-76	50
Oh2	Octahedra rotation	**21**	-1	-68	100	-6	48	-96	19	-10	-14	21	-5	-19	-10	0	18	-13	-59	9	-6	54	-2
Oh3	Octahedra rotation	**22**	-4	-46	-6	100	51	-4	-20	-12	31	-10	-8	-17	31	4	5	72	-5	46	-30	20	-47
Oh4	Octahedra rotation	**23**	0	-92	48	51	100	-57	-46	-43	27	0	-15	-31	24	4	16	48	-65	56	-47	69	-62
Oh5	Octahedra rotation	**24**	1	75	-96	-4	-57	100	-17	12	8	-16	7	21	4	-3	-19	6	65	-16	8	-64	12
Oh6	Octahedra rotation	**25**	0	30	19	-20	-46	-17	100	10	-11	2	17	8	-18	1	-3	-47	13	-38	71	-3	43
b1	Pb thermal parameter	**26**	-3	33	-10	-12	-43	12	10	100	5	-28	15	-4	34	2	2	-10	24	-16	8	-28	21
b2	I thermal parameter	**27**	20	-11	-14	31	27	8	-11	5	100	-87	-7	-36	72	10	0	3	-11	17	-27	-1	-30
b3	I thermal parameter	**28**	-7	-9	21	-10	0	-16	2	-28	-87	100	1	27	-54	-5	2	8	-1	-2	14	13	12
b4	FA thermal parameter	**29**	-4	22	-5	-8	-15	7	17	15	-7	1	100	34	-7	5	0	-12	34	2	14	-23	-7
b5	FA thermal parameter	**30**	0	26	-19	-17	-31	21	8	-4	-36	27	34	100	-34	1	-18	5	36	-2	30	-20	9
scale37a57c8_	Scale parameter	**35**	29	-12	-10	31	24	4	-18	34	72	-54	-7	-34	100	6	12	14	1	16	-27	-5	-28
a1	a=b axis	**36**	9	-4	0	4	4	-3	1	2	10	-5	5	1	6	100	-39	-1	-2	4	0	2	-5
c3788bd0_	c-axis	**37**	-3	-15	18	5	16	-19	-3	2	0	2	0	-18	12	-39	100	2	-13	4	-11	12	-4
rx37a5de0_	Octahedra translation	**38**	-15	-47	-13	72	48	6	-47	-10	3	8	-12	5	14	-1	2	100	-7	58	-6	37	-53
ry37a5e58_	Octahedra translation	**39**	2	73	-59	-5	-65	65	13	24	-11	-1	34	36	1	-2	-13	-7	100	-14	19	-83	15
rz37a5ed0_	Octahedra translation	**40**	-6	-53	9	46	56	-16	-38	-16	17	-2	2	-2	16	4	4	58	-14	100	-17	24	-94
rx37a64e8_	Octahedra translation	**41**	4	31	-6	-30	-47	71	8	-27	14	14	30	-27	0	-11	-6	19	-17	100	11	25	
ry37a6560_	Octahedra translation	**42**	-7	-76	54	20	69	-64	-3	-28	-1	13	-23	-20	-5	2	12	37	-83	24	11	100	-21
rz37a65d8_	Octahedra translation	**43**	-6	50	-2	-47	-62	12	43	21	-30	12	-7	9	-28	-5	-4	-53	15	-94	25	-21	100

(c) Set 10 correlation table for 80 K

Figure C.18: Set 10 correlation tables for 315, 90 and 80 K

Appendix D

CsFAMA parametric refinement sets

Contents

D.1 Visual data comparison **319**
D.2 Parametric refinement sets **320**

D.1 Visual data comparison

Figure D.1 shows the intensity difference of the 14° 2θ peak which is more intense after the cooling and heating process. The remainder of peak in the pattern are have virtually identical peak profiles and intensities. The (110)/(001), (220)/(002), (330)/(003) reflects are at 14.1, 28.4, ∼43.1° 2θ respectively for the 310 K patterns.

Figure D.2, presents modelled X-ray diffraction patterns for the sample compositions of Cs0 and Cs10 in Chapter 8. Both variants use identical refinement conditions with the exception of the A-site occupancy which is scaled to represent the electron density for each composition.

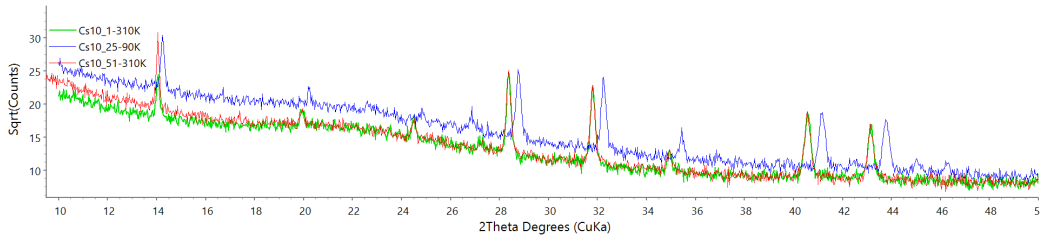

Figure D.1: A visual comparison of Cs10 1-310K, 25-90K and 51-310K

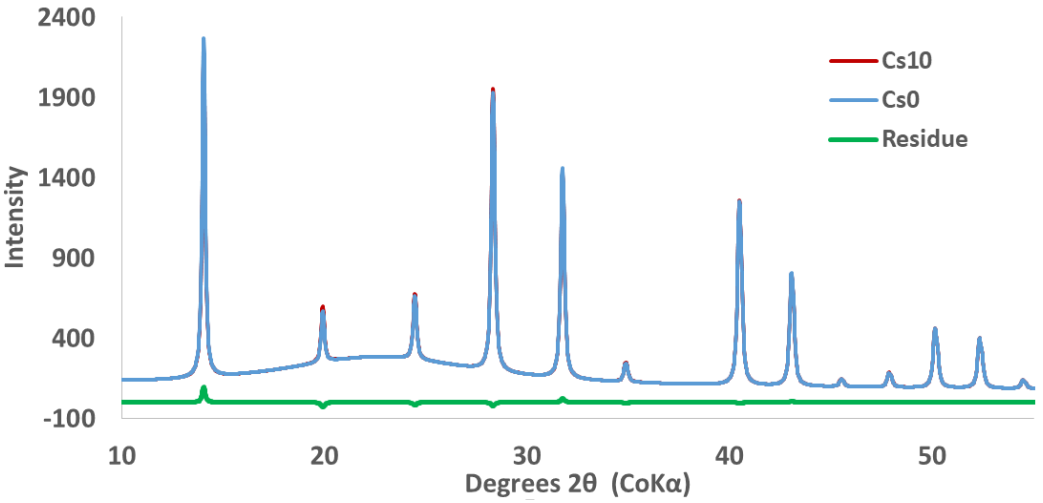

Figure D.2: Modelled intensities for the α phase of Cs0 and Cs0 compositions using refinements that only differ by the representative atoms' electron density.(blue) Cs0, (red) Cs10, (green) residue between Cs0 and Cs10.

D.2 Parametric refinement sets

Figure D.3 presents R_{wp} values for refinements on the Cs0 data-set. Cs0_21_2 has a fixed Pb position, while Cs0_23 has the Pb atom refined to allow it to spread it electron density in the ab plane. This has an indirect implication on the possible distribution of the halide electron density as discussed in Chapter 6. We see an improved (reduced) R_{wp} value at higher temperatures for the Cs0_23 set.

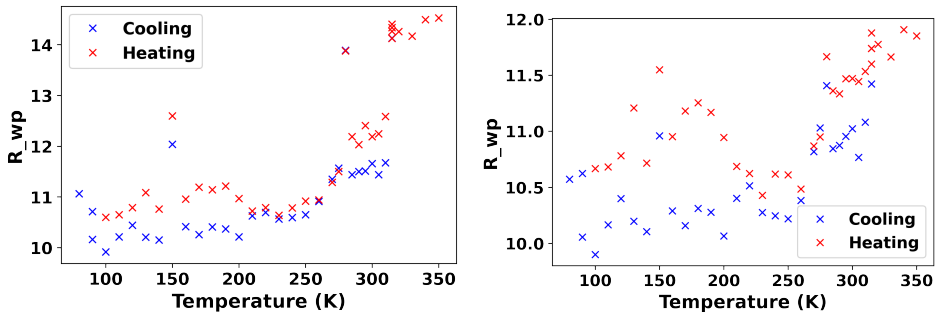

(a) (b)

Figure D.3: Fit quality comparison between the (a) Cs0_21_2 and Cs0_23 refinement sets

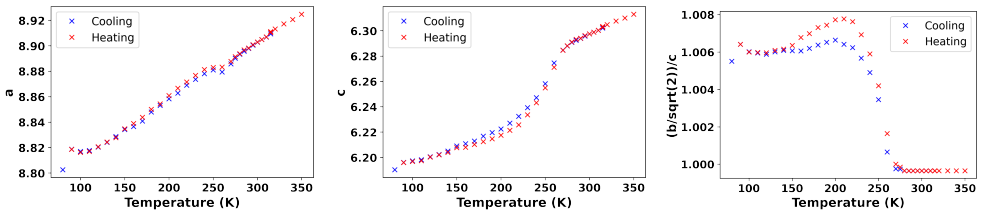

(a) Cs0 Set 23

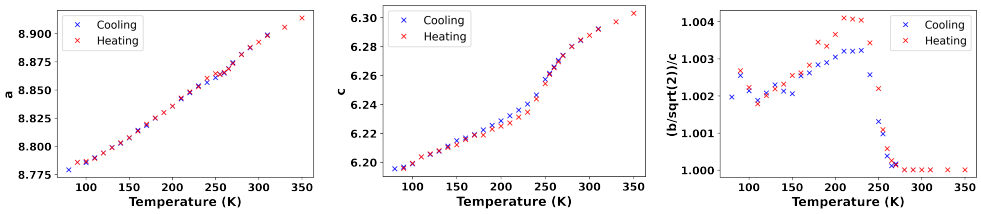

(b) Cs5 Set 22

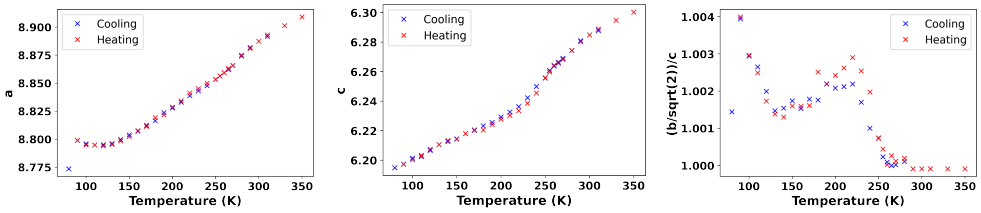

(c) Cs8 Set 22

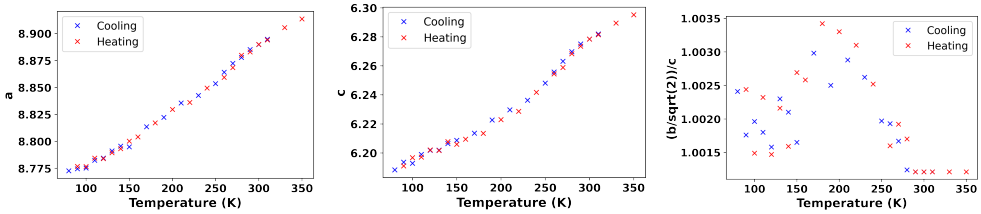

(d) Cs10 Set 22

Figure D.4: Lattice parameters (left) a, (middle) b, and (right) lattice parameter ratio for (a) Cs0, (b) Cs5, (c) Cs8, and (d) Cs10 refinement sets on cooling and heating. Lattice parameters are presented in Å.

Appendix E

Mixed PA/MA based lead bromide perovskites systems

Contents

E.1 Optical data for Chapter 9 . . . . . **325**

E.1.1 Photoluminescence measurements of: $(PABr)_{2x}(MABr)_{1-x}PbBr_2$ 325

E.2 Optical data reprocessed from literature for Chapter 9 . **327**

E.3 Additional XRD reference patterns and structures for Chapter 9 . . . . . **328**

E.3.1 List of structure database searches for organo-lead halides 328

E.3.2 Single-crystal structure of HOEABr 329

E.3.3 TOPAS rigid body for PA_2PbBr_4 model in Chapter 9 332

E.3.4 PA_2PbBr_4 structure file determined in Chapter 9 333

E.3.5 Additional reference pattern comparisons 334

E.3.6 Additional structures model visualisation 335

E.4 Additional optical data and diffraction patterns for Chapter 9 . . . . . **336**

E.4.1 Additional diffraction patterns of PABr on $MAPbBr_3$ 336

E.4.2 Ageing data on $(PABr)_{2x}(MABr)_{1-x}PbBr_2$ 338
E.5 The identification of a problematic diffraction pattern $x = 0.95$ of $(PABr)_{2x}(MABr)_{1-x}PbBr_2$ 9-step data-set. **341**
E.6 Reproducibility of $(PA)_2PbBr_4$ thin-films and the effect of short-term sample ageing **344**
E.7 Structure parameters of layered lead bromide perovskites **345**

E.1 Optical data for Chapter 9

E.1.1 Photoluminescence measurements of: $(PABr)_{2x}(MABr)_{1-x}PbBr_2$

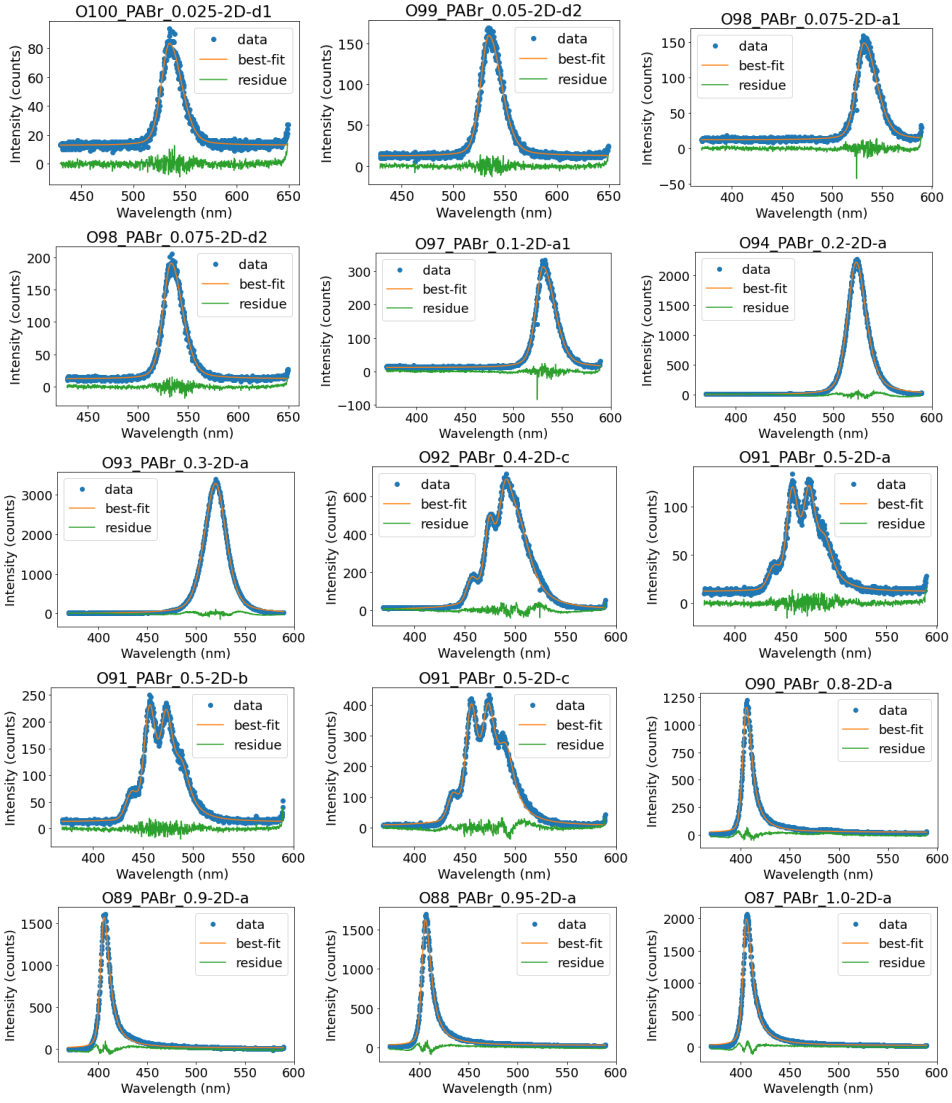

Figure E.1: Photo-luminescence measurements of $(PABr)_{2x}(MABr)_{1-x}PbBr_2$ modelled using split pseudo-Voigt functions for single peak patterns and multiple symmetric pseudo-Voigt functions for the deconvolution of multi-peak patterns. A combination of *least-square* and *Nelder* regression methods were utilised in the fitting.

E.2 Optical data reprocessed from literature for Chapter 9

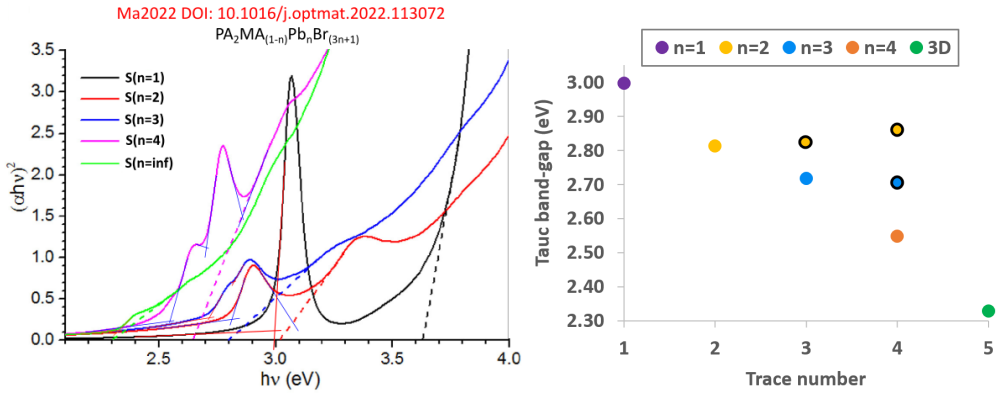

(a) (b)

Figure E.2: (a) Tauc plot modified from [Ma et al., 2022] with new intercepts drawn as solid lines using Inkscape, (b) Band-gaps extracted from Tauc intercepts.

Table E.1: Tauc plot band-gap values for a $(PA)_2(MA)_{1-n}Pb_nBr_{3+n}$ system derived from Figure E.2a using Inkscape and plotted with assignments in Figure E.2b.

Sample code	Trace	Peak number	Pixel tick (px) left	Pixel tick (px) right	Energy tick (eV) left	Energy tick (eV) right	Intercept (px)	Band-gap (eV)
S(n=1)	1	1	40.84	239.05	2.1	4.0	134.45	2.997
S(n=2)	2	1	40.84	239.05	2.1	4.0	115.30	2.814
S(n=2)	2	2	40.84	239.05	2.1	4.0		
S(n=3)	3	1	40.84	239.05	2.1	4.0	105.22	2.717
S(n=3)	3	2	40.84	239.05	2.1	4.0	116.35	2.824
S(n=3)	3	3	40.84	239.05	2.1	4.0		
S(n=4)	4	1	40.84	239.05	2.1	4.0	87.64	2.549
S(n=4)	4	2	40.84	239.05	2.1	4.0	103.90	2.704
S(n=4)	4	3	40.84	239.05	2.1	4.0	120.00	2.859
S(n=inf)	5	1	40.84	239.05	2.1	4.0	64.72	2.329

Figure E.2a was modified from [Ma et al., 2022] to better capture the multi-phase nature of the structure present in each sample they presented. Intercepts from the original literature figure are present as dashed lines with colours matching the trace they correspond to. New intercepts and background lines are drawn as red or blue solid lines as appropriate to ensure reasonable contrast. The pixel position of the intercepts are collected in Table E.1 with band gap values plotted in Figure E.2b where data points with ambiguity in the background determination are presented with a black boarder.

E.3 Additional XRD reference patterns and structures for Chapter 9

E.3.1 List of structure database searches for organo-lead halides

This section provides an incomplete list of structure database searches of the Crystallography Open Database (COD) and Inorganic Crystal Structure Database (ICSD) carried out in this work with a focus on structures for which direct comparisons were not available. [Gražulis et al., 2009, Hellenbrandt, 2004]

Propylammonium lead halide and 3-Bromopropylammonium lead bromide based structures

- Target: Propyl-ammonium lead bromide related structures.
  ICSD database,
  Elements: {Pb, Br, N, C}, excluding {D}
  number of elements: 4 to 5
  contains text "propyl"
  including "Experim. inorganic structures", "Experim. metal-organic str.", "Theoretical structures"
  Results: No relevant entries
- Target: Propyl-ammonium lead iodide related structures.
  ICSD database,
  Elements: {Pb, I, N, C}
  number of elements: 4 to 5
  contains text "propyl"
  including "Experim. inorganic structures", "Experim. metal-organic str.", "Theoretical structures"
  Results: No entries
- Target: Propyl-ammonium lead iodide related structures.
  COD database,
  Elements: {Pb, I, N, C}, excluding {D}
  number of elements: 4 to 5
  contains text "propyl"
  including theoretical structures
  Results: $n = 3$ and $n = 4$ structures by [Hoffman et al., 2019]. Various structures of mixed corner and face sharing octahedra connectivity.

E.3.2 Single-crystal structure of HOEABr

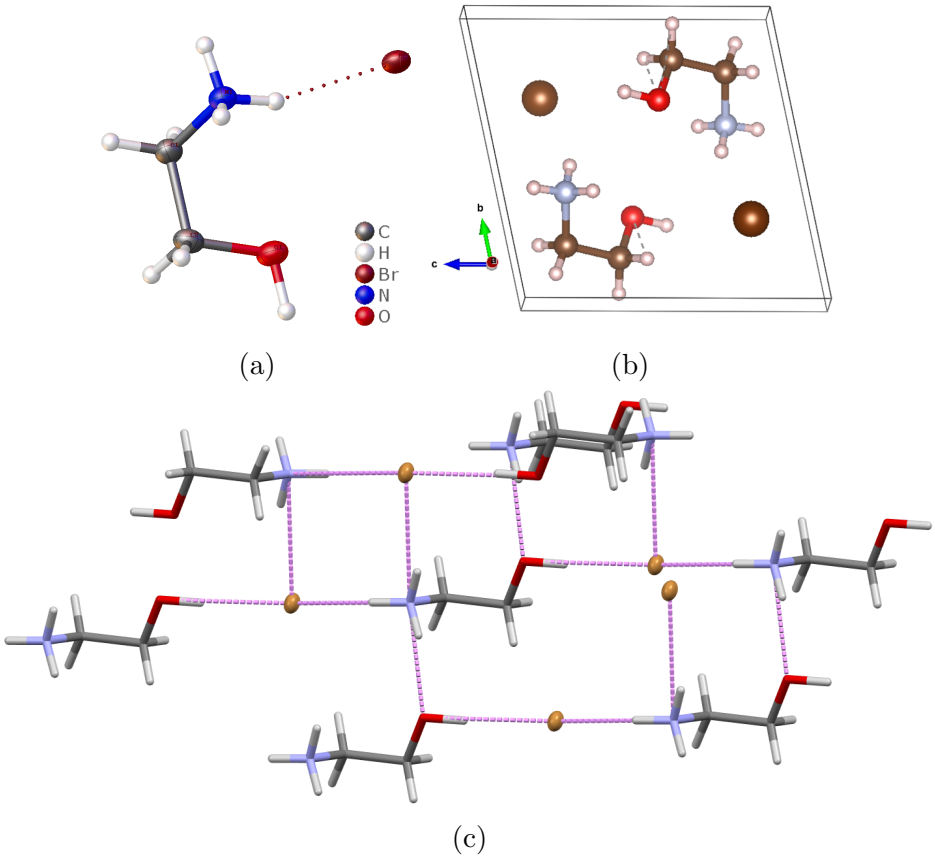

Figure E.3: Single-crystal XRD derived structure of HOEABr (a) motif, (b) packed unit cell, (c) hydrogen bond. (blue) nitrogen, (red) oxygen, (white) hydrogen.

Single crystals of $HO(CH_2)_2NH_2 \cdot HBr$, (HOEABr) were prepared for single crystal diffraction. A suitable crystal was selected from the synthesis HOEABr. These were mounted on a loop type goniometer head on a Bruker D8 Venture Bio PHOTON III 28 pixel array area detector (208×128 mm^2) diffractometer with a Mo Kα IμS DIAMOND source (50 kV, 1.4 mA). The crystal was cooled to and measured at 173.0 K during data collection. The collection method involved ω- and ϕ-scans, and 1536×1024 bit data frames. The unit cell and full data set were collected using APEX4 [Bruker, 2021]

; SAINT was used to integrate the data, and SADABS was used to make empirical absorption corrections and scale the data. Space group assignments were made using XPREP on all compounds. Using Olex2 [Dolomanov et al., 2009], the structure was solved with the SHELXT [Sheldrick, 2015b] structure solution program using Intrinsic Phasing and refined with the SHELXL [Sheldrick, 2015a] refinement package using Least Squares minimisation. Non-hydrogen atoms were first refined isotropically followed by anisotropic refinement by full matrix least-squares calculations based on F^2. The crystal structure is displayed in Figure E.3 with the crystal data that follows:

> **Crystal Data:** $C_4H_{16}Br_2N_2O_2$ (M =284.01 g/mol): triclinic, space group P-1 (no. 2), a = 4.4654(3) Å, b = 7.5370(6) Å, c = 7.6781(5) Å, α = 77.535(3)°, β = 87.828(3)°, γ = 77.434(3)°, V = 246.27(3) Å^3, Z = 1, T = 173.00 K, μ(MoKα) = 8.186 mm^{-1}, Dcalc = 1.915 g/cm^3, 8044 reflections measured (5.434° $\leq 2\theta \leq$ 56.606°), 1197 unique (Rint = 0.0707, Rsigma = 0.0493) which were used in all calculations. The final R1 was 0.0388 (I > 2σ(I)) and wR2 was 0.1071 (all data).

This structure forms a triclinic unit cell with inversion symmetry as seen in Figure E.3b. The organic molecule and halide from hydrogen bonds between Br−OH, Br−NH_3, and NH_3−OH pairs which are shown with a turquoise lines in Figure E.3. The shortest interatomic distances between these pairs, neglecting hydrogen is 3.233 Å, 3.326 Å and 2.869 Å. The N-H and O-H bond lengths are 0.91 and 0.97(6) Å respectively which informs on the extent to which the H is offset from the N or O atoms. Using distance between atoms as an indicator of bond strength, we see notice relatively strong NH_3−OH hydrogen bonding which reflected in the formation of a dimer in the structure of $(HOEA)_2PbBr_4$, COD 4312212, Figure E.4. [1]

[1]The formation of additional hydrogen bonds is detailed in Figure 2 of Mercer *et al.* [Mercier et al., 2004]

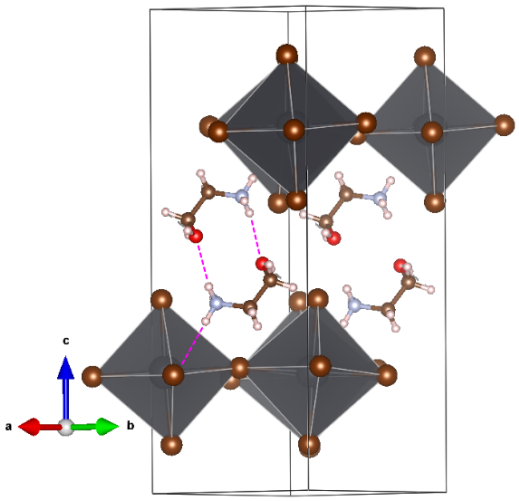

Figure E.4: Literature structure of $(HOEA)_2PbBr_4$, COD 4312212 with selected hydrogen bonds shown by purple lines.

E.3.3 TOPAS rigid body for PA_2PbBr_4 model in Chapter 9

The following code snippet is from a TOPAS-Academic Rietveld refinement used for the modelling of PA_2PbBr_4, specifically *refinement set 3, revision 2*. The model was used on a PA_2PbBr_4 powder sample prepared from thin-films using the measured diffraction pattern `d2_2019_1549.raw`.

```
prm Oh1 -0.0465411837‘_1.72529335 min -5 max 5
prm Oh2 -5.74012564‘_1.19387832 min -6 max 5
prm Oh3  14.7411252‘_0.539389728 min 0 max 30
prm del1  0.03‘_4.24374075 min -0.03 max 0.03
prm rPbX  3.00889116‘_0.023515021 min 2.7 max 3.05
prm rPbX2 = rPbX + del1 ;:3.03889116‘_4.2438059
rigid
  load z_matrix {
  Pb1
  Br1 Pb1 = rPbX;
  Br2 Pb1 = rPbX2; Br1 @  84.55266‘_3.52343 min 83 max 97
  }
  Rotate_about_axies( =Oh1; , =Oh2; , =Oh3-45;)
  Translate( 0.5,0.5,0.5)

rigid ’ Using PA+ from Meresse1989 (PA)2PbCl4, layered n=1 structure
    load z_matrix {
        C1
        C2 C1 1.5327
        N1 C1 1.4744  C2 110.687
        C3 C2 1.5211  C1 110.701 N1 179.887
    }
    Rotate_about_axies( @ -4.55770‘_11.65468 min -30 max 30,
                        @  142.82010‘_6.69802 min 140 max 190 ,
                        @  20.00000‘_53.73271 min 20 max 35)
    Translate( @ -0.07674‘_0.02498 min -0.1 max 0.1,
               @  0.50711‘_0.07173 min 0.46 max 0.54,
               @  0.35433‘_0.00431 min 0.29 max 0.42 )

AI_Anti_Bump(Pb*, N*, 4.28, 10)
```

E.3.4 PA_2PbBr_4 structure file determined in Chapter 9

The structures of the PA_2PbBr_4 phases were identified and modelled in Section 9.2. The refinement was executed on a PA_2PbBr_4 powder sample prepared from thin-films using the measured diffraction pattern `d2_2019_1549.raw`. The structure file (.cif) is provided below from *refinement set 3, revision 2*.

```
data_
_chemical_name_mineral ?(PA)2PbBr4 SG:Pbca?
_cell_length_a 8.152(3)
_cell_length_b 8.255(3)
_cell_length_c 25.092(9)
_cell_angle_alpha 90
_cell_angle_beta 90
_cell_angle_gamma 90
_cell_volume 1688.6(11)
_symmetry_space_group_name_H-M Pbca
loop_
        _symmetry_equiv_pos_as_xyz
         'x, y, z '
         '-x, y+1/2, -z+1/2 '
         '-x+1/2, -y, z+1/2 '
         '-x+1/2, y+1/2, z '
         'x, -y+1/2, z+1/2 '
         '-x, -y, -z '
         'x+1/2, -y+1/2, -z '
         'x+1/2, y, -z+1/2 '
loop_
_atom_site_label
_atom_site_type_symbol
_atom_site_site_symmetry_multiplicity
_atom_site_fract_x
_atom_site_fract_y
_atom_site_fract_z
_atom_site_occupancy
_atom_site_B_iso_or_equiv
Pb1 Pb   4 0.5 0.5 0.5 1 2.796
Br2 Br   8 0.185(8) 0.686(6) 0.500(9) 1 4.227
Br1 Br   8 0.476(12) 0.515(13) 0.6179(12) 1 4.227
N1 N   8 0.01(5) 0.54(7) 0.412(8) 1 5(14)
C1 C   8 -0.07(4) 0.50(5) 0.361(6) 1 3(6)
C2 C   8 0.05(5) 0.50(11) 0.315(10) 1 3(6)
C3 C   8 -0.03(7) 0.46(9) 0.263(7) 1 3(6)
```

E.3.5 Additional reference pattern comparisons

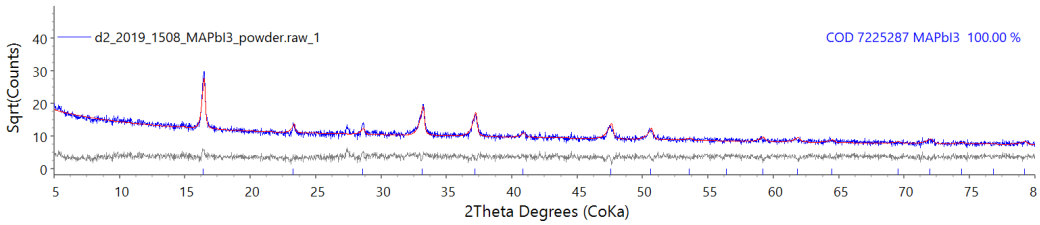

Figure E.5: X-ray diffraction pattern refinement of an $MAPbI_3$ sample prepared from thin-film samples.

An X-ray diffraction pattern for the $MAPbI_3$ phase is refined against the COD 7225287 literature pattern in Figure E.5 using a fundamental parameters based instrument profile. The powder sample was prepared from multiple thin-film samples which were scraped using a steel razor blade onto a silicon zero-background sample holder for measurement. The starting model was defined as the literature structure COD 7225287 of $MAPbI_3$ in the $Pm\bar{3}m$ space group. The cubic unit cell parameter was refined to 6.275 $\pm$ 0.001 Å compared to the literature value 6.272 Å which is a small difference in this context. Thermal parameters were kept to the literature values for a Goodness of Fit (χ) of 1.156 which is close to 1 thus indicative of a reasonable fit, χ defined in Section 3.4.

E.3.6 Additional structures model visualisation

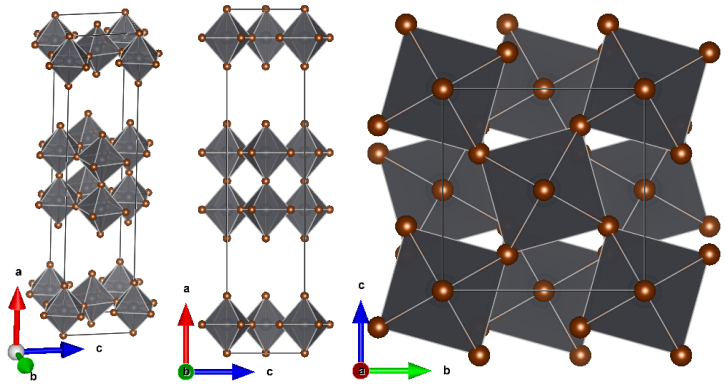

(a) (b) (c)

Figure E.6: XRD structure model of a Pb-Br framework of the layered $n = 2$ phase after reduction to an equivalent model in a *Cmce* space group using ISOCIF [Stokes et al., 2017].

E.4 Additional optical data and diffraction patterns for Chapter 9

E.4.1 Additional diffraction patterns of PABr on $MAPbBr_3$

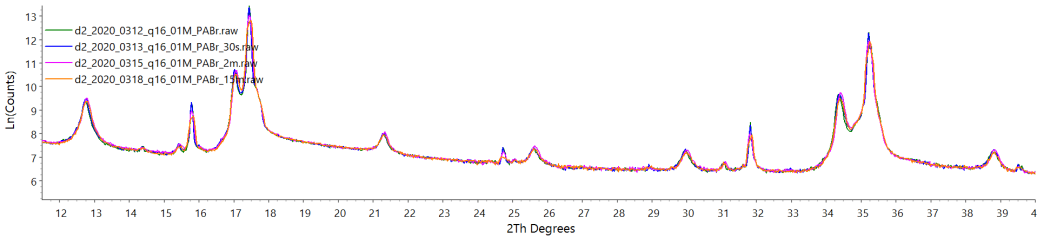

(a) 0.1M PABr on $MAPbBr_3$, plotted with a natural logarithm scale. This shows a slight broadening of the $MAPbBr_3$ phase seen in the (200) peak at 35.3° 2θ

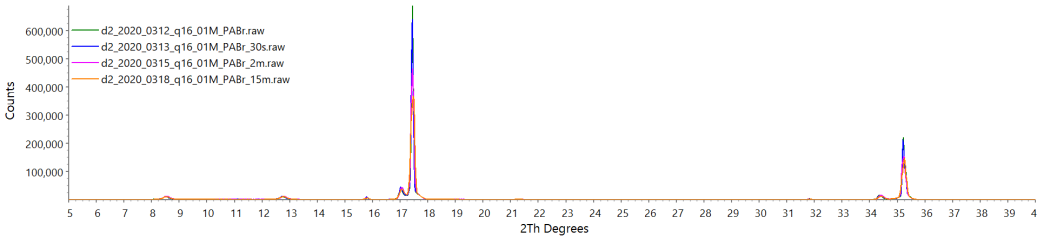

(b) 0.1M PABr on $MAPbBr_3$, plotted on a linear scale. This shows a gradual decrease in the $MAPbBr_3$ phase intensity with no significant differences in the $n = 3$ phase.

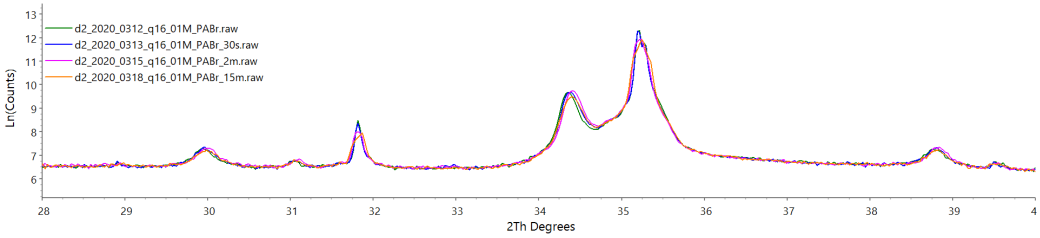

(c) 0.1M PABr on $MAPbBr_3$, plotted with a natural logarithm scale, This plot shows a slight peak shift in the $n = 3$ phase peak at 34.4° 2θ to higher angles (smaller d-spacing) with annealing. This could be due to an effect such as strain relaxation. This data in not corrected for peak shifts due to sample displacement as such this was consider against the stability of the $MAPbBr_3$ (200) peak at 35.3° 2θ.

Figure E.7: PABr on $MAPbBr_3$

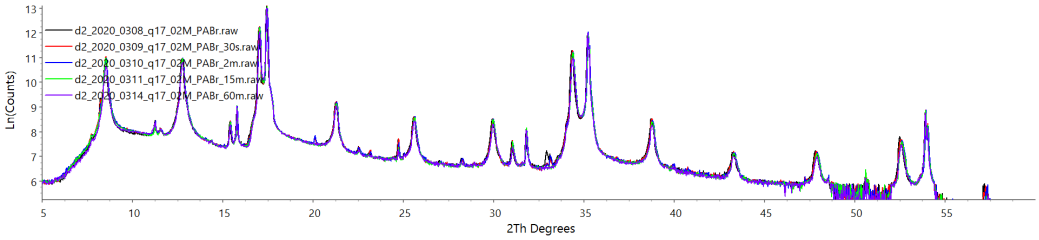

(a) 0.2M PABr on $MAPbBr_3$, plotted with a natural logarithm scale

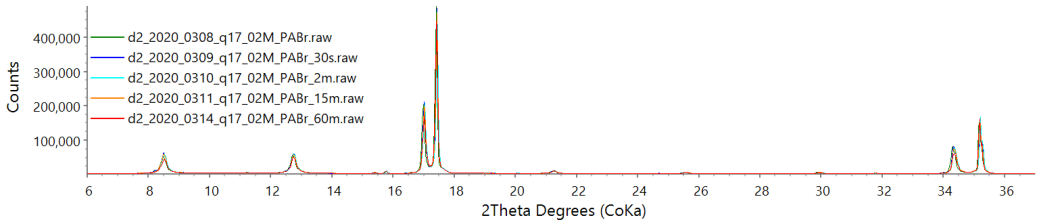

(b) 0.2M PABr on $MAPbBr_3$, plotted with a linear intensity scale

Figure E.8: PABr on $MAPbBr_3$

Figure E.9 presents micro-strain and crystallite size broadening parameters for the PABr on $MAPbBr_3$ refinements of Section 9.4. Figures E.9a and E.9b show the effect of including strain in the diffraction pattern refinements. A small consistent increase in crystallite size is noted for the 0.1 M, $n = 3$ phase, with a slightly larger effect for the 0.2 M $n = 3$ sample. This could be an indication of the crystallite size broadening partially compensating for any micro-strain broadening present. The "perov" phase shows a less consistent trend especially for the 0 and 0.5 min diffraction patterns.

Figures E.9c and E.9d present micro-strain and crystallite size where the former has a notable trend in micro-strain for the "perov" phase, while the latter does not. This variation between the similar systems may relate to correlation between the micro-strain and crystallite size parameter or may reflect the sample characteristics. Additionally, it is strange for the "perov" phase to exhibit increased strain with annealing for the 0.1 M variant where a lower concentration of the PABr salt is present with less of an effect for the higher concentration 0.2 M variant. For these reasons the micro-strain on the "perov" phase is considered unreliable in this system, while effect of modelling micro-strain on the crystallite size parameter for the $n = 3$ phase is smaller and more consistent allowing for its consideration.

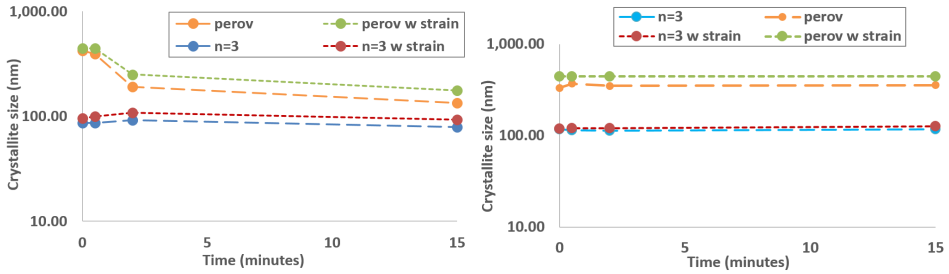

(a) 0.1 M PABr solution

(b) 0.2 M PABr solution

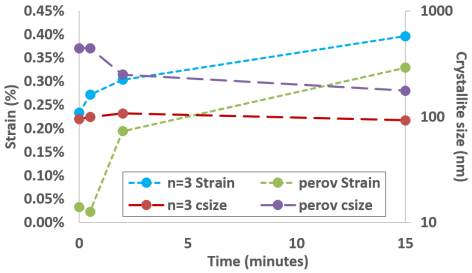

(c) 0.1 M PABr solution

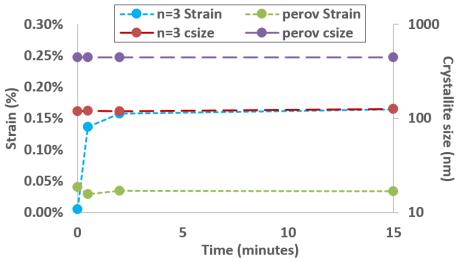

(d) 0.2 M PABr solution

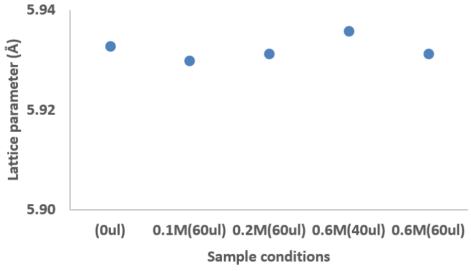

(e) $MAPbBr_3$ lattice parameter

Figure E.9: Diffraction derived micro-strain and crystallite size parameters of PABr on $MAPbBr_3$ samples. (a,b) "w strain" are parameter values with micro-strain and the adjacent traces without micro-strain modelled in the refinement, (c,d) crystallite size and micro-strain refined parameters with each figure referring to a set with identical refinement considerations, (e) $MAPbBr_3$ lattice parameter for PABr coating of different molar concentrations using a volume (X μl) of 0.X M solution.

E.4.2 Ageing data on $(PABr)_{2x}(MABr)_{1-x}PbBr_2$

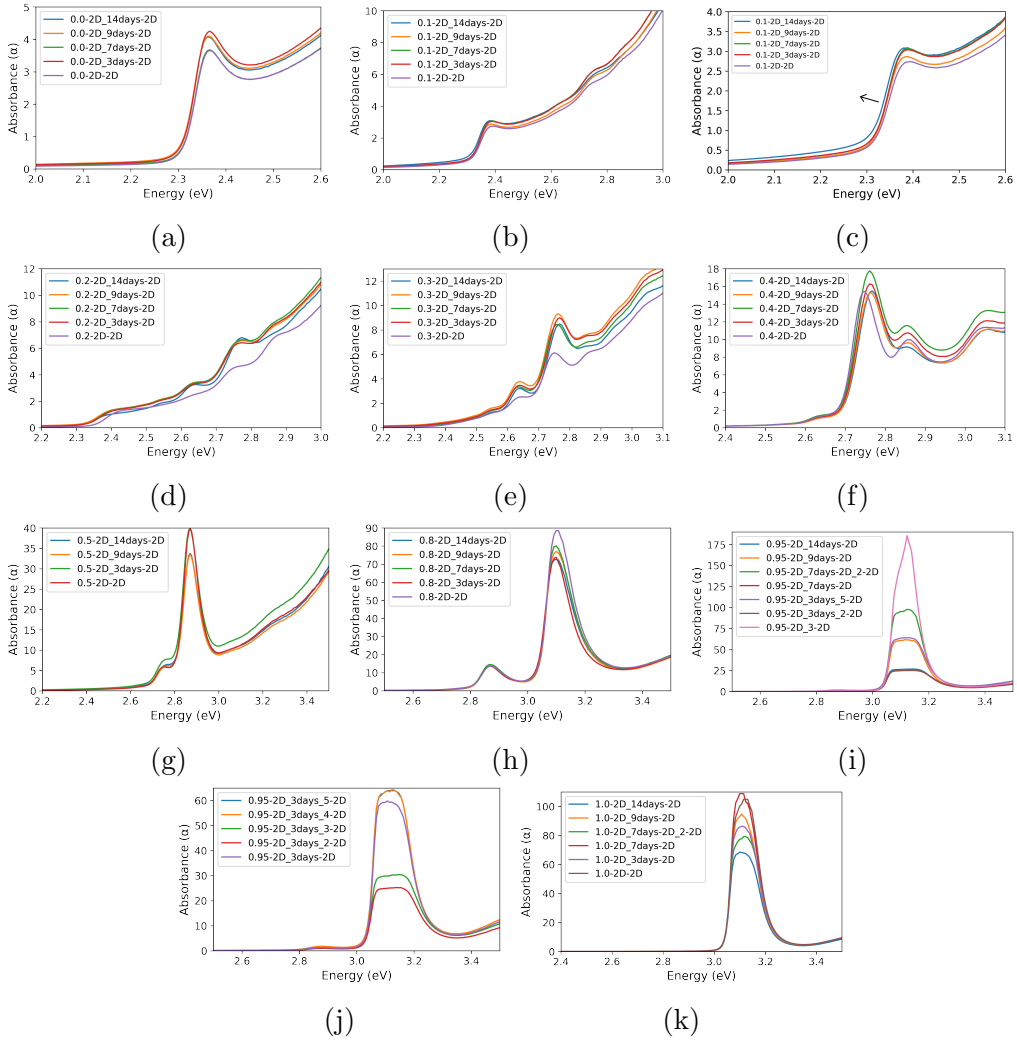

Figure E.10: Ageing of $(PABr)_{2x}(MABr)_{1-x}PbBr_2$, optical absorption data over 14 days.

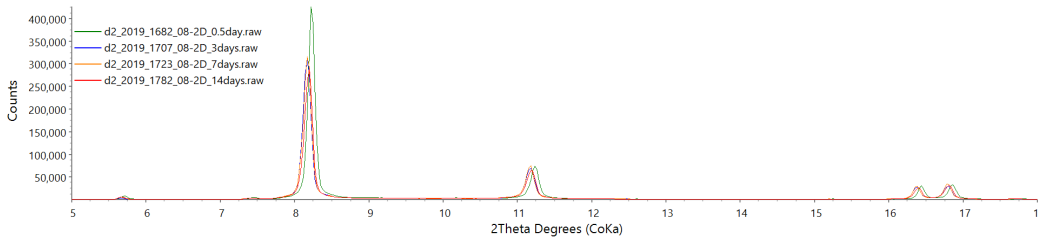

Figure E.11: Ageing of $(PABr)_{2x}(MABr)_{1-x}PbBr_2$, $x = 0.8$, X-ray diffraction patterns over 14 days.

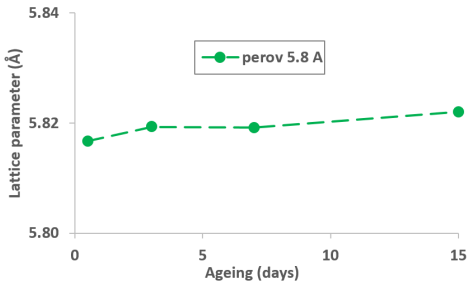

(a)

Figure E.12: Interplanar spacing of the "perov 5.8 A" phase of $(PABr)_{2x}(MABr)_{1-x}PbBr_2$, $x = 0.8$, aged over 15 days. As a "perov 5.8 A" rather then a "perov 5.9 A" phase, this is considered a quasi-2D phase with a large n value as discussed in Section 9.3.1.

E.5 The identification of a problematic diffraction pattern

$x = 0.95$ of $(PABr)_{2x}(MABr)_{1-x}PbBr_2$ 9-step data-set.

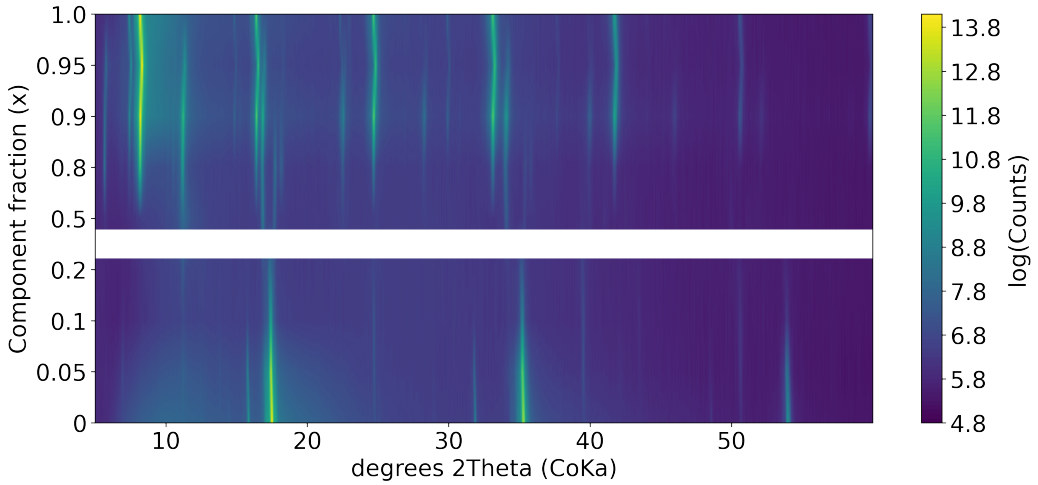

Figure E.13: $(PABr)_{2x}(MABr)_{1-x}PbBr_2$, (9-step data-set, including $x = 0.95$) this data set was collected to 80° 2θ and plotted to 60° 2θ.

Table E.2: Sample displacement correction parameters for 9- and 13-step $(PABr)_{2x}(MABr)_{1-x}PbBr_2$ data-sets in millimetres.

13-step		13-step		9-step			
x	**disp.**	**x**	**disp.**	**x**	**disp.**	**stat**	**value**
0.00	-0.060	0.40	-0.048	0.00	-0.105	**9-step**	
0.025	-0.041	0.50	0.000	0.05	-0.064	mean	-0.063
0.05	-0.055	0.80	-0.058	0.10	-0.058	st. dev.	0.031
0.075	-0.027	0.90	-0.034	0.20	-0.026	min	-0.122
0.10	-0.049	0.95	-0.036	0.50	-0.053		
0.20	-0.033	1.00	-0.042	0.80	-0.041	**13 step**	
0.30	-0.068			0.90	-0.054	mean	-0.042
				0.95	-0.122	st. dev.	0.018
				1.00	-0.044	min	-0.068

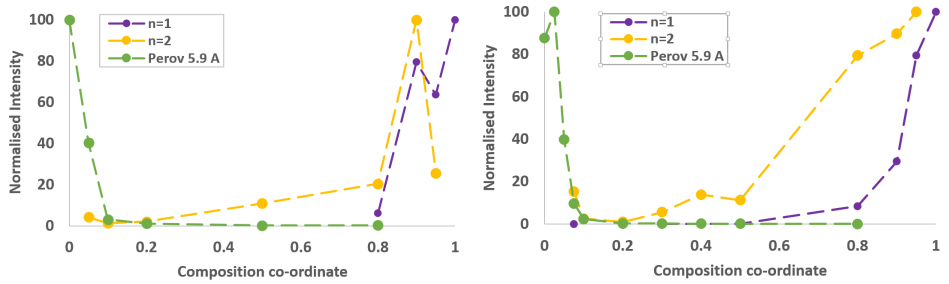

(a) 9-step

(b) 13-step

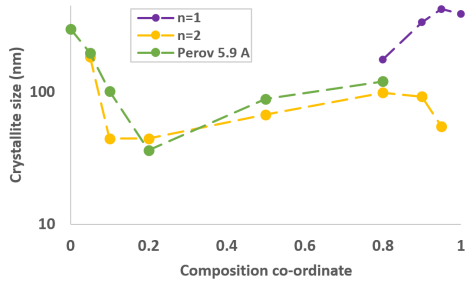

(c) 9-step

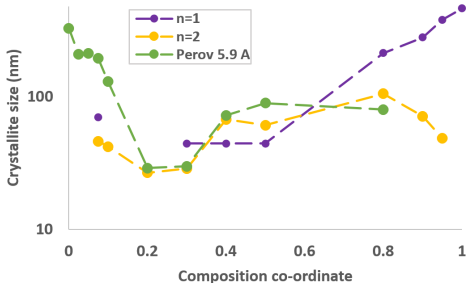

(d) 13-step

Figure E.14: Diffraction derived unit cell parameters and normalised peak intensities of $(PABr)_{2x}(MABr)_{1-x}PbBr_2$, both 9 and 13 step data-sets.

The first major difference between the two data-sets is the simultaneous intensity drop of both the $n = 1$ and $n = 2$ phases at $x = 0.95$ present in the 9-step and not observed in the 13 step data-sets. This is accompanied by a large refined sample displacement parameter of -0.122 mm compared to the mean values of -0.063 (σ 0.031) and -0.042 (σ 0.018) mm for the 9- and 13-step data sets respectively, Table E.2. The peak shifts which the sample displacement describes is noticeable in SI Figure E.13 where there is a shift to a higher angle for the peaks of $x = 0.95$.

The sample are in the form of 12.5 by 12.5 mm coated glass substrates mounted in the sample holder using modelling putty. As this putty heats during measurement it softens, if the sample is placed off-centre on a pillar of putty a possibility of sample tilt may arise. In a powder sample, a degree peak broadening would be expected with sample tilt due to the presence of gradient of sample displacement and corresponding peak shifts. In a highly orientated sample such as a single crystal or highly orientated thin-films, this can result in a portion of the peak accessible in the reciprocal space probed

by the instrument configuration, reducing both peak width and intensity. A comparison of SI Figures E.14c and E.14d, the 9-step data-set shows a maximum in crystallite size for $n = 1$ at $x = 0.95$ and the value for $n = 2$ is higher than that in the 13-step data-set. Along with the simultaneous intensity drop is attributed to sample placement during measurement, the $x = 0.95$ diffraction pattern of the 9-step data-set is considered an outlier with measurement conditions the most likely cause.

On this basis, the $x = 0.95$ diffraction pattern of the $(PAI)_{2x}(MAI)_{1-x}PbI_2$ 9-step data-set is not considered in Section 9.3

E.6 Reproducibility of $(PA)_2PbBr_4$ thin-films and the effect of short-term sample ageing

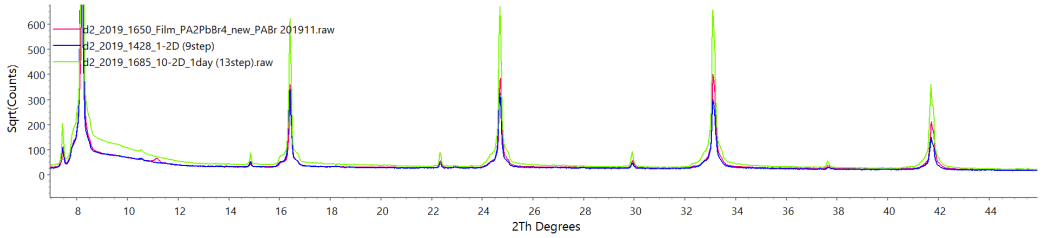

Figure E.15: PA_2PbBr_4 thin-films prior to ageing.

SI Figure E.15 presents PA_2PbBr_4 thin-films produced from a precursor solution of 1.2 M PABr and 0.6 M $PbBr_2$. Spin-coated at 2000 rpm over 60 s, from 60 μl of precursor followed by 100 μl of ethyl-acetate anti-solvent. Annealed at 90 °C under N_2 gas (hotplate set to 135)

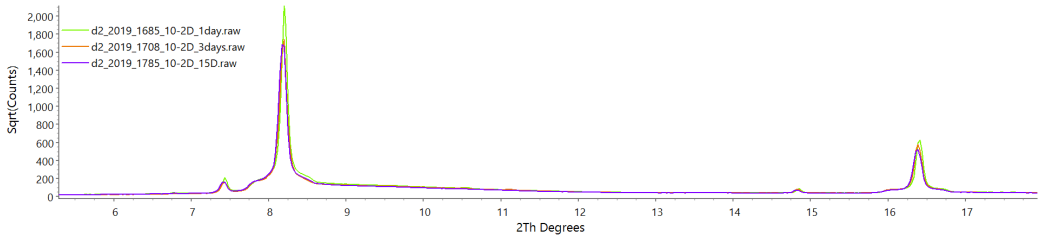

Figure E.16: PA_2PbBr_4 thin-films measured after 1, 3 and 15 days.

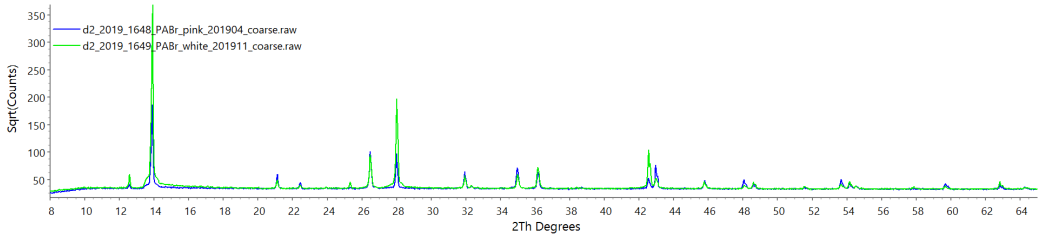

Figure E.17: PABr salts, where older salt has a pink tint. (white) fresh, (pink) aged in a desiccator.

E.7 Structure parameters of layered lead bromide perovskites

Table E.3: Structural parameters of $(A')_2A_{n-1}Pb_nBr_{3n+1}$ and $APbBr_3$ perovskites.

Organic layer (A')	**A site (A)**	(n)	**Space Group**	**a (Å)**	**b (Å)**	**c (Å)**	β (^{c}irc)	**n*Oh+ Organic**	**Organic spacing**	**Temp. (K)**	**Reference**
-	MA^+	3D	$Pm\bar{3}m$	5.920	5.920	5.920	90	-	-	294	COD 1545320
-	MA^+	3D	$Pm\bar{3}m$	5.997	5.997	5.997	90	-	-	293	COD 7130785
EA^+	-	n=1	$P2_1/c$	11.755	8.237	8.170	108.9	11.755	5.321	298	COD 1554139
EA^+	EA^+	n=3	$C2ce$	8.427	46.351	8.430	90	23.176	5.192	293	ICSD 254262
PA^+	-	n=1	$Pbca$	8.152	8.257	25.096	90	12.548	6.630	293	This work
PA^+	MA^+	n=2	$Cmce$	36.753	8.312	8.312	90	18.376	*6.541*	293	This work
BA^+	-	n=1	$Pbca$	8.334	8.223	27.617	90	13.809	7.817	298	COD 1545801
BA^+	MA^+	n=2	$Ccc2$	8.326	39.247	8.363	90	19.624	7.683	297	COD 8000498
BA^+	FA^+	n=2	$Cmc2_1$	38.910	8.446	8.342	90	19.455	7.515	293	ICSD 263594
$PentylA^+$	MA^+	n=2	$P1$	8.325	42.717	8.325	90	21.359	9.441	297	COD 8000499

Italics: The organic spacing for the $(PA)_2MAPb_2Br_7$ $n = 2$ structure is calculated using octahedra dimensions of the $(PA)_2PbBr_4$ $n = 1$ phase.

The "*n*Oh + organic*" values in Table E.3 refer to the length of n layers of octahedra, with a single organic layer. This is derived from the unit cell parameters, and corrects for the angles of the monoclinic unit-cells where applicable. In Table E.3, the "organic spacing" values are calculated from unit cell parameter and halide fractional co-ordinates, to represent the spacing between the octahedra layers.

Appendix F

Python code

F.1 Sequential refinement process

Sequential refinements were performed preparing a single manually run refinement to be used as the first input file. An array of file names called *files* generated containing the location and order of the diffraction patterns to be run. This was passed to the code below with the manually refined input file. The array of files was iterated through by the *Python* script using the output of the nth refinement as the input of the $(n+1)^{\text{th}}$.

```
import subprocess, os.path

def Topasxdd(infile, rawname):
    array2 = []
    with open(infile, "r") as ins:
        for line in ins:
            #assumes no spaces before "xdd", else .strip can be used
            cifspace = line.find("Out_CIF_STR(")
            fcfspace = line.find("Out_FCF(")
            if line[0:4] == 'xdd ':
                array2.append('xdd "'+rawname+'"\n')
            elif line.strip()[0:7] == "xdd_out":
                line[0:line.find("xdd_out")-1]
                array2.append(line[0:line.find("xdd_out")]+"xdd_out " +
                                        rawname[0:len(rawname)-nEXT] +
                                        "txt load out_record out_fmt out_eqn
    \n")
            elif cifspace > -1:
                array2.append(line[0:cifspace]+'Out_CIF_STR(" ' +
```

```
                                        rawname[0:len(rawname)-nEXT] + 'cif
    ")\n')
            elif fcfspace > -1:
                array2.append(line[0:fcfspace]+'Out_FCF(" ' +
                                        rawname[0:len(rawname)-nEXT] + 'fcf
    ")\n')
            else:
                array2.append(line)

    # Write input file
    file2t = rawname[0:len(rawname)-nEXT]+"inp"
    fileout = open(file2t,"w")
    for i in array2:
        fileout.write(i)
    fileout.close()

# Call Topasxdd for all files in the "files" array.
for i in range(0, len(files)):
    Topasxdd(filein, files[i])
    lenfile = len(files[i])

    subprocess.run("C:\\Topas-6\\tc.exe "+files[i][0:lenfile-nEXT]+"inp")

    filein = files[i][0:lenfile-nEXT]+"out"
      # Wait for refinement to finish
    t1 = 2
    while os.path.exists(filein) == False:
        time.sleep(t1)
        if t1 == 2:
            t1 = 5
        elif t1 < 300:
            t1 = 2*t1
        else:
            break
        print("waiting for topas .out file creation trying in (s): "+str(t1)
    )
```

F.2 Parametric refinement input generation

For each parametric refinement, a template input file was processed to generate the input file. An example of the template is given in Appendix Section F.2.1 with the *Python* script in Section F.2.2. For this Sections 2 and 3 of the template are expanded to reflect the full data-set by the *Python* script in Appendix Section F.2.2.

Section 1 of the template includes the creation of a file *"paraPrep.txt"* which is appended to with important parameters from each individual diffrac-

tion pattern in the refinement through the append statement *out "paraPrep.txt" append* in Section 3. Global parameters are defined in Section 4. The instrument profile is described in Section 5. Section 6 is a list of an external parameter (temperature) for the data-set, accessible through an index. The list in Section 6 has been abridged for presentation.

F.2.1 Input file template

```
'==========
'==Section 1
'==========
r_exp 10.8001 r_wp 14.87402 weighted_Durbin_Watson 1.102601 gof  1.377206
iters 200
conserve_memory
'do_errors
#define param_cell

out "paraPrep.txt" append
Out_String("Scan  Temp(C)  a  c  Beq1_Pb  Beq2_I  Beq4_FA  p1
    Pb-I-Pb_angle  (b/sqrt(2))/c  Pb-I_bond_length(ab-plane)  R_wp")

'==========
'==Section 2
'==========

#define use_XXXXX  macro filename_XXXXX {C:/rest-of-path/Cs10FAMA/XXindexXX}
     prm !XXXXX temp(XXindex-1XX) macro r_XXXXX {XXindexXX}

'==========
'==Section 3
'==========

#ifdef use_XXXXX
    RAW(filename_XXXXX)
    bkg @ -40.5148107`  46.3438003`  4.18924747`  -3.44735432`
    One_on_X(@, 1898.09412`)
    Zero_Error(@, -0.01651` min -0.1 max 0.1)

    xo_Is
        xo @  22.0219032`_LIMIT_MIN_21 min =21; max =23.5;
        LVol_FWHM_CS_G_L( 1, 0.53598`, 0.89, 0.74930`,,,@, 0.84191` min 0.01
     max 5)
        I @  9954.34873`

    str
        r_bragg  13.0257476
        phase_MAC  265.751406
        phase_name "Pba2-P1"
        MMW( 1281.308, 499.179`, 100.000`)
        space_group P1
        Phase_LAC_1_on_cm( 1132.71916`)
        Phase_Density_g_on_cm3( 4.26233`)
```

```
    scale @  0.000953427262‘

    local !m_b1 0.5
    local m_b2 1 min 0.5 max 15
    local !m_b4 30

    local mlpa = valA(XXindex-1XX); min 8 max 10
    local mlpc = valC(XXindex-1XX); min 5.5 max 7.5
    local !ratioCurr = (mlpa/(Get(c)*(2^(0.5))));: 0

    a = mlpa;:8.901840‘
    b = mlpa;:8.901840‘
    c = If(XXXXX >= Ttrans2, (mlpa/(2^(0.5)))/ratioHi, mlpc);:6.299362‘
    penalty = If(XXXXX < Ttrans2, If(ratioHi > ratioCurr, ((ratioHi-
ratioCurr)*1000000),0),0);:0

    al = 90;
    be = 90;
    ga = 90;

    local b1 = m_b1;: 0.50000
    local b2 = m_b2;: 1.46395
    local b4 = m_b4;: 10.00000

    ' I position
    local p1_free 0.00681‘_LIMIT_MIN_-0.0001 min -0.0001 max 0.15
      ' In the following polynomial, values are scaled to
      '   prevent parameters being truncated to 0 in the
      '   output file.
    local !p1_mid = (p1_a*(XXXXX^4)*0.000000000001) +
                    (p1_b*(XXXXX^3)*0.000000001) +
                    (p1_c*(XXXXX^2)*0.000001) +
                    (p1_d*XXXXX*0.001) + p1_e ;: 0
    local !p1 = If(XXXXX >= 82, If(XXXXX >= Ttrans2, p1hi, If(XXXXX >=
Ttrans3, p1_free, p1_mid)), p1_free);: 0

    site Pb1a occ Pb+2  1 beq = b1; x = 0; y = 0; z = 0;
    site Pb2a occ Pb+2  1 beq = b1; x = 0.5; y = 0.5; z = 0;

    site I1 occ I-1  0.85 beq = b2; occ Br-1 0.15 beq = b2;
                       x = 0.25 + p1; y = 0.25 - p1; z = 0;
    site I2 occ I-1  0.85 beq = b2; occ Br-1 0.15 beq = b2;
                       x = 0.75 + p1; y = 0.25 + p1; z = 0;
    site I3 occ I-1  0.85 beq = b2; occ Br-1 0.15 beq = b2;
              x 0.0 min -0.1 max 0.1 y 0.0 min -0.1 max 0.1
              z 0.5 min 0.4 max 0.6
    site I4 occ I-1  0.85 beq = b2; occ Br-1 0.15 beq = b2;
                       x = 0.75 - p1; y = 0.75 + p1; z = 0;
    site I5 occ I-1  0.85 beq = b2; occ Br-1 0.15 beq = b2;
                       x = 0.25 - p1; y = 0.75 - p1; z = 0;
    site I6 occ I-1  0.85 beq = b2; occ Br-1 0.15 beq = b2;
                x 0.5 min 0.4 max 0.6 y 0.5 min 0.4 max 0.6
                z 0.5 min 0.4 max 0.6

    ' occupancy set for 5% Cs+ 95% FA+
    ' Electrons for (FA0.85 MA0.15)1-x Csx mixes
    ' Mn = 25
```

```
        ' x=0.05: 25.65 = Mn1.026
        ' x=0.08: 26.57 = Mn1.063
        ' x=0.10: 27.19 = Mn1.088

        site FA1 x 00 y  0.5 z  0.5 occ Mn  1.088 beq = b4;
        site FA2 x 0.5 y 0.0 z  0.5 occ Mn  1.088 beq = b4;

        local !ratio = (Get(a)/(2^0.5))/Get(c) ;
        local !bondPbI = (2*(Get(a)^2)*(0.25^2 + (p1^2)))^0.5; 'PbI bond
    length in the ab plane
        local !angle = 180 - (Rad*ArcCos(((0.25+p1)*(0.25-p1)*2)/((0.25+p1)
    ^2+(0.25-p1)^2)));
        out "paraPrep.txt" append
            Out_String("\nXXXXX")
            Out(XXXXX, " %11.5f")
            Out(Get(a), " %11.5f")
            Out(Get(c), " %11.5f")
            Out(b1, " %11.5f")
            Out(b2, " %11.5f")
            Out(b4, " %11.5f")
            Out(p1, " %11.5f")
            Out(angle, " %11.5f")
            Out(ratio, " %11.5f")
            Out(bondPbI, " %11.5f")
            Out(Get (r_wp), " %11.5f")

       Out_CIF_STR("XXindexXX.cif")

        xdd_out XXindexXX.txt load out_record out_fmt out_eqn
      {
       "%15.6f" = X;
       "%15.6f" = (4*Pi/Lam)*Sin((X/2)*Pi/180);
       "%15.6f" = Yobs;
       "%15.6f\n" = Ycalc;
       }
       'Out_FCF("C:/GDrive/PhD/Duties/Collabs_and_routine/
    Sheffield201907Claire/Cs5FAMA/XXindexXX.fcf")

#endif 'XXflagXX

'==========
'==Section 4
'==========
#ifdef param_cell
    prm !Ttrans2 283
    prm !Ttrans3 265
    prm p1hi 0 min 0 max 0.15
    prm ratioHi 1 min -0.95 max 1.05 ' This is to have a common ratio for
    the high temp phase

    prm p1_a -55.8903505 min -80 max -20 'x10^-12
    prm p1_b 37.7252191 min 10 max 70 'x10^-9
    prm p1_c -9.49571561 min -20 max 0 'x10^-6
    prm p1_d 0.991839192 min -2 max 10'x10^-3
    prm p1_e 0.00832115106 min -0.1 max 5 'x10^0
#endif
```

```
'==========
'==Section 5
'==========

for xdds {
    lam
        ymin_on_ymax  0.0001
        la  0.0159 lo  1.534753 lh  3.6854
        la  0.5691 lo  1.540596 lh  0.437
        la  0.0762 lo  1.541058 lh  0.6
        la  0.2517 lo  1.54441 lh  0.52
        la  0.0871 lo  1.544721 lh  0.62

    LP_Factor(!th2_monochromator, 0)
    One_on_X(, 252.65415`_305.60101)
    Zero_Error(, -0.02645`_0.00654)
    convolution_step 3
    Rp 217.5
    Rs 217.5
    capillary_diameter_mm    0.06042`_0.00234 max =1.2;
        capillary_u_cm_inv    433.27649`_131.81041
        capillary_divergent_beam
    Simple_Axial_Model(, 0.01097`_805.61880_LIMIT_MIN_0.0001)
    Cylindrical_2Th_Correction(, 0.19605`_0.03052)
    Cylindrical_I_Correction(@, 2.69002`_0.16294)
    prm !c1  0.07263`_0.00060 min 0.00001
    prm !c2  0.02378`_0.00050 min 0.00001
    gauss_fwhm = c1 / Cos(Th);
    lor_fwhm = c2 / Cos(Th);

    for strs 1 to 1 {
        LVol_FWHM_CS_G_L( 0.89, 3399.54958, 0.89, 5340.00000,,,@, 300_3
    .95075 min 30 max 1000)
    }
} 'end of for xdds

'==========
'==Section 6
'==========

 ' This is a shortened list for illustration
#list temp {
310
300
290
...
}
```

F.2.2 Python script

```
 # Hard-coded working directory
opendir = "C:\\NextCloud\\PhD\\rest-of-path\\"
parafile = opendir + "paraPrep\\1_protoPara.inp"
```

```
# Hard-coded template file location
writefile = opendir + "paraPrep\\1_protoPara_py.inp"

skip = [44,46]
sample = "cs10fama"
index = []
for i in range(1,54):
    if not(i in skip):
        index.append(str(i))

section = 0
arrOut = []
arr3 = []
b3 = False

with open(parafile,"r") as ins:
    for i in ins:
        # define section
        if i[0:10] == "'==Section":
            section = int(i[10:len(i)].strip())

        # write arrOut
        if section in (2,3):
            if i[0:3] == "'==":
                arrOut.append(i)

            elif section == 2: # the reference to files here are in single
    lines
                if i.find("XXXXX") >= 0:
                    for j in range(0,len(index)):
                        newstr = i.replace("XXXXX",sample+index[j].zfill(2))
                        newstr = newstr.replace("XXindexXX",index[j])
                        newstr = newstr.replace("XXindex-1XX",
                                                str(int(index[j])-1))
                        arrOut.append(newstr)
                else: # if the inp is not formatted appropriately
    duplication may occur.
                    arrOut.append(i)

            elif section == 3:
                if b3 == False:
                    arr3.append(i)
                if i.strip() == "#endif 'XXflagXX": # requires this flag
                    b3 = True
                    for j in range(0,len(index)):
                        for k in arr3:
                            newstr = k.replace("XXXXX", sample +
                                               index[j].zfill(2))
                            newstr = newstr.replace("XXindexXX",index[j])
                            newstr = newstr.replace("XXindex-1XX",
                                               str(int(index[j])-1))
                            arrOut.append(newstr)
        else:
            arrOut.append(i)

if 0:
    for i in arrOut:
```

```
        print(i.strip("\n"))
else:
    file = open(writefile,'w')
    for i in arrOut:
        file.write(i)
    file.close()

print("written to: \n", writefile)
```

F.3 Modelling a photoluminescence peak with pseudo-Voigt and split pseudo-Voigt models

In modelling photoluminescence data, a split pseudo-Voigt function has primarily been applied to photo-luminescence data where a single peak is present and in cases where a single peak is dominant to the point that analysis of the smaller peaks present becomes unreliable. Where multiple peaks are present, this is modelled using multiple symmetric pseudo-Voigt peaks as discussed in Section 4.6.2.

The algorithms in this section were run as code blocks in *Jupyter* notebooks. A list of file names is first read into *Python*. From these the absorbance vs. wavelength data is read into *Python* as the *arrX* and *arrI* arrays where each entry per array is an array of values corresponding to the file name of the same index.

F.3.1 Setting up equations for pseudo-Voigt and split pseudo Voigt models

```
# #################
# Set up equations
# #################
import numpy as np
Pre4ln2 = 4 * np.log(2) # np.log() is ln() and np.log10() is log base 10

def pvoigt(x, amplitude=1.0, center=0.0, sigma=1.0, fraction=0.5):
    lor = (sigma**2)/((4*((x - center)**2)) + (sigma**2))
    gau = np.exp(-1*(Pre4ln2*((x-center)**2)/(sigma**2)))
```

```
    # Proof: FWHM is given by sigma for gau
    # # assume 1/2 intensity
    # # 1/2 = gau
    # # take ln of both sides
    # # ln(1/2) = -1*(Pre4ln2*((x-center)**2)/(sigma**2))
    # # 1 = 4*((x-center)**2)/(sigma**2)
    # # sigma = 2 * abs(x-center)
    # # sigma = FWHM

    return amplitude * (fraction*lor + (1-fraction)*gau)

def spvoigt(x, amplitude=1.0, center=0.0, sigma=1.0, sigma_r=None, fraction
    =0.5, fraction_r=0.5):
    if sigma_r == None:
        sigma_r = sigma
    left = (x < center) * pvoigt(x, amplitude, center, sigma, fraction)
    right = (x >= center) * pvoigt(x, amplitude, center, sigma_r, fraction_r
    )
    return left + right


def para_spvoigt(x, param):
    amp = param['spV_amplitude'].value
    cen = param['spV_center'].value
    sig = param['spV_sigma'].value
    sig_r = param['spV_sigma_r'].value
    frac = param['spV_fraction'].value,
    frac_r = param['spV_fraction_r'].value
    spvoigt(x, amp, cen, sig, sig_r, frac, frac_r)

def R2(y, fity):
    import math, statistics
    ssres = 0 # sum of squares, residual
    sstot = 0
    meany = statistics.mean(y)
    for i in range(0,len(y)):
        ssres = ssres + math.pow(y[i]-fity[i] ,2)
        sstot = sstot + math.pow(y[i]-meany ,2)
    return (1-(ssres/sstot))
```

F.3.2 Modelling of split pseudo-Voigt peaks

```
# ########################
# Build model and fit
# ########################
from lmfit import Model
from lmfit.models import ConstantModel
from lmfit import Parameters, minimize, report_fit
import matplotlib.pyplot as pl

mod_spV = Model(spvoigt, prefix='spV_')
bkg = ConstantModel(prefix='b_')
mod = mod_spV + bkg
```

```
lim_sig_min = 0
lim_sig_max = 100
lim_cen_min = 380
lim_cen_max = 560
def FitandPlot(i):
    bVerbIters = 0
    R2_round = 10
    Chi_round = 4
    I_max = np.max(arrI[i])
    amp_max = I_max*1.5

    # # Set up paramters for symmetric peak shapes
    paras = Parameters()
    paras.add('spV_center', value=540, min=lim_cen_min,
              max=lim_cen_max, vary=1)
    paras.add('spV_amplitude', value=I_max, min=0, max=amp_max, vary=1)
    paras.add("spV_sigma", value=1,
              min=lim_sig_min, max=lim_sig_max, vary=1)
    paras.add("spV_sigma_r", expr="spV_sigma",
              min=lim_sig_min, max=lim_sig_max)
    paras.add("spV_fraction", value=0.5, min=0, max=1, vary=1)
    paras.add("spV_fraction_r", expr="spV_fraction",
              min=0, max=1, vary=1)
    paras.add("b_c", value=0, min=0, max=500, vary=1)

     # First optimisation, least-squared method
    out = mod.fit(np.array(arrI[i]), paras, x=np.array(arrX[i]))
    if bVerbIters:
        print(i,": R2 (1st LSq): \t\t\t\t",round(R2(arrI[i], out.eval()),
    R2_round),
              ", Chi2:", round(out.chisqr,Chi_round))
     # Second optimisation, Nelder method
    out = mod.fit(np.array(arrI[i]), out.params, x=np.array(arrX[i]),
                  method="nelder")
    if bVerbIters:
        print(i,": R2 (2nd nelder): \t\t\t\t",round(R2(arrI[i], out.eval()),
    R2_round),
              ", Chi2:", round(out.chisqr,Chi_round))

      # Refine asymmetric peak shapes
    out.params["spV_fraction_r"].set(expr=None,
                                     value=out.params["spV_fraction"].value,
                                     vary=1)
    out.params["spV_sigma_r"].set(expr=None,
                                  value=out.params["spV_sigma"].value,
                                  vary=1)

    out = mod.fit(np.array(arrI[i]), out.params, x=np.array(arrX[i]),
                  method="Leastsq")

    R2_val_old = 0
    R2_val = R2(arrI[i], out.eval())
    if bVerbIters:
        print(i,": R2 (3rd LSq, right != left (freed)): \t",round(R2(arrI[i
    ], out.eval()),R2_round),
              ", Chi2:", round(out.chisqr,Chi_round))
```

```
        print()

      # Repeat the fitting process until the fit stops improving by a given
    tollerence
    while (abs(R2_val - R2_val_old) > 0.00001):

        R2_val_old = R2_val

        out = mod.fit(np.array(arrI[i]), out.params, x=np.array(arrX[i]),
                      method="nelder")
        R2_val = float(R2(arrI[i], out.eval()))

        out = mod.fit(np.array(arrI[i]), out.params, x=np.array(arrX[i]),
                      method="Leastsq")
        R2_val = float(R2(arrI[i], out.eval()))

    R2_val = float(R2(arrI[i], out.eval()))

    print(i,": R2 (Final LSq, right != left (freed)): \t",
          round(R2_val,R2_round), ", Chi2:", round(out.chisqr,Chi_round))

    if R2_val < 0.995 or 0:
        out.plot_fit()
        pl.plot(arrX[i], -1*out.residual, label="residue")
        pl.legend()
        pl.show()
        print(out.fit_report(min_correl=0.25))
        print("\n")
    else:
        print("\n")

    return out

# Control for single vs bulk execution
if 0:
    i = 0
    FitandPlot(i)
else:
    out2 = []
    for i in range(0, len(arrX)):

    out2.append(FitandPlot(i))from lmfit import Model
```

F.3.3 Modelling of multiple pseudo-Voigt peaks

```
from lmfit import Model
from lmfit.models import ConstantModel
from lmfit import Parameters, minimize, report_fit
import matplotlib.pyplot as pl

lim_sig_min = 0
lim_sig_max = 20
```

```
def FitandPlot(i, mod, peaks = [[540, 390, 560]]):
    bVerbIters = 0
    R2_round = 10
    Chi_round = 4
    I_max = np.max(arrI[i])
    amp_max = I_max*1.5

    # # Set up paramters for symmetric peak shapes
    paras = Parameters()
    for j in range(0, len(peaks)):
        paras.add("pV"+str(j)+"_center", value=peaks[j][0],
                  min=peaks[j][1], max=peaks[j][2], vary=1)
        paras.add("pV"+str(j)+"_amplitude", value=I_max,
                  min=0, max=amp_max, vary=1)
        paras.add("pV"+str(j)+"_sigma", value=1,
                  min=lim_sig_min, max=lim_sig_max, vary=1)
        paras.add("pV"+str(j)+"_fraction", value=0.5,
                  min=0, max=1, vary=1)
    paras.add("b_c", value=0, min=0, max=500, vary=1)

    out = mod.fit(np.array(arrI[i]), paras, x=np.array(arrX[i]))
    R2_val_old = 0
    R2_val = R2(arrI[i], out.eval())
    print(i, filename(files[i]))

    # Repeat the fitting process until the fit stops improving by a given
    tollerence
    while (abs(R2_val - R2_val_old) > 0.00001):
        if bVerbIters:
            print("Delta(R2):", R2_val - R2_val_old)
        R2_val_old = R2_val

        out = mod.fit(np.array(arrI[i]), out.params, x=np.array(arrX[i]),
                      method="nelder")
        R2_val = float(R2(arrI[i], out.eval()))

        out = mod.fit(np.array(arrI[i]), out.params, x=np.array(arrX[i]),
                      method="Leastsq")
        R2_val = float(R2(arrI[i], out.eval()))

    R2_val = float(R2(arrI[i], out.eval()))
    print(i,": R2 (Final LSq: \t",round(R2_val,R2_round), ", Chi2:",
          round(out.chisqr,Chi_round))
    if 1:
        pl.rcParams.update({'font.size': 18})
        out.plot_fit()
        pl.plot(arrX[i], -1*out.residual, label="residue")
        pl.legend()
        point = filename(files[i]).replace("_0p","_0.").replace("_1p","_1.")
        pl.title(point)
        pl.ylabel("Intensity (counts)")
        pl.xlabel("Wavelength (nm)")
        if 0:
            pl.savefig(incrPathName(fileext(files[i], 0) +
                       "_PL-fitted",".png"))
        pl.show()
        print(out.fit_report(min_correl=0.25))
```

```
        print("\n")

    return [out, R2_val]


  # Manually set peak initial position and limits for files no. 10 - 12
peaks_mid = [440,430,450],[460,450,470],[480,470,485],[490,485,500]
  # Manually set peak initial position and limits for file no. 13
peaks_13 = [458,440,465],[476,472,480],[492,490,494],[502,500,503]

mod_mid = ConstantModel(prefix='b_')
for i in range(0, len(peaks_mid)):
    mod_mid = mod_mid + Model(pvoigt, prefix="pV"+str(i)+"_")

if 0:
    i = 0
    FitandPlot(i)
else:
    out3 = []
    for i in range(0, len(arrX)):
        if i == 2:
            pass
        elif i in range(10,13):
            lim_sig_max = 20
            out3.append([filename(files[i])] +
                        FitandPlot(i, mod_mid, peaks_mid))
        elif i == 13:
            lim_sig_max = 30
            out3.append([filename(files[i])] +
                        FitandPlot(i, mod_mid, peaks_13))
```